Fundamentals of Ergonomic Exoskeleton Robots

André Schiele

Fundamentals of Ergonomic Exoskeleton Robots

Proefschrift

ter verkrijging van de graad van doctor
aan de Technische Universiteit Delft,
op gezag van de Rector Magnificus prof. dr. ir. J.T. Fokkema,
voorzitter van het College voor Promoties,
in het openbaar te verdedigen op woensdag 14 mei 2008 om 10:00 uur

door

André SCHIELE

Diplom-Ingenieur für Mikrosystemtechnik,
University of Applied Sciences Kaiserslautern,
geboren te Bad Bergzabern, Duitsland

Dit proefschrift is goedgekeurd door de promotor:
Prof. dr. F.C.T. van der Helm

Dit proefschrift is goedgekeurd door de promotor:
Prof. dr. F.C.T. van der Helm

Samenstelling promotiecommissie:
Rector Magnificus, voorzitter
Prof. dr. F.C.T. van der Helm, Technische Universiteit Delft, promotor
Prof. Dr. Ing. G. Hirzinger, DLR, Technische Universität München
Prof. dr. A.M.L. Kappers, Universiteit Utrecht
Dr. ir. R.Q. van der Linde, Technische Universiteit Delft
Prof. dr. ir. R.H. Munnig Schmidt, Technische Universiteit Delft
Dr. C. Stavrinidis, ESTEC/ESA, European Space Agency
Prof. dr. ir. M. Steinbuch, Technische Universiteit Eindhoven
Prof. dr. ir. P.P. Jonker, Technische Universiteit Delft, reservelid

ISBN: 978-90-8559-379-9

Preface

With this thesis, I would like to lay the foundations for designing human interfacing wearable exoskeleton robots that are truly designed *for* the human.

Before starting the development of the first human arm exoskeleton prototype, tasked to telemanipulate a space robot, I extensively searched for prior art in databases to potentially find guidelines on how to design a wearable robotic exoskeleton.

Information was very scarce, however, and I found only a handful of information at all. Previous records have either shown device concepts only, incomplete devices or devices built to interact with only a sub-set of joints of the human arm. No record has provided evidence of a successful robot control with a portable exoskeleton, let alone with force-feedback to the operator. Not even to speak of finding quantitative analyses about the goodness of physical human–robot interaction or about bilateral control performance with such exoskeletons. Most of the reference material rather raised new questions than providing answers to me.

I noticed that previous exoskeleton devices had been designed similar to typical robotic manipulators, but aiming to encapsulate the human limb. This was done despite the fact that *artificial* robotic systems are fundamentally different in structure from *biological* human limbs. Moreover, all prior exoskeletons had been developed with anthropometric data of specific individuals. This seemed like a wrong approach to me and inspired me to investigate how these fundamental differences between robots and humans can be harmonized. I was motivated to start this scientific research about finding the fundamentals of ergonomic exoskeleton design.

Now, a couple of years later, I can present with this thesis a novel quantitative analysis approach for assessing combined physical human–exoskeleton interaction. The theory presented allows the design analysis and evaluation of exoskeletons, and the solutions provided offer a clear set of design guidelines helpful to the community in the future.

The guidelines show, on scientific grounds, how to best conceive exoskeleton kinematics, motorization and mechanical structures for enabling smooth and comfortable physical human robot interaction with portable exoskeletons.

Technological solutions are proposed as well, that allow conceiving of lightweight exoskeletons with little apparent inertia and good force-feedback performance for robotic telemanipulation. The feasibility of developing a portable and body-grounded exoskeleton for the entire human arm is shown for the first time. It is proven that the device can interact seamlessly with natural motion of the human arm, without variation of its mechanical structure, for different operators. A new paradigm for the design of kinematic exoskeleton structures is developed, as well as a novel actuator concept, based on Bowden Cable transmissions.

The results presented in this thesis provide the lacking theoretical fundament and the technological solutions, which together enable the design of physically interacting human–robot systems that are truly conceived *for* the human.

André Schiele, 2008

Contents in Brief

Preface v

Summary ix

1. Introduction 1

Part I: Ergonomic Design Principles

2. Kinematic Compatibility Between Human Limbs and Exoskeleton Structures 19
3. Kinematic Design to Improve Ergonomics in Human Machine Interaction 25

Part II: Validation of Ergonomic Design

4. An Explicit Model to Predict and Interpret Constraint Force Creation in pHRI with Exoskeletons 53
5. Influence of Attachment Pressure and Kinematic Configuration on pHRI with Wearable Robots 67

Part III: Robot Control

6. Kinematic Redundancy in Exoskeleton Systems 95
7. Towards Intuitive Control of Space Robots: A Ground Development Facility with Exoskeleton 101

Part IV: Actuation

8. Bowden Cable Actuator for Force-Feedback Exoskeletons 117
9. Performance Difference of Bowden Cable Relocated and Non-Relocated Master Actuators in Virtual Environment Applications 129

Part V: Exoskeleton Prototypes

10. The ESA Human Arm Exoskeleton for Space Robotics Telepresence 145
11. The Ergonomic EXARM Exoskeleton 159

12. Discussion 169

13. Future Directions 183

14. Conclusions 189

References 193

Summary

This thesis is the first to provide the fundamentals of ergonomic exoskeleton design. The fundamental theory as well as technology necessary to analyze and develop ergonomic wearable robots interacting with humans is established and validated by experiments and prototypes. The fundamentals are (1) a new theoretical framework for analyzing physical human robot interaction (pHRI) with exoskeletons, and (2) a clear set of design rules of how to build wearable, portable exoskeletons to easily and smoothly interact with varying users in a haptic telemanipulation scenario. The fundamentals aim at providing the basis for truly human compatible exoskeleton design from a human as well as technological perspective.

Since decades engineers have tried to develop robot manipulators that resemble us in external form and shape. To execute tasks for us remotely, with similar or better dexterity than ourselves. We have sent robots to explore outer space, to research the depths of our oceans and to access many other places that are otherwise impossible or dangerous for us to reach. Since decades research is being performed to enhance robotic remote control. Since decades we have tried to build telepresence systems with man–machine interfaces that allow us to feel fully in place of such robots. In an ideal *telepresence* system, the body's exteroceptive senses, as well as sensory and motor capabilities would be tightly interwoven with the perception, sensing and activation of the remotely located robot. It is the ideal goal of master–slave *telemanipulation*, with robotic exoskeletons, to extend our physical proprioception to the robotic manipulators, while lending our cognitive capabilities to plan the higher levels of the task. Exoskeletons are robots worn around the human limbs to sense and apply movement and forces, e.g. to the human arm. They could be ideal interfaces for achieving the goals of telemanipulation.

The key problem with prior exoskeletons is their limited ability to physically interact with the human. Ideally, the exoskeleton's sensorics, mechanics, actuator systems and motor controllers would be transparent – meaning to not filter, to the extent noticeable by a human, the incoming or outgoing flow of information. However, existing actuated exoskeletons for the human arm are still (1) bulky and heavy and therefore unable to interact with all joints of the human arm. They (2) limit the natural workspace of the human limb and are reported to be (3) uncomfortable to use, especially for long durations. It has been recognized that they (4) place kinematic constraints on the human limbs during movement, but the detailed reasons have neither been analyzed nor resolved. Since the development of exoskeleton systems is still emerging from its childhood, no rigorous analysis of the interaction with human limbs has been provided or formulated theoretically. A major difficulty reported earlier is the conception of appropriate kinematic structures that can fit to varying users. This is due to the (5) difficulty of obtaining statistical data about human anthropometry and its distribution.

Now, exoskeletons still (6) require complex alignment and calibration procedures for each new user, which is time-consuming and causes long dress-on times.

Another source of problems is the lightweight and compact technological implementation of exoskeletons. This has not been achieved due to (7) lack of appropriate materials and (8) lack of appropriate actuator technologies.

For those reasons, the design of wearable exoskeletons has been recognized as a major challenge. Still no wearable actuated exoskeleton has been proposed since the research started in this field over 36 years ago, that would be able to interact with all joints of the human arm, let alone with varying users. Instead, existing devices either attach to the hand only (hence they are not wearable and able to actuate all joints, thus, actually not exoskeletons) or match their joints only to a sub-set of human joints, for specific operators. Such challenges have, up to now, prevented usability of exoskeleton devices on a larger scale.

The goal of this thesis is to search and establish the fundamentals of ergonomic exoskeleton design. This research was motivated by the need of building exoskeletons that can be used truly naturally by a large range of users for force-feedback *haptic* telemanipulation. It is the goal to find out how a *truly human compatible* exoskeleton can be conceived, that is lightweight, compact, comfortable and does not otherwise limit the human performance – a device that is transparent. In particular, the goals of this thesis are:

- To research how a kinematic exoskeleton structure can be made robust to the variation of physical parameters between users.
- To investigate the human reception to such ergonomic exoskeletons with regard to the optimum of extended physiological proprioception.
- To research how an ergonomic exoskeleton can be used to control non human-like robots.
- To investigate how an actuation system needs to be designed to enable implementing a lightweight, compact and portable exoskeleton that can create body-grounded force-feedback.

The solutions of this research are applied to the development of an arm exoskeleton, as intuitive interface for astronaut crew to control an anthropomorphic space robot manipulator. Yet, the goals of this research are generic and fundamental.

This thesis approaches the problem of human compatible exoskeletons by: (1) investigating and establishing, for the first time, the basic theory necessary to analyze physical human–exoskeleton interaction; (2) the formulation of appropriate and generic design goals for kinematic, mechanical and actuator systems of exoskeletons, and; (3) the experimental validation of the design goals by means of a series of successive prototypes.

A novel, nine degree of freedom kinematic model of the human arm has been established, that supports the analysis of combined human arm and exoskeleton interaction in *multiple degree of freedom* movement. The model is distinguished by it's accurate prediction of natural human limb motion in the entire workspace. A simulation approach is elaborated, that allows verification of interaction capability of kinematic exoskeleton structures already at the design stage. Furthermore, an explicit physical human–robot interaction (pHRI) model is established and validated for *single degree of* *freedom* interaction analysis. The model is used to investigate and analyze the causes of interface force creation between human and exoskeletons and to research the influence of kinematic constraints. The pHRI model is based on real geometric design parameters of an exoskeleton and allows optimization of kinematic parameters of an exoskeleton to reduce interface loads. Both models together provide a basic set of tools that can be used for exoskeleton design, analysis and optimization.

They were instrumental in defining the kinematic design goals for ergonomic exoskeletons, that state that: An exoskeleton must be explicitly *non-anthropomorphic* in its kinematic structure and wearable, to be truly human compatible. It needs to offer the same range of motion than the human limb, must explicitly not copy their kinematic structure to be robust to misalignment and not possess more than six degrees of freedom between two consecutive attachments. In order to enable a lightweight, compact and portable implementation of an exoskeleton, a second design goal was established to state that some of the actuators of the device should be relocated from the mechanical structure by means of Bowden Cable transmissions, in order to enable the reduction of mechanical complexity. In order to make the overall implementation of an ergonomic exoskeleton feasible, a third design goal is stated, postulating that some joints of the exoskeleton kinematic structure should be passive, non-actuated.

In order to validate those goals, a series of four prototypes was developed and successfully tested. Two full arm exoskeletons were built incorporating an ergonomic kinematic structure. The first, was used to validate the simulation predictions of multiple degree of freedom interaction in an experiment that determined the total available workspace. The second was used to analyze for the very first time the causes and effects of interface forces and kinematic constraints. It was used in a single degree of freedom experiment to quantify the magnitudes of such forces and to determine the effects of their variation on subjective and objective performance metrics in a tracking task. To analyze the advantages of the exoskeletons kinematic structure towards prior designs, some of the passive compensatory joints in its structure could be locked. It's kinematic design was then optimized with the geometrical pHRI model, by parameter estimation. Two novel Bowden Cable based actuators were developed to analyze and test their suitability of well performing in a typical bilateral force-feedback telemanipulation scenario with real and virtual slave joints. They are benchmarked against low-reduction direct drive actuators, which are typical for other haptic devices. The second full arm exoskeleton prototype was implemented successfully to demonstrate master–slave control with a redundant robotic manipulator. In experiments it was determined whether it provides a more intuitive interface than conventional joystick-type interfaces.

The major conclusions from this research are: Prior exoskeleton devices were designed with wrong assumptions on the human anatomic structure. All prior wearable prototypes required aligning their joints to the human joints. It is shown by experimental results that such non-ergonomic exoskeletons create large interaction forces during movement and it is shown that such interaction forces are responsible for a limitation of workspace. The interface forces are proven to stem from misalignments between the centres of rotation of exoskeleton and human limb and it is shown by experimental

results that alignment is not possible. To conceive of ergonomic exoskeleton structures, they must not require alignment to the human joints.

The kinematic design goals stated above are validated. An exoskeleton with such kinematic structure does not need alignment, is able to interact with an unprecedented portion of the natural limb workspace, with all joints of the human arm, creates significantly smaller interface forces, causes a decreasing mental load of operators during a tracking task, and can be dressed on quickly and easily. It is shown that the ergonomic design improves the overall human performance in a tracking task. These advantages, moreover apply to different operators with large variation of statures and mass, which makes *non-anthropomorphic* exoskeletons robust to variation of individuals.

An exoskeleton with non-anthropomorphic structure provides an intuitive interface for control of an anthropomorphic robot of equal or different kinematic structure. It reduces task execution times with respect to joystick-type interfaces.

It is feasible to build low mass, compact and portable ergonomic exoskeletons since their actuators can be relocated and some of their joints can be passive. Bowden Cable relocated actuators reach similar contact stiffness, low free movement friction and stability in hard contact situations than low reduction direct drive motors in typical haptic, force-feedback scenarios. They increase by multiple times the power density and specific power of the movable exoskeleton structure. The remote actuation of an exoskeleton by such transmissions is an enabling technology for portability and lightweight design.

An optimum synthesis between compactness of exoskeletons and performance in a control with force-feedback can be achieved by using the new Bowden Cable actuators for the proximal joints in an exoskeleton, where human torque sensing resolution is low, and using direct drive actuators with low gear reduction in the distal joints of an exoskeleton, where human torque sensing resolution is higher. This choice of actuation suits the human sensing capabilities best and reduces mass of the exoskeleton optimally, which enables portability and good haptic feedback – without compromising on human performance.

With the models, tools and design fundamentals presented in this thesis it is possible to design exoskeletons for the first time such, that they are *independent from individual anthropometry* and thus, truly compatible with humans while being wearable and portable. This makes their design and implementation significantly easier for the researchers to come and opened the way for using exoskeletons for a broad range of applications in the future.

Contents

Preface v

Contents in Brief vii

Summary ix

Contents xiii

1. Introduction **1**
- 1.1 Fundamentals of Ergonomic Exoskeleton Robots 1
- 1.2 A brief introduction to telemanipulation 2
- 1.3 Arm Exoskeletons – State of the Art 5
  - 1.3.1 Arm Exoskeletons for bilateral robot control 5
  - 1.3.2 Arm Exoskeletons for human power enhancement 6
  - 1.3.3 Arm Exoskeletons for virtual environment applications 7
  - 1.3.4 Arm Exoskeletons for neuro-rehabilitation 7
- 1.4 Problem Statement 9
  - 1.4.5 Key problems 11
  - 1.4.6 Overcoming current problems with exoskeletons 12
- 1.5 Motivation 12
  - 1.5.1 Haptic Exoskeleton for Space Robotics 12
- 1.6 Goal 14
- 1.7 Approach 14
- 1.8 Thesis Outline 16

Part I: Ergonomic Design Principles

2. Kinematic Compatibility Between Human Limbs and Exoskeleton Structures **19**
- 2.1 Introduction 20
- 2.2 Causes of kinematic incompatibility and their negative effect 20
- 2.3 Overcoming kinematic incompatibility 22

3. Kinematic Design to Improve Ergonomics in Human Machine Interaction **25**
- 3.1 Introduction 26
- 3.2 Problems of current rehabilitation robot designs 27
  - 3.2.1 Wearable devices and problems related with alignment 27
  - 3.2.2 End-effector based robotic devices and problems related to redundancy 30
- 3.3 Design goals for ideal human robot interaction in rehabilitation 30

3.4 Method 31
    3.4.1 Procedure for ergonomic design 31
    3.4.2 Model of the human arm 32
    3.4.3 Human arm motion simulation 34
    3.4.4 Kinematic design 37
3.5 Results 37
    3.5.1 Ergonomic design for human arm exoskeleton 37
        Interaction with the shoulder-girdle 38
        Interaction with the elbow 40
        Interaction with the wrist 42
    3.5.2 Prototype 44
    3.5.3 Experiments 45
3.6 Discussion 47
3.7 Conclusion 50
3.8 Acknowledgment 50

Part II: Validation of Ergonomic Design

4. An Explicit Model to Predict and Interpret Constraint Force Creation in pHRI with Exoskeletons 53
4.1 Introduction 54
4.2 pHRI Model 55
    4.2.1 Approach 55
    4.2.2 Mechanical Model for single D.o.F. pHRI 55
4.3 pHRI model identification 59
    4.3.1 Goal 59
    4.3.2 Experiment Method 59
    4.3.3 Experiment Data 60
    4.3.4 Identification procedure 61
4.4 Results 61
    4.4.1 Measurements of constraint forces F_d during experiments 61
    4.4.2 Model outputs for constraint displacements d_{tot} 62
    4.4.3 Model identification with “locked” data set 63
        Resulting model parameters 63
        Model validation 63
    4.4.4 Constraint force difference in “unlocked” and “locked” exoskeleton setting 64
4.5 Discussion 64
4.6 Future work 66
4.7 Conclusion 66

5: Influence of Attachment Pressure and Kinematic Configuration on pHRI with Wearable Robots 67
5.1 Introduction 68

5.2 Rationale 69
5.3 Method 70
  5.3.1 Experimental setup 70
  5.3.2 Experiment protocol 70
  5.3.3 Statistical design and analysis 72
    Independent Variables 72
    Dependent Variables 72
    Statistical analysis 73
5.4 pHRI model 74
  5.4.1 Model structure 74
  5.4.2 Model parameter estimation 75
5.5 Results 76
  5.5.1 Interaction force prediction from pHRI model 76
  5.5.2 Measured Interaction Forces and Torques 76
  5.5.3 Identification of pHRI model parameters from measured interaction forces in *L* condition 79
  5.5.4 Signal tracking performance 81
  5.5.5 Voluntary range of motion 81
  5.5.6 Motion of passive compensatory joints 82
  5.5.7 Preferred attachment pressure of the subject group 82
  5.5.8 Subjective metric I: comfort questionnaire 83
  5.5.9 Subjective metric II: motion hindrance questionnaire 83
  5.5.10 Subjective metric III: NASA TLX ratings 83
5.6 Discussion 85
5.7 Future work 90
5.8 Conclusion 90
5.9 Appendix 90
5.10 Acknowledgment 91

Part III: Robot Control

6. Kinematic Redundancy in Exoskeleton Systems 95
6.1 Introduction 96
  6.1.1 Types of kinematic redundancies 96
  6.1.2 Advantages of redundant systems 97
6.2 Redundancies in human–exoskeleton systems 97
  6.2.1 Matching redundancy at the human–robot interfaces 98

7. Towards Intuitive Control of Space Robots: A Ground Development Facility with Exoskeleton 101
7.1 Introduction 102
7.2 Implementation 103
  7.2.1 Overview 103
  7.2.2 Eurobot prototype 104

Mechanical setup 104
Controllers 105
7.2.3 Robot workstation 105
Overview of experiment software 105
Summary of control approach 107
Graphical user interface 108
Joystick interface 108
7.2.4 Exoskeleton 108
Description of the mechanical system 108
Exoskeleton workstation 109
7.2.5 Virtual reality workstation 110
7.3 Experimental validation 111
7.3.1 Experimental setup 111
7.3.2 Discussion of first results 111
Trajectory tracking 111
Task execution duration 112
7.3.3 Summary of first experiment results 113
7.4 Conclusions and future work 113

Part IV: Actuation

8. Bowden Cable Actuator for Force-Feedback Exoskeletons 117
8.1 Introduction 118
8.2 Geometric characteristics of Bowden cable transmissions 119
8.2.1 Implementation 119
8.2.2 Specific Bowden system characteristics 119
8.3 Bowden cable transmission in force feedback 124
8.3.3 Mechanical setup 124
8.3.4 Controller 125
8.3.5 Force-feedback performance experiments 125
8.4 Future work 128
8.5 Conclusions 128

9. Performance Difference of Bowden Cable Relocated and Non-Relocated Master Actuators in Virtual Environment Applications 129
9.1 Introduction 130
9.2 Overview of experimental setup 131
9.2.1 Architecture of haptic loop simulator 131
9.2.2 Master actuator I: direct drive motor with cable capstan reducer 131
9.2.3 Master actuator II: direct drive motor with cable capstan reducer and Bowden cable transmission 132
9.2.4 Haptic loop controller implementation 133
9.2.5 Slave joint simulator and visualization client 134
9.3 Method 135

9.4 Results 136
    9.4.1 Torque and position tracking capability 136
    9.4.2 Residual friction torques in cyclic free movement 137
    9.4.3 Contact stiffness in hard contact situations 138
9.5 Discussion 139
9.6 Future work 140
9.7 Conclusion 140

Part V: Exoskeleton Prototypes

10. The ESA Human Arm Exoskeleton for Space Robotics Telepresence 145
10.1 Introduction 146
10.2 A brief review about drawbacks of prior exoskeletons 148
10.3 Design requirements 149
10.4 Design methodology 149
10.5 Approach 149
10.6 Results from mechanism design 152
10.7 Description of the prototype 152
    10.7.1 The shoulder assembly 153
    10.7.2 The elbow assembly 154
    10.7.3 The wrist assembly 154
    10.7.4 Tendon actuation 155
10.8 Novelties 156
10.9 Future work 156

11. The Ergonomic EXARM Exoskeleton 159
11.1 Introduction 160
11.2 Challenges and innovation for an ergonomic exoskeleton 161
11.3 The EXARM implementation 162
    11.3.1 Mechanical 162
    11.3.2 Motorization 165
    11.3.3 Interface to Eurobot 166
11.4 Summary and conclusion 167

12. Discussion 169
12.1 Recapitulation of the goal 169
12.2 Fundamentals of ergonomic exoskeletons 170
12.3 On mechanical design 173
12.4 On human acceptance 174
12.5 On robot control 176
12.6 On actuation 178
    12.6.1 Single degree of freedom actuation 178
    12.6.2 Full actuation 180

13. Future Directions **183**
13.1 The new X-Arm-II exoskeleton 183
  13.1.1 Mechanical improvements 184
  13.1.2 Actuator implementation 185
13.2 Exoskeleton motor control and actuator system 186
13.3 Bowden cable actuator identification 187
13.4 Multi-axis robot control with force feedback 187
13.5 Man–machine interface comparisons 187
13.6 Materials for flight model exoskeleton 188

14. Conclusions **189**

References **193**

Acknowledgment **201**

Curriculum Vitae **205**

Chapter 1

Introduction

1.1 Fundamentals of Ergonomic Exoskeleton Robots

The topic of this thesis is the search for the fundamentals of ergonomic exoskeleton robots. This search is motivated by the need to provide design guidelines and performance metrics to design and analyze exoskeletons that are able to smoothly and naturally interact with the human limbs. This knowledge is a fundamental requirement to build exoskeletons for long duration use, such as for tele-robotics, power enhancement or robotic rehabilitation applications. No such fundamentals exist until today.

In this chapter, first, a general introduction to tele-robotics is provided (Section 1.2), which is the reference application for the exoskeleton developed in the frame of this work. It is shown for which cases human arm exoskeleton robots are required. Next, results of a systematic literature review (Section 1.3) show that no prior attempts of developing fully actuated, portable human arm exoskeletons have succeeded until the start of this thesis in 2003. The major problems encountered (Section 1.4) during those efforts are shown to be (1) the lack of design requirements, (2) the difficulty of conceiving an appropriate kinematic structure suitable for interaction with varying operators, (3) the difficulty of implementing a compact and lightweight design with existing actuator technologies. It is shown (Section 1.5) why the limitations of prior developments need to be overcome for building an exoskeleton haptic device for space robotics. The goal of this thesis (Section 1.6) is to establish fundamental design guidelines for exoskeletons that are natural and intuitive to use by varying operators, that are comfortable, lightweight, portable and offer good performance in a haptic telemanipulation scenario. These goals are achieved (Section 1.7) by, (1) investigating and establishing the basic theory of physical human–exoskeleton interaction, (2) the formulation of appropriate generic design goals for kinematic and actuator systems, and (3) the successful validation by means of prototypes as outlined in Section 1.8.

1.2 A brief introduction to telemanipulation

Whenever places of work are difficult or dangerous to access by humans, it is preferred to let a machine, or a robot, execute the task for us remotely. This is the case, for instance in nuclear “hot” cells, in underwater and deep-sea worksites, or in non-accessible environments such as interplanetary space.

If places are not reachable by humans themselves, robots can be pre-programmed to execute well defined tasks alone, in purely automatic control. An example of this is e.g. the investigation of planetary surfaces by autonomous planetary rovers such as with the Mars Exploration Rover (MER) (Squyres et al. 2003), Soujourner (Golombek et al. 1999) or the Nanokhod (Schiele et al. 2008) rovers. In such a scenario, also called *tele-operation*, tasks of the robot are pre-programmed and sequenced by humans and then executed on-board the machine without human supervision. The human–robot interaction typically takes place on a *once a day* timescale. In the case of planetary rovers certain local autonomy is available on board, to prevent disastrous failures happening to the robot that could stem from unforeseen situations. Such unforeseen events can be e.g. the presence of a non-forecasted surface geometry that could tip over the vehicle, or anomalies such as sudden change in environment variables like temperature, winds, particle events, and so forth.

In other cases, despite the fact that a place is reachable by humans, it is safer for a robot to execute the tasks for the human. Imagine performing works inside a hot nuclear cell, for instance, within a research laboratory for nuclear technologies. It is safer to control a robot immersed into the hot-cell from outside. In such a scenario, the human interfaces to the robot in a much shorter time-scale. Preferably, the human operator can control the robot *ad-hoc*, which means that actions of the robot are executed nearly simultaneously with the input of the human user. In such *tele-manipulation* systems, the human performs the task-level coordination and planning of the robot and commands the low-level motion execution to the robot. The human acts as the master and the robot as an immediate slave in this so-called *master–slave* control scenario.

Indeed, some of the first telemanipulation systems were developed for nuclear operations within the Marshall Programme at the Argonne National Laboratory in the U.S. (Johnson and Corliss 1967). But quickly, the use of such systems spread also to other fields, such as underwater robotics, remote control of de-mining vehicles (Parker and Draper 1998), and ultimately also to space robotic applications in near earth orbit (Ruoff 1994) (Oda et al. 1999). The use of master–slave control became an ideal tool for real-time operation in remote, unstructured or un-modelled environments. This was enabled by the quick dawn of the computer age in the 1970ies, which suddenly enabled controlling robots that were dissimilar to the master device and even relocated physically through data networks such as the internet or dedicated communication links. Fig. 1.1 depicts the typical elements of a telemanipulation system. The human operator interacts with the man–machine interface, the master device. This in turn interacts via its controllers and communication channels with the slave device, in the depicted case a simple robot manipulator. And the slave robot interacts with the environment.

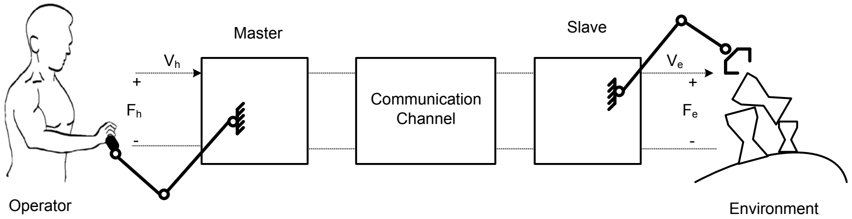

Fig. 1.1. Schematic illustration of a Master–Slave bilateral telemanipulation. Force and velocities existing between slave and environment (V_e, F_e) should ideally exactly be reproduced between the human operator and the master device (V_h, F_h).

In *bilateral* telemanipulation, the goal is to link the human as closely to the robot as possible. It is the idea to transmit velocities V_e and force F_e experienced between the slave and environment to the human and the master such that the transmission is as transparent as possible. Then, the human can feel fully in place of and acting on behalf of the robot. These force-feedback systems are called *haptic* or *telepresence* systems, relating to the sense of touch they can transmit from the robot to the human operator. In this thesis, we will focus on haptic devices for force-feedback.

It is logical that haptic telemanipulation will be the better and more intuitive for the operator, the less the systems between human and environment influence the exchange of information. Theoretical analysis of such master–slave systems has been introduced by Hannaford, then at JPL (Hannaford 1989a) (Hannaford 1989b) and Sheridan at the M.I.T. Their approach to model the system as a two-port network allows predicting performance in terms of teleoperator control stability. Based on this introduction of network based modelling, many more researchers have deepened the field of telemanipulation modelling. New controllers were introduced, e.g. based on passivity theory, that could cope with the presence of time delay (Anderson and Spong 1989) and performance evaluation was extended to define the teleoperator system transparency (Lawrence 1993). Transparency conditions were defined for instance by (Hashtrudi-Zaad and Salcudean 2002) for time-delayed teleoperation. Many control architectures have been introduced since, to optimize the teleoperator system performance.

At the highest level, however, at the level of the mechanical, kinematic and mechantronic design of the input and output devices already a significant improvement on the overall efficiency of the teleoperator system can be achieved.

The ultimate question to ask is how we can best make a human feel at home as part of a telepresence system? Should we match the human to the machine or the machine to the human?

It is usually easier for a human operator to learn and work with teleoperators that have been matched to him rather than the inverse. Cognitive load decreases if the system to control behaves similar to the operator body and the control becomes more intuitive. This is why, in the past decades, robots used as slave devices have become more human like, anthropomorphic in structure. The first master–slave devices developed for nuclear task, were simple mechanically linked systems featuring only

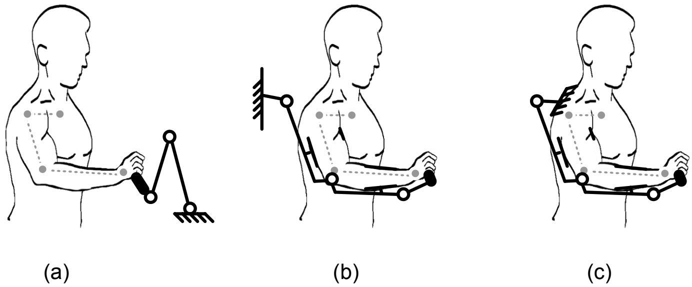

Fig. 1.2. The three main categories of master input devices for haptic telemanipulation. (a) encounter devices, (b) wall grounded exoskeletons, (c) body grounded exoskeletons

few degrees of freedom (Goertz 1964) and grippers which did not allow execution of fine manipulation tasks. Today, slave robots are agile dexterous systems that allow manipulation in complex environments with nearly human-like hands and skill. With mostly seven degrees of freedom (d.o.f.) or even more, such robots can steer their end-effectors through the workspace while adapting their configuration to avoid obstacles or to minimize energy consumption. More detail about the control of such redundant devices is given in Chapter 6. Robots such as the generation of lightweight robots of the German Aerospace Centre LWR-II (Hirzinger et al. 2001) and LWR-III (Hirzinger et al. 2002), the NASA robonaut arms (Ambrose et al. 2000), or even industrial robots such as the PA-10 (Mitsubishi-Heavy-Industries-Ltd.) are relatively similar in external size and structure to the human arm. In a telemanipulation scenario, they can perform with great dexterity and agility, similar to the capabilities of the human. If equipped with dexterous end-effectors, such as dextrous robotic hands (Butterfass et al. 2001), (Jacobsen et al. 1986), they can grasp objects of varying size and shape naturally and carefully. The similarity of the slave device to the human arm and hand, naturally asks for an appropriate master device as well.

Mainly three different classes of master input devices for force-feedback telemanipulation exist. Fig. 1.2 depicts encounter-type devices in (a), externally-mounted wearable robots in (b) and the concept of body-grounded portable robots in (c).

Encounter devices were the first ones to be used in telemanipulation. They are typically mounted on a static surface and only the tip, or *end-effector* is operated by the human. Force-feedback joysticks such as the first notable two degree of freedom (d.o.f.) haptic device (Adelstein and Rosen 1992) or the three d.o.f. magnetically levitated device Maglev developed and used for teleoperation by Salcudean (Salcudean et al. 1995) are typical encounter devices. More recently, commercial devices such as e.g. the Delta Device have been proposed (Grange et al. 2001). But also more complex devices offering a greater working range belong to this class, such as for instance the 6 d.o.f. JPL Hand Master (Bejczy and Salisbury 1980) with a cubic workspace of 0.3 × 0.3 × 0.3 m, the 6 d.o.f. Phantom device (with 3 actuated d.o.f.) (Massie and Salisbury 1994), which is one of the most popular force-feedback devices of this class up to today, or the recent 3 d.o.f. isometric FCS Haptic Master (Linde et al. 2002). Encounter-type devices interface easily with the human, since only the hand grasps the device. The master device is not influenced by the specific kinematics of the operator arm, limb or fingers, which makes combined physical movement easily attainable.

A disadvantage, however, is their limitation to reflect forces from the slave environment to individual joints of the human operator. Forces created for instance by impacts of the robot limb structure with its environment can not be reflected to the operator arm. Body-grounded force-reflection can not be performed by such devices either. When aiming to use force-feedback in a reduced gravity environment, this fact becomes important as we shall see. Furthermore, since encounter type devices can only map the end-effector movement from the human to the robot they are not suitable to control anthropomorphic redundant robots intuitively. A discussion of potential solutions is included in Part III which are based on solving the robots redundancy by local controllers; however, the operator can then not exploit the robots redundancy intentionally, such as for avoiding obstacles while executing a task.

The gaining similarity of slave robots to the human arm thus demands for adequate control devices, able to steer all degrees of freedom intuitively. Ideally, an *extended physiological proprioception* (Simpson 1974) will be enabled for the operator in a master–slave system. The term stems from the field of prosthetics and was coined within the Simpson's Theory. Extended physiological proprioception, or E.E.P., simply means that a human–machine system is configured so that the body's own physiological mechanisms are directly related to the activation and sensing of action in the device to be controlled. This term explains why it has been attempted to develop wearable robots, such as exoskeletons since the 1960ies.

1.3 Arm Exoskeletons – State of the Art

An exoskeleton robot is a mechatronic system consisting of multiple joints that are designed to interact with joints of the human body like an outside skeleton. Exoskeleton robots have been proposed to interface with parts of the human limbs, fingers, or even with the human torso. They are supposed to provide a physical connection to the human body such that positions, velocities or torques from each joint of the limb can be exchanged with the robot. An exoskeleton can thus be seen as a direct interface from the human body to the machine world. In the following paragraphs, all results from a systematic literature review on arm exoskeletons are presented. The review considered published material up to the start of this thesis in 2003. It is shown that no portable exoskeleton device has yet been proposed that is able to control an anthropomorphic robot remotely with force-feedback.

1.3.1 Arm Exoskeletons for bilateral robot control

Up to now, exoskeleton arm masters for bilateral robot control have been implemented as wall-grounded devices, like schematically illustrated in Fig. 1.2 (b). With such exoskeletons, the human operator was to intuitively control all degrees of freedom of an anthropomorphic robot arm. Also, force reflection from the robot to the human arms was the goal, however, up to the start of this thesis this was only partially achieved.

One of the earliest records of a supposedly complete human arm exoskeleton is the General Electric Handyman, a bilateral electrohydraulic master device developed at the Argonne National Laboratory for the Aircraft Nuclear Propulsion (ANP) Programme (Johnson and Corliss 1967). It was meant to be an intuitive master device for the control of a servicing robot for nuclear aircraft engine maintenance. The system was based on Cartesian Motion mapping and consisted of a heavy duty construction. No exact reference exists and no performance of the device has been reported. However, the handyman's mass and inertia alone must have prohibited creating meaningful force-feedback to the operators. At Wright-Patterson Air Force Base (AFB), twenty-three years later, the group around S.J. Remis had for the first time aimed at building a full arm exoskeleton to control a 7 d.o.f. robots redundancy with kinesthaetic feedback, the MB Associates Exoskeleton. Their undertaking did not succeed due to lack of data about human anthropometry, human biodynamics as well as due to lack of suitable materials and actuator technologies (Repperger et al. 1990) (Remis 1990). Consequently the device was not actuated. Eight years later, in 1998 the Human Sensory Feedback Lab at Wright-Patterson AFB then proposed the FreFlex exoskeleton (Fig. 1.3, top middle), a 7 d.o.f. actuated anthropomorphic device meant to control a six d.o.f. industrial robot (Williams-II. et al. 1998). The only reference of this bilateral control, however, shows an architectural design of the hybrid controllers only and refers to testing the controller in a Matlab simulation. No successful control of the slave robot has been shown. The only exoskeleton that seemed to have worked in a bilateral control was the hydraulically actuated TOPS master–slave system developed for underwater applications under contract of the U.S. Navy (Hollerbach and Jacobsen 1996; Shimamoto 1993). For that time, the TOPS was certainly a very advanced system with 10 d.o.f. in total, featuring 3 d.o.f. for interaction with the hand. However, apart from design information no performance is reported in literature. It is reported that the system required direct analog wiring between the master and an isomorphic slave. Analog controllers were implemented and it is reported that no gravity compensation had been available, which casts doubt on a good haptic teleoperation performance, given the high mass, this device featured. The Sarcos Arm Master, was a commercialization of the TOPS system (Jacobsen et al. 1991), developed by Sarcos Inc. in the time frame from 1991 to 1999. It also consists of powerful hydraulic actuators in a wall-mounted configuration (Fig. 1.3, bottom right). Both, the FreFlex, as well as the Sarcos Arm Master are externally-grounded heavy-duty devices that must weight in the order of 50–100 kilograms.

Interestingly, only one exoskeleton-like master device (the TOPS) has been built and used successfully in a master–slave teleoperation in the 36 years covered by this literature research. Its control with a robot relies on identical kinematic structures and direct interconnection by wiring. Its hydraulic actuation certainly prevents portability. No other exoskeleton for bilateral robot control has been found.

1.3.2 Arm Exoskeletons for human power enhancement

In parallel with the development of the first telemanipulation exoskeletons, researchers became interested to use exoskeletons to enhance human power. Then, the slave was installed directly around the master device, both worn around the human. This was first attempted with the Hardiman I exoskeleton developed by General Electric in 1970ies (Mosher 1967). The device weighted about 750 kg and only one arm functioned. The programme was stopped afterwards. A group around Prof. Vukobratovic in Lubljana developed an exoskeleton for enhancing power in the human legs in 1974 (Vukobratovic et al. 1974). Both machines were tethered to a fixed station for power supply and could not interact well with the human movement. The first implementation of the FreFlex exoskeleton, was also used in tests to analyze the effects of strength enhancement on achievable human performance in a peg-in-hole task (Repperger et al. 1996). Only preliminary results were shown. However, this is the first paper trying to investigate the compatibility of an exoskeleton with human movement. Ideally, strength enhancing exoskeletons would be portable and body-grounded such as illustrated schematically in Fig. 1.2 (c). Though, due to the mechanical complexity, requirements on structural materials, mass and limitation of power density of actuators (Jansen et al. 2000), no power enhancing portable exoskeleton exists until the start of this thesis in 2003. The FreFlex externally grounded device is the only one that showed at least functionality.

1.3.3 Arm Exoskeletons for virtual environment applications

In the mid 1990ies, when computer graphics and virtual environment modelling became a novel field of research in its own, the first human arm exoskeletons were proposed for haptic interaction with virtual environments. Based on significantly more sophisticated computer platforms than in the 60–80ies, such devices could be designed more compact and with better controllers. An externally grounded arm exoskeleton for virtual applications is the 5 d.o.f. Glad-in-Art Exoskeleton developed at the laboratory of Prof. Bergamasco in Pisa (Bergamasco et al. 1994). It provides joints to interact with the shoulder and elbow of a human operator (Fig. 1.3, bottom left). The Glad-In-Art exoskeleton was the first human arm exoskeleton built in Europe aiming to be portable but the functioning and performance of the device is unknown. No quantitative results have been reported. In 1995 Prof. Caldwell proposed a dual-armed exoskeleton for virtual environment applications, providing tactile feedback to the fingers, and sensors to sense the motion of the human arm (Caldwell et al. 1995). The device featured nine d.o.f. to align and move together with the human arm and the sternum. This device is the first, for which a coverage of 90% of the human workspace was claimed, however, without actuators and without showing measured results. The EXOS Inc. Force Arm Master EAM (Burdea 1996) was a commercial development in the U.S. that, as it appears, reached the highest development standard, being actuated and partially portable with 5 d.o.f. to interact with the shoulder and elbow motions of a human (Fig. 1.3, top right). It's mass was stated to be only about 10 kg in total. Unfortuantely, no publication exists, which leaves the performance of the human–exoskeleton interaction as well as the feedback sensation unknown.

1.3.4 Arm Exoskeletons for neuro-rehabilitation

Triggered by extensive research in the U.S. on using human interfacing robots for the rehabilitation therapy of neurologically injured patients, for instance with the MIT-

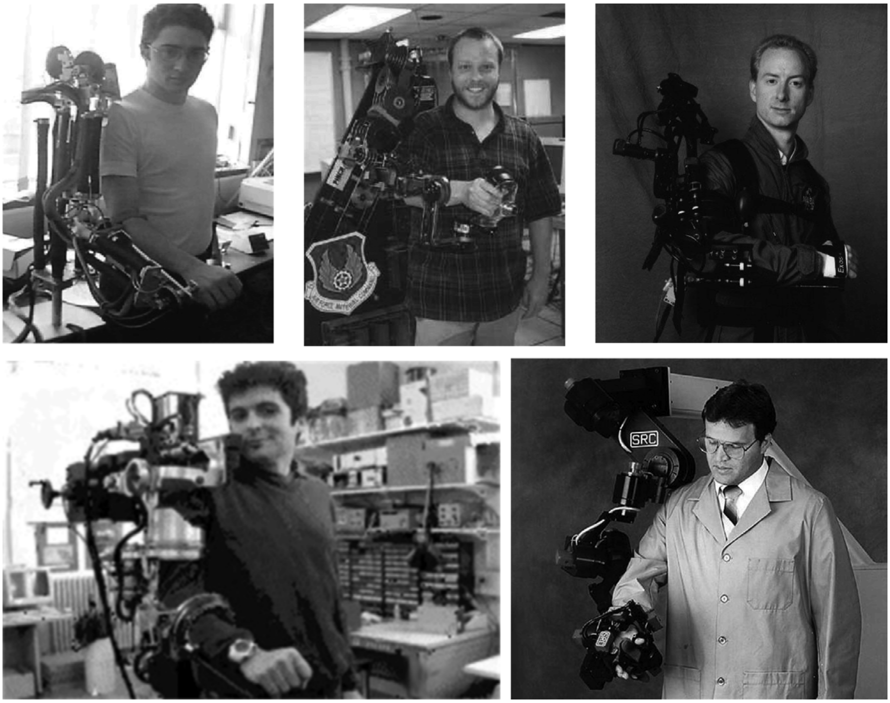

Fig. 1.3. Overview of existing exoskeleton systems. Top (left to right): Salford Exoskeleton, FreFlex Exoskeleton, Exos Inc. Arm Master. Bottom (left to right): Perco Glad-in-Art Exoskeleton, Sarcos Inc. Arm Master

Manus (Hogan et al. 1992), the ARM-Guide (Reinkensmeyer et al. 1999), WREX (Rahman et al. 2000) or the MIME robotic device (Lum et al. 2003), also in Europe this application of robotic ortheses created some attention. While those U.S. developments are not exoskeletons in the strict sense (they interact only with the tip of the hand or with a small set of one or two joints) in Europe the problem of robotic rehabilitation was approached by using exoskeletons. A fully actuated 7 d.o.f. arm exoskeleton was proposed again by Univ. of Salford in 1999 (Tsagarakis et al. 1999) for use in rehabilitation therapy (Fig. 1.3, top left). The final arm exoskeleton is based on pneumatic McKibben actuators (Tsagarakis and Caldwell 2003). Unfortunately, only behaviour of one joint in torque following is shown quantitatively. In Japan, Prof. Kiguchi has proposed a 3 d.o.f. exoskeleton based on electromyography control (Kiguchi et al. 2003). A good overview of other human arm exoskeletons under development during the start of this thesis is presented in (Brown et al. 2003).

In summary, no fully portable exoskeleton was found to exist. Also, only one directly interconnected master–slave setup using an externally grounded exoskeleton was shown to exist (TOPS). Control was limited to an isomorphic slave robot. The only other exoskeletons, able to interact with all joints of the human arm are the FreFlex, the Sarcos Arm Master (which is a follow-up on the TOPS) and the Univ. of Salford Exoskeleton.

They all interface to the hand only, which causes them to have similar disadvantages than end-point based devices introduced in Section 1.2. They can not be used for force-feedback from a redundant robot to the human arm and can not relate feed-back forces to the human body. The other wearable exoskeletons shown above (Kiguchi, EAM, Glad-in-Art) can only interface with a sub-set of the joints of the human arm.

The performance of physical interaction of all those devices with the human arm is unknown and there is a clear lack of metrics and performance measures to estimate the goodness of such devices. Testing of a leg exoskeleton, the Lokomat™ has revealed that kinematic mismatch between a device and the human limb can lead to pain, skin sores and disturbed interaction (Colombo et al. 2000). The major difficulty reported for the designs of prior systems is the availability of anthropometric data, as well as clear performance requirements for actuator torques, limb length, kinematic structure or workspace required to satisfy the human needs. This is why, definition of human capabilities has become a major field of research on its own, for establishing haptic device requirements (Tan et al. 1994), and especially for requirements on exoskeleton design (Romilly et al. 1994) (Ramanathan et al. 2000) (Venema and Hannaford 2001) (Rosen et al. 2003) (Acosta et al. 2003).

This is where this thesis aims at offering a solution.

1.4 Problem Statement

Up to the start of this thesis, no portable body-grounded exoskeleton existed that has been able to interact with or provide force-feedback to all joints of the human arm. Only one non-portable exoskeleton has been developed that could control a slave robot in bilateral telemanipulation. It is, however, directly wired to the slave and force-feedback performance is unknown. No quantitative performance analysis or theoretical basis of physical human robot interaction with exoskeletons has been proposed and a significant lack of information exists on how to design human interfacing exoskeletons well. Therefore, the search for exoskeleton design requirements has become a research field in its own (Section 1.3).

The few exoskeletons that have been proposed so far feature following key problems:

- Limitation of the **available workspace** together with the human arm.
  To achieve a large workspace while wearing an exoskeleton is difficult. This is especially true for interaction with the complex joints in the human body, such as the shoulder or the wrist. The difficulty to interact with those joints was outlined e.g. in (Romilly et al. 1994). No actuated body-grounded exoskeleton exists that can interact with all joints of the human arm (Section 1.3).
- **Singularities** within the mechanical moving system.
  Existing singularities within the workspace of an exoskeleton hinders smooth movement together with the human arm. Singularities prevent the mechanical linkages of the device from moving with continuous speed in certain directions. It

is then the responsibility of the operator to avoid them consciously, which causes high mental load and distracts from the actual task he should perform with the exoskeleton. Singularities are especially encountered with the shoulder interfaces of exoskeletons.

- Requirement of exact **adjustment of linkages** to each new operator.
  When operators with different size or statue wear an exoskeleton, the distances between the exoskeleton joints need to be adjusted. Also, calibration of the limb length then needs to be done in order to calibrate the exoskeletons kinematics for interaction with a robot in a master–slave telemanipulation scenario. To derive good design goals for link lengths in exoskeletons is a major difficulty.
- **Discomfort**.
  This is one of the biggest shortcomings of exoskeletons today. Especially for the wearable designs, kinematic constraints are placed on the human arm by the device and vice versa. This was apparent, for instance with the Lokomat Gait Orthosis, which caused pressure sores and stumbling of patients during clinical trials (Colombo et al. 2000). Pain or discomfort induced to the operator becomes more critical if long-duration tasks are to be performed. The comfort of exoskeletons was never quantitatively measured.
- Lack of **portability**
  The mass and inertia of existing actuated exoskeletons is too large to enable a portable design. While this seems understandable for power-extender exoskeletons, it is less obvious for the class of haptic exoskeletons. No portable device has been proposed until the start of this research.
- Unknown **performance** of physical human–robot interaction
  No theoretical ground work for performance analysis of human–exoskeleton systems exists. It is unknown how existence of kinematic constraints affects the physical human–exoskeleton interaction and it is unknown how they affect overall wearability. While this is not a problem of exoskeletons per se, it still affects their design and implementation. Since no performance criteria have been established, it is impossible to conceive and validate exoskeleton designs before building prototypes, which is then expensive and a high risk.

The problems encountered with prior exoskeletons can be related to only a few but fundamental causes:

- **Mass caused by exoskeleton actuation**
  Currently, no actuation means exist, that match the capabilities of biological muscles (Hunter and Lafontaine 1992). This lack of actuators with sufficient specific power and power density dictates the building of movable exoskeleton structures that are heavy, large and stiff. Any actuator that is integrated directly with the exoskeleton structure requires an even stronger actuator for the preceding link. The FreFlex exoskeleton design for instance, aimed to circumvent this problem by relocating the actuators by means of cable transmissions. The consequence, again, is a bulky and non-portable design, in this case containing 102 pulleys for cable routing, 92

bearings and coupled axes of motion. The Salford PMA exoskeleton has a compact structure due to the used McKibben actuators and the authors claim a total mass of only 2 kg, however, mass of the pressurized air supply is not taken into account for the total mass estimates and successful performance of such actuators in a haptic control has not been shown. Due to their intrinsic way of pulsed activation it can not be achieved.

Due to the bulk of mechanics incorporated in exoskeletons today, smooth interaction with the human operator is prevented by reducing the available workspace. The high mass prevented the design of portable and body-grounded devices. Also, a high structural mass counteracts reaching good haptic device properties, which would be enabled by low mass, absence of backlash, low apparent inertia, high structural stiffness and bandwidth, as generally assumed (Hayward and Astley 1996).

- **Wrong assumptions on the biological kinematics of the human limb**
  All wearable exoskeletons designed up to now, try to simply envelope a human arm with a robotic manipulator similar in kinematic structure to the standard anthropomorphic slave robots used. Since the human arm is a significantly more complex system with more degrees of freedom, kinematic constraints must be forced on the human limb by such systems. Their effect on available workspace and their contribution to the 'mushy' uncomfortable feel created at least near the workspace boundaries of existing devices is unknown and unproven. A consequence from trying to match a rigid seven d.o.f. mechanical exoskeleton structure to the biological limb is the need for meticulous alignment to each new human user. This causes long dress-on and calibration times. Singularities in the workspace, similar to the ones present in anthromoporphic robots disturb smooth interaction with the human user. The user has to consciously avoid singular poses of the exoskeleton, which makes the device's use unintuitive.
- **Unknown Real-life variability of human subject's anthropometry**
  All military master interfaces need to interface with at least the 5th to 95th percentile of U.S. male population as requested by the applicable standards (Military-Handbook 1991). This large spread of human statures and mass causes the physical shape and anthropometry of the exoskeleton users to vary with great range. A device designed to align to the human joints can therefore not work ideal with every operator. First, detailed anthropometric data is difficult to retrieve, and secondly, some subjects still possess non-nominal body shape or unusual motion-pattern preferences.

1.4.5 Key problems

(1) Lack of design requirements, guidelines and performance analysis tools for exoskeletons.
(2) Difficulty of conceiving of appropriate kinematic exoskeleton structures suitable for interaction with varying operators in the entire workspace of the human limb.
(3) Difficulty of implementing a compact and lightweight exoskeleton design with existing actuator technologies.

1.4.6 Overcoming current problems with exoskeletons

In this thesis, an entirely new approach of exoskeleton design is pursued, that is based on making the exoskeleton *independent from individual anthropometry*. This will allow designing a device, even in the absence of accurate and statistical anthropomorphic data. The theory of physical human–exoskeleton interaction shall be established to analyze the influence of kinematic constraints on the achievable comfort and working range. Furthermore, this thesis shall research a better way of exoskeleton actuation, which can enable a lightweight and thus, portable exoskeleton design with low inertia that still fulfils the requirements of an acceptable haptic device for telemanipulation. This research is thus aimed at finding the fundamentals of ergonomic and truly human compatible exoskeletons.

While the research is performed with a target application in mind, the findings for ergonomic design are claimed to be fundamental principles. Thus, enabling exoskeleton designs for building better teleoperators, rehabilitation devices or power enhancers that truly fit to a vast range of users.

1.5 Motivation

1.5.1 Haptic Exoskeleton for Space Robotics

To build a haptic exoskeleton for space robot telemanipulation requires a device that is fully compatible with human users, as following description will make clear.

The European Space Agency ESA is currently building a humanoid-like astronaut partner robot for the exterior servicing of the International Space Station ISS. The robot, called Eurobot (Schoonejans et al. 2004) shall also be able to serve as an accompanying platform for later human planetary exploration missions.

Depending on the application, Eurobot will be equipped with two or three redundant, 7 degree of freedom (d.o.f.) robotic arms. Each arm of Eurobot is equal in function and size to a human arm. When used for the ISS, the third arm functions as a leg for fixing the robot to the exterior structure of the station. During planetary applications, Eurobot will possess two arms and be supported by a movable base.

A manual master–slave control mode is envisaged for the control of the robot in unstructured environments. Those are environments that can not be modelled and used in off-line motion planning. Force-feedback with a human operator in the loop shall enable the users to get good awareness of the robot worksite and contact environment. A typical unstructured environment would be a regolithic or sandy planetary surface that is scattered with rocks. Unstructured environments containing soft structures, such as Multi-layer insulation foils, fluid lines, or similar exist on ISS. Those environments are typical for active ISS work-sites of astronauts during extra vehicular activities (EVA). But also during close cooperation of the remote controlled robot with an astronaut during an EVA, the kind of reactivity is required that can best be provided by a human teleoperating the slave-robot. In order to make the master–slave control mode as intuitive as possible for the astronauts, a wearable body-grounded exoskeleton shall be developed.

An exoskeleton provides significant advantages over encounter type input devices, such as e.g. force-feedback joysticks in space. With an exoskeleton, the joint-space motion of the redundant robot can be exactly controlled, to avoid obstacles during movement and thus contain the robot envelope within a safe distance from life-critical systems. If an end-point based device would be used, the robot was required to resolve it's redundancy by computational means, which only under great computational effort could take the environment into account (that is, if distance sensors would be present at all limbs of the robot). In an exoskeleton based master–slave control, contacts of the robots geometry other than the tip, can be conveyed to the operators. Such contacts can result from virtual constraints that will be superimposed to the real scenario for restriction of the robot envelope. This will give the operators an intuitive feel during robot control and keep the robot configuration similar to the one of the human arm.

Another advantage of wearable body-grounded, or portable exoskeletons in space is their capability to relate feedback forces to the operator torso. Encounter-type devices or non portable exoskeletons would rather cause a reaction motion in the operator's body in micro-gravity, instead of creating meaningful force-feedback information. This was observed already without force-feedback during the ROTEX experiment (Hirzinger et al. 1993) onboard the space shuttle. A spring-loaded space mouse required strapping down the arms of the astronauts before.

The requirements of the exoskeleton to be human compatible stem from it's particular application scenario. The device must be capable of supporting long-duration commanding of the slave robot. An EVA supported operation on ISS can easily last 6 hours or more. This is why, the device must be intuitive to use, in order to keep cognitive load to a minimum. Furthermore, the exoskeleton must be comfortable such that the operator does not experience pain or excessive fatigue during remote operations. Moreover, the specification of statue and mass of Astronaut crew is demanding. Crew statures can lie within the range of 5th percentile of Japanese female and 95th percentile of U.S. male population (NASA-STD-3000/T 1999). Therefore, the exoskeleton must be capable of interacting with a vast range of individuals (1.49–1.90 m stature). In addition to this requirement, the device must be able to be used for quick intervention in the case of emergencies. This means, that the exoskeleton must not require lengthy procedures for dressing on and calibration. Otherwise, dressing-up an EVA suit and sortie would probably be a better solution to intervene a critical EVA.

Besides these requirements for on-board use in the station, the exoskeleton must also be compatible for 1-G use. This is crucial for development and testing on ground. Therefore, the exoskeleton to be developed must be as lightweight as possible. Compactness of the device is another requirement that is dictated by the need to stow the exoskeleton if it is not used by the crew.

In order to enable the design of such an exoskeleton, it is necessary to find the fundamentals of ergonomic exoskeleton robots.

1.6 Goal

It is the goal of this thesis to research how a wearable exoskeleton-type robot can be designed to be ergonomic and *truly compatible* with human operators.

This overall goal can be divided into the following sub-goals:
- Research how a kinematic exoskeleton structure can be made robust to variation of physical parameters between users.
- Investigate the human acceptance to such ergonomic exoskeletons with regard to the optimum of extended physiological proprioception.
- Research how an ergonomic exoskeleton can be used to control non human-like robots.
- Research how an actuation system needs to be designed to enable implementing a lightweight, compact and portable exoskeleton that can create body-grounded force-feedback.

While solving the research goals posed above, it is pursued to:
- Understand and establish the underlying geometrical and physical principles of smooth physical human–robot interaction (pHRI) with exoskeletons.
- Keep the resulting architecture of the exoskeleton *truly human compatible*, such that it offers interaction with the complete functional workspace of the human arm without generation of kinematic constraints.

The fulfilment of this goal will provide the fundamentals of ergonomic exoskeleton design.

1.7 Approach

The research approach taken in this thesis is based on three cornerstones, which are (1) the understanding of the theory of physical human–robot interaction, the (2) formulation of design goals for reaching optimal human–robot interaction, and (3) the validation of the formulated design goals by means of prototypes.

(1) Theory of physical human–robot interaction
To understand the performance of a combined human–robot system fully, first, it is necessary to model both systems mathematically. Kinematic models of the human limb and the robot are developed, to analyze their capability for combined interaction in motion simulations. Correct model assumptions, especially reflecting the variability of the mechanical properties of the human arm between subjects, are crucial.

To study the influence of the exoskeletons kinematic structure on (a) the achievable common workspace, (b) on the mechanisms behaviour during motion, as well as on (c) the susceptibility to reach into singularities during movement, a *multi d.o.f.* modelling approach was chosen. This approach does not only allow a priori validation of given kinematic structures, but also enables the formulation of the general kinematic design principles.

To analyze the exact transfer of loads at the human–robot interfaces, explicit mathematical models are required to understand the causes of interface forces generation. A *single d.o.f.* explicit mathematical modelling approach is chosen for this problem. In particular, it is modelled how loads are transferred from robots to a human joint during movement, if offsets exist between their major axes of rotation.

(2) Formulation of the design goals

The formulation of design goals for exoskeletons featuring optimal pHRI is a major goal of this thesis. It is the aim to derive sensible rules for (a) the kinematic design of the wearable robot structure, (b) the actuation, control and sensor system and the (c) means for attaching the robot comfortably and easily to varying human users. It needs to be determined which of those factors are most important for better comfort. The design goals are formulated to overcome the gap between *artificial* and *biological* mechanically moving systems. While the large part of incompatibility can be bridged already by appropriate kinematic and human interface design of the robot, also the influence of the actuation system is to be addressed. The peripheral systems of the exoskeleton, like actuators and sensors need to fully support the ergonomic design.

(3) Experimental validation of the design

The last step in the research is the experimental validation of the formulated and implemented design hypotheses. This is done by means of prototypes. For different aspects of the exoskeleton systems, different prototypes have to be built and tested. For the verification of the *multi d.o.f.* interaction aspects with the human (i.e. workspace, wearability, comfort, stowage, mass), two full exoskeleton prototypes were developed and successfully tested. The second prototype was used to successfully test controllability of a non-human like robot in a simple telemanipulation task without force-feedback. To test the feasibility of actuation of the exoskeleton in bilateral control, a series of single d.o.f. actuator prototypes were developed and tested in full master–slave teleoperation experiments. Implementation of a fully actuated multi d.o.f. exoskeleton and bilateral control with a slave robot is outside the scope of this thesis.

1.8 Thesis Outline

This thesis is composed of five parts that correspond to the research goals posed above. All articles are exact reproductions of submitted or published material. Therefore, there might be some overlap between the chapters. The formatting of the chapters was altered to integrate them well into this thesis.

In **Part I**, the ergonomic design principles are introduced. **Chapter two** illustrates the problem of compatibility between human and robotic limbs. It is shown which important factors need to be addressed to enable ergonomic wearable robot design. **Chapter three** formulates a new ergonomic design paradigm for smooth pHRI and presents a validation thereof in terms of the operator workspace.

Part II deals with the validation of the ergonomic design. **Chapter four** introduces the single d.o.f. model used for interface force quantification. **Chapter five** presents results from a large experimental validation of the exoskeleton design with 14 different test persons.

Part III is dedicated to robot control. It is shown in **Chapter six**, how redundancies in an exoskeleton can be resolved. **Chapter seven** shows the implementation of the exoskeleton-robot control workcell that validates the feasibility of using the exoskeleton to control redundant manipulators.

In **Part IV**, the possible actuation of the ergonomic exoskeleton is introduced. **Chapter eight** presents the Bowden Cable actuator that enables remote actuation of the ergonomic exoskeleton. **Chapter nine** presents performance differences of this actuator with respect to conventional actuators used inside wearable robots.

In **Part V**, the multi d.o.f. exoskeleton prototypes are presented. **Chapter ten** shows the first prototype ARMEX used for workspace and interaction validation. **Chapter eleven** shows the second EXARM prototype, developed for validation of the single d.o.f. interaction and robot control.

The last three chapters, conclude this thesis with **Chapter twelfe** providing the discussion, **Chapter thirteen** presents future work and **Chapter fourteen** presents the conclusions of this thesis.

Below, a brief summary of the contents in terms of research questions that can be posed for the goal and sub-goals stated above:

- How does the exoskeletons mechanical system need to be designed?
    - **Part I** and **Part V**
- How is the human-compatible exoskeleton perceived by humans?
    - **Part II**
- How can a human-compatible exoskeleton be used to control non human-like robots?
    - **Part III**
- How does the exoskeletons actuation system need to be designed?
    - **Part IV**

Part I

Ergonomic Design Principles

Chapter 2: Kinematic Compatibility between Human Limbs and Exoskeleton Structures

A. Schiele
Extracts of Chapter 5.2, Invited Contribution: *Wearable Robots: Biomechatronic Exoskeletons, Jose Pons Ed., John Wiley & Sons, 2008, pp. 130–134*

Chapter 3: Kinematic Design to Improve Ergonomics in Human Machine Interfaces

A. Schiele and F.C.T. van der Helm
IEEE Transactions on Neural Systems and Rehabilitation Engineering, Vol. 14, No. 4, Dec. 2006, pp. 456–469

Chapter 2

Kinematic Compatibility Between Human Limbs and Exoskeleton Structures

A. Schiele

Extracts of Chapter 5.2, Invited contribution: *Wearable Robots: Biomechatronic Exoskeletons, Jose Pons Ed., John Wiley & Sons, 2008, pp. 130–134*

This Chapter introduces the basic issues of compatibility between human limbs and exoskeletons. The concept of Macro and Micro-misalignment between humans and exoskeletons is introduced, that stem from variation of the physiological parameters of exoskeleton users. The approach to use passive compensation joints to solve the problem of alignment is outlined.

2.1 Introduction

A good design of a wearable exoskeleton starts with the choice of a suitable kinematic structure of the device. That is to say, even before implementing actuation and control to a device, already the purely mechanical structure must enable wearability, ease of use and comfort to the operator. Comfort is related to the capability of the exoskeleton to smoothly interact with the human. We mean thereby that the exoskeleton must not limit the range of motion of the operator and otherwise be as transparent as possible.

For the sake of simplicity, we will focus on arm exoskeletons in this chapter, without loosing applicability to other devices, for instance for the human leg, torso or the fingers.

For the design process of an exoskeleton, it is important to have a good model describing the human limb first. This model, which we will hereafter call *human limb model* allows testing proposed exoskeleton mechanisms in simulations for their capability to interact with the human limb. Therefore, it makes great sense to use the same modelling approach for both, the human limb and the exoskeleton. CAD tools or other computer simulations can then be used to quantify the human–machine interaction prior to building hardware. However, in order to design an exoskeleton that is truly compatible with human movement, ergonomic, safe and comfortable once it is built, we have to be aware of the fact that the human biomechanics is not actually behaving like a conventional serial chain robot in reality.

2.2 Causes of kinematic incompatibility and their negative effect

There is a great number of effects, that can contribute to kinematic incompatibility between an wearable exoskeleton and a real human limb, once an exoskeleton has been implemented in hardware. The reason for that is the real life variability of biomechanic parameters between subjects, and also the variability of some parameters within subjects during movement. Unpredictability of joint axes locations and body segment sizes, for instance, can lead to a disturbed interaction between an exoskeleton and the human operator, depending on the exoskeleton kinematic design. This especially applies to exoskeletons that are wearable and kinematically equivalent to the human arm.

Typical biomechanical effects that can not easily be captured within a human arm model used for exoskeleton development are:

- The between subject variability of the human limb link parameters (the Denavit Hartenberg DH parameters, such as length of bones, distances between rotation axes, orientations of rotation axes).
- The variability of the joint centre of rotations during movement within a subject. The instantaneous centres of rotation (ICR's) of each anatomical joint move slightly during joint motion.
- The between subject variability of the body segment dimensions: mass, size, volume and so forth.

Those anatomical variations make an exoskeleton design difficult that fits a large range of users without problems. A challenge to the physical human–robot interface (pHRi) design is also the fact that precise anatomic data is not known for the operators. All joints are covered with soft-tissue, cartilage and muscles, such that the ICR's are not visible and hardly measurable by other in-situ means.

Causes of kinematics incompatibilities between humans and exoskeletons can be classified into two groups: (1) Macro-misalignments and (2) micro-misalignments that exist between human joint axes and exoskeleton joint axes.

Macro-misalignments occur, if exoskeleton joints for interacting with specific human joints or joint groups are oversimplified. Oversimplification, in this case, means that the degrees of freedom of an exoskeleton joint or joint-group is essentially less then the number of degrees of freedom of the corresponding human joint or joint group. This is the case for all wearable exoskeletons that feature 7 degrees of freedom. Probably the best example for that can be found when investigating interaction with the human shoulder. Typically, shoulder movement involves not only motions in the glenohumeral joint, which is often modelled as the three degree of freedom spherical joint base in the human arm, but also involves movements of the shoulder-girdle (to which the clavicle and the shoulder blade belong). The movement of the shoulder girdle in turn, influences the location of the glenohumeral joint. Fig. 2.1 illustrates the vertical translation of the glenohumeral ICR caused by shoulder abduction. A significant shift of the glenohumeral ICR occurs at abductions exceeding 90 Degrees, i.e. already in the middle of the joint range of the shoulder. The pure vertical shift is still simplified, but helps to illustrate the concept. In reality, also a horizontal translation of the joint occurs. If an exoskeleton kinematic structure for the shoulder is now designed such that it aligns to the glenohumeral joint only, the corresponding human joint increasingly

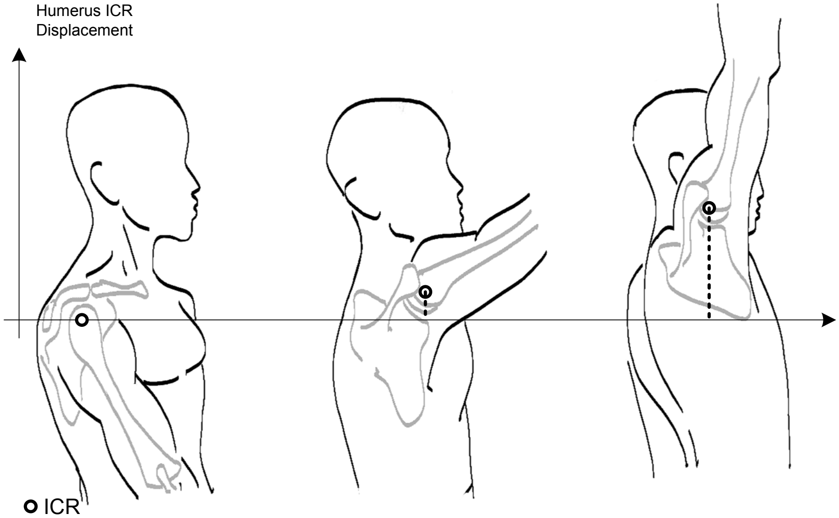

Fig. 2.1. Translation of the Instantaneous Centre of Rotation of the Glenohumeral shoulder joint during Shoulder abduction. This shows how human joint centers of rotation are non-stationary. An ergonomic exoskeleton will have to cope with such alterations of the human anatomical structure during movement.

translates away from the exoskeleton joint ICR during motion. Large offsets between the exoskeleton joints and the anatomical joints are a consequence.

Macro-misalignments are thus induced by a mismatch of the degrees of freedom of human limb motion to exoskeleton link motion. In end-point based exoskeletons, those macro-misalignments do not have a significant negative effect. In wearable exoskeleton interfaces, however, they impose severe restrictions of the common available workspace with the human limb. Most arm exoskeletons currently known that feature a spherical joint set for the shoulder, have a restricted shoulder workspace.

Micro-misalignments are less obvious but occur in all wearable exoskeleton designs. They occur, even if the number of degrees of freedom between the exoskeleton and the human joints is correct. Say, if an exoskeleton had joints to track shoulder-girdle movement by aligning two additional axes to the sternoclavicular joint (the joint that connects the shoulder girdle to the torso). Micro-misalignments are still caused by non-coincident joint rotation axes between exoskeleton and human limb. This is almost always the case, because aligning of an exoskeleton perfectly to the human joints is impossible. This is due to the subject variability and coverage of the joints explained above. Now, suppose an elbow exoskeleton as shown in Fig. 2.2 (a) that is worn by an operator on its elbow. The devices ICR will always have a small offset toward the human elbow ICR. Firstly, because the operators elbow ICR is not exactly known, so perfect manual alignment of the exoskeleton to this joint is impossible. Secondly, because the biological joint surfaces are not ideally circular. This means that the ICR is shifting during motion. Micro-misalignment can furthermore be caused by slippage of the exoskeleton attachments on the human skin during motion. Slippage induced offsets were reported in literature (Colombo et al. 2000), for the LOKOMAT gait orthesis. There, it caused greater misalignments between the orthosis joints and the human ones, which led to stumbling of the patients during test sessions with patients. A further negative effect of micro-misalignments is the creation of interaction forces, such as shear forces between the exoskeleton attachment point and the human limb. Those forces are created by displacements (Fig. 2.2 a) of the exoskeleton along the limb. In the figure below, the stiffness and damping between the human and the exoskeleton robot is represented by a Voigt-element.

In (Hidler and Wall 2005), the authors show that interaction forces alter the natural motion patterns in combined human–exoskeleton motion.

Macro- as well as micro-misalignments contribute to discomfort of an operator and can limit and alter the natural movement of a human limb inside an exoskeleton. The question arises, how a kinematic structure of an exoskeleton needs to be designed to provide a maximum of comfort and ease of use despite the variability of anatomic properties within and between users?

2.3 Overcoming kinematic incompatibility

While a purely end-effector based exoskeleton is independent from joint alignments, no exact motion can be induced in the human joints, due to the natural redundancy

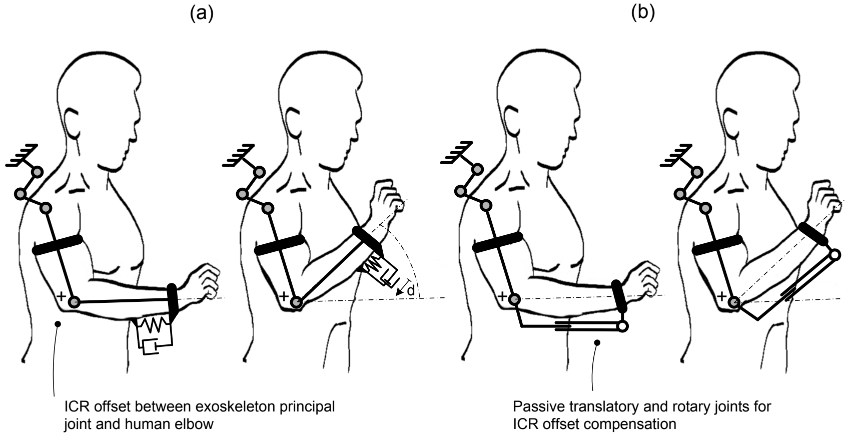
(a)
(b)
+
d
ICR offset between exoskeleton principal joint and human elbow
Passive translatory and rotary joints for ICR offset compensation

Fig. 2.2. Illustration of the creation of interaction force as a consequence from joint misalignments between exoskeleton and human limb (a). During motion, the exoskeleton slides on the human limb. If passive joints are added into the structure (Schiele and Helm 2006) those forces are not created (b), the joints compensate for the slipping of the device.

of the human limbs. Such devices can not resolve the natural human limb redundancy and therefore have the potential to apply harmful loading to the human joints.

Imagine a force onto a stretched out human arm that is directed towards the shoulder (in line with the arm). Such a force could move the operator's joints in arbitrary directions extension or hyper-extension. Great harm could be done to the operator. This is why, a safe and ergonomic interface should not be end-effector based.

The first *Ergonomic Design criteria* for exoskeleton based human–robot interaction were presented in (Schiele and Helm 2006). In order to enable a truly ergonomic exoskeleton design, the authors postulate that an exoskeleton must be able to:

- Interact with the complete functional workspace of the human limb of interest
- Induce exact torque, position and velocities to the human joints (thus, be able to resolve the redundancy)
- Must not cause discomfort or safety hazards for the users.

This can be achieved by applying the ergonomic design paradigm presented in the referenced article:

- An exoskeleton should be wearable.
- An exoskeleton should never have more then 6 d.o.f. between 2 consecutive attachments.
- An exoskeleton kinematic structure must explicitly not copy the kinematic structure of the adjacent human limb. Thus, the exoskeleton should be not kinematically equivalent to the human limb it interacts with.

The last point aims at solving negative effects stemming from micro-misalignments. If an exoskeleton has a kinematic structure that is different to the human arm but can provide the same Cartesian motion between 2 attachments, no misalignment can negatively affect motion or user comfort. Additional passive compensation joints can be incorporated into an exoskeleton kinematic structure to compensate constraint displacements between the device and the human limb. Fig. 2.2 (b) illustrates an elbow articulation with such passive joints. An exoskeleton designed with an according kinematic structure will be easy to use. No adjustments to individuals are required anymore.

Chapter 3

Kinematic Design to Improve Ergonomics in Human Machine Interaction

A. Schiele and F.C.T. van der Helm

IEEE Transactions on Neural Systems and Rehabilitation Engineering, Vol.14, No.4, Dec. 2006, pp. 456–469

This paper introduces a novel kinematic design paradigm for ergonomic human machine interaction. Goals for optimal design are formulated generically and applied to the mechanical design of an upper arm exoskeleton. A nine degree of freedom model of the human arm kinematics is presented and used to develop, test and optimize the kinematic structure of an human arm interfacing exoskeleton.

The resulting device can interact with an unprecedented portion of the natural limb workspace, including motions in the shoulder-girdle, shoulder, elbow and the wrist. The exoskeleton does not require alignment to the human joint axes, yet is able to actuate each degree of freedom of our redundant limb unambiguously and without reaching into singularities. The device is comfortable to wear and does not create residual forces if misalignments exist. Implemented in a rehabilitation robot, the design features of the exoskeleton could enable longer lasting training sessions, training of fully natural tasks such as activities of daily living and shorter dress-on and dress-off times.

Results from inter-subject experiments with a prototype are presented, that verify usability over the entire workspace of the human arm, including shoulder and shoulder girdle.

3.1 Introduction

Robotics are increasingly playing an important role in neurorehabilitation of patients suffering from injuries to the nervous system, i.e. stroke, traumatic brain injury or spinal cord injury.

Stroke patients, for example, often develop disabling movement disorders, which are based on sensory and motor impairments such as muscular weakness, loss of muscle coordination (Dewald et al. 1995), and other spastic symptoms such as increased muscle tone and exaggerated reflexes (Thilmann et al. 1993). The consequent inability to perform elementary functional tasks with their limbs, such as walking or eating, makes autonomous daily life impossible.

An encouraging treatment aiming at faster and better recovery is intensive movement therapy. It is assumed that this form of therapy improves recovery of functional and motor control capabilities within the patient, by stimulation of neuronal motor learning effects (Reinkensmeyer et al. 2002) (Barbeau et al. 1999) (Asanuma and Keller 1991). It is believed that repetitive movement exercise activates the damaged motor pathways and increases their efficiency and reliability (Reinkensmeyer et al. 2000). Another target of the therapy is the extension of shortened soft tissue, to increase the passive range of motion, and to improve muscular strength (Goldspink and Williams 1990). Regarding efficiency of therapy, it was shown in (Sunderland et al. 1992) that recovery significantly improves with longer duration of the therapy. The patient can expect a better recovery if therapy starts early after injury (Smith et al. 1982) and involves highly repetitive movement training (Butefish et al. 1995). In (Dietz and Harkema 2004) it is moreover suggested that the quality of induced movement is crucial for neuro-recovery. It is suggested there, that for lower limb rehabilitation a critical combination of afferent input signals is essential for generation of locomotion patterns in the lower spine. This leads to the conclusion that a therapy is more efficient if movement input is cyclic, reproducible, rhythmical and physiological.

Up to the present, movement therapy is mostly carried out manually by occupational and physical therapists. A known disadvantage of this approach is fatigue of the therapist, who often has to perform the treatment in ergonomically very unfavorable positions. As a result, induced movements might become inconsistent when fatigue sets on in the therapist, at the expense of the patient. Training sessions are often shortened or even omitted if the patient has severe spastic symptoms. This is where manual therapy has its limits and robotic therapy comes into play. Robots are certainly well suited to perform precisely repetitive and mechanically power consuming tasks.

Indeed, first clinical results already underline that robot aided sensorimotor training positively affects the reduction of impairment in patients (Krebs et al. 2000). In (Burgar et al. 2000) it is reported that patients had greater improvements in voluntary reaching of the arm towards a target after robotically assisted treatment then patients after conservative treatment. Furthermore, it is shown in (Lum et al. 2004) that robotic training improves muscle activation patterns in subjects suffering from cerebrovascular accidents. One major advantage of robotic rehabilitation is the possibility to offer therapeutic sessions more often. Moreover, robotic rehabilitation improves therapeutic quality, which is a result from enabling longer training sessions and more repetitive and cyclic stimulus (Colombo et al. 2000a).

However, critics of robotic rehabilitation challenge the capabilities of robots to spontaneously adapt to specific needs and ergonomic movement particularities of the patients. This is why currently a second generation of rehabilitation robots is under development in many laboratories. Such robots will aim at fulfilling important clinical requirements such as being lightweight and back drivable for safety and offering advanced control schemes, such as impedance control for better patient interaction (Hogan 1985) (Lemay et al. 1998). Furthermore, psychological aspects, such as acceptance by patients and therapists are becoming increasingly important. An overview of such devices is presented in (Riener et al. 2005). While most researchers concentrate on improving control aspects, important characteristics that are too little considered in rehabilitation robot design are the workspace available for training and the devices compatibility to function properly even when misalignments with respect to the biological joints occur. It is shown in (Hidler and Wall 2005) that a limitation in available degrees of freedom during robotic therapy can lead to changes in muscle activation patterns, which could have negative influence on the outcome of therapy.

The goal of this paper is to propose a paradigm for truly ergonomic mechanical design of human interfacing robots. The paradigm aims at enabling interaction within a maximum natural limb workspace and avoiding creation of residual forces in the joints if misalignments between the device and the human limb occur. This shall enable building human interfacing robots that can smoothly interact with human limb motion.

3.2 Problems of current rehabilitation robot designs

Currently, wearable and non-wearable rehabilitation robotics exist, which both have intrinsic disadvantages preventing an optimal use for movement therapy. Disadvantages prevail from a mechanical design, which does not take biological mechanical properties of the adjoining human limbs into account.

3.2.1 Wearable devices and problems related with alignment

Wearable robotic ortheses enclose the entire limbs of the patient, aiming at imitating the kinematics of the impaired extremity. One key requirement for such devices to ensure proper functioning is exact alignment between the mechanism joints and the patients' biological joints, which is difficult to achieve, for several reasons.

First of all, the exact locations of the human joint axes of rotation cannot be known on living subjects, due to coverage of the joints. Biological joints are not ideal *single degree of freedom* joints, but have rather complex joint surface geometries, which cause shifting axes of rotation during motion. Additionally, fixation of a robotic device on a human limb is never rigid, such that slippage between the device and the limb will occur. This will lead to further misalignment between the mechanism and human joints. These facts are likely to create micro-misalignments between any attached robotic joint and the human joint in the order of a couple of centimeters. A human limb is schematically shown in Fig. 3.1 with an attached robot.

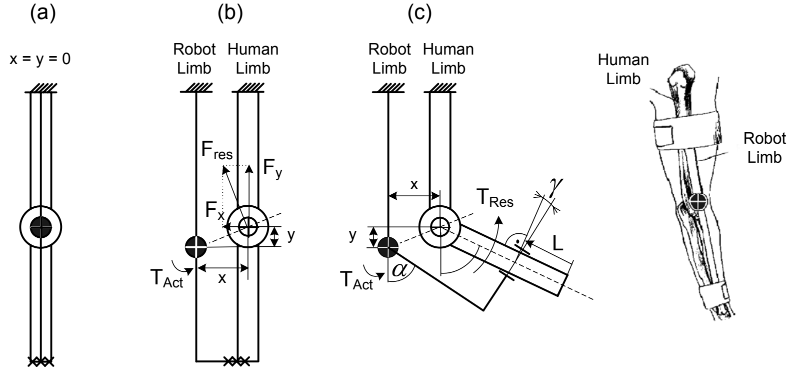

Fig. 3.1. Small misalignments (x, y) between human joints and actuated joints of rehabilitation robots can prevent smooth human–machine interaction. If the robot were rigidly attached to the human limb (b), shear-forces F_{res} could impart the joints resulting from applied torque T_{Act} on the robot. Rotary movement would not be possible. However, in a more realistic case (c), application of T_{Act} through a robot will rather cause slip between the robot attachments and the limb (L, γ). This will create discomfort for the patients.

The case depicted in (a) shows both joints perfectly aligned. This would allow ideal interaction between human and machine. However, if the actuated joints of any wearable robot have offsets towards the biological counter-joints, such as shown in (b), torques applied on the robot joints would theoretically generate reaction forces in the biological limb. If, for instance, a torque T_{Act} of 6 Nm is applied to the rehabilitation robot with an assumed offset of 1 cm in y-direction and 2 cm in x-direction, theoretically, reaction forces of $F_x = 120$ N and $F_y = 240$ N could be created in the human joint, if the robot was rigidly attached to the human limb and started moving.

In reality, however, the case illustrated in (c) applies. The attachment on the soft-tissue of the arm allows the robot to move. The same misalignments in directions x and y will cause a skin movement in the order of $L = 4$ cm, at rotation $\alpha = 45°$ and $l = 20$ cm. The displacement increases with bigger angles. Furthermore, a small angular misalignment γ between the attachment and the human arm will be created. However, it will be very small and not contribute to discomfort of the patient.

The situation shown in (c), will still lead to interaction forces and can lead to pressure sores on the skin of a patient. Interaction forces of such type have been reported in (Hidler and Wall 2005) as a consequence of bad alignment. In addition to skin injuries, long-term damage to the human joint could take place if the robot actuators are strong. Especially in patients suffering from decreased muscular strength, joint dislocations and cartilage damage could occur more easily then in healthy persons. However, clinical studies to underline this are yet to be performed. Risk of injury to the patient has also been identified in (Colombo et al. 2000a) for the LOKOMAT wearable leg orthesis. The orthesis requires five mechanical adjustments to align the powered joints of its leg braces to the patients' hip, knee and ankle joints. In fact, in (Colombo et al. 2000b) compatibility problems have already been reported. Skin sores and stumbling of the patient were caused by the slipping robotic orthosis during the training session.

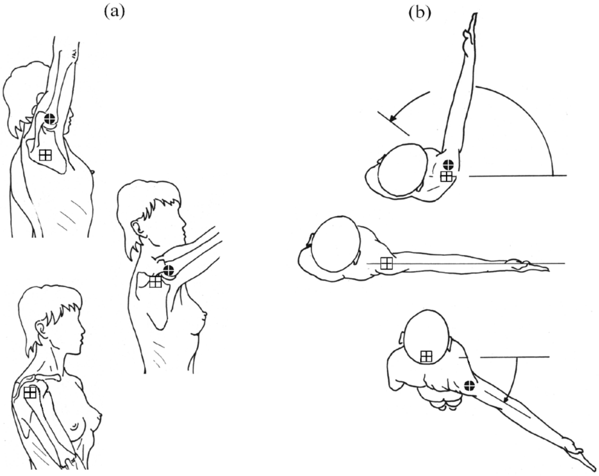

Fig. 3.2. Big misalignments occur in certain joints through shifting motion axes. The estimated true centers of rotation in the shoulder are indicated with a white cross in (a) and (b) for shoulder flexion and horizontal ante-retro-version. The moving center of rotation of the "spherical" glenohumeral joint is indicated with a black dot. (Figure adapted from Kapandji 1995)

A second common type of misalignment between wearable robots and the biological limbs arises from misinterpretation or oversimplification of the human joint kinematics. Such misalignments can typically be in the order of tens of centimeters or more. A common mistake is the definition of a *ball and socket type* joint for describing movement in the human shoulder. While this assumption nearly holds for small angles exerted or exclusive glenohumeral motion, it significantly deviates during larger motions, as the thoracohumeral joint has a moving center of rotation. The location of the glenohumeral joint is indicated in Fig. 3.2 with a black dot, while the location of the real center of rotation is indicated with a white cross during extension (a) and horizontal anteversion (b).

The relatively large offsets between both locations are evident. When designing the kinematics of a rehabilitation robot, it is therefore important to apply realistic assumptions about degrees of freedom of human functional movement and the underlying anatomy of the human limbs. Otherwise, combined movement of robot and human will be heavily disturbed. Most current wearable devices for the human upper limb do not feature such design (Riener et al. 2005), especially for the shoulder (He et al. 2005). Their interaction workspace is thus limited 'a priori' to avoid misalignment and related problems. Training of daily living tasks such as eating with a spoon, combing hair or drinking from a cup is then difficult or even impossible. The same limitation of workspace applies to a class of exoskeletons that is developed for telemanipulation applications with robots, such as e.g. (Bergamasco et al. 1994) or the devices presented in (Brown et al. 2003). The problem of micro-misalignment applies even to devices that have joints to support glenohumeral movement, such as (Caldwell et al. 1998) or (Carignan et al. 2005).

3.2.2 End-effector based robotic devices and problems related to redundancy

The problem of joint alignment does not apply to End-effector based rehabilitation robots, which attach only to the distal end of a limb. However, difficulties for the therapy arise from naturally prevailing kinematic redundancies in the human limbs. Such redundancies allow us to position and orient our distal extremities with different configurations of the joints and are crucial to execute daily tasks. Redundancy enables us to avoid obstacles while reaching out with our limbs. For rehabilitation devices that only attach to our hands or feet, this redundancy forbids inducing accurate joint trajectories, a problem known for inverse kinematics. Thus, cyclic and exactly repetitive joint motion can never be performed with such kind of therapeutic device alone.

An example of an end-effector based therapeutic robot for the lower limb is the GAIT Trainer (Hesse and Uhlenbrock 2000), which must be attached to the feet of the patients. Due to the leg redundancy, a therapist is still needed to support and stabilize the paretic knee during therapy. If this support is omitted in weak patients, imposed trajectories to the foot can lead to hyperextensions of the paretic knee and can cause severe injuries of the human joint. The redundant behavior of the limb furthermore makes the analysis of joint movements, e.g. by means of kinesiological electromyograms, less accurate.

Current end-effector based robotic trainers for the upper limbs seek to constrain the redundancy of the human arm. The MIME and MIT MANUS (Krebs et al. 2000) devices for instance, attach to the forearm of the patient, thus limiting the application of therapy to movements in the shoulder and elbow. A consequence of this restriction is the lack of improvement in hand and wrist function after therapy that was reported in (Burgar et al. 2000) and (Krebs et al. 2000). The ARM Guide (Reinkensmeyer et al. 2000) is another rehabilitation robot for the upper limb, which is restricted to linear motions of the arm excluding motions of the wrist.

3.3 Design goals for ideal human robot interaction in rehabilitation

Three important points need to be taken into consideration when aiming at truly ergonomic mechanical design for rehabilitation robots. Ideal robotic rehabilitation devices must be able to (1) train the complete functional workspace of a human limb, as the benefit of sensorimotor training is specific to the muscle groups and limb segments, which are exercised (Krebs et al. 2000). Furthermore, to improve efficiency of therapy, the robotic devices must be capable to (2) activate joint by joint, to induce exact ergonomic movements in a patient. This is important to trigger realistic afferent input to the nervous system (Dietz and Harkema 2004) (Dietz et al. 1996). Moreover, an ideal human interfacing robot (3) must not cause discomfort or safety hazards for the user during movement. At present, no wearable or end-effector based rehabilitation device does suite all of these points.

In order to enable a truly ergonomic design, according to the goals stated above, first of all it is assumed that a wearable design is preferred over a non-wearable design – in general. A non-wearable design would easier satisfy point (1), however would contradict with (2) and (3). All three points above can be fulfilled with a wearable exoskeleton design, if problems related to misalignment to biological joints can be overcome by design. A new design paradigm will be shown in this paper, which provides a solution to this problem.

It is postulated that a human interfacing wearable robot should be designed to explicitly not imitate the kinematic structure of a human limb, to avoid requiring alignment. Instead, the robot should provide an alternative moving system bridging in parallel over the human joints. This alternative serial robot must have the same capabilities to perform Cartesian trajectories than the adjoining human limb, which allows the robot to perform exactly equivalent motion trajectories than the biological counterpart. Furthermore, the robot should be fixed onto the human operator such, that between two consecutive attachments, not more then six human joint degrees of freedom are contained. Each robot joint should be equipped with mechanical end-stops.

The number of actuators for the man-machine interfacing robot can be lower then the total degrees of freedom, if the robotic actuators are placed such that each natural degree of freedom of the human limb can be agitated with a single or a set of actuators. This will keep the overall complexity of the robot minimal.

A rehabilitation robot, which is based on such design rules will integrate the benefits from wearable and non-wearable devices into one and fulfill all three major goals that have been specified for ergonomic design. In the following, the design of an exoskeleton for the human upper extremity will be shown, to illustrate an implementation of the novel design approach.

3.4 Method

3.4.1 Procedure for ergonomic design

The first important step towards ergonomic design is a good model of the kinematics and dimensions of the interacting human limb. The capability of the arm model to perform Cartesian space motion equivalent to a real human arm is important. The precise modeling of the involved biological components, such as bones or muscles is secondary, which is why a more simplified approach than the already established human arm models can be sufficient.

In the next step, the model is used to define realistic ergonomic movement trajectories in 3D Cartesian space. This simulation allows checking following ability of a proposed attached robotic human machine interface and optimizing its kinematic structure.

To check robustness towards v-arious subjects, the arm model generates trajectories for subject statues ranging from the 5th to 95th percentile of male population. If a robotic mechanism is capable of interacting with the model, the chance is high that also in reality it will be able to interact with human arm motion over the entire workspace.

After the kinematic design of the rehabilitation robot, a prototype is used to test interaction performance with several individuals.

3.4.2 Model of the human arm

For the human upper limb, a model with 9 degrees of freedom (d.o.f) was established. The kinematic parameters of the model are illustrated in Table 3.1 for a subject statue of 1.80 m. Link lengths were computed from statistical data according (Chaffin and Andersson 1984).

Knowing that the sternoclavicular joint provides the major attachment of the human arm to the thorax, this joint forms the base of the kinematic model for the upper arm. The shoulder girdle is modeled as a five degree-of-freedom serial linkage as shown in Fig. 3.3. The kinematic frames are assigned according Denavit-Hartenberg notation (Denavit et al. 1955) to allow the reader to combine the graphs with the given tables. In the following, the standard naming for joint axes, proposed in (Wu et al. 2005), is used. For the sternoclavicular joint (SC) 2 joint axes, Z_0 for SC Pro/retraction and Z_1 for SC Depression/Elevation are implemented.

Joint Parameter	$\mathbf{A_i}$ [cm]	$\mathbf{D_i}$ [cm]	α_i [deg.]	θ_i
1	0	0	90	$^*\theta_1$
2	–23.0	0	0	$^*\theta_2$
3	0	5.0	270	$^*\theta_3$
4	0	0	90	$^*\theta_4$
5	0	33.5	270	$^*\theta_5$
6	0	5.0	90	$^*\theta_6$
7	0	26.0	90	$^*\theta_7$
8	–2.0	0	90	$^*\theta_8$
9	0	0	90	$^*\theta_9$
10	0	6.0	0	–

Table 3.1. Denavit Hartenberg Parameters for Human Arm: This table shows the kinematic parameters used to establish the human arm model in the Denavit-Hartenberg convention [A_i: link length, D_i: link offset, α_i: link twist]. Parameters shown with (*) indicate the joint variable.

Axial rotation of the clavicle is not modeled. It has only little effect on the positioning of the humerus bone. The joints around Z_2, Z_3 and Z_4 build a spherical joint simulating the glenohumeral articulation (GH).

The scapulothoraic as well as the acromioclavicular joints are not included in the shoulder model, as their function is of purely biologic character. To describe upper arm motion from an *external* point of view, they are not required.

Two offsets, A_2 in medial-lateral and D_3 in anterior-posterior direction describe the distance in a horizontal plane between the sternoclavicular and glenohumeral joint articulations.

Furthermore the offset of the longitudinal axis of the humerus bone to the glenohumeral joint is included in the model as parameter D_6. The length of the humerus bone is parameterized through D_5.

The elbow is a synovial joint located between the humerus bone and the bones of the forearm. The elbow comprises two joint articulations and is described with 2 d.o.f., as shown in figure Fig. 3.4.

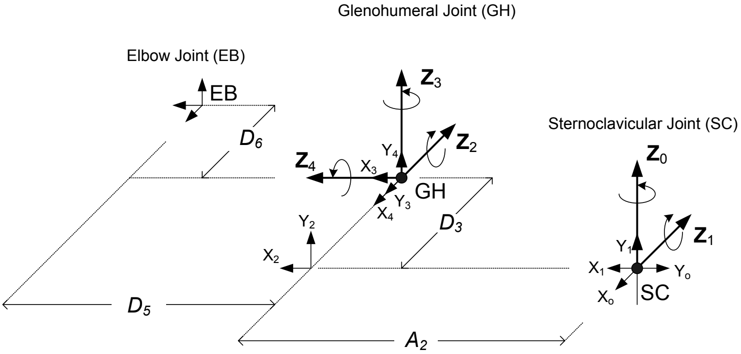

Fig. 3.3. Description of kinematic frames for the shoulder according DH Convention. 2 degrees of freedom (d.o.f.) are modeled for the sternoclavicular joint articulation (θ_1, θ_2), while 3 d.o.f. are implemented for the glenohumeral joint (θ_3, θ_4, θ_5). Axial rotation and scapula motions are neglected, as they are less essential to describe functional motion of the limb in Cartesian space.

The humero-ulnar joint, which enables elbow flexion and extension is described by axis Z_5. Parameter D_7 defines the offset between elbow and the abduction axis of the wrist. Axis Z_6 permits forearm pro-supination. Strictly speaking, the real pro-supination rotation axis is neither parallel to the forearm nor perpendicular to the flexion-extension axis. The movement, which takes place in the real proximal and distal radio-ulnar joints during pro-supination, imposes rolling of radius around ulna. This is why the human hand translates as a consequence. This translation can voluntarily be avoided by upper arm rotation. For modeling of the kinematic structure, however, this fact is not so important as from 'outside' the intra skeletal translations are hardly noticeable. Yet, for modeling of functional movement they are taken into consideration and can be simulated by a superimposed rotation around the longitudinal humerus axis in the presented model.

The wrist joint-complex includes the radio-carpal joint, the midcarpal joints, the inter-carpal joints and the carpo-meta-carpal joints. However, the joint, which is mostly exclusively responsible for movement in the wrist, is the radio-carpal joint. This joint is

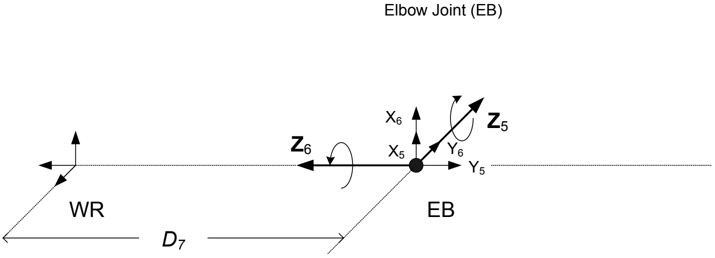

Fig. 3.4. Kinematic frame definition for the elbow joint articulation (EB). 2 d.o.f are included in the model, representing flexion / extension around θ_6 and pro-supination axis around θ_7. The two axes are orthogonal. The apparent translation of the forearm during pro-supination can be simulated by superimposition of upper arm longitudinal rotation. D_7 is the proximal-distal offset to the wrist abduction axis.

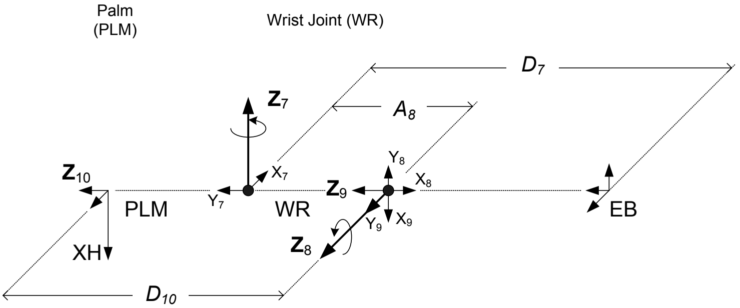

Fig. 3.5. Kinematic frame definition of the wrist (WR) as ellipsoid joint. The proximal-distal offset between abduction axis θ_8 and flexion axis θ_9 is included by parameter A_8. D_{10} describes the distance to the mid-point of the palm (PLM).

an ellipsoid joint located between the distal end of the radius and the proximal row of the carpal bones. The radio-carpal joint is responsible for wrist flexion and extension, as well as for wrist abduction and adduction.

A 2 d.o.f. model of the wrist is shown in Fig. 3.5.

Because the radius of the two convex joint surfaces of the radio-carpal joint is different, the two axes of motion Z_8 for flexion/extension and Z_7 for abduction/adduction must not intersect in one single point. The distance A_8 between those two axes is assumed to be about 2 cm.

A representation of the complete human arm model that was established in ROBCAD™ (UGS, Tecnomatix) for the 3D graphical simulations is shown in Fig. 3.6.

3.4.3 Human arm motion simulation

The model established above, is used to describe motion trajectories, such as the ones naturally occurring in the human upper arm (Kapandji 1992). Despite neglecting several physiological joint articulations in the model, their influence on limb motion was respected and included in the motion simulations.

In reality, flexion of the shoulder in a sagittal plane, for instance, can only occur until about 55° exclusively in the glenohumeral joint. All movements beyond cause a rotation in the sternoclavicular and acromioclavicular joints of about 30°, to allow the scapula gliding downwards over the torso. These rotations enable further flexion and are induced by tension in the ligaments (*ligamentum coracohumerale*) and the passive resistance of the muscles (*teres minor, teres major, infraspinatus*).

From 120° onwards, the humerus bone must additionally rotate around its longitudinal axis to be able to reach into 180° flexion. The motion trajectory for shoulder flexion has been simulated accordingly and is a part of the simulated trajectory for shoulder circumduction in Fig. 3.7 (a). Motions of the glenohumeral and scapulothoraic joints were simulated simultaneously, by using inverse kinematics.

Abduction in the shoulder in a frontal plane can only reach about 90° by pure glenohumeral motion. Above 90° up to about 150°, tension in the ligaments (*ligamentum glenohumerale*) prevents collision of the scapula bone with the humerus head and causes

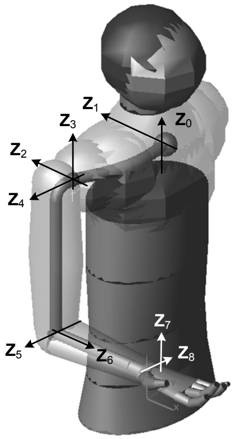

Fig. 3.6. Graphical 3D model of the 9 d.o.f. human arm. The model was created in ROBCAD™ simulation software. The modeled joint axes Z_0–Z_8 are highlighted. Direct as well as inverse kinematic routines are applied to the model to perform Cartesian as well as joint trajectories.

the axis of shoulder abduction to translate medially. The claviscapular, scapulothoracic and sterno-clavicular joints participate in the motion. Until about 150° abduction, the shoulder blade typically translates by more then 10 cm and in addition rotates laterally about 60°. Abduction of up to 180° can only be reached by an additional lateral flexion of the spine or by rotating the upper arm about 180° around its longitudinal axis. In the simulated abduction trajectory shown in Fig. 3.7 (b), the longitudinal rotation of the humerus above 150° abduction is superimposed.

During movement of the 90° abducted arm in a horizontal plane, hereafter called horizontal anteversion, the entire shoulder girdle participates as well. During this functionally important movement, the vertical motion axis translates medial from the glenohumeral joint into the sternoclavicular joint. The trajectory shown in Fig. 3.7 (c) simulates the motion from 45° retroversion up to 90° anteversion.

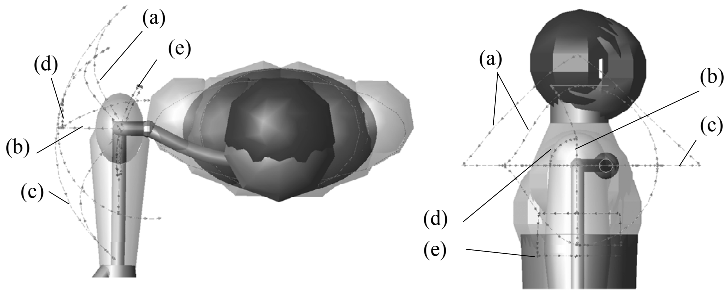

Fig. 3.7. Simulated Cartesian motion trajectories of the 3D model of the human arm in ROBCAD™. Simulated movements are shoulder circumduction (a), shoulder abduction (b), horizontal retro-anteversion of the 90° abducted arm (c), humerus longitudinal rotation (d), shoulder elevation-depression and protraction-restraction (e). Model shown in zero-(reference) position.

Longitudinal rotation of the adducted arm is the only motion in the shoulder that takes place entirely in the glenohumeral joint. The approximate range is 110° in medial rotation and 80° in lateral rotation and limited again by tension in the ligaments (*ligamentum glenohumerale*). The trajectory in Fig. 3.7 (d) was included to verify a part of that motion.

Depression and elevation of the shoulder were simulated from –5° to 15° in a frontal plane. Retraction and protraction of the shoulder girdle were modeled from –20° up to 20° in a horizontal plane. For the simulation depicted in Fig. 3.7 (e), both motions occur exclusively in the sternoclavicular joint.

Shoulder circumduction, is modelled entirely (Fig. 3.7 a) as it excites the extremes of all involved joints in the shoulder girdle.

Realistic trajectories of the elbow were modelled as well. For elbow flexion, the range is dependent on the type of motion. For active flexion, the range is limited to approximately 145° by the contact of the muscles of the upper arm and forearm. Passive flexion can reach up to about 160°. The limiting factors are the contact of radius and humerus bones and the tension in the joint encapsulation. For the simulation in Fig. 3.8 (a) passive flexion was chosen and a hyperextension of 5° was furthermore added.

Supination is limited to about 90° in the model. In reality it is limited by tension in the muscle extensor (*carpi ulnaris*). The implemented limit of pronation amplitude is 85°. In a human, pronation movement is limited through the bone geometry, when ulna and radius are crossed. In Fig. 3.8 (b) the trajectory of pro-supination is shown.

The range of wrist flexion and extension is simulated with 90° maximal amplitude of both movements (Fig. 3.9 a). For radial abduction, which is the movement for which the thumb moves towards the radius, amplitude of 15° is reported. For robustness, 30° are implemented in the simulation as shown in Fig. 3.9 (b). For ulnar abduction the

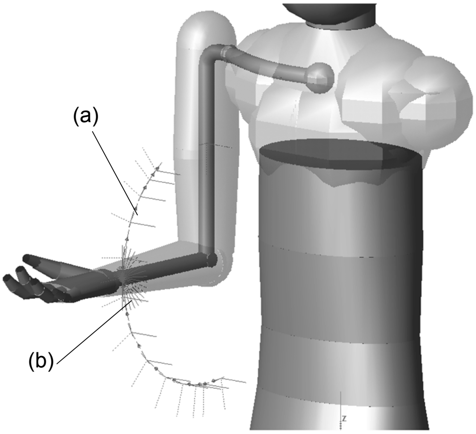

Fig. 3.8. Simulated Cartesian motion trajectories of the 3D model of elbow and forearm. Simulated movements are flexion-extension (a) as well as pro-supination (b). Model shown in 90° flexed elbow position with fully supinated forearm.

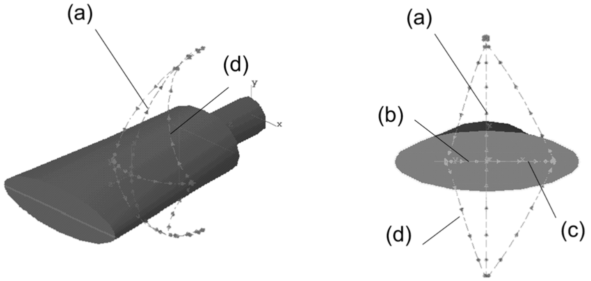

Fig. 3.9. Cartesian trajectories generated with a simulation model of the human wrist in ROBCAD™. Trajectories are shown for wrist flexion-extension (a), radial abduction (b), ulnar abduction (c) and wrist circumduction (d). The circumduction movement indicates the underlying model of the ellipsoid joint.

maximum range is about 45° in supination position. In pronation position, the amplitude of ulnar abduction is smaller. For the simulation (Fig. 3.9 c), an upper bound of 55° was chosen. As can be seen in the simulated circumduction movement of the wrist (Fig. 3.9 d), the circumduction cone has no exact geometric base. The base which is identified by the trajectory of the finger-tip during circumduction is elliptic which matches the real human joint.

3.4.4 Kinematic design

The proposed design paradigm has been applied to an upper arm exoskeleton. The kinematics of the exoskeleton was developed during an iterative design process. Optimization was done between design iterations by geometric intuition. The capability of the mechanism to smoothly interact with the simulated arm motion without reaching into singular positions or ending in a deadlock situations was optimized. Thereby, the robot was attached to several locations on the human torso. This location was optimized as well. Collision detection during simulated motion was enabled between the mechanism of the robot and the approximated dimensions of the human limbs. The minimum distance of the device's limbs to the human envelope size during motion was maximized.

3.5 Results

3.5.1 Ergonomic design for human arm exoskeleton

The resulting ergonomic exoskeleton design features 15 DOF in total. It consists of three distinguished parts for the shoulder, elbow and the wrist that assembled together build the exoskeleton. The shoulder assembly is attached to the thorax proximally and to the upper arm along D_5 (Fig. 3.3) distally. The elbow proximal attachment is shared with the shoulder part distal attachment. The elbow distal attachment is shared with the wrist proximal attachment along D_7 (Fig. 3.4). Each of those parts consists of one serial kinematic chain with actuated and non-actuated joints. The serial structures do not imitate the setting of bridged biological joints, but provide an alternative moving system with the same freedom of motion at the connection between the exoskeleton

Joint No.		A_i [cm]	D_i [cm]	α_i [deg.]	Θ_i
1	Shoulder	0	d_1	90	$*\Theta_1$
2		0	0	90	$*\Theta_2$
3		0	$*\Delta_3$	−90	0
4		0	d_4	90	$*\Theta_4$
5		0	0	−90	$*\Theta_5$
6		0	d_6	−90	$*\Theta_6$
7	Elbow	a_7	0	−90	$*\Theta_7$
8		$-a_8$	$*\Delta_8$	90	0
9		$-a_9$	0	90	$*\Theta_9$
10		0	$-d_{10}$	−90	$*\Theta_{10}$
11	Wrist	0	d_{11}	−90	$*\Theta_{11}$
12		$-a_{12}$	0	0	$*\Theta_{12}$
13		$-a_{13}$	0	180	$*\Theta_{13}$
14		0	0	90	$*\Theta_{14}$
15		0	d_{15}	90	$*\Theta_{15}$

Table 3.2. Denavit Hartenberg parameters for the human arm exoskeleton: This table summarizes the arrangement of joints for the exoskeleton in Denavit Hartenberg Parameters. Parameters shown with (*) indicate the joint variable.

and the human arm. The kinematic parameters of the mechanism are depicted in Denavit-Hartenberg representation in Table 3.2.

Interaction with the shoulder-girdle

The shoulder-girdle comprises 5 DOF, hence, the rehabilitation robot must also have a minimum of 5 DOF. We found out that any mechanism interacting with the ergonomic motion of the shoulder-girdle will actually require a total of at least six degrees of freedom. Mechanisms with less then that will drive very fast into singular positions and collide with the human body when participating in cyclic human motions such as shoulder circumduction.

The exact arrangement of the six degrees of freedom of the mechanism is crucial. A set of joints is necessary to place the mechanism's distal end near the human arm. Moreover, the distal end of the mechanism must be fixed with another set of joints on the human arm to provide orientation. Many different joint-settings are possible for this and were investigated.

The optimal arrangement of joints is shown in Fig. 3.10. The names of variables are in-line with Table 3.2. The five joints Θ_1, Θ_2, Θ_4, Θ_5 and Θ_6 are rotary, while joint Δ_3 is prismatic. It was found out that to enable smooth interaction between the robot and the shoulder, a spherical joint is required between the robot and the upper arm attachment. The spherical joint is illustrated by the joint variables Θ_4, Θ_5 and Θ_6 (Fig. 3.10). Its task is the decoupling of rotation from translation movement components. It was furthermore discovered that it is of utmost importance that the three motion axes of the spherical joint intersect in a point along the longitudinal humeral axis and form an orthogonal set.

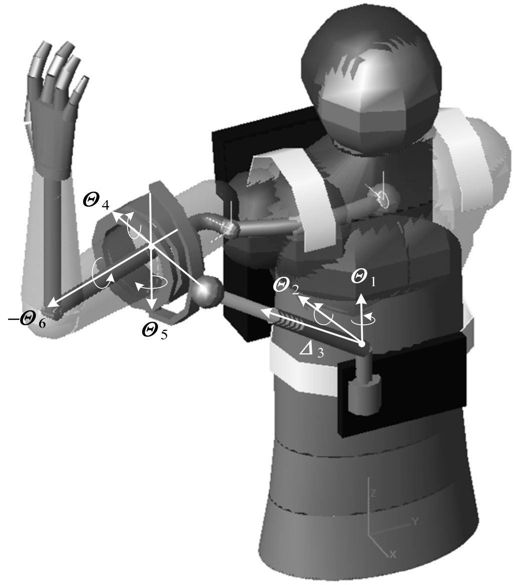

Fig. 3.10. Graphic simulation of ergonomic kinematic robot structure for the shoulder articulation. Shown attached to human torso and upper arm. The rotary joints Θ_1, Θ_2, Θ_4, Θ_5, Θ_6 and the prismatic joint Δ_3 are highlighted. For actuation of shoulder movements, Θ_4 and Θ_5 can be passive joints.

Otherwise, the mechanism will provoke a self-motion, which will lead to collision with the human limbs during circumduction. Such behaviour of inappropriate kinematic design can be seen in Fig. 3.11.

Joint Θ_6 permits longitudinal rotation of the upper-arm at each location in the workspace, independent from the orientation of the rest of the mechanism. This is necessary for some motions, such as abduction in a frontal plane, where longitudinal rotation is a naturally occurring constraint. The first three joints (Fig. 3.10) Θ_1, Θ_2, and Δ_3 are responsible for positioning the mechanisms distal spherical joints in the Cartesian workspace, regardless of its orientation. Thus, each point in the human workspace can be reached with unique position and orientation.

A specific requirement to extend the workspace of the device is the inclusion of the prismatic joint Δ_3. The spherical joint, as well as the prismatic joint are essential to allow continuous movement together with the simulated arm. In the simulations the kinematic structure enabled interaction with the circumduction trajectory, even far behind the body without reaching into singularities. To attain a maximum workspace while allowing a minimum size of the mechanism itself, it was found out that fixing the base of the robot in front of the human at the level of the chest is most optimal.

In order to actuate functional movement in the simulated arm, four actuators, on joints Θ_1, Θ_2, Δ_3 and Θ_6 are required as a minimum. Due to the parallelism with the human joints, some of the mechanism joints can be non-actuated, passive. However, to be able to fully actuate motions in the shoulder girdle, Θ_4 and Θ_5 require actuation as well.

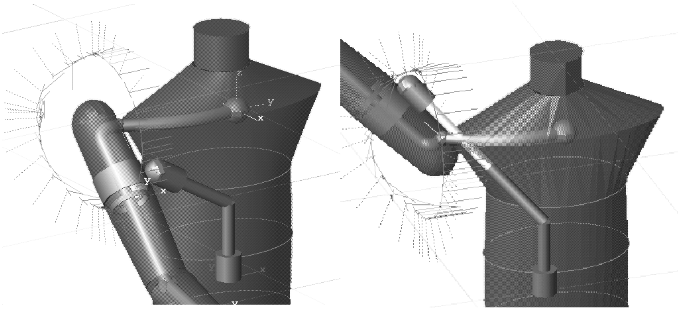

Fig. 3.11. Intersection between a non-optimal 6DOF kinematic structure and the human body in simplified graphical simulation. No spherical joint is used for distal attachment of the mechanism on the arm. Self-motion results in a collision between kinematic structure and shoulder girdle as a consequence.

Interaction with the elbow

Even for simpler biological joints, the formulated design requirements hold. For the flexion and extension joint in the elbow, let us recall Fig. 3.1 (c), which illustrates the constraint motions in case of misalignments to the biological joint. In order to create a natural and pure torque transfer to the elbow, one additional rotary and one additional linear joint must be included in the mechanics of the robot. Both joints can be passive. All possible configurations of the passive joints into the mechanism were analyzed and tested in kinematic simulations. A few examples are shown in Fig. 3.13. The kinematic structure presented in Fig. 3.14 was optimal. It was best able to cope with offsets that were injected between the mechanisms active joint and the elbow flexion axis of the simulated human arm. An advantageous feature of the chosen arrangement of joints is the fact that independently from the direction of offset between the mechanism axis

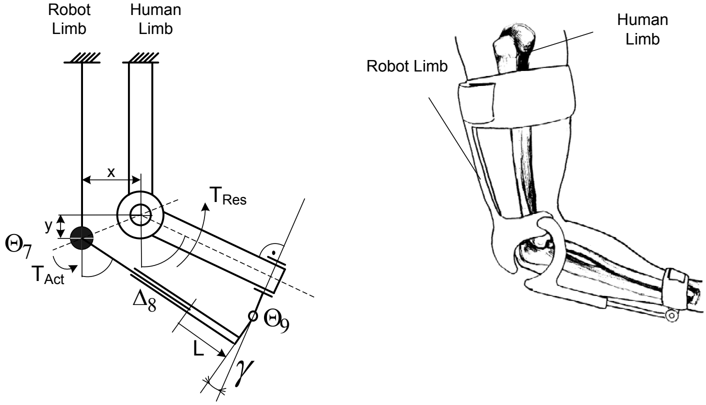

Fig. 3.12. Illustration of ergonomic joint arrangement (robot limb) that makes exoskeletons robust against misalignments to the human joints. Passive, non-actuated joints Θ_9 and Δ_8 compensate misalignments and resulting motion disturbance resulting from offsets x and y. The shown arrangement of joints enables a pure transfer of torque from the exoskeleton to the human joint.

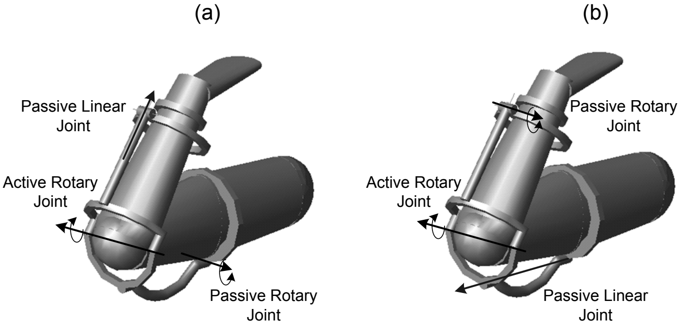

Fig. 3.13. Examples of two non-optimal kinematic structures for the elbow articulation of the exoskeleton, as used during the graphic simulations. (a) The rotary compensation joint is placed on the upper arm, while the linear compensation joint is placed on the forearm. (b) The passive joint placements are vice versa. Both settings cause the robotic limbs to collide with the human limbs during motion, if offsets exist between the active rotary axes and the human elbow flexion axis.

Θ_7 and the humero-ulnar joint, the mechanism links never collide with the human arm during movement. All other implementations of passive joints will cause such collisions. The kinematic parameters of the optimal solution are depicted in Table 3.2. With respect to Fig. 3.1 (c), Fig. 3.12 explains the compensation of misalignments by the additional joints.

To induce torque for flexion or extension into the human arm, only joint Θ_7 needs actuation. Joints Δ_8 and Θ_9 can be passive, and non-actuated.

Joint Δ_8 compensates for L, while Θ_9 compensates for γ. Together; they balance the effects of eventual joint misalignments x and y between Θ_7 and the humero-ulnar joint.

The series of three joints enables a pure torque transfer from the exoskeleton to the human joint, independent from their alignment. While joints Θ_7, Δ_8 and Θ_9 are responsible for elbow flexion and extension, joint Θ_{10} induces forearm pro-supination.

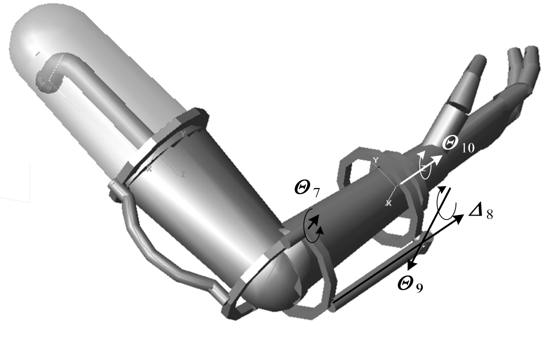

Fig. 3.14. Graphical model of the ergonomic elbow exoskeleton in ROBCAD™. The optimum kinematic structure includes 4 d.o.f. for elbow flexion-extension and forearm pro-supination. Only rotary joint Θ_7 needs an actuator to induce elbow flexion-extension, while the actuated joint Θ_{10} will induce forearm pro-supination. The linear joint Δ_8 as well as Θ_9 is passive.

Misalignments of the robotic device with respect to the forearm pro-supination axis are not critical. A simple rotary joint Θ_{10} for pro-supination suffices. The axis of rotation is parallel to the forearm in the simulations. In reality, joint Θ_6 of the shoulder interface and joint Θ_7 of the elbow interface will be able to compensate misalignment resulting from a pro-supination axis that is naturally not parallel to the forearm.

Interaction with the wrist

It was found out that for the wrist a series of 6 d.o.f. is necessary to allow smooth interaction with the eccentric motion dictated by the ellipsoid radio-carpal joint. The correct placement of each single degree of freedom is essential again. Some concepts, which were investigated with kinematic simulations, are shown schematically in Fig. 3.15.

Both concepts (a) and (b) require a spherical attachment on the hand. Concept (a) comprises a prismatic joint but is essentially the same as concept (b). However, the mechanism type shown in (b) proves to have a larger workspace. The implementation of a spherical joint on the attachment on the hand is expected to be difficult from a mechanical design point of view, especially as some of the degrees of freedom of that spherical joint would require actuation. Therefore, another alternative of kinematic structure was chosen.

To cover both planar movements of the wrist, a three-dimensional pantograph-like mechanism was implemented as depicted in Fig. 3.16. The variable names are referenced to Table 3.2. Together with the bony structure of the human wrist, the mechanism builds a parallel kinematic loop and allows implementation of passive, non-actuated joints to reduce mechanical complexity. For interaction with flexion and extension of the wrist, a two-linkage system in a sagittal plane comprising joints Θ_{11} and Θ_{15} is responsible. The exoskeleton builds a pantograph-type structure together with the human joint as illustrated in Fig. 3.17 (a).

Joints Θ_{12}, Θ_{13} and Θ_{14} compensate for misalignments towards the flexion axis of the human wrist by adjusting the distance between Θ_{11} and Θ_{15} like a 'virtual' prismatic joint, contained in a plane. It is sufficient to actuate joint Θ_{11} to induce flexion or extension in the wrist.

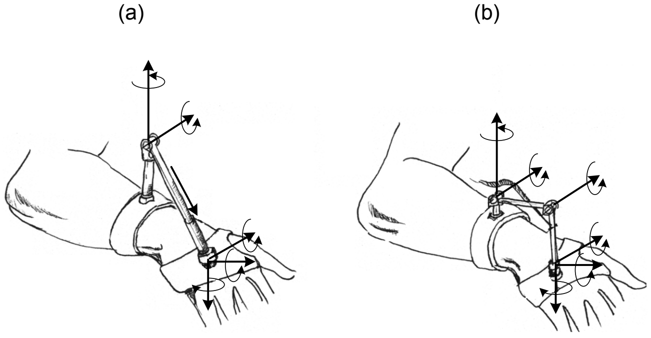

Fig. 3.15. Exemplary sketches of possible motion axes to establish a wrist exoskeleton. Both sketches employ a spherical attachment of the mechanism on the backside of the hand.

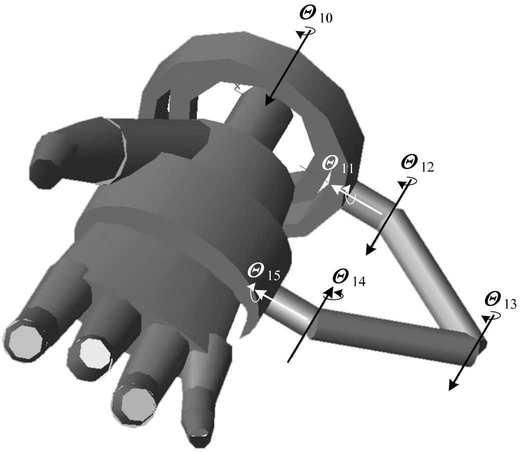

Fig. 3.16. Graphical simulation of kinematic structure of ergonomic wrist articulation. The 6 d.o.f. mechanism can contain only 2 actuators on rotary joints Θ_{11} and Θ_{13} to actuate wrist flexion-extension and radial abduction-adduction respectively. Rotary joints Θ_{12}, Θ_{14} and Θ_{15} can be passive compensatory joints.

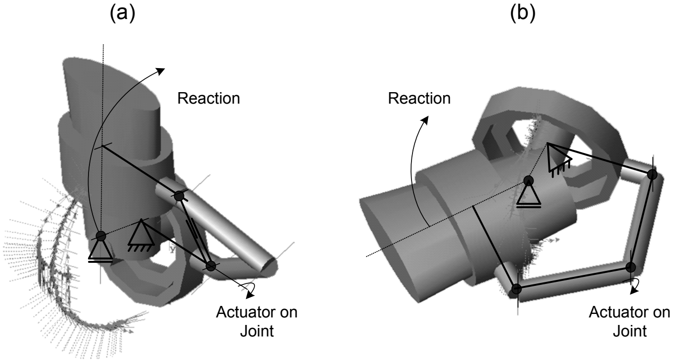

Fig. 3.17. Closed kinematic loops over the human limb can be used to enable under actuation. For wrist flexion-extension (a), actuation of one joint will be sufficient. All other joints will compensate for misalignments occurring through the ellipsoid wrist joint. The same approach is valid for wrist abduction-adduction, which is illustrated in (b).

For abduction and adduction in the wrist, the three rotary joints Θ_{12}, Θ_{13} and Θ_{14} are mainly responsible. They build a pantograph-like structure with the human bones and the radio-ulnar joint, which is illustrated in Fig. 3.17 (b). Due to this closed kinematic loop, actuation of Joint Θ_{13} is sufficient to induce wrist abduction. Joints Θ_{12} and Θ_{14} are purely passive.

The wrist exoskeleton articulation could also be attached in a sagittal plane instead of in a horizontal one. Fig. 3.18 (a) schematically illustrates such a case. 3 Joints are then responsible for wrist flexion and extension, while only two joints interact with wrist abduction and abduction.

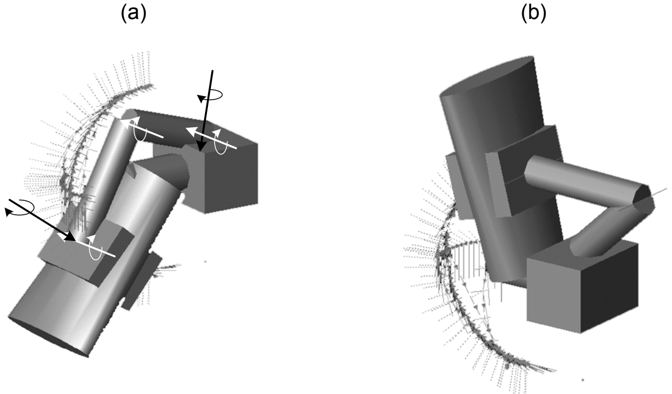

Fig. 3.18. Graphic kinematic simulation of the structure presented in Fig. 3.16, now attached in a sagittal plane to the wrist (wrist approximated by cubes). The sagittal fixation is more prone to joint extremes as shown for maximum flexion (a) and extension (b).

However, in contrast to the geometric intuition, the three-linkage mechanism is not well suited for large motion ranges. As can be seen in Fig. 3.18 (b), large angles of flexion easily drive the device into joint extremes, requiring more complicated mechanics. The most compact mechanical design is achieved by the mechanism outlined before (Fig. 3.16).

The series of 5 joints can cover both planar motions of the wrist. However, for circumduction an additional degree of freedom is required. Fig. 3.19 illustrates how the mechanism slightly inclines due to tilt of the hand, which is a consequence from combined planar movements in the wrist during circumduction. Therefore a further rotation φ around the axis of the forearm is required for the presented mechanism, in order to be able to interact smoothly with the simulated wrist. This additional degree of freedom can be provided by the pro-supination joint of the forearm, which is implemented in the robot as joint Θ_{10}. In the real device, some soft deformation of the tissue around the forearm might suffice to allow rotation φ. In the simulation, the established parallel mechanic design is able to actuate wrist motion without alignment of the exoskeleton structure to the functional biological axes.

3.5.2 Prototype

In order to prove validity of the assumptions taken in the simulation part of the work, a real prototype was developed with an equivalent kinematic structure and tested with real human subjects.

The prototype was build in lightweight construction with carbon fiber reinforced plastics and machined aluminum parts (Fig. 3.20). The total mass is below 4.5 kg. The design is implemented for interfacing to the right arm. Position sensors are integrated into each axis to have the possibility of recording and analyzing the performed movements. The exoskeleton is worn via a carbon fiber vest attached to the chest, and two inflatable attachments on the upper and lower arm. The hand is inserted in the glove

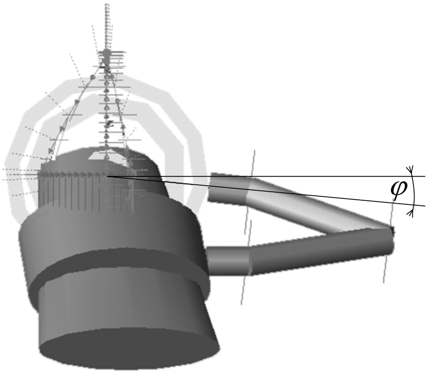

Fig. 3.19. Graphical simulation showing a rotational offset induced by the asymmetric motion occurring in the wrist during circumduction. An additional rotational degree of freedom along the longitudinal axis of the forearm is required in the simulation to allow interaction between wrist mechanism and simulated arm.

of a DAHO™ Hand Orthesis System, provided by Biedermann Motech, Germany. The detailed actuation approach is still under investigation and implementation.

The exoskeleton prototype is designed such, however, that remote actuation via Bowden cable transmissions can be implemented without requiring a major redesign, e.g. similar to the principle presented in (Veneman et al. 2005). Cable pulleys are therefore foreseen. Such remote actuation will not significantly increase the mass of the exoskeleton itself, yet allow active gravity compensation of the entire arm via strong DC motors. Another actuation principle still under investigation is based on integration of smaller actuators directly into the mechanical structure. This would enable the exoskeleton to be used as force-feedback interface for robot control. To compensate the mass of the exoskeleton with integrated actuators, an external counter balancing system can be used. In both cases, some loss of the current full portability will likely be the consequence. However, workspace is not expected to be effected.

3.5.3 Experiments

The ergonomic exoskeleton prototype was tested with various human subjects of different size and statue in a pilot experiment. In the following section, an extraction of the experimental data is presented. Four male subjects participated in the experiment. The subject's statue ranged from 1.74 m – 1.90 m. The exoskeleton was dressed to all subjects in exactly the same configuration, without any adjustments of its mechanical structure, to check robustness against misalignment.

During the experiment, the compatibility of the mechanical structure with motion of different subjects was analyzed. By the experimental protocol every subject was asked to perform a set of predetermined movements, which were, among others, shoulder abduction, shoulder flexion-extension, arm horizontal retro-anteversion and random motion of the arm in the total available workspace. Furthermore, capability to execute activities of daily living, such as drinking from a cup, combing hair and perineal care was assessed. The experimental protocol was executed per subject, first with the exoskel-

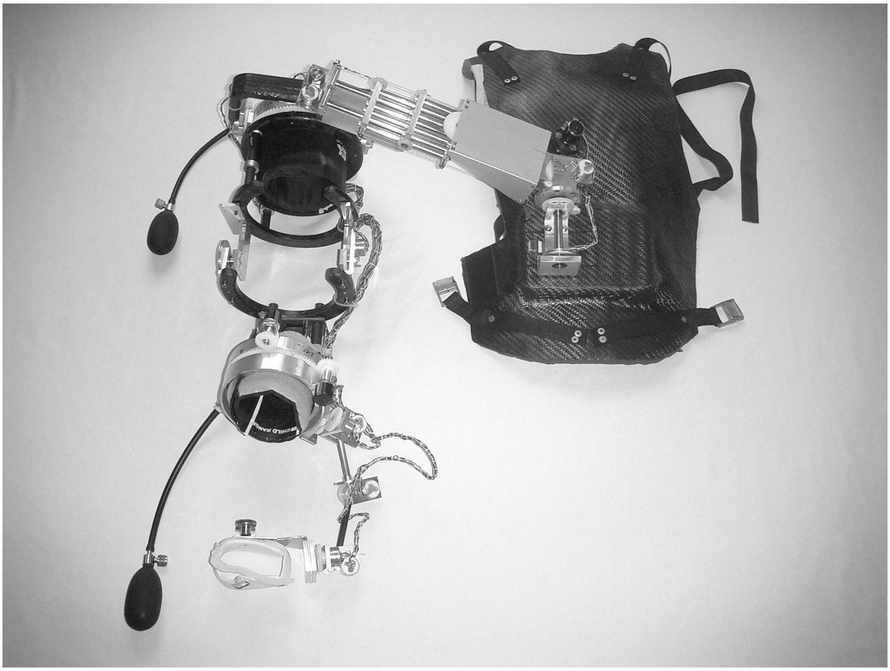

Fig. 3.20. Picture of the ergonomic exoskeleton prototype. The Exoskeleton is attached to a rigid CRP vest and interfaces to the human arm at three levels, the upper arm, forearm and the palm.

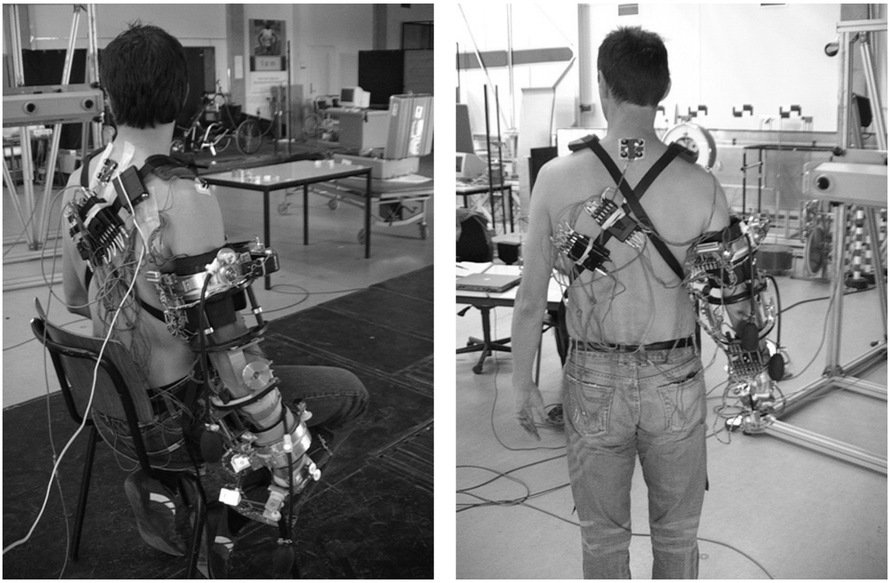

Fig. 3.21. Two subjects wearing the exoskeleton prototypes and optical markers to determine difference in available arm workspace while wearing and not wearing the exoskeleton.

eton dressed on and then repeated without the exoskeleton. During both experiments, the arm motion of the subjects was recorded with an optical motion capture system (Optotrack 3020). Optical markers were attached to the human arm directly, and did not change for both experiments. The dress-on procedure took about 2 min. for the exoskeleton and about 10 min. for attachment of the markers. Landmarks recommended in (Wu et al. 2005) were probed in order to relate the marker positions to the bony landmark positions, which are used for data evaluation.Fig. 3.21 shows some of the subjects, while wearing the markers and the exoskeleton during the session.

All subjects were able to execute the protocol with and without the exoskeleton. During some motions, especially during movements of the hand very near to the thorax, some mechanical parts of the exoskeleton interfered with each other by contacting. This disturbed the motion in that area. However, execution of all daily living tasks was possible with the exoskeleton.

A major goal of the experiments was to analyze the differences in available total arm workspace, while wearing and not wearing the exoskeleton.

Fig. 3.22 shows the workspaces computed from marker measurements projected onto a human skeleton. The graphs show the outmost boundaries that can be drawn by the MPII bony landmark in the real scale. Two workspace boundaries for the right arm, one available while wearing the exoskeleton and one naturally available in healthy subjects are projected onto each other. Dark areas indicate common areas. The lighter areas show the naturally available workspace, which extends further in certain areas. Both surfaces have their origin in the IJ bony landmark on the human thorax.

All subjects reported that motion with the exoskeleton felt comfortable. However, the weight of the device, which had to be fully carried by the arm, tired the subjects during the session. Several pauses were therefore done during the 60 min. lasting sessions, in which the subjects could rest on a chair. The exoskeleton remained attached.

3.6 Discussion

The proposed ergonomic design approach was applied to a wearable exoskeleton for the upper extremity and tested with a prototype.

The presented 9 DOF model of the human arm seems to be a suitable reference, to optimize and develop kinematic structures of wearable human interfaces to. The presented simulation of human arm movement is believed to be sufficiently realistic to describe naturally appearing human arm motions. It is important to consider the human biomechanical structure during simulations such that resulting limb motion is adequate and influence of complex joint articulations such as the shoulder or the wrist are correctly represented. Especially modeling of cyclic movement such as joint circumduction has proven to be important. It allows to check the robots ability to follow natural motion without reaching into kinematic singularities. Such singularities mostly lead to self collisions or collisions with the human body. The suitability of the chosen design approach is confirmed by the experimental results with the real prototype. Major incompatibilities with human motions had already been discovered early in the design process and were eliminated.

It is favorable to design a wearable interface for the human arm such, that alignment to the human joints is not required. Most of the shoulder girdle bones and articulations are for instance covered by muscles, tissue and the skin and are therefore not exactly accessible without dissection. A design based on a parallel mechanism, which can cover exactly the same range of motion as the biological counterpart is a better approach then trying to align a mechanism to the natural joints.

This saves adjustment time and allows to perform rehabilitation tasks in a bigger set of the natural workspace. For the training of activities of daily living, for instance, mostly a large share of shoulder and wrist workspace is required. With the presented exoskeleton structure, the full range of motions of those joints can be actuated, while being wearable. Experimental results have shown this for the shoulder. Currently known wearable devices, such as e.g. the LOKOMAT are only able to actuate a much smaller sub-set of the naturally available workspace. Wearable robots interfacing to the upper extremity for rehabilitation purpose are relatively new, and currently no device is known to the authors, which can interact with motions in the shoulder, to the extent shown above. For more simple joints, such as the elbow, the problem of alignment also exists. The results show that even without alignment to the subjects elbow, the presented device can smoothly interact with the patient arm. This allows using the mechanism for rehabilitation exercises very efficiently.

High comfort can be guaranteed throughout the entire training session. Slippage during training, for instance, will not change the interaction between the human and the device.

The presented experimental results are consistent with the predicted performances from the simulations. The kinematic arrangement of 15 joints can successfully interact with a large portion of the natural human motion.

As can be seen in Fig. 3.22, the available workspace in the subject's front and left of the mid-sagittal plane is restricted by the exoskeleton. This is a limitation from the mechanical design of the first joint, which has an end-stop. However, this restriction is not a major one because the left arm usually executes tasks in the left hemisphere. It was shown that workspace is accessible with the exoskeleton even behind the subject in both, upper and lower hemispheres. This greatly adds to the possibilities of currently known rehabilitation interfaces. The large reachable workspace offered by the exoskeleton is mainly enabled by the attachment of the entire structure on the level of the users chest, which proofed to be optimal already in the performed simulations.

Some occurring collisions between segments of the exoskeleton that were reported are the result of a non-optimized mechanical design, which will be overcome in the next prototype.

Additional gravitational compensation, either actively or passively would likely only increase the usability of the device (Sanchez et al. 2004). In both cases, motion performance as well as workspace will not be negatively affected.

It was shown, how the overall complexity of design can be kept relatively low, by actuating only a set of the joints. The details of the actuation approach will still need to be demonstrated, which is a next step in the current research.

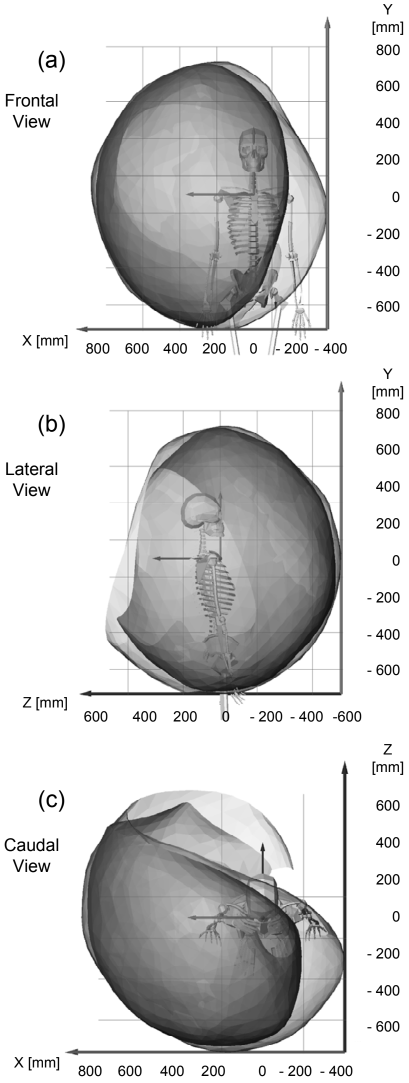
(a)
Frontal View
Y [mm]
800
600
400
200
0
- 200
- 400
- 600
X [mm]
800 600 400 200 0 - 200 - 400
(b)
Lateral View
Y [mm]
800
600
400
200
0
- 200
- 400
- 600
Z [mm]
600 400 200 0 - 200 - 400 -600
(c)
Caudal View
Z [mm]
600
400
200
0
- 200
- 400
- 600
X [mm]
800 600 400 200 0 - 200 - 400

Fig. 3.22. Representation of maximum workspace boundaries of right human arm that can be drawn with MPII bony landmark (units in mm). The graphs represent the available workspace while wearing the exoskeleton (darker common areas) and while freely moving the unconstrained arm (light areas). Data recorded with optical motion capture system (Optotrack^{TM}), wrapped with surface and smoothened.

The Exoskeleton was developed at the European Space Research and Technology Centre (ESTEC) with the intention to serve as Man-Machine Interface for force-feedback telemanipulation with anthropomorphic robotic arms. As such, similar requirements in terms of ergonomics and long duration use are applicable then for rehabilitation robots. However, because usually the transmitted torque per joint in rehabilitation robots is even larger, it is believed that an ergonomic design is even more important for this class of applications. Whether the proposed design can ultimately improve recovery in rehabilitation therapy will need to be investigated during controlled clinical trials.

3.7 Conclusion

The problem of currently known rehabilitation robotics is their limitation in workspace and lack of ability to smoothly interact with human limb motion. Existing wearable devices have the disadvantage to require exact alignment to the biological joints, whereas non-wearable designs have disadvantages related to redundancies of the human arm, which prevents actuation of all possible degrees of freedom.

(1) An ergonomic design was developed, built into a prototype and experimentally tested, which allows rehabilitation robots to interact with a much bigger portion of the functional workspace with respect to other currently known systems.

(2) The design requires no alignment with the human joints and is therefore inherently robust against alignment errors. This results in much shorter time required for dressing on and off (about 30 sec. for dressing on; 30 sec. for dressing off). A further advantage is increased safety for the user, because no residual forces can be created in the human joints if misalignments of the mechanism to the human joints exist.

(3) The overall complexity of the presented device can be reduced by actuation of only a set of the available joints. This is possible, because the novel approach dictates to exploit the fact of closed loop mechanical structures formed between the human arm and the robot.

The presented design guidelines for ergonomic human–machine interfaces are globally applicable and should lead to building rehabilitation robots that can better interact with the patients and provide more comfort during long training sessions. This will allow to train each degree of freedom of the human limbs optimally and to exercise activities of daily living. The presented 9 DOF model of the human upper limb can serve to simulate and develop kinematic structures for upper arm exoskeletons.

3.8 Acknowledgment

The authors would like to thank Ir. H.E.C. Veeger and his colleagues at the V.U. Amsterdam for their support during the measurement campaign and all subjects who kindly took part in the evaluation of the prototype.

Part II

Validation of Ergonomic Design

Chapter 4: An Explicit Model to Predict and Interpret Constraint Force Creation in pHRI with Exoskeletons

A. Schiele
IEEE International Conference on Robotics and Automation, ICRA, Pasadena, May, 2008, in press

Chapter 5: Influence of Attachment Pressure and Kinematic Configuration on pHRI with Wearable Robots

A. Schiele and F.C.T. van der Helm
IEEE Transactions on Robotics, Submitted

Chapter 4

An Explicit Model to Predict and Interpret Constraint Force Creation in pHRI with Exoskeletons

A. Schiele

IEEE International Conference on Robotics and Automation, Pasadena, May, 2008, in press

It is the goal of this paper to introduce an analytical model that allows predicting and interpreting the appearance of constraint forces between human operators and wearable robots during physical human–robot interaction (pHRI). The model helps to understand the mechanisms involved in constraint force generation and is applied in this paper to interpret measured constraint forces from a pHRI experiment.

The geometrical parameters, that the model is based on, are identified from experimental force and position measurements in a non-linear parameter optimization. The attachment stiffness of the exoskeleton on the human forearm is identified. The model is validated and it is shown how and why misalignments between the rotation centers of a human limb and a wearable robot create constraint forces. For the tested subject, constraint forces in the order of ± 10 N were measured. Furthermore it is shown that an ergonomically designed wearable robot with passive compensation joints can reduce such interaction forces.

4.1 Introduction

Robotic Exoskeletons are currently being developed in many research lab's for the rehabilitation of patients suffering from injuries to the nervous system. A multitude of exoskeletons for interaction with the human limb are proposed for rehabilitation training, ranging from external, end-point based devices to wearable full limb exoskeletons (Riener et al. 2005). Their ability to smoothly interact with the human subject is crucial for successful application in physical therapy. It is important that devices interacting closely with a human limb are intrinsically safe, comfortable and are able to exploit the full range of natural motion for movement training. The two main aspects that need good consideration are the implementation of the actuation and motor control, as well as the intrinsic mechanical and kinematic design of their structure.

Still a couple of years ago, such rehabilitation exoskeletons were mostly equipped with motor controllers that dictated movement to the patient. While this seemed to suffice during the childhood of such devices, now, researchers want more freedom to implement assistive therapy protocols as well. In patient assist therapies, the robots actuation supports, but does not impose, the natural movement of the patient during training. Sophisticated controller concepts based on impedance control (Hogan 1985) are currently being implemented in such rehabilitation devices. Hybrid controllers in rehabilitation exoskeletons provide significantly better safety for the user than the earlier position controllers. Thus, from an actuation and motor control point of view, safety and user comfort criteria can be satisfied for wearable robots, or at least will be soon.

An area, however, to which too little attention is paid, is the appropriate kinematic design of wearable robot structures. If the kinematic setting of a exoskeleton robot is not well matched to the user, undesired interaction forces can be created during motion, even if no actuation is provided at all. Those constraint forces could be large in magnitude and provide a safety hazard as well as discomfort to the user. It is interesting to note that such forces, stemming mostly from misalignments between the device's axis of motion and the human limb, can usually not be compensated by the device's actuators. Kinematic mismatches between the Lokomat leg orthosis and patient legs, for instance, were already shown to be responsible for injuries and discomfort. This was reported in (Colombo et al. 2000a) and (Colombo et al. 2000b). Furthermore, it was shown in (Hidler and Wall 2005) that kinematic mismatch between an orthosis and a patient can alter the natural muscle activation patterns. This is counterproductive during physical therapy and could also lead to injury.

Based on such observations, in 2006, we have developed a novel design paradigm for better mechanical and kinematic exoskeleton designs. The paradigm was presented in (Schiele and Helm 2006) on the example of the ESA ergonomic human arm exoskeleton. Currently we are performing an extensive experiment study to analyze the differences between ergonomic and non-ergonomic exoskeleton designs in terms of user comfort and task performance. One element that we measure during this campaign is the constraint forces in a variety of device settings along with their characteristic over the movement angle of the limbs. Looking at the first graphs we immediately noticed that a model will be required to interpret the characteristics of the forces measured.

Fitting a general model does not yield the relation between the measured data and the physical model parameters. Therefore an explicit model is required.

It is the goal of this paper to establish and validate an explicit analytical model that can be used to predict and interpret constraint interaction forces between human operators and robots during physical human–robot interaction (pHRI). This paper will moreover show how the model can be used to determine center of rotation offsets and the attachment stiffness in the combined human–robot system, from measured data.

4.2 pHRI Model

4.2.1 Approach

A mechanical model can describe the causes and effects of centre of rotation offsets between a human joint and a wearable robot joint. Such offsets create displacements of the robots attachment points along the human limb during joint motion. Those displacements will cause forces on the operator limbs.

For simplicity, a one degree of freedom model of human and robotic joint motion will be presented in this paper. The model is illustrated for the elbow joint, but is equally applicable to all other single degree of freedom joints of the human body that can interact with a wearable robot. The model will also be used to estimate unknown experimental parameters such as offsets and attachment stiffness from a real pHRI experiment. A model verification will be performed with a set of experiment data.

Once the model is proven suitable to explain apparent forces in terms of the physical model parameters, it will provide invaluable help in analyzing the effects of wearable robot design to operator comfort.

4.2.2 Mechanical Model for single D.o.F. pHRI

A combined physical human–robot interaction system can be simplified as illustrated in Fig. 4.1. A human operator wears an exoskeleton that is attached at two locations on his limbs. In the example shown, those two locations are the upper-arm and the forearm respectively.

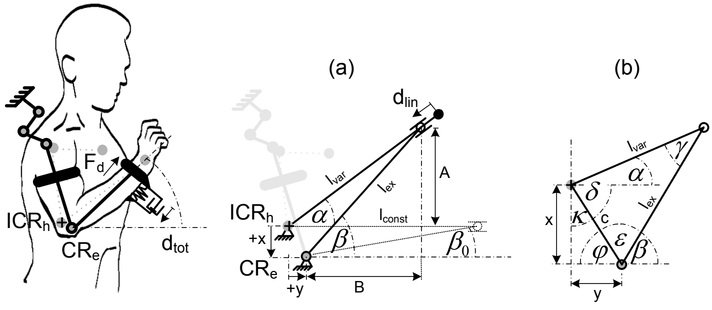

Fig. 4.1. Mechanical model of single degree of freedom interaction between a human joint and a wearable robot. The model is used to predict the constraint displacements d_{tot} that exist between the limb and the robot if their centre of rotations (ICR_h, CR_e) have offsets (x,y).

On the left illustration in the figure, the estimated kinematic structure of a human limb is shown in light grey colored lines. The estimated, but unknown position of the true human elbow rotation axis, or instantaneous centre of rotation (ICR_h) is indicated with a grey dot and black cross. The exoskeleton structure is schematically shown as well. Its elbow joint centre of rotation (CR_e) does not align well to the operator elbow.

For this explicit model, a rigid fixation of the exoskeleton on the upper arm is assumed, while a soft, more compliant fixation is assigned to the forearm fixation. The soft fixation can be modeled for instance with a Voigt-element, that simulates viscoelastic properties. The element-parameters would then describe the lumped viscoelastic properties of the entire coupling between the rigid human forearm and the rigid exoskeleton mechanism. Thus, including muscles, soft tissues, the skin as well as the soft attachment pads of the exoskeleton. It is important to notice, that also the upper-arm fixation will have an influence on the interaction displacements and forces created between the robot and the human limb. For sake of simplicity, however, this will be neglected in this model. The sketch in Fig. 4.1 (a) abstracts the pHRI of this situation into a static mechanical problem. Any offset x or y between the ICR_h and the CR_e will create a constraint displacement d_{tot} of the distal exoskeleton fixture along the forearm of the operator. Through the soft coupling between human and robot, a force F_d will be created according to

$$F_d = k \cdot d_{tot}(\beta, x, y, l_{ex}, z_{ex}) + b \cdot \dot{d}_{tot}(\dot{\beta}, x, y, l_{ex}, z_{ex}) \tag{4.1}$$

In this simplified case, d_{tot} is a function of the elbow exoskeleton rotation angle β. The offsets x,y as well as the design parameters l_{ex} and z_{ex} of the exoskeleton, are the parameters characterizing the constraint force. In (4.1), k denotes the lumped stiffness and b the lumped velocity dependent damping of the coupling between wearable robot and the human bone. In order to understand the magnitudes and behaviour of the constraint force, it is most important to first derive the magnitudes and characteristics of the constraint displacement d_{tot} in dependence of the robot parameters and offsets. This allows us to establish an explicit kinematic model.

The displacement d_{tot} has a linear (d_{lin}) and a rotary (d_{rot}) component. Let us first concentrate on the linear component d_{lin} depicted in Fig. 4.1 (a). For the purpose of this paper, all equations will be derived in dependence of the angle β. They could be derived for α but β can be directly measured on the exoskeleton and thus the measured data can be used as input to the parameter identification later on. It is more difficult to measure the human rotation angle α during an experiment. The angles α and β are geometrically related, however, as we shall see. In order to establish $d_{lin}(\beta)$, from Fig. 4.1 we determine the relationship

$$d_{lin}(\beta) = l_{const} - l_{var}, \text{ with} \tag{4.2}$$

$$l_{const} = y + \cos(\beta_0) \cdot l_{ex};\ \beta_0 = \sin^{-1}(x/l_{ex}).$$

$$l_{const} = l_{ex} \cdot \sqrt{1 - (x^2 / l_{ex}^2)} + y \tag{4.3}$$

The parameter l_{const} describes the distance between the distal attachment of the exoskeleton and the limb rotation axis if the flexion is zero.

Now, only l_{var} remains to be determined. From Fig. 4.1 (a), l_{var} can be expressed as

$$l_{var} = \sqrt{(B+y)^2 + A^2};\ A = \tan(\alpha)\cdot(B+y),\ B = \cos(\beta)\cdot l_{ex}. \tag{4.4}$$

Consequently,

$$l_{var} = \sqrt{\left(y + l_{ex}\cdot\cos(\beta)\right)^2 \cdot \sec(\alpha)^2} \tag{4.5}$$

Equation (4.5) allows expressing d_{lin} in dependence of either α, β or both. Deriving for α will not be further performed in this paper. In order to express d_{lin} only in dependence of β, we must derive the relationship $\alpha(\beta)$ between the two angles. The relationship between α and β is to be purely dependent on the geometric conditions l_{ex}, x and y. Refer to Fig. 4.1 (b) for the following assumption

$$\delta + \gamma + \varepsilon = \pi. \tag{4.6}$$

With,

$$\delta = \pi - ((\pi/2 - \alpha) - \kappa;\ \kappa = \tan^{-1}(y/x), \tag{4.7}$$

and

$$\varepsilon = \pi - \phi - \beta;\ \phi = \tan^{-1}(x/y), \tag{4.8}$$

follows the relationship between α, γ and β

$$\alpha = -\gamma + \beta. \tag{4.9}$$

Under consideration of the property

$$\pi/2 = \tan^{-1}(y/x) + \tan^{-1}(x/y). \tag{4.10}$$

In order to derive $\alpha(\beta, x, y, l_{ex})$ from (4.9), we must express γ also as a function of β and the geometric conditions. It can be seen in Fig. 4.1 (b) that the height on the side l_{var} of the triangle equals

$$c\cdot\sin(\varepsilon) = l_{\mathrm{var}}\cdot\sin(\gamma). \tag{4.11}$$

With the general law of cosines we can express l_{var} alternatively as

$$l_{var} = \sqrt{c^2 + l_{ex}^{\ 2} - 2\cdot c\cdot l_{ex}\cdot\cos(\varepsilon)},\ c = \sqrt{x^2 + y^2} \tag{4.12}$$

Thus, substituting (4.12) with (4.8) into (4.11), and solving for γ yields after simplification

$$\gamma(\beta) = \sin^{-1}\left(\frac{\sqrt{x^2+y^2}\cdot\sin\left(\beta+\tan^{-1}(x/y)\right)}{\sqrt{l_{ex}^{\ 2}+x^2+y^2+2\cdot l_{ex}\cdot\sqrt{x^2+y^2}\cdot\cos\left(\beta+\tan^{-1}(x/y)\right)}}\right) \tag{4.13}$$

It is worth mentioning here that γ creates also a rotary displacement of the attachment cuff on the forearm. We will therefore come back to γ when we discuss the contribution of d_{rot} to d_{tot}. Now, $\alpha(\beta, x, y, l_{ex})$ can be easily derived by factoring (4.13) into (4.9).

The linear displacement d_{lin} is then determined by inserting $\alpha(\beta, x, y, l_{ex})$ into (4.5), and then into (4.2). After simplification we get

$$d_{lin}(\beta) = l_{ex}\cdot\sqrt{1-\frac{x^2}{l_{ex}^{\ 2}}}+y$$

$$-\sqrt{\left(y+l_{ex}\cdot\cos(\beta)\right)^2\cdot\csc\left(\beta+\cos^{-1}\left(\frac{c\cdot\sin\left(\beta+\tan^{-1}(x/y)\right)}{\nabla}\right)\right)},\ \text{with}$$

$$\nabla = \sqrt{l_{ex}^{\ 2}+x^2+y^2+2\cdot l_{ex}\cdot c\cdot\cos\left(\beta+\tan^{-1}(x/y)\right)} \tag{4.14}$$

Equation (4.14) describes the linear displacement of a wearable robot of a structure shown as in Fig. 4.1. Often, however, a wearable robot features an additional link offset z_{ex} around its distal attachment point, similar than depicted in Fig. 4.2.

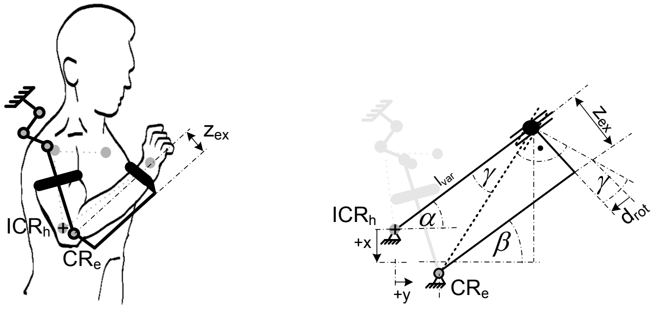

Fig. 4.2. If the wearable robot features mechanical offsets z_{ex}, a further constraint displacement d_{rot} is introduced that can create torques around the attachment point.

If such an offset exists, the rotation introduced by γ will alter the total constraint displacement d_{tot} with an error contribution d_{rot} according to

$$d_{rot} = \tan(\gamma)\cdot z_{ex} \tag{4.15}$$

The total constraint displacement d_{tot} therefore can be calculated by

$$d_{tot}(\beta, x, y, l_{ex}, z_{ex}) = d_{lin} - d_{rot} \tag{4.16}$$

With d_{tot} known, the interaction force F_d can be estimated by (4.1) if the stiffness and damping constants are known.

4.3 pHRI model identification

4.3.1 Goal

The model will be crucial to assign specific force characteristics over the range of motion to the geometric parameters at stake. Without it, no explanation could be offered about the characteristic shapes of forces over workspace.

Mostly, the offsets between a wearable robot joint and a human limb are not known in practice. Equally, the stiffness and damping parameters of the attachments are hardly known for the current experimental setting. It is not practical to measure the parameters x, y, l_{ex}, z_{ex}, k and b directly. We will use the model presented before to identify those parameters from experimentally measured force and position data.

Currently ESA is carrying out an experimental investigation aiming at deriving the influence of interaction forces created by ergonomic and non-ergonomic designed wearable robot interfaces on operator comfort and task performance during pHRI. In the course of those experiments, interaction force is measured between test persons and wearable robots during execution of a set of tracking tasks. In this paper, the data of one subject was used for the verification of the pHRI interaction model presented above.

It is the goal of this identification to derive the geometric parameters x, y, l_{ex} as well as the attachment parameters (stiffness k and damping d) from measured experimental data. This allows proofing suitability of the model to help in the interpretation of the results.

4.3.2 Experiment Method

The subject conducted the following experiment with the ESA human arm exoskeleton. The EXARM exoskeleton is an ergonomic device, as presented in (Schiele and Helm 2006) (Schiele et al. 2006a) (Schiele et al. 2006b). It features passive joints which shall compensate for any misalignments between the human and exoskeleton centers of rotation. Therefore, the EXARM, in this setting, is supposed to not create large interaction forces F_d during motion. In this experiment, the subject performed 12 tracking tasks. For 6 tasks the exoskeletons passive compensatory joints were locked, to emulate a conventional, non-ergonomic robot. For the other 6 tasks, the compensatory joints were free to move. We call this setting the “unlocked” setting. In both settings, the attachment pressure of the device on the limb was randomized between 10–60 mmHg. The “unlocked” and “locked” settings were randomized as well. Before each task, the exoskeleton was dressed to the subject to approximately match the CR_e to the ICR_h. The test person had a statue of 1.71 m and a body mass of 63.0 kg.

Once the device was dressed on, the test person was asked to track a multisine position signal on a computer screen with his elbow movement. The elbow movement was also displayed on the screen. All forces between the human forearm and the exoskeleton were measured with a 6 DOF Force and Torque Sensor (ATI, Nano Series) integrated in the exoskeleton mechanical structure. The tracking signal contained a range of varying random frequencies from 0.05 to 0.7 Hz and amplitudes from 0 to Pi. Each experiment run had a duration of 60 s and data was acquired every 1 ms. The test person wearing the exoskeleton is shown in Fig. 4.3.

4.3.3 Experiment Data

For the purpose of the parameter identification and pHRI model verification, data collected during the "locked", non-ergonomic experiment runs are used. All compensation joints of the exoskeleton were locked.

The data from the "unlocked" runs is used to show the motion of the exoskeletons linear compensation joint that should match the displacement d_{tot}. Data acquired during all experiments is the rotation angle β of the exoskeleton and the force F_d measured by the F/T sensor along the axis of the forearm (in the direction corresponding to Fig. 4.1). The rotation angle is measured by a precision potentiometer on the exoskeleton. For the "unlocked" setting, also the displacement d_{tot} (that takes then place in the, free-to-move linear compensation joint) is measured directly by a precision potentiometer. All signals were filtered analog to reduce noise to less than the quantization level (12 bit).

In order to investigate the forces over the entire range of joint motion, the data was binned for processing. Depending on the desired output, angle bins of 2 degrees ranging from $0-\text{Pi}$ were used (42 bins). For some illustration purposes, larger bins were produced in 10 degree steps of β. The mechanical linkages of the exoskeleton have the following geometric parameters. The forearm linkage length l_{ex} ranges from 0.16–0.21 m and the distal offset z_{ex} ranges from 0.06–0.13 m, depending on the actual contact point of the arm inside the fixation cushion.

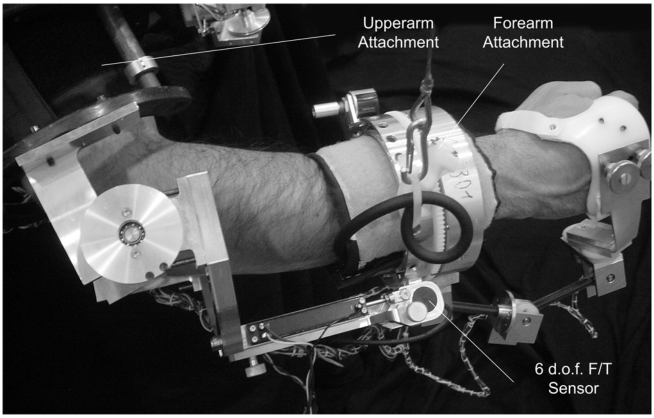

Fig. 4.3. The ESA exoskeleton's elbow articulation is used to collect measurement data of interaction forces F_d and constraint displacements d_{tot}.

4.3.4 Identification procedure

The identification aims at finding suitable model parameters $\vec{\varepsilon}$ for the pHRI model to optimally match the experimental data (F_{di}, β_i). The pHRI model presented above is non-linear in its parameters, which is why we chose to formulate the identification as a non-linear optimization problem in the least squares sense. The parameters were identified by minimizing

$$Q(\vec{\varepsilon}) = \sum_{i=1}^{42} \left[F_{di} - k \cdot d_{tot}\,(\beta_i, \vec{\varepsilon})\right]^2 \quad \vec{\varepsilon} = (\hat{x}_i, \hat{y}_i, \hat{l}_{exi}, \hat{z}_{exi}). \tag{4.17}$$

A linear relationship between displacement and force was taken as a first assumption for the validation in this paper. Velocity dependent effects were not considered.

The optimization was solved numerically using an implementation of the Levenberg-Marquardt algorithm. Initial guesses of the parameters were based on experience, visual analysis of the center of rotation offsets and the geometric design data of the EXARM exoskeleton. Also, manual manipulations with the model parameters where performed to find the correct behavior of the constraint force over the motion range. The starting guesses of the search were $k = 300$ N/m, $x = 0.03$ m, $y = 0.04$ m, $l_{ex} = 0.2$ m, $z_{ex} = 0.12$ m. The upper and lower bounds for searching l_{ex} and z_{ex} were set to the range of possible values for the given EXARM mechanical design.

To quantify how good the model matches the measured data, we used a variety of measures. First, the coefficient of determination R^2 was used to analyze the proportion of variability in the measured data that is accounted for by the model. R^2 was determined according to

$$R^2 = \left(\sum_{i=1}^{n} (F_{di} - \bar{F}_{di})^2 - \sum_{i=1}^{n} (F_{di} - \hat{k} \cdot \hat{d}_{tot})^2\right) / \sum_{i=1}^{n} \left((F_{di} - \bar{F}_{di})^2\right). \tag{4.18}$$

Next, we performed a graphical analysis of the residuals, to check whether the model structure represents the measured data well. The graphical analysis of the residuals included plotting the residuals over the angle β to check whether they are randomly distributed. A second plot, showing a histogram of the residuals was performed to check for normal distribution of the residuals. Normal distribution of the residuals was then checked by the Lilliefors adoption of the Kolmogorov-Smirnov test.

4.4 Results

4.4.1 Measurements of constraint forces F_d during experiments

The resulting constraint forces during motion of the elbow articulation with the exoskeleton are shown in Fig. 4.4 plotted over the exoskeleton elbow rotation angle β. In Fig. 4.4 (a), the results for the “locked” settings of the exoskeleton are depicted, whereas Fig. 4.4 (b) depicts the interaction forces that were present during the trials with the “unlocked” setting. Boxplots respectively show the accumulated F_d measurements for 6 experiment tasks of 60 s each (at 1 kHz sampling). It can be seen that the constraint forces range from about −13.5 N – 10 N for the conventional “locked” setting, while for the “unlocked” setting they range only from about −6 N – 2.6 N. For both cases,

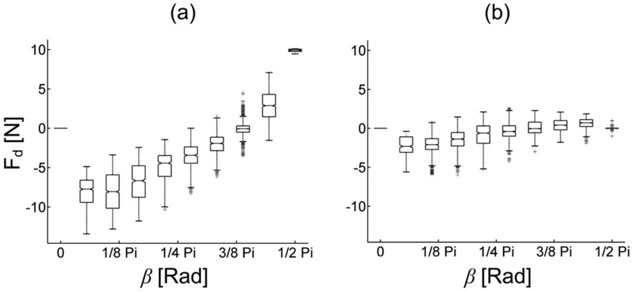

Fig. 4.4. Measured constraint forces F_d along the axis of the test subjects forearm. Boxplots show the characteristics of those forces for (a) non-ergonomic exoskeleton settings without passive joints (“locked”) and (b) ergonomic exoskeleton setting with compensation joints (“unlocked”), over 10 different elbow rotation angles β.

the force bins are significantly different ($p < 0.01$) from one angle bin to another. Thus, there is a clear trend apparent in the data.

4.4.2 Model outputs for constraint displacements d_{tot}

Predictions of the constraint displacement d_{tot} from the model established above are depicted in Fig. 4.5. Whereas the surface plot shown in Fig. 4.5 (a) depicts displacements exclusively induced by offsets in x direction, Fig. 4.5 (b) depicts the displacements as a function of offsets in the y direction only.

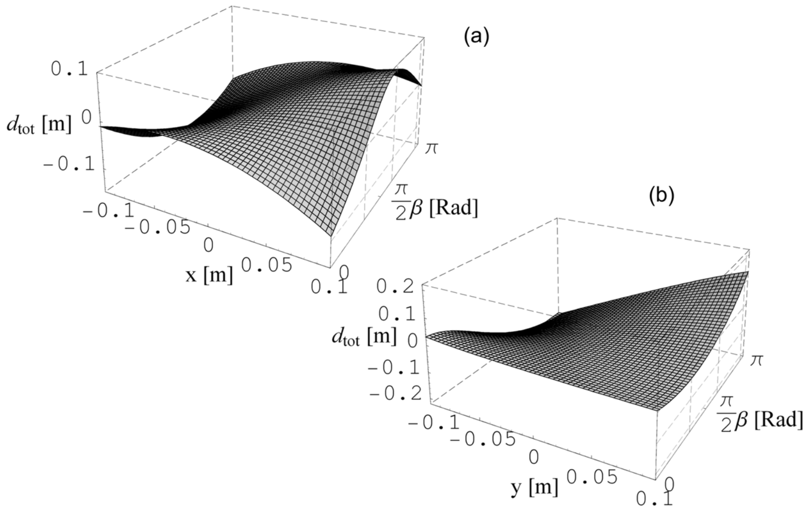

Fig. 4.5. Predicted constraint displacements d_{tot} [m] in dependence of the offsets x and y between the human limb rotation axis ICR_h and the exoskeleton rotation axis CR_e. In (a) the model output is shown for variable x offsets with y equal to zero. In (b) the model output is shown for variable y offsets with x equal to zero.

For both plots, l_{ex} was set to 0.2 m while z_{ex} was set to 0.08 m. It can easily be seen that the behavior of the displacements is complex and very dependent on the offsets. The graphs show that individual misalignments create displacements that are not negligible. A pure y displacement of 10 cm for instance, can create a displacement of a wearable robot along the forearm of about 15 cm during total flexion of the elbow (corresponding to $\beta \sim$ ¾ Pi).

4.4.3 Model identification with "locked" data set

Resulting model parameters

The measured data presented in Fig. 4.4 (a) was used as input to the optimization algorithm. However, a finer discretization of the angle bins was performed and the mean value of the constraint force F_d in each angle bin was used as actual input. The mean values are depicted in Fig. 4.6 by black dots over the exoskeleton elbow joint angle. The optimal parameters that the algorithm converged to are:

$$k = 222.43 \text{ N/m},\ x = 0.048 \text{ m},\ y = 0.059 \text{ m},\ l_{ex} = 0.169 \text{ m},\ z_{ex} = 0.127 \text{ m}$$

The estimated model with the above parameters is displayed as a solid line in Fig. 4.6. Note that towards $\beta = 0$, no data exists. This is the case, because the test person did not reach the 0 degree stroke end with the exoskeleton in the setting with the compensation joints locked.

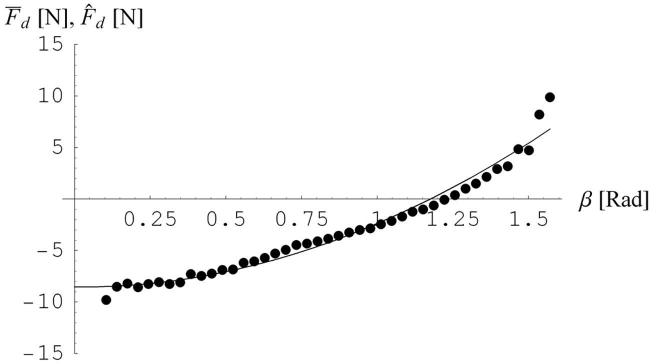

Fig. 4.6. Means of all measured interaction forces F_d during "locked" trials over the exoskeleton elbow angle (points). The result of the estimated interaction force F_d with identified parameters x, y, l_{ex} and z_{ex} of the pHRI model is shown by the superimposed line.

Model validation

The coefficient of determination R^2 shows that the regression line approximates the real data points well ($R^2 = 0.973$). The coefficient was determined with a different data set then the original input data to the model.

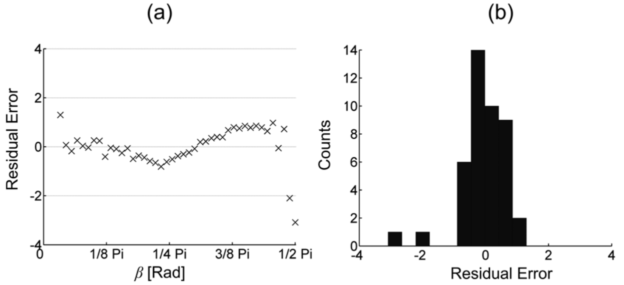

Fig. 4.7. In (a) a plot of the residual errors between the measured data and model estimates show good distribution around 0. In (b), the histogram indicates a normal distribution of the fitting residuals. This indicates that the model structure is suitable for interpreting the measured data.

This alone, however, does not confirm that the underlying model is suitable. Fig. 4.7 depicts the graphical residual analysis. In Fig. 4.7 (a), the residuals are plotted over the input angle β. The residuals are spread around 0 and seem to be equally present in the positive and negative half of the plot. However, the residual might reveal a still underlying trend of the data. Therefore Fig. 4.7 (b) was created that depicts a histogram of the residuals. The residuals are centered around a mean of −0.006 N, with the median at −0.033 N and standard deviation of ±0.782 N. Two outliers are visible close to the data minimum of −3.088 N. The Lillieforts test showed that the residuals are normally distributed ($p < 0.05$).

4.4.4 Constraint force difference in "unlocked" and "locked" exoskeleton setting

The measured constraint forces F_d are shown for both settings, "locked" (dots) and "unlocked" (circles) in Fig. 4.8. All data presented there is averaged over 6 trials and binned into 2 Deg. narrow angle bins. The measured displacement d_{tot} of the compensatory exoskeleton joint is shown (crosses). The displacement was acquired during the trials with the compensation joint of the exoskeleton free. In the other trials this value is constantly zero because the joint is locked.

It can be seen that in the "unlocked" setting of the wearable robot, the force F_d approximates null, when the compensatory joint starts displacing. In contrast, during the "locked" trials, the force builds up during larger angles.

4.5 Discussion

From Fig. 4.4 it can be seen that the characteristics of the constraint forces are intrinsically different for the assumed ergonomic setting, in which passive exoskeleton joints are present and the "locked" setting, for which the passive joints have been locked. Also, when looking at the characteristic of the trend, it is not apparent why a constraint force exists close to $\beta = 0$. Our established model is now instrumental to find out which geometric parameters are responsible for this characteristic. The negative force F_d at $\beta \sim 0$ is attributed in this case to a combination of offsets of the centers of rotation in

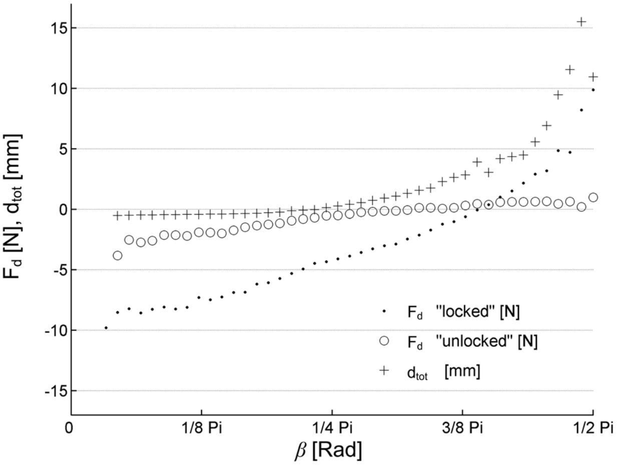

Fig. 4.8. The measured constraint forces F_d are shown for both exoskeleton settings, "unlocked" (compensation joints free to move) and "locked" (compensation joints fixed). The measured displacement of the exoskeleton compensation joint during "unlocked" trials is superimposed. This shows that the setting with passive compensation joints yields lower interaction forces for the test subject.

$+x$ and $+y$ direction. This was revealed from the model identification performed above. (See Fig. 4.6) From manually altering some of the parameters of the model we learned furthermore that the offset z_{ex} plays a crucial role in the large negative forces at small β angles. If z_{ex} is zero, the force offsets at small angles β converge towards zero as well. It can be seen in (4.15) that then d_{rot} converges to zero, which is the cause. In Fig. 4.4 (b), the initial offset is smaller. This is due to the fact, that the exoskeleton has also a passive rotary joint that was free to move in this condition. The rotary joint removes a large share of the influence of z_{ex} on the force. A main difference between the force trends shown in Fig. 4.4 (a) and Fig. 4.4 (b) is also the fact that one force rises after crossing from negative to positive (a) and the other levels off after approaching null from below. This can be explained under the consideration of Fig. 4.8. A negative force F_d pushes the distal attachment of the wearable robot toward the proximal direction (See the sign convention in Fig. 4.1 for reference). We can see in Fig. 4.8 that also in the "unlocked" setting of the exoskeleton, a negative constraint force exists up to an elbow rotation angle of about 55 Deg. This was unexpected. At the same time, there is no excursion of the linear compensation joint that is normally free to move in this exoskeleton configuration. By knowing the meaning of a negative force F_d through our model, we can explain the situation. Logically, this must mean that the negative stroke end of that linear compensation joint is still too large for this test person. The linear joint starts moving only, after the force levels off. For the kinematic design of the exoskeleton this means that the minimum of the passive joint stroke end must be further decreased. Then, the negative force component, that could be felt as disturbance can be reduced.

This way, our model allows drawing direct conclusions about improving the ergonomic exoskeleton design. In the conventional setting, depicted in Fig. 4.8 by the black dots, we see that the locking of the passive compensatory joint creates a positive constraint force along the direction of the forearm for elbow rotations larger then about 67 Deg. There, the force is not cancelled out by the passive joint movement.

The performed parameter identification of the model shows that an attachment stiffness of about 222 N/m exists between the human and the wearable robot. By using this identification technique, we will be able to determine relations between attachment stiffness and comfort of the operators in future experiments. The identified parameters of l_{ex} and z_{ex} make physically sense. They lie perfectly within the possible ranges dictated by the mechanical exoskeleton design. Given those geometric distances, we can determine the exact location of the contact point between the human arm and the exoskeleton. This, in turn, helps to identify the precise torque that can be transferred from attached actuators to the human joint.

The scatter plot of the fit residuals shown in Fig. 4.7 shows a roughly equal distribution of the residuals around 0, which is a good sign for a model fit. Also, the residuals are normally distributed. In general, we can conclude from that that the model is sufficiently well in structure, to explain the trends of the measured data.

The parameter identification procedure has revealed the precise offsets between the human and exoskeleton joint, which, without the model, would have stayed a mystery.

4.6 Future work

In an ongoing experiment campaign, we will investigate with more subjects, what the influence of constraint forces is on task performance, user comfort and mental load. The established and validated model will help to assign subjective and objective performance measures to geometric conditions of the human–robot interaction. The model has already revealed some possible improvements to the EXARM exoskeletons kinematic structure. For the second prototype, that we are currently building, the passive compensatory joint design will be adapted accordingly. Furthermore, the novel prototype shall not contain an offset z_{ex} that contributes significantly to creation of constraint forces even at small limb flexion angles.

4.7 Conclusion

(1) An analytical model for predicting and analyzing constraint force in pHRI has been proposed and validated with experimental data.
(2) The pHRI model is suitable to relate measured characteristics of constraint forces to geometric conditions of a combined human–robot system. The model therefore provides crucial insights into pHRI that otherwise can not be explained.
(3) By identifying the physically meaningful parameters of the model, shortcomings in our current exoskeleton design have been discovered.
(4) For one experiment subject it was shown that the EXARM exoskeleton with passive compensation joints yields significantly smaller interaction forces than an exoskeleton without such joints.

Chapter 5

Influence of Attachment Pressure and Kinematic Configuration on pHRI with Wearable Robots

A. Schiele, F.C.T. van der Helm

IEEE Transactions on Robotics, submitted

The goal of this paper is to show influence of exoskeleton attachment, such as pressure on the fixation cuffs and alignment of the robot joint to the human joint, on subjective and objective performance metrics like comfort, mental load, interface forces, tracking error and available workspace during a typical physical human–robot interaction (pHRI) experiment.

A novel mathematical model of single degree of freedom pHRI is presented and used to explain the causes and characteristics of interface forces in wearable robots. The pHRI model paramters are derived from non-linear parameter estimation. The offsets between robot and human joints, and the attachment stiffness for all 14 subjects are determined from real forces data. Insights gained by the model allow optimization of the exoskeleton kinematics.

Offsets of more than ± 10 cm exist, even if at the start of motion the two axes are aligned. Such offsets can create interface loads of up to 200 N and 1.5 Nm, in the absence of actuation. The optimal attachment pressure is determined to be 20 mmHg, the attachment stiffness is about 300 N/m. Inclusion of passive compensation joints in the exoskeleton is shown to lower interaction forces significantly, which enables a more ergonomic pHRI.

5.1 Introduction

Exoskeletons are subject to intense interest and research at this point in time, for a large field of applications that spans from haptics and fundamental haptic device research (Frisoli et al. 2005) over bilateral tele-robotics (Schiele et al. 2006a) (Bergamasco et al. 1994) and defense applications (Zoss and Kazerooni 2006) (Kazerooni and Steger 2006), up to the relatively new field of robotic physical therapy (Nef et al. 2007) (Tsagarakis and Caldwell 2003) (Carignan et al. 2007) (Riener et al. 2005b). All types of wearable robots must be safe, comfortable and able to smoothly interact with the human user. Safe physical human–robot interaction (pHRI) is difficult to achieve and to quantify and therefore is still a relatively new and important area of research in the field of robotics (Alami et al. 2006).

Two of the most important aspects influencing comfort and safety in wearable robots, is the actuation & control, and the kinematic design of the movable structure.

Up to now, many researchers published novel actuation concepts such as compliant drives (Zinn et al. 2004) (Pratt and Williamson 1995) or antagonist actuators, as well as advanced control architectures (Raibert and Craig 1981) (Hogan 1985) that help to improve the safety of human–machine interaction for wearable robots substantially. Hybrid position and force controllers are now being developed for exoskeletons used in physical therapy (Riener et al. 2005a) that make the robots safer than earlier purely position controlled devices.

An area however, to which only little attention was paid, is the mechanical and kinematic design of wearable robots, for optimal pHRI. This is despite the fact that kinematic mismatch between a human and a robot can cause injury or at least significant discomfort for the operators, as was reported in (Colombo et al. 2000a) and (Colombo et al. 2000b). For robotic physical therapy, the field in which pHRI certainly requires to be the most natural and least constraining, kinematic mismatches between the axes of motion of the robot and the human was shown to reduce the effect of therapy by altering the natural patterns of movement (Hidler and Wall 2005). In (Neckel et al. 2007) the authors report that natural joint moments are altered in stroke patients if they train with a robotic orthosis that is not well harmonized with the human physiology. Causes of such kinematic disparity can be joint center of rotation offsets between human and robot limb and oversimplified kinematic structures of the wearable robot. The LOKOMAT orthesis, for instance, features poor pHRI due to the absence of degrees of freedom for pelvic motion and due to the difficulty of aligning the principal axes of motion correctly. All types of kinematic offsets between human and robot create disturbance or interaction forces at the human–robot interface. Also in other wearable robot applications, improved kinematic design and, in particular, design *for* the human will be important. Presence of disturbance forces in haptic devices, for instance, would be detrimental to their performance if the created interaction forces are in the same order of magnitude than the feedback forces. A mechanically more “transparent” device design alone (transparent in the sense that no disturbing forces are created during movement) could improve perception of sensory feedback and thus, device performance.

It is crucial to note that the causes and characteristics of force artifacts in pHRI stemming from kinematic inequality and from non-ideal attachment between human and robot are poorly explained and covered in literature today. Effects of interaction forces on subjectively perceived metrics are not known, nor are the objective effects explained on mathematical grounds. This paper aims at linking subjective and objective performance metrics acquired during an experiment with a wearable robot to the geometry of the combined human–exoskeleton system. A theoretical pHRI model for one degree of freedom (d.o.f.) interaction is proposed that allows interpreting the measured data and explaining cause and characteristics of interface force creation. A solution to the problem of kinematic alignment is presented, that is based on inclusion of passive compensatory joints in the wearable robot structure. The experiment presented is conducted with and without such compensatory joints to analyze their effect on pHRI.

5.2 Rationale

Recently we have presented a novel design paradigm for human centered exoskeleton kinematics (Schiele and Helm 2006). We have hypothesized there, that smooth pHRI is disturbed by creation of interaction loads during movement that stem from offsets between the main axes of rotation of robot and human limb. In particular, we have shown that *macro-misalignments*, resulting from multi-d.o.f. mismatch between human and robot, e.g. between a 3 d.o.f. shoulder interface of a wearable robot and a real human shoulder girdle (with more than 5 d.o.f.), can be compensated effectively by a wearable robot structure according to the kinematics paradigm presented in (Schiele and Helm 2006). We have hypothesized that inclusion of passive compensatory joints for single-d.o.f interaction with human limbs can compensate interaction forces experienced by the user stemming from *micro-misalignments*, that are offsets of the main rotary joints of human and robot. Fig. 5.1 (a) illustrates the concept of interaction force F_d creation

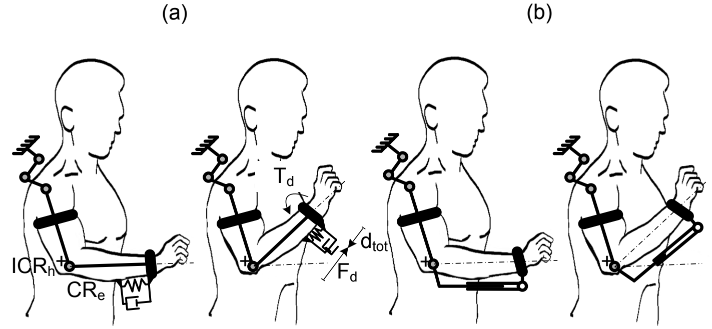

Fig. 5.1. Offsets between the instantaneous center of rotation of a human arm ICR_e and the center of rotation of an exoskeleton CR_e can create constraint displacements d_{tot} that result into perceived interaction forces F_d and torques T_d during movement (a). In (b), an exoskeleton kinematic structure is shown that includes passive compensation joints that aim at reducing such interface forces.

during movement, based on offsets between the human limb center of rotation ICR_h and the wearable robot limb's center of rotation CR_e. In Fig. 5.1 (b), the concept of passive compensatory joints is illustrated. It is not known, however, what the magnitude of such micro-misalignments is in a typical task, and how exactly the misalignments influence the creation of constraint forces. We have therefore developed an analytical model of interaction force depending on the geometric attachment parameters between the exoskeleton and the limb.

This model will be used in this paper for parameter estimation of the pHRI of our subjects.

The goal of this paper is to quantify the effect of joint misalignments in a typical scenario, i.e. the magnitudes of resulting interaction forces. Furthermore, the goal is to relate subjective perception and objective performance metrics to (1) the attachment pressure between exoskeleton and the human limb and to (2) the presence or absence of kinematic compensatory joints in the mechanical structure of the exoskeleton. It shall be investigated if the geometry of the attachment between human and robot influences the creation of interaction forces and how they can be optimally reduced by incorporating compensatory joints into a wearable exoskeleton.

5.3 Method

An experiment was conducted, in which a group of subjects was asked to perform a proportional visual tracking task with their elbow, while wearing the EXARM exoskeleton. The kinematic structure of the exoskeleton, as well as the interface pressure on the operator was altered between experiment runs.

5.3.1 Experimental setup

The experiment was carried out with the elbow interface of the EXARM (Schiele et al. 2006a) (Schiele 2008b) exoskeleton. The exoskeleton is attached to the operator's upper- and forearms by means of two inflatable air cushions and gravity-balanced by a cable system with compensation masses (Fig. 5.2). The EXARM comprises 3 joints for the elbow articulation. The first, Θ_7 is the main joint for flexion-extension (approximately aligned with the anatomical flexion-extension axis), the second, Δ_8 is a linear passive joint and the third, Θ_9 a rotary passive joint. *(The joint naming corresponds to the previous description in (Schiele and Helm 2006))*

All in all, its kinematic structure is similar to the one illustrated in Fig. 5.1 (b). The joints Δ_8 and Θ_9 can be locked with quick lock pins, in order to emulate a conventional kinematic structure for wearable robots, not featuring compensation joints. This makes the device similar to the one illustrated schematically in Fig. 5.1 (a).

5.3.2 Experiment protocol

The experiment was conducted with 7 male and 7 female subjects (stature: 1.75 m ± 0.09 m, mass: 68.7 kg ± 12.8 kg) that were un-trained and not informed about the detailed scope of this experiment. Each subject was asked during 12 experiment trials to visually track a random crested multisine signal, the target signal v, on a computer

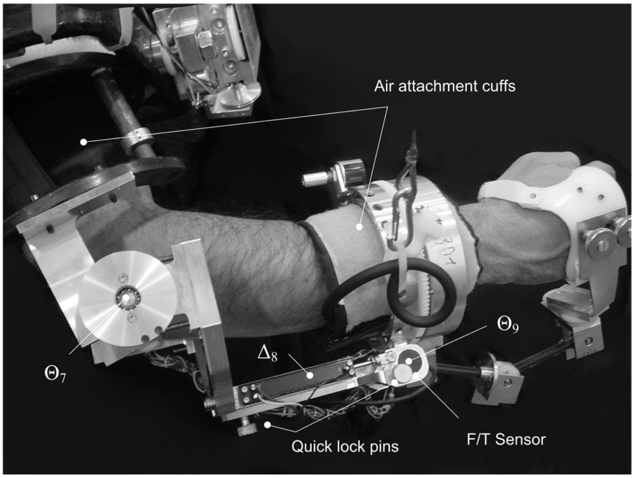

Fig. 5.2. Overview of the elbow articulation of the ergonomic EXARM exoskeleton used to conduct the experiments. Θ_7 is the main elbow rotation axis of the exoskeleton. The effect of it's alignment on the creation of interaction forces was a main measure in the experiment. Δ_8 is a linear and Θ_9 a rotary compensation joint. The compensation joints can be locked by quick lock pins to emulate a non-ergonomic device design.

screen with the motion of their elbow. The angle β on the EXARM elbow joint (Θ_7) was measured and displayed along with v as moving bars on a computer screen. The instantaneous tracking error was shown as a third bar on the screen, to give some feedback of the current tracking performance. The duration of each trial was 60 s. The target signal demanded elbow rotation from 0–90 Deg. with frequencies ranging between 0.05–0.35 Hz. Between the 12 trials, the *kinematic setting* of the exoskeleton, as well as the *interface pressure* between the fixation cuffs of the exoskeleton and the human limb was varied randomly. Each combination of factors was tested once per subject and the subjects were blinded to the experiment conditions. The kinematic settings were called *'locked'*, when all passive compensatory joints of the exoskeleton were fixed, and *'unlocked'*, when all passive compensatory joints were free to move. The interface pressure P was varied between 10–60 mmHg in steps of 10 mmHg, always equal on the two cuffs. During the trials, the multisine target signal v, the displacements β (joint Θ_7), d_{lin} (joint Δ_8) and Θ_{rot} (joint Θ_9) and the interaction force F_d and moment T_d (Fig. 5.1) were recorded at 1 kHz sampling frequency. While the joint motion was measured with high precision potentiometers, the interaction loads were measured with a 6 d.o.f. load cell (ATI Nano Series) inserted between the forearm cuff of the exoskeleton and the exoskeleton structure (Fig. 5.2). All recorded signals were anti-aliased by analog filters to limit noise to levels smaller than the quantization noise of the A/D converters (12 bit).

After each trial, the subjects were asked to rate a subjective questionnaire on a visual rating scale with a pen. They marked their rating on 8 linear rating scales that ranged from 0 (low) to 100 (high) points, for (1) *"comfort" (definition: How comfortable was this setting of the exoskeleton during movement?)*, (2) *"motion hindrance" (definition: How much hindrance to the movement did you experience?)* and (3–6) the six NASA TLX rating scales of physical- (*PD*), mental- (*MD*), temporal- demand (*TD*), operator performance (*OP*), effort (*EF*), and frustration level (*FR*). The definitions presented to the subjects were adopted from (Hart and Staveland 1988). After all 12 trials the weighting factors for the TLX rating scales were acquired for each subject by pair wise comparisons and computed into an overall set of group weights. Next, the most comfortable attachment pressures were determined per subject by inflating the cuffs and asking the most comfortable setting.

To get the subjects used to the set-up before the real experiment, a five-trial training session had been carried out. Pilot experiments had confirmed that this was sufficient to get the subjects used to the task. The test runs were conducted with a different input signal and no variation of the attachment and kinematic properties. This accustomed the subjects to the task and to the rating on the subjective rating scales. To each subject the exoskeleton was attached such, that at the fully extended limb angle the exoskeleton joint was aligned with the human joint as good as possible. All tracking movements were conducted with a horizontally elevated arm in a horizontal plane, in order to remove the effect of gravity on the force measurements as good as possible. This way, the measured axes did not show influence on gravitational force.

5.3.3 Statistical design and analysis

A series of statistical tests was performed to determine the effects of the experiment conditions (independent variables) on the output measures (dependent variables). All statistical tests were factored analyses of variance (ANOVA) that test for equality of sample population means.

Independent Variables

The experiment features two main independent factors, which are (F1) the kinematic condition, with two levels *'locked'* and *'unlocked'*, hereafter called *L* and *U* respectively; and (F2) the interface pressure with six levels ranging from 10–60 mmHg. The Subjects were used as a third factor (F3) in some presented statistical analyses, in order to take into account the variability between the subjects that may provide a large part of the overall measured variance.

Dependent Variables

Objective, as well as subjective performance measures are analyzed in this study. Both groups consist of mean output measures that are averaged over each full experiment run (1 min. at 1 kHz sampling). For the objective metrics, those measures are (1) the mean absolute interaction force $|\bar{F}_d|$ per trial, (2) the mean absolute interaction torque $|\bar{T}_d|$ per trial, and (3) the RMS error of the signal tracking E_{Tr} per trial, defined as

$$E_{Tr} = \sqrt{\sum_{i=1}^{s} (\beta_i - v_i)^2 / s}\,, \tag{5.1}$$

with v_i, the angle of the multisine signal at the *i*-th sample, β_i the exoskeleton elbow angle at the *i*-th sample, and *s* the signal length in samples ($s = 60000$). For the subjective metrics, the measures are (4) the comfort rating $\bar{C}$ that was acquired after each trial, (5) the motion-hindrance rating $\bar{M}$ acquired after each trial, (6) the group weighted NASA

TLX workload rating $\overline{W}_{WL}$, and (7–12) the group weighted ratings on the individual TLX scales ($PD-FR$).

In order to reveal also the influence of the experiment factors, mainly the kinematic setting, on the combined human–exoskeleton system during movement (thus, within each trial), five additional objective measures were processed into angle bins, per experiment. The binned dependent variables are (13) the raw, signed interaction Force $\overline{F}_{d\beta}$, (14) the raw, signed interaction Torque $\overline{T}_{d\beta}$, (15) the voluntary range of motion R_β derived from the exoskeleton elbow joint angle β, (16) the displacement of the linear compensation joint d_{lin}, and (17) the displacement of the rotary compensation joint Θ_{rot}. The first variables, $\overline{F}_{d\beta}$, $\overline{T}_{d\beta}$, d_{lin} and Θ_{rot} were accumulated for each trial into 9 bins that each spanned 10 Deg. of the exoskeleton elbow joint angle β, in the range from 0–90 Deg. This span of the bins was chosen to have sufficient data points to derive the main trend of the data during movement, while keeping a sufficiently good resolution. The voluntary range of motion R_β is expressed in percent of multisine target angle v reached. It is defined as the ratio $(s_\beta \cdot 100)/s_v$, with s_β, the total number of samples for which β lies inside a 10 Deg. wide bin per trial, and s_v the total number of samples for which v lies within the same 10 Deg. bin. Thus, for this measure, the samples do not have to lie within the same bin at the same time. This calculus had to be done in order to arrive at an estimate of the available limb angle workspace, since the true human elbow joint angle α was not measured directly.

Statistical analysis

In order to analyze all aspects of the results, a series of six 2-way ANOVA's were performed on each dependent variable of the experiment.

First, the influence of the kinematic condition on the dependent variable was tested (test: *T1*) by a 2-way ANOVA considering the kinematic condition as main and the subjects as secondary factor, with 6 repetitions per subject (*T1*: $n_{F1} = 84$, $df_1 = 1$; $n_{F2} = 12$, $df_2 = 13$, $rep. = 6$). Next, the influence of the pressure variation was tested (*T2*) as main, with subjects as secondary factor (*T2*: $n_{F1} = 28$, $df_1 = 5$; $n_{F2} = 12$, $df_2 = 13$, $rep. = 2$). Then (*T3*), the influence of the kinematic setting was tested as main with the influence of pressure variation as secondary factor (*T3*: $n_{F1} = 84$, $df_1 = 1$; $n_{F2} = 28$, $df_2 = 5$, $rep. = 14$). This test allows investigation of the interaction between the main factors, with high statistical power.

In order to investigate differences between kinematic conditions only, excluding additional variance due to interface pressure variation (*T4*), six two factor ANOVA's were done for each pressure increment, with the kinematic configuration as main and again with subjects as secondary factor (*T4*: $n_{F1} = 14$, $df_1 = 1$; $n_{F2} = 2$, $df_2 = 13$, $rep. = 1$). To test the pressure variation independent of the variance contributed by the kinematic levels (*T5*), two 2-way ANOVAs were performed for each dependent variable, with pressure condition as primary and subjects as secondary factor (*T5*: $n_{F1} = 14$, $df_1 = 5$; $n_{F2} = 6$, $df_2 = 13$, $rep. = 1$). At last, one 2-way ANOVA was computed per subject (*T6*) with kinematic condition as main and pressure condition as secondary factor (*T6*: $n_{F1} = 6$, $df_1 = 1$; $n_{F2} = 2$, $df_2 = 5$, $rep. = 1$). *T6* allowed determining the interaction effects between the first two factors for each subject.

To reveal effects of the kinematic setting on the binned measures during elbow motion, *T1* was used for each bin. With those six tests, the main effects of all factors as well as their interaction can be analyzed. All testing and analysis was performed in MATLAB. In the results section only significant results at 5%-level or higher are reported.

5.4 pHRI model

5.4.1 Model structure

Fig. 5.3 shows the basic structure of the one d.o.f. pHRI model. In order to analyze the effects of geometric alignment between the human limb center of rotation ICR_h and the wearable robot axis of motion CR_e on interaction force, the mathematical model relates the offsets x and y between the two axes to the resulting displacement d_{tot} of the exoskeleton attachment at the forearm. The total displacement d_{tot} is created by a combination of linear d_{lin} (Fig. 5.3 a) and rotary d_{rot} (Fig. 5.3 b) terms. The offsets are described in a fixed coordinate frame of the upper-arm. Their direction is defined for a fully extended human limb in the right illustrations of (a) and (b).

The model considers the limb angle of rotation α (α equals zero for the fully extended limb), or alternatively the robot's joint angle of rotation β, as well as the Denavit-Hartenberg (DH) parameters of the robot, the link length l_{ex}, and the link offset z_{ex}. β_0 is the resting angle of the robot if the human limb is fully extended (if: $\alpha = 0$). The rotary offset between human limb and robot link is described by γ. To keep this monograph to appropriate size, we refer to (Schiele 2008c) for the detailed calculus required to arrive at the model and the model validation.

However, we included the two main output equations for d_{tot} resolved for α and β in the Appendix. We consider model dependence from β in this article, since this is the variable that we could actually measure during the experiment. In (Schiele 2008a) we show outputs of the model in dependence of the pure elbow rotation α. The force creation during motion is a linear approximation depending on the displacement output of the model according to

$$F_d = k \cdot d_{tot}(\beta, x, y, l_{ex}, z_{ex}) + b \cdot \dot{d}_{tot}(\dot{\beta}, x, y, l_{ex}, z_{ex}). \tag{5.2}$$

Where, k is the lumped stiffness between the human and the robot and d the damping, according to the viscoelastic attachment property described as a Voigt-element in Fig. 5.3 (a).

Different displacement-force relationships can be assumed, however, we showed in (Schiele 2008a) that a simple linear relationship between displacement and force suffices to describe measured forces accurately with the model. Therefore in the present study, all parameter identifications that will be performed, will assume a linear displacement-force relationship without velocity dependent effects according to

$$F_d = k \cdot d_{tot}(\beta, x, y, l_{ex}, z_{ex}). \tag{5.3}$$

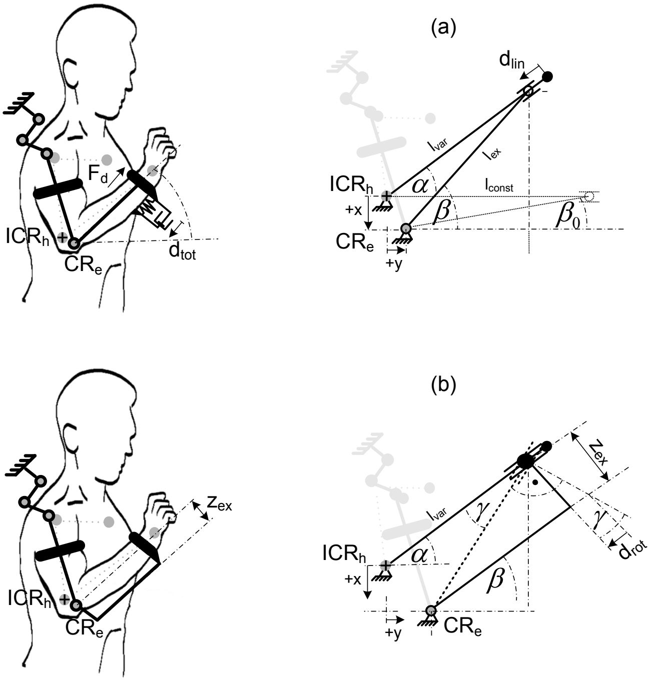

Fig. 5.3. Graphical illustration of the main parameters of the 1 d.o.f. *p-HRI* model that describes the creation of the interaction force F_d depending on offsets x and y between the human elbow center of rotation (ICR_h) and the wearable robot center of rotation (CR_e). The offsets are described in the upper-arm coordinate system for a fully extended limb. The Denavit-Hartenberg parameters of the robot l_{ex} (link length) and z_{ex} (link offset) are inputs to the model. The angle of the human limb is described by α, whereas the angle of the exoskeleton joint is described by β. In (a), the linear displacement contribution d_{lin} is depicted. β_0 describes the rest position of the robot during the fully extended human limb. In (b), the displacement contribution d_{rot} stemming from rotary offsets γ and the robot link offset is illustrated.

5.4.2 Model parameter estimation

The binned measured force $\overline{F}_{d\beta}$ acquired during the L trials was used as input to the parameter estimation with the pHRI model for each subject and the subject group. This way the geometric model parameters x, y, l_{ex} and z_{ex} as well as the attachment stiffness k could be estimated from measured data. To identify the parameters for the subject group, the mean forces $\overline{F}_{d\beta}$ of all 14 subjects were used. For the individual subjects, mean forces $\overline{F}_{d\beta}$ over all 6 L trials were used. The parameter estimation was performed by means of non-linear least squares optimization as described in (Schiele 2008c). Goodness of fit was determined by the coefficient of determination R^2, the norm of the residuals $|res.|$, and graphical residual plots.

5.5 Results

5.5.1 Interaction force prediction from pHRI model

Fig. 5.4 shows the predicted outputs of the pHRI model for interaction forces F_{dm} depending on combination of offsets *x* and *y* over the robotic limb model angle β_m.

Influence of the link parameter z_{ex} on the force is shown for a range of values from 0–0.14 m. The attachment stiffness was taken from (Schiele 2008c) to be 200 N/m and the link length l_{ex} was set to 0.167 m, which is the true value for the EXARM exoskeleton in *locked* configuration. For all graphs shown in Fig. 5.4, *x* was, like *y* equal to 0.05 m and the directions of the offsets are indicated atop each graph. This represents a typical example. It can be seen that the interaction force shows very different characteristics over the workspace, depending on the directional combinations of offsets between ICR_h and CR_e. Here, predicted peak forces are in the order of ± 30 N.

5.5.2 Measured Interaction Forces and Torques

The full spectrum of measured raw peak-to-peak interaction forces F_d span for the group from −232 – 165 N for the *L* and from −57 – 70 N for the *U* condition, as shown

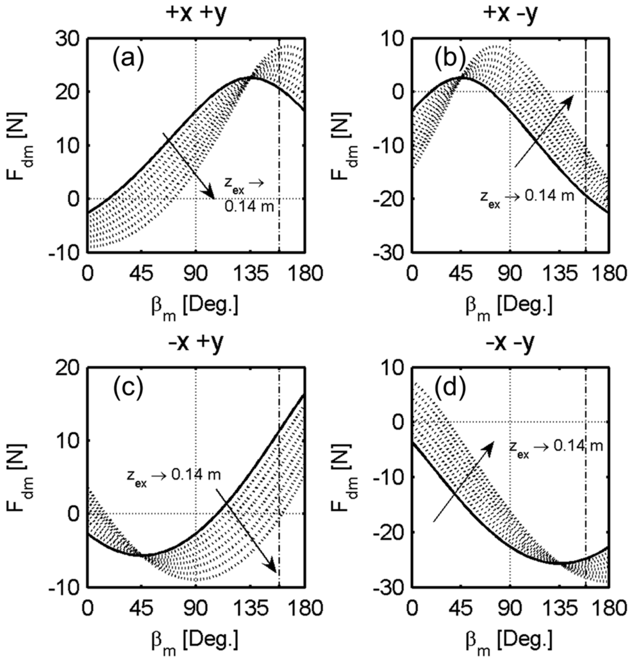

Fig. 5.4. Exemplary model output from the 1 d.o.f. pHRI model. Interaction force F_d experienced between the human arm and the robot attachment is depicted over the angle β_m of a wearable robot model, for different link offsets z_{ex} ranging from 0 to 0.14 m. The force is displayed for $|x| = |y| = 0.05$ m, with the sign of the offset indicated on top of each graph. Dashed lines indicate the maximum elbow rotation angle for the 95th percentile of U.S. male population.

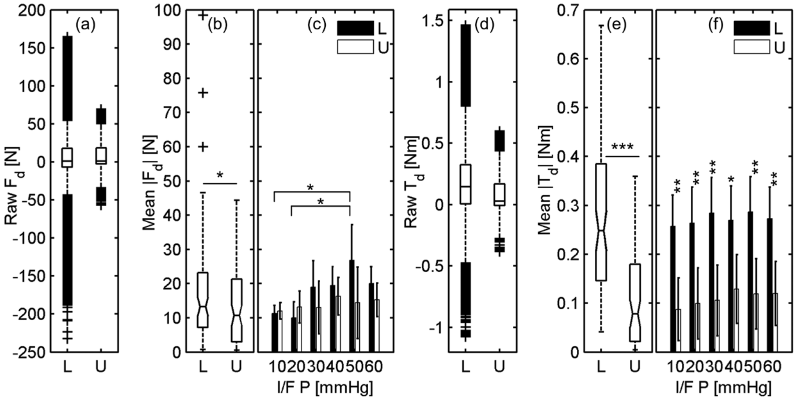

Fig. 5.5. Illustrations (a) and (d) show the raw measured force F_d and torque T_d over all experiments as boxplots with outliers (indicated by + markers). (b) and (c) show the mean absolute interaction force $|\overline{F}_d|$. (b) shows boxplots of the force over the two levels of the kinematic setting factor, with the full measured variance (n = 84 per level). This data was used for the 2-way ANOVA test *T1*. (c) Shows the mean force values that are output from six 2-way ANOVA's *(T3)* that compared means between kinematic settings per pressure increment. The 95% CI of the mean computed for *T3* is displayed by errorbars. The variance due to subjects is removed by the ANOVA. Test *T4* compared the means between pressure increments of equal kinematic level. (e) and (f) show the mean absolute interaction torque $|\overline{T}_d|$ in the same way as (b) and (c) do for the force. Significance levels are coded as (*, $p < 0.05$; **, $p < 0.01$; ***, $p < 0.001$).

in Fig. 5.5 (a). The full spectrum of measured raw peak-to-peak interaction torques T_d for the group span from −1.0 – 1.46 Nm for *L* and from −0.4 – 0.60 Nm for the *U* kinematic condition as shown in Fig. 5.5 (d). The mean loads $|\overline{F}_d|$, and $|\overline{T}_d|$ over all experiment trials and subjects are shown as boxplots in Fig.1 (b),(e) and show differences over the kinematic setting levels *L* and *U*. Bargraphs in Fig. 5.5 (c) and (f) show the group means of the interaction loads over attachment pressure for both kinematic levels. Errorbars indicate their 95% confidence interval (*CI*) on correct estimate of the means.

T1 reveals that the mean interaction force per trial $|\overline{F}_d|$, is significantly lower in the *U* (14.02 ± 11.95 N) than in the *L* (17.75 ± 16.33 N) condition for the entire subject group ($F_{FdLU}[1,140] = 4.66$; $p = 0.0326$). The subjects contribute heavily to the measured variance ($F_{FdS}[13,140] = 7.16$; $p < 0.001$), which is apparent in the large spread of the data presented in the Fig. 5.5 (b). The kinematic setting factor shows interaction with the subject factor (F_{FdLU} [13,140] = 2.94, $p < 0.001$).

The mean torque per trial $|\overline{T}_d|$ is also significantly lower in the *U* (0.109 ± 0.099 Nm) than in the *L* (0.272 ± 0.153 Nm) condition ($F_{TdLU}[1,140] = 333.1$, $p < 0.001$) for the subject group. The subjects contribute significantly to the measured variance ($F_{TdS}[13,140] = 25.7$, $p < 0.001$).

The kinematic setting shows again interaction with the subjects ($F_{TdLU}[13,140] = 27.4$, $p < 0.001$). At all six pressure increments (*T4*), the interaction torque is smaller for the *U* condition than for the *L* condition, as can be seen in Fig. 5.5 (f).

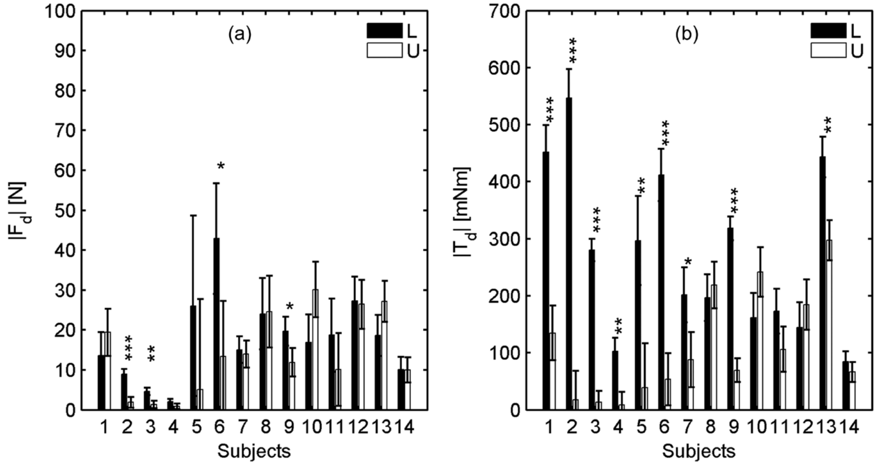

Fig. 5.6. Mean absolute interaction force $|\overline{F}_d|$ (a) and mean absolute interaction torque $|\overline{T}_d|$ (b) exerted per subject over both kinematic setting levels *L* (locked) and *U* (unlocked). Each bar shows the mean loads per experiment per condition (n = 6). The errorbars indicate the 95% confidence interval of the means, that are computed by the 2-way ANOVA's *(T5)*. Main factor analyzed is the kinematic configuration (*L, U*), secondary factor is the interface pressure. While significant differences exist for the kinematic setting factor, no differences exist between the pressure levels. Significant differences for the kinematic setting are encoded according (*, $p < 0.05$; **, $p < 0.01$; ***, $p < 0.001$).

The effect of the kinematic setting on the interaction loads per subject is shown in Fig. 5.6. Depicted are the mean values of the load for each kinematic condition. The 95% *CI* is computed from *T6*. The statistical testing reveals that 4 subjects experience significantly less force in the *U* condition (Fig. 5.6 a) (*All* $F[1,5]$: $F_{S2} = 51.67, p < 0.001$; $F_{S3} = 22.83, p = 0.005$, $F_{S6} = 8.71, p = 0.032$; $F_{S9} = 9.02, p = 0.03$).

No subject experiences significantly less force in the *L* condition.

With respect to the interaction torque (Fig. 5.6 b), the effect is even more pronounced (*T6*), with 9 subjects experiencing significantly less interaction torque in the *U* kinematic condition (*All* $F[1,5]$: $F_{S1} = 83.3$, $p < 0.001$; $F_{S2} = 208.6$, $p = < 0.001$, $F_{S3} = 366.3$, $p < 0.001$; $F_{S4} = 31.6$, $p = 0.003$; $F_{S5} = 21.1$, $p = 0.006$; $F_{S6} = 117$, $p < 0.001$, $F_{S7} = 10.72$, $p = 0.022$; $F_{S9} = 273.2$, $p < 0.001$; $F_{S13} = 32.85$, $p = 0.002$), and no subject that experiences less torque in the *L* condition.

The binned interaction forces $\overline{F}_{d\beta}$, and torques $\overline{T}_{d\beta}$ of the subject group are depicted in Fig. 5.7 for the exoskeleton elbow rotation angle β. The standard deviation is shown as upper and lower bounds on each curve.

The mean force exertion $\overline{F}_{d\beta}$ (Fig. 5.7 a) is significantly smaller for the *U* kinematic setting in the 85 Deg. angle bin, if the variance due to subjects is removed (*T1*) ($F_{Fd\beta/85}[1,140] = 9.03, p = 0.003$). The exerted interaction torque $\overline{T}_{d\beta}$ over the workspace (Fig. 5.7 b) is smaller in the *U* kinematic condition (*T1*), for the first six bins, spanning from 0 to 60 Degrees (*All* $F[1,140]$: $F_{Td\beta/5} = 89.5, p < 0.001$; $F_{Td\beta/15} = 293.22, p = < 0.001$, $F_{Td\beta/25} = 169.9$, $p < 0.001$; $F_{Td\beta/35} = 67.4$, $p < 0.001$; $F_{Td\beta/45} = 21.8$, $p < 0.001$; $F_{Td\beta/55} = 3.9$,

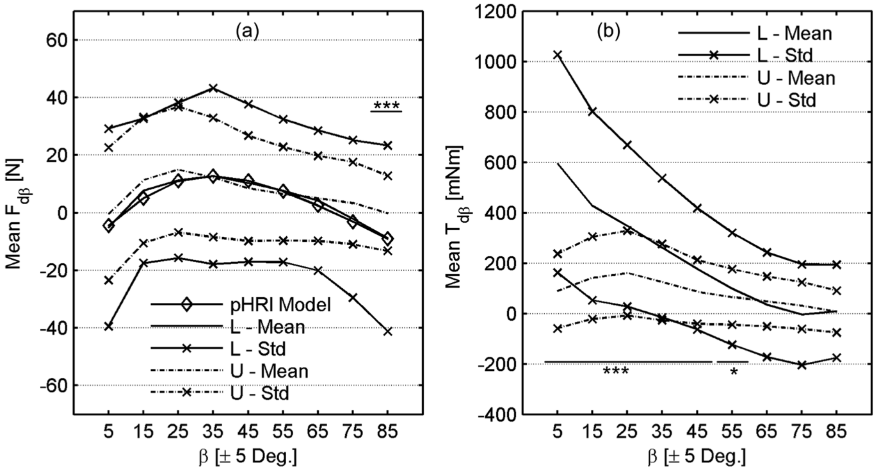

Fig. 5.7. Binned interaction force output measure $\overline{F}_{d\beta}$, and output torque $\overline{T}_{d\beta}$ exerted during motion of the elbow joint of the exoskeleton. In (a) the mean force exerted by all subjects and all experiments over the exoskeleton elbow angle is shown together with the full measured standard deviation, for both levels of the kinematic setting factor (*L* and *U*). The output of the pHRI-model with identified parameters from the *L* force- data is shown in addition. Bins indicated by asterisk feature significantly different mean load between the two kinematic settings. Significance tests were performed on each bin by 2-way ANOVA *(T6)*, for which the kinematic setting was the first and the subjects were the second factor, thus, the variance due to subjects that is shown in the figure, was removed by the test. In (b), equivalent outputs are shown for the mean interaction torque. Coding of the asterisk: (*, $p < 0.05$; ***, $p < 0.001$).

$p = 0.049$). Also here, for both dependent variables, the two factors kinematic setting and subjects show a strong interaction term for each bin ($p < 0.001$).

5.5.3 Identification of pHRI model parameters from measured interaction forces in *L* condition

The offset estimates $\hat{x}$, $\hat{y}$, as well as the estimated attachment stiffness $\hat{k}$ are shown per subject in Table 5.1. The table also shows the coefficient of determination R^2 and the norm of the residuals $|res.|$ which indicate the goodness of fit between the identified pHRI model and the measured $\overline{F}_{d\beta}$. Graphs of the model fits for each subject are depicted in Fig. 5.8, along with the raw force values in 2 Deg. wide bins over the exoskeleton elbow angle. The graphs are sorted according to the direction of the offsets similar to Fig. 5.4, to show the capability of the model to identify the measured force characteristic in *L* condition.

The model parameters identified from the mean force measures $\overline{F}_{d\beta}$ for the entire group are:

$$\hat{k}_G = 311.5 \text{ N/m},\ \hat{x}_G = 0.0076 \text{ m},\ \hat{y}_G = -0.097 \text{ m},\ \hat{l}_{exG} = 0.167 \text{ m},\ \hat{z}_{exG} = 0.13 \text{ m}.$$

S.	$\hat{\mathbf{k}}$ [N/m]	$\hat{\mathbf{x}}$ [$\cdot 10^{-3}$ m]	$\hat{\mathbf{y}}$ [$\cdot 10^{-3}$ m]	$\mathbf{R^2}$ [%]	**|res.|** [N]
1	251	–22.3	–78.9	89.2	17.7
2	249	68.4	18.6	98.9	5.2
3	222	48.2	58.5	97.3	5.1
4	249	2.1	2.1	21.6	6.3
5	256	124.4	–48.7	93.5	23.0
6	286	136.2	7.9	83.8	47.2
7	264	–17.2	–116.9	99.2	8.3
8	374	3.5	–87.7	98.6	11.2
9	237	78.3	10.3	66.4	26.0
10	250	1.8	–76.6	91.6	16.3
11	253	–15.0	–54.2	56.2	42.7
12	271	5.6	–77.1	94.5	15.9
13	373	–0.5	–81.3	98.4	8.1
14	284	25.2	–115.6	95.7	10.1

Table 5.1. Extract of Identified pHRI Model Parameters From Measured Interaction Forces – Per Subject: Results of the pHRI model parameter identification (S: Subjects, $\hat{k}$: estimated attachment stiffness, $\hat{x}$: estimated offset of exoskeleton joint in x-direction; $\hat{y}$: estimated offset of exoskeleton joint in y-direction; R^2: coefficient of determination; |*res.*|: norm of residual errors).

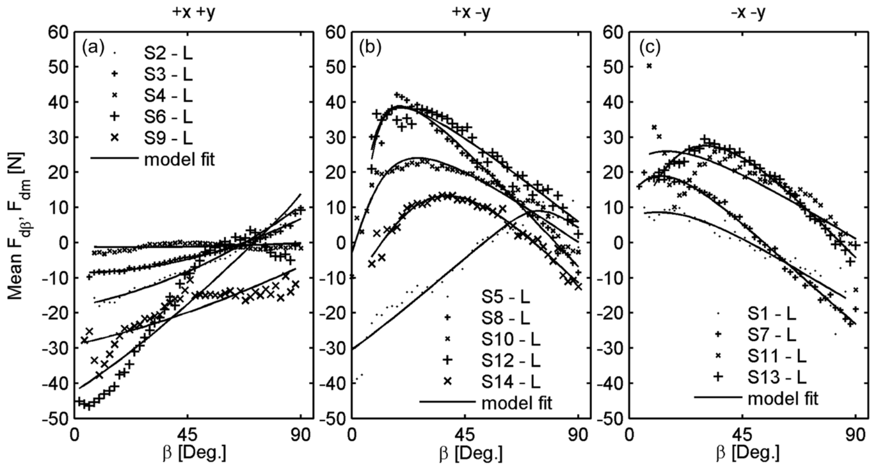

Fig. 5.8. Raw force measurements F_d of the subjects (S) over the exoskeleton angle β per 6 trials. The model fitted force characteristic F_{dm} is shown per subject on the same graphs. All measured forces are acquired during the *L* exoskeleton trials (6 per subject) and averaged within 2 Deg. wide angle bins. The illustrations are sorted for identified offsets from $+x, +y$ (a), $+x, -y$ (b), and $-x, -y$ (c). There are no subjects that had $-x, +y$ offsets in this experiment.

The output graph of the pHRI model with those parameters is displayed for the group measures in Fig. 5.7 (a) ($R^2 = 97.53\%$, $|res.| = 3.45$ N).

5.5.4 Signal tracking performance

The RMS tracking error E_{Tr} for the subject group, over all trials, varies within 13.27 ± 2.8 Deg. A boxplot in Fig. 5.9 (a) shows the entire spread ($n = 168$) of E_{Tr} measurement points. The subjects (*T1*) contribute significantly to the variability of the RMS tracking error measures ($F_{ETrS}[13,140] = 18.92$, $p < 0.001$). It can be seen from Fig. 5.9 (b), that in the range from 10–30 mmHg, 2 measures are lower (*T4*) for the *U* condition, while in the range from 40–60 mmHg, 2 measures are higher for the *U* condition. Two post-hoc tests on the effect of kinematic setting over the two pressure ranges confirmed that in the range from 10–30 mmHg subjects perform better in the *U* configuration ($F_{ETrLU10\text{-}30}[1,56] = 13.47$, $p < 0.001$) whereas in the range from 40–60 mmHg they perform better in *L* configuration ($F_{ETrLU40\text{-}60}[1,56] = 21.72$, $p < 0.001$).

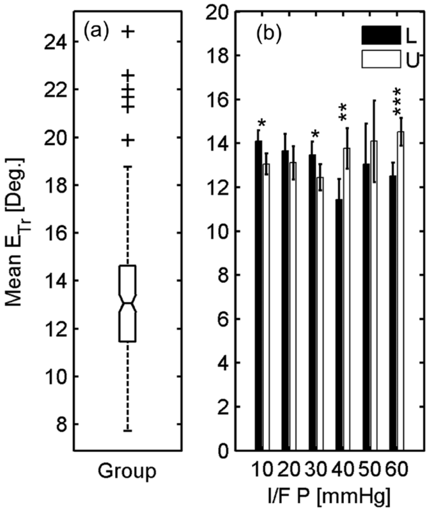

Fig. 5.9. Boxplot (a) of overall signal tracking error E_{Tr} of the subject group. In (b), mean values of E_{Tr} of the group is shown over kinematic condition and attachment pressure levels. The 95% *CI* that is shown results *T3* (*, $p < 0.05$; **, $p < 0.01$; ***, $p < 0.001$).

5.5.5 Voluntary range of motion

In Fig. 5.10 (a), a full spectrum of the target and tracking signals is shown. It can be seen how often (s_v) the multisine target signal v and the subject's tracking signals in *L* or *U* kinematic configuration ($s_{\beta U}$ and $s_{\beta L}$) resided within one of the nine bins of elbow workspace α during the experiments (range $R(v) = R(\alpha)$). In Fig. 5.10 (b), the group mean of the voluntary range of motion R_β for both kinematic configurations is shown, in percent of the target signal v over the workspace. It can be seen that on both stroke-ends, the subjects reached the target signal substantially less than 100%. While in the range of 0–10 Deg., the subjects reach the target signal equally often for the two kinematic configurations, there is a significant difference at the 80–90 Deg. stroke end. The test *T1* reveals that the subjects reach the far stroke end about 20% more

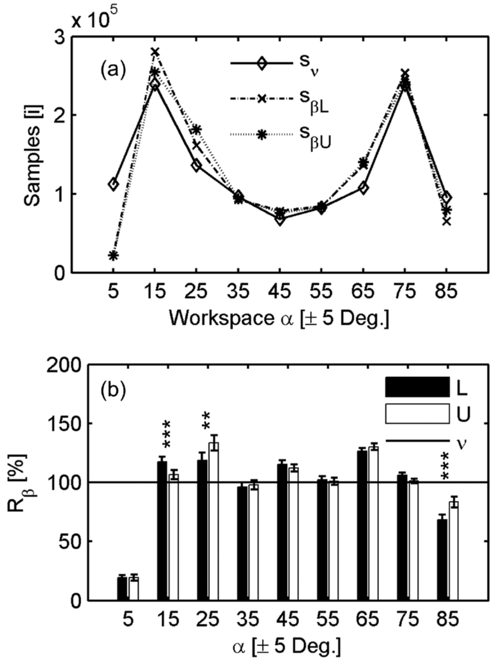

Fig. 5.10. In (a): Range of motion available with exoskeleton in both kinematic configurations. Total number of samples *i* for which the target multisine signal *ν* and the tracking signals in *L* and *U* kinematic setting reside within the same nine, 10 Deg. wide bins of the elbow workspace. In (b): The voluntary range of motion R_β for both kinematic settings in % of input signal reached over the workspace (*, $p < 0.05$; **, $p < 0.01$; ***, $p < 0.001$).

often (83.4% versus 68.2%) in the *U* kinematic configuration than in *L* configuration ($F_{R\beta 85}[1,140] = 20.9$, $p < 0.001$).

The kinematic setting affects the range of motion also in other parts of the workspace, however, there subjects can all reach 100% of the tracking signal in both conditions. Only the overshoot over the target signal is affected and the differences are less profound ($F_{R\beta 15}[1,140] = 14.0$, $p < 0.001$; $F_{R\beta 25}[1,140] = 10.23$, $p = 0.002$).

5.5.6 Motion of passive compensatory joints

The linear passive compensation joint d_{lin} of the exoskeleton operated within a range of 0–35 mm in the *U* trials. The rotary compensation joint Θ_{rot} operated within a range of −11 to +25 Degrees. Fig. 5.11 depicts the mean motion of d_{lin} in (a) and of Θ_{rot} in (b), over all trials and subjects.

5.5.7 Preferred attachment pressure of the subject group

When asked after the experiments, the subject group selected their preferred "most comfortable" attachment pressures to be within 21.6 ± 8.7 mmHg for the upper-arm air-cuff and to be within 20.1 ± 7.7 mmHg for the forearm air-cuff.

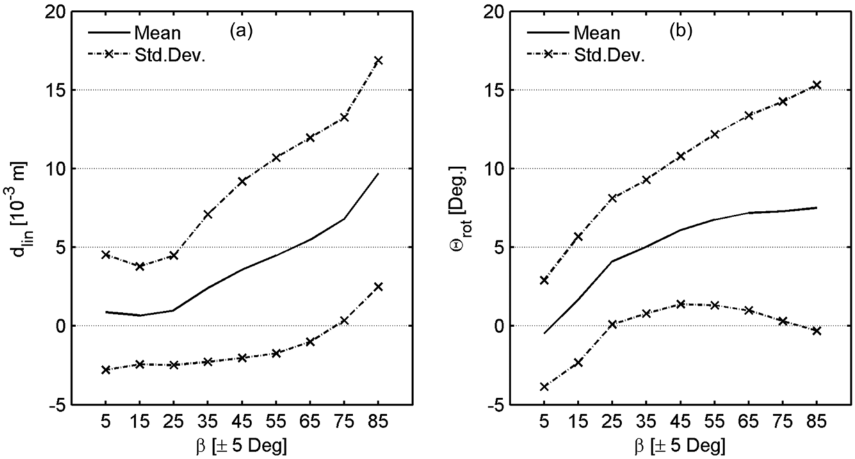

Fig. 5.11. Mean motion caused in the passive compensation joints during trials with the *U* kinematic setting. In (a) motion of the linear compensation joint d_{lin} is shown over the exoskeleton elbow rotation angle β. In (b) motion of the rotary compensation joint Θ_{rot} is depicted also over the exoskeleton elbow angle β. By their movement, the joints lower the perceived interaction force stemming from misalignment of the axes of rotation between exoskeleton and human limb.

5.5.8 Subjective metric I: comfort questionnaire

The interface pressure has an influence on the perceived comfort of the subjects.

T2 revealed that at least for one pressure, the comfort ratings were different for the subject group ($F_{CP}[5,85]=9.5$, $p<0.001$). Post-hoc testing revealed that at 60 mmHg the perceived comfort was lower than at all other pressure increments.

In particular, the perceived comfort at 60 mmHg was lower than at 50 mmHg ($F_{CP50/60}[1,28]=7.88$, $p=0.009$) and with a more profound effect lower than at 10 mmHg ($F_{CP10/60}[1,28]=30.93$, $p<0.001$). Fig. 5.12 depicts the measured $\overline{C}$ ratings for the group over the original scale.

Testing for influence of the kinematic setting over specific pressures (*T5*) revealed that at 30 mmHg, the subjects rated the perceived comfort higher in the *U* configuration than in the *L* configuration ($F_{CPLU30}[1,13]=5.12$, $p=0.041$). The highest mean comfort rating of the group was given for 20 mmHg in the *U* condition (Fig. 5.12 b).

5.5.9 Subjective metric II: motion hindrance questionnaire

The subjects did not rate the motion hindrance differently between the kinematic or the pressure factors of the experiment.

5.5.10 Subjective metric III: NASA TLX ratings

Following mean group weighting factors were determined for the NASA TLX rating scales after the experiment (mental demand: 1.93, physical demand: 2.21, temporal demand: 3.0, performance: 2.71, effort: 2.79, frustration: 2.36).

Analysis of the total perceived WWL scores $\overline{W}_{WL}$ did not reveal effects from the kinematic or pressure variation on workload. The effects of kinematic variation on the

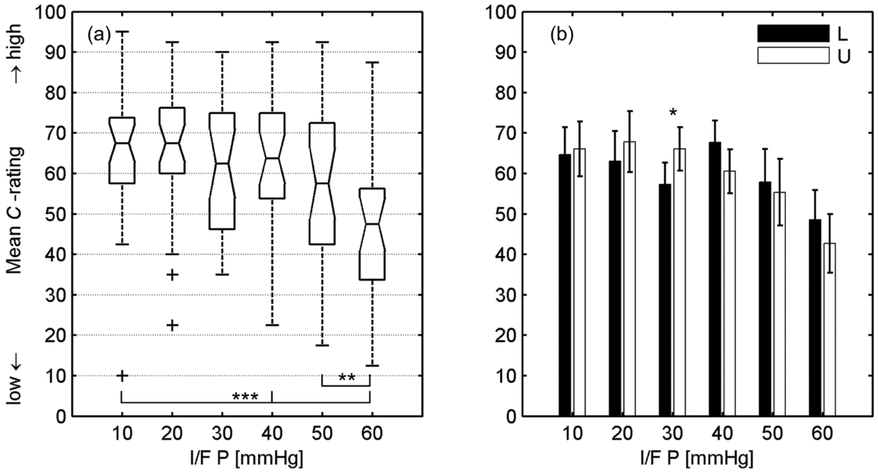

Fig. 5.12. Mean comfort rating $\overline{C}$ of the subject group is shown as boxplots in (a) over the six different attachment pressure increments. The means between the groups were compared by *T2*. Significant differences are coded by asterisk. In (b), the mean comfort ratings of the group are shown over attachment pressure and kinematic setting. The 95% *CI* shown results from comparison of the kinematic setting factors at each pressure increment *T3*. Significant differences between means are indicated per pressure increment by asterisk (*, $p < 0.05$; **, $p < 0.01$;***, $p < 0.001$).

individual rating scales is shown in Fig. 5.13 (a), while the effects of pressure variation on the six individual rating scales is illustrated in Fig. 5.13 (b). *T1* identified that the kinematic setting has an influence on the mental demand rating. The subjects experience less mental demand in the *U* condition than in the *L* condition ($F_{MDLU}[1,140] = 3.95$, $p = 0.048$).

The pressure settings showed influence on the ratings of the subjects on the individual TLX scales.

T2 revealed effects of pressure on mental demand ($F_{MDP}[5,84] = 2.46$, $p = 0.04$). Post-hoc testing (2-way ANOVA's with 2 pressure increments as main and subjects as second factor) revealed that perceived mental demand decreases towards higher pressures. With mental load experienced at 60 mmHg being lower than at 10, 30 and 50 mmHg (*All* $F[1,28]$: $F_{MDP10/60} = 6.78$, $p = 0.015$; $F_{MDP30/60} = 9.21$, $p = 0.005$; $F_{MDP50/60} = 5.08$, $p = 0.032$). Physical demand ratings are influenced by the pressure factor as well (*T2:* $F_{PDP}[5,84] = 3.51$, $p = 0.006$). In particular, physical demand shows an increasing trend with higher pressures. Again, post-hoc tests confirmed higher physical demand ratings for 60 mmHg than for 10, 20 and 40 mmHg (*All* $F[1,28]$: $F_{PDP10/60} = 10$, $p = 0.004$; $F_{PDP20/60} = 7.04$, $p = 0.013$; $F_{PDP40/60} = 8.84$, $p = 0.006$).

The subject's rating on the effort scale showed influence to the pressure variation (*T2:* $F_{EFP}[5,84] = 4.31$, $p = 0.002$). In particular, subjects rated higher effort at higher interface pressures. The post-hoc tests revealed that at 50 mmHg the subjects rate effort higher than at 10 mmHg, and at 60 mmHg they rate effort higher than at 10 and 20 mmHg (*All* $F[1,28]$: $F_{EFP10/50} = 10.1$, $p = 0.004$; $F_{EFP10/60} = 24.25$, $p < 0.001$; $F_{EFP20/50} = 8.85$, $p = 0.006$).

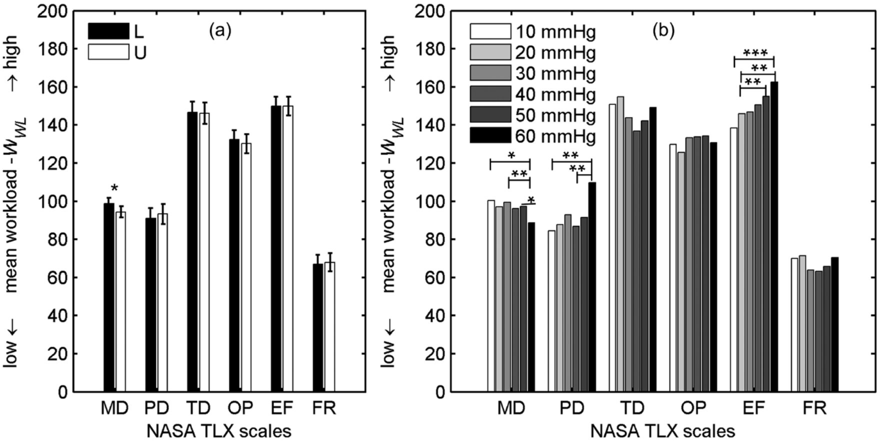

Fig. 5.13. Results of the subject group weighted workload ratings $\bar{W}_{WL}$ for the individual NASA TLX scales (MD: Mental Demand, PD: Physical Demand, TD: Temporal Demand, OP: Operator Performance, EF: Effort, FR: Frustration Level) In (a), influence of the kinematic setting on the TLX scales is depicted. Differences between *L* and *U* were tested with *T1*. The 95% *CI* on the difference between the means is shown as computed by ANOVA analysis. In (b), mean workload ratings are shown per TLX scale for each attachment pressure settings, ranging from 10–60 mmHg. Significant differences are shown by asterisk. Coding of the asterisk is (*, $p < 0.05$; **, $p < 0.01$;***, $p < 0.001$).

5.6 Discussion

From the results presented above, it is evident that a kinematic wearable robot structure incorporating passive compensation joints is better.

It can be seen from Fig. 5.5 and Fig. 5.6 that the *U* kinematic condition causes significantly less interaction loads between the exoskeleton and the human arm. Peak loads (Fig. 5.5 a and d) at the human–machine interface of up to 232 N and 1.46 Nm were created for experiments in *L* condition, whereas in the *U* condition, the additional passive joints ensured to reduce those peak forces by 70% to 70 N and the torques by 60% to about 0.6 Nm.

From Fig. 5.7 it can be seen that the exoskeleton in *U* configuration reduces the interaction forces most significantly in the motion end ranges. Here, the peak loads are created during movement in *L* configuration. The passive joints of the exoskeleton reduce significantly the force in the far stroke-end (Fig. 5.7 a) and the torque in the near stroke-end (Fig. 5.7 b). Fig. 5.11 (a) shows that the linear compensation joint starts moving at about the same angle in workspace (~25 Deg.) where the mean interaction force of the group starts to peak. Towards the far stroke-end the linear joint moves more. The mean force for the U condition consequently has a smaller spread in this range and decreases towards 0 near the 90 Deg. stroke-end. This is where the linear compensation joint experiences most stroke (Fig. 5.11 a). From the narrower range of forces experienced in *U* condition (Fig. 5.7) it can be seen, that the linear joint works to remove peak forces. This offers an explanation to the differences seen between the two kinematic conditions in Fig. 5.5 (a), where the *U* setting does not contain nearly as large forces as the *L* condition does. The mean force in the *U* condition decreases faster over the working range than the mean force measured with the exoskeleton in *locked* kinematic condition (Fig. 5.7 a). However, as can be seen in the behavior of the mean force in the *locked* trials in Fig. 5.7 (a), the leveling-off of the force is not only caused by the passive joints involved in the U configuration, but also by the geometric properties of the attachment itself. The pHRI model fit shown in (Fig. 5.7 a) indicates that, with the average offsets of the group of +7.6 cm in x and −9.7 cm in y direction, the force experienced by most subjects changes direction from distal to proximal at about 35 Deg., then starts to increase in proximal direction continuously. This trend can also be seen in Fig. 5.8 b–c. The subjects featuring $+x/+y$ offsets create force in proximal direction near the extended limb position and have no turning-point. The mostly negative forces near both stroke-ends explain the large negative peak forces that are shown in Fig. 5.5 (a) for the *L* trials. The model prediction in Fig. 5.4 (b) shows that the trend of the force in *L* configuration for the group would continue to increase towards larger angles. Needless to say that in a real application, angles above 90 Deg. for the elbow are quite natural and that therefore a kinematic design with compensatory joints is better (where such forces are removed). The individual interaction force measures shown in Fig. 5.8, clarify how the force trend of the group is composed. It can be seen there that the pHRI model is able to fit the various apparent trends.

For the group, we see in Fig. 5.10 that the voluntary range of motion in the far stroke-end is more limited for the *L* than for the *U* condition. Subjects can reach closer to the target signal in the 85 Deg. angle bin. They have about 20% more range of motion available in the *unlocked* condition. It appears that the voluntary range of motion is decreased by increasing interaction forces over large angles in the workspace. The *U* kinematic setting lowers such forces by adjusting the passive compensatory joints (Fig. 5.11) and thus allows a greater range of motion in the far stroke-end.

However, for both kinematic settings, the voluntary range of motion close to the fully extended (0 Deg.) stroke-end is limited. This can also be explained. The average offsets for the subject group in x direction is positive ($+x$), according to the sign convention of our model (Fig. 5.3). For some subjects, the forearm link length l_{ex} of the exoskeleton must have been longer than their forearm. In fact, to such extend that the linear compensation joint in *U* condition could not compensate for the difference (by moving further proximal). In order to adjust for the difference in length, the only possibility for the system is to force an offset in $+x$ direction between the human and robot joints. This "forced" offset, also induces an offset in the exoskeletons elbow rotary joint, which causes the measurement of β to be offset from the true limb angle α. Thus, the extension of the limb is not limited, but the sensing in the extended limb position is faulty. This can only happen for both kinematic configurations, if compensation joint Δ_8 does not offer sufficient stroke in proximal direction to compensate for the length-offset in the fully extended position of the limb. Only the identification of model parameters helped us to arrive at a suitable explanation of this effect. To improve the sensing accuracy as well as the available range of motion of the device, the joint design must be up-dated accordingly.

The statistical analysis of the force and torque measures has revealed a strong interaction between the levels of the kinematic setting and the subjects. This means that the subjects must have a different response to the *L* and *U* kinematic settings with respect to interface load creation. It can be seen in Fig. 5.6 that subjects cause creation of interaction force (a) and torque (b) differently, with respect to the kinematic setting. The question to solve is why the interaction force for some subjects is much lower in *U* condition, while for others it is not? This can be answered by considering that subject variation is apparent mainly as variation between physiological parameters, which in turn causes variation in geometric attachment properties between exoskeleton and each subject. Table 5.1 confirms that a main source of variability between the subjects can indeed be attributed to variation of their ICR_h joint alignment to the exoskeleton CR_e. Even though we aimed at aligning the device well, still relatively large misalignments (from −2.2 to +13.6 cm for *x* and from −11.7 to 5.9 cm for *y*) occurred between the principal axes of human and robot. And offsets that exist during attachment are even amplified during movement. The offset-shifts during motion are indirectly caused by variation of anthropometry. Some subjects, for instance, had rather large upper-arm diameters, such that the exoskeleton upper-arm fixation could not be moved sufficiently far towards the shoulder. The exoskeleton had to be attached at the level of the biceps, which typically caused positive *y* offsets (in distal direction) between ICR_h and CR_e. Some subjects (mainly the female ones S.7–S.14) had very thin upper-arms, such that the exoskeleton could be attached above the biceps, which was preferable for comfort (the exoskeleton not pressing onto the biceps). In that case, the contracting biceps appeared to move the exoskeleton main axis proximally, showing as offsets in −*y* direction. On top of that the link lengths of the subject's limbs varied significantly, which can affect offsets in *x* direction, as was outlined before. Clearly it was not possible to control the variation of offsets better, without altering the experimental setup to such extends as to loose equivalence to a real application. The different combinations of offsets cause different behavior in the passive joints. This is the reason why different subjects experience different behavior of interaction forces between the two kinematic settings. It can be seen in Table 5.1 that e.g. Subject 4, to which the exoskeleton fitted very well (very small offsets in both, *x* and *y* directions) experienced the smallest interface loading in general (Fig. 5.6 a) – for both kinematic conditions. The model identification therefore did not show good coefficient of determination, however, only a very small norm of the residuals exists. Interestingly, for all other subjects in Table 5.1 that have offsets in both, +*x* and +*y* direction, significantly less force is created in the *U* kinematic setting of the exoskeleton with respect to the *L* setting (Fig. 5.6 a). For those subjects, the passive compensation joints in the EXARM worked better than for others. Subjects having offsets in −*x* or −*y*, or even in both directions do not experience significantly less force in the *U* condition. For them, the passive joints of the EXARM did not create sufficient reduction of forces. We aim at interpreting this result by consulting the pHRI model outputs presented in Fig. 5.4 and the graphs presented in Fig. 5.8.

We can see that if positive *x* and *y* offsets are present, force in the measured range of motion is mostly pointing in positive, distal direction near the end-range (were the peak forces are caused). The data presented in Fig. 5.6 (a) shows us that this direction must be the preferred direction of motion of our linear compensation joint Δ_8. If forces with a positive sign can activate the linear compensation joint in the EXARM better, or more often, the force in the *U* kinematics setting will be removed better as well. Forces from such combinations of offsets (+*x*, +*y*) are larger in magnitude near the 90 Deg. stroke end (Fig. 5.4 a, Fig. 5.8 a) than forces created by most other offsets. This means that in the *L* kinematic setting, the measured force will be relatively high, compared to the ones measured in *U* condition, which is what is shown by the significant results for the subjects in Fig. 5.6 (a). For the other offset combinations, differences between measured *L* and *U* forces were not sufficiently spread apart to show significance. For our exoskeleton device we learn that the range of the passive joints needs to be up-dated. Then, the design will be more robust to variation between individuals.

To improve the design of the passive compensatory joints in general, we can state that sufficient margin of motion in both primary directions must be present at all limb positions.

The mitigation of torque loads in our design with passive joints is better. More subjects experience less torque in *U* condition (Fig. 5.6 b). Also for the group (Fig. 5.7 b, Fig. 5.5 d–f), the difference in interaction torques is more profound between the *L* and *U* setting. This indicates that the rotary passive joint does not have a preferred direction of motion and can thus compensate more interaction torques stemming from particular offsets of individuals.

Another reason for the better force reduction in subjects with positive *x* and *y* offsets can also be the monotonically increasing, nearly linear, force characteristic over the workspace in this configuration. This characteristic enables an optimal combined functioning of the compensatory joints. All other subjects in Fig. 5.8 b–c experience a direction change of the force within the workspace. They have a less pronounced reduction of forces in the U condition (Fig. 5.6 a). We hypothesize that a changing direction of force in the workspace causes disturbances that might be caused by additional dynamic effects between the human and the exoskeleton. The compensation joints can hit the stroke ends more often during movement, which by itself can create more peak forces. A linear force-position characteristic allows the passive compensation joints to work more smoothly and optimal. This hypothesis is supported by the fact that also Subject 5, whose force characteristic is similarly linear, has a greatly reduced force in *unlocked* condition, despite the fact that its offsets are in +*x* and −*y* direction.

The tracking performance during the experiments showed strong dependence on the capability of the subjects. This was expected. However, some subtle effects were revealed that were rather unexpected. At low attachment pressures from 10–30 mmHg, the subjects track the target signal better in the *U* kinematic setting, whereas at higher pressures ranging from 40–60 mmHg, the subjects track the signal better in the *L* condition. This raises the question at which pressure the subjects did prefer to perform the tracking experiment?

When asked directly, the tested persons preferred to wear the exoskeleton at pressures between roughly 10–30 mmHg overall. Even though a large range of pressures was tested, the preferred pressure of the group lies within a relatively narrow range. The mean subjective comfort ratings are highest for 20 mmHg in the *U* kinematic setting of the exoskeleton. This indicates a good optimum attachment pressure of about 20 mmHg. The subjects only noticed a comfort difference between the kinematic settings at 30 mmHg, however, where the comfort in the *U* kinematic setting was rated higher. This allows us to summarize that low pressures along with the *U* kinematic configuration of the exoskeleton feels more comfortable. This combination of settings also allows good signal tracking performance. But why do the test persons prefer a low pressure for the task?

The weighting factors determined for the individual TLX rating scales show that the main workload of the task is associated with temporal demand, followed by effort. Effort rated by the human subject's increases with higher pressures. Also the physical demand of the task increases with higher pressures. Even though the group preferred high pressures to reduce mental demand, the other effects are dominant, which is why, in summary the physical demand and effort caused selection of a lower interface pressure, at the expense of increased mental demand. However, if we consider our preferred selection of the *U* kinematic setting for low pressures from the tracking results, we see that also the mental demand ratings are positively affected by the choice of kinematic configuration of the exoskeleton.

Pressure variation thus shows more effect on the subjective measures in our tracking experiment, whereas the kinematic variation shows more effect on the objective measures. Interestingly, the subjects did, with the exception of mental load, not clearly perceive the differences in kinematic setting. Since the pressure variation was the more dominant influence on subjective measures, it seems that underlying physical effects of lower interaction loads between kinematic settings of the exoskeleton were *masked* by the imposed pressure variation of the experiment.

However, we have clearly seen that interface loads are lower for the *U* setting and have found a good way to optimize for ergonomics in our exoskeleton design by analyzing measured forces of different individuals with a pHRI model.

In a motorized wearable robot, we believe, the differences of interface load will be even more profound and, depending on the task, also subjectively experienced. In particular for applications, where force-perception with high resolution and dynamic range is critical, e.g. in haptic devices, the inclusion of passive compensatory joints might improve the *feel* and mechanical *transparency* of the device. For such systems, a linear force characteristic would be ideal that enables an optimal functioning of the passive joints. Especially with regard to the level of typical force-feedback loads applied to the human joints, which are in the order of 1/20th of the maximum human joint strength, the elimination of interface force of up to 230 N and torques of up to about 1.5 Nm seems utterly important. (As an example, the exoskeleton presented in (Tsagarakis and Caldwell 2003) transfers a torque of 6 Nm to the elbow. The exoskeleton from (Frisoli et al. 2005) can apply a force of 50 N cont. or 100 N peak to the tip of the hand.) For robots that transfer large forces and torques, such as e.g. rehabilitation robots, the inclusion of compensation joints will mainly allow a larger range of movement and contribute to reducing safety critical peak loads.

We can summarize that low attachment pressures, along with the *unlocked* kinematic setting of the exoskeleton is optimal for comfort, signal tracking performance, range of movement and low interaction loading. A low attachment pressure of 20 mmHg is optimal for the subject group tested.

5.7 Future work

In order to further improve the ergonomics of the ESA exoskeleton, we will up-date the implementation of the compensation joints, as learned from the analysis above. The joints need to be able to move over the entire workspace in both directions. The length of the upper-arm and forearm links of the exoskeleton will be re-designed in the next prototype, to further improve robustness against physical parameter variations between subjects. The diameter of the upper-arm cuff will be increased to better fit to more muscular operators.

5.8 Conclusion

(1) Offsets between the axes of rotation of a human and a robot, can easily be in the order of ± 10 cm in various directions, even if, at the start of movement, the two axes are well aligned.
(2) Such offsets create large interaction forces during movement between the attachment of a human operator limb and the robot limb that can peak at up to 230 N along the axis of the human limb. Large interaction torques around the attachment cuffs can be created that rise up to about 1.46 Nm.
(3) In conventionally designed exoskeletons, these interaction loads limit the voluntary range of motion near the stroke ends.
(4) An attachment stiffness of about 300 N/m is created between the human and robot interface.
(5) An exoskeleton that features passive compensation joints can lower such interaction forces by 70% and the torques by at least 60% and allows an about 20% larger range of motion in the far stroke-end.
(6) In order for an exoskeleton device with passive joints to work optimally, its passive joints must feature sufficient stroke margin in both directions over the entire workspace.
(7) An exoskeleton with passive compensation joints can then be called "ergonomic".
(8) The optimum interface pressure between exoskeleton and human arm, from both subjective as well as objective points of view is 20 mmHg on both attachment cuffs.
(9) The best combination of subjective and objective performance for the task can be reached by an ergonomic exoskeleton that is attached with the optimum attachment pressure.

5.9 Appendix

The pHRI model derives the total displacement d_{tot} along the movable link in dependence of α and β according to:

$$d_{tot}(\alpha, x, y, l_{ex}, z_{ex}) =$$

$$l_{ex} \cdot \sqrt{1 - \frac{x^2}{l_{ex}^{\,2}}} + y - \frac{\sqrt{x^2 + y^2} \cdot z_{ex} \cdot \cos[\alpha - \arctan(y/x)]}{l_{ex} \cdot \sqrt{1 - \frac{(x^2 + y^2) \cdot \cos[\alpha - \arctan(y/x)]^2}{l_{ex}^{\,2}}}} - \sqrt{\Psi^2 + \Psi^2 \cdot \tan[\alpha]^2},$$

with:

$$\Psi = y - l_{ex} \cdot \sin\left(\alpha + \arcsin\left(\frac{\sqrt{x^2 + y^2} \cdot \cos[\alpha - \arctan(y/x)]}{l_{ex}}\right) - \arctan(y/x) - \arctan(x/y)\right).$$

$$d_{tot}(\beta, x, y, l_{ex}, z_{ex}) =$$

$$l_{ex} \cdot \sqrt{1 - \frac{x^2}{l_{ex}^{\,2}}} + y - \sqrt{(y + l_{ex} \cdot \cos(\beta))^2 \cdot \csc\left(\beta + \arccos\left(\frac{\sqrt{x^2 + y^2} \cdot \sin[\beta + \arctan(x/y)]}{\sqrt{\Upsilon}}\right)\right)^2}$$

$$- \frac{\sqrt{x^2 + y^2} \cdot z_{ex} \cdot \sin[\beta + \arctan(x/y)}{\sqrt{\Upsilon} \cdot \sqrt{1 - \frac{(x^2 + y^2) \cdot \sin[\beta + \arctan(x/y)]^2}{\Upsilon}}},$$

with:

$$\Upsilon = l_{ex}^{\,2} + x^2 + y^2 + 2 \cdot l_{ex} \cdot \sqrt{x^2 + y^2} \cdot \cos[\beta + \arctan(x/y)].$$

5.10 Acknowledgment

The Authors would like to kindly thank all 14 volunteers that very enthusiastically have participated in the experiment campaign.

Part III

Robot Control

Chapter 6: Kinematic Redundancy in Exoskeleton Systems

A. Schiele
Extracts of Chapter 3.4, Invited Contribution: *Wearable Robots: Biomechatronic Exoskeletons, Jose Pons Ed., John Wiley & Sons, 2008, pp. 70–74*

Chapter 7: Towards Intuitive Control of Space Robots: A Ground Development Facility with Exoskeleton

A. Schiele, M. De Bartolomei, F.C.T. van der Helm
Adopted from *IEEE/RSJ International Conference on Intelligent Robots and Systems, Beijing, Oct. 2006, pp. 1396–1401 (Added section 7.3.3)*

Chapter 6

Kinematic Redundancy in Exoskeleton Systems

A. Schiele

Extracts of Chapter 3.4, Invited contribution: *Wearable Robots: Biomechatronic Exoskeletons, Jose Pons Ed., John Wiley & Sons, 2008, pp. 70–74*

This Chapter first provides a general introduction to kinematic redundancies and their different types. The reasons are shown on mathematical grounds, why intrinsically redundant manipulators have advantages over non-redundant manipulators. Possible approaches for redundancy resolution are explained that can enable a higher manipulative dexterity. The topic of redundancies is then applied to human–exoskeleton systems. The interplay between redundancy in human limbs, exoskeleton structures and anthropomorphic robots in bilateral control is discussed. Solutions for resolving redundancies in human–exoskeleton systems of different classes are outlined and discussed.

6.1 Introduction

6.1.1 Types of kinematic redundancies

The redundancy of manipulators is task dependent. A manipulator, such as for instance a robot or a human limb, is called "*kinematically redundant*" if it possesses more degrees of mobility than is necessary for performing a specific task. Redundancy of a manipulator always relates to its number of n joint space variables, the number m of operational space variables and the number r of operational space variables required for performing a specific task. "*Functional redundancy*" describes a situation for which a given manipulator has a larger number of joint space variables n then task space variables r ($n > r$). This can occur in manipulators with less then six degrees of freedom ($n < 6$), if the task space dimension r is restricted with respect to the Cartesian space ($m = 6$).

A manipulator is called "*intrinsically redundant*" if its number of the joint space variables is bigger than the dimension of the operational space ($n > m$). All manipulators consisting of 7 degrees of freedom or more are intrinsically redundant. We have seen in the previous sections that the human arm is an instrinsically redundant system. A model of 7 degrees of freedom was proposed there. If further degrees of freedom of the human arm are considered, it can be modelled even with a higher degree of redundancy. Also, most exoskeletons that interface with the human upper limb are instrinsically redundant. This supports smooth interaction with the human arm. In this chapter, when speaking of redundancy, we will denote intrinsic redundancy.

The redundancy of a manipulator can be analyzed by using the differential kinematics equation (6.1) that linearly maps the joint velocity space of a manipulator to its end-effector velocity space:

$$\vec{v} = J(q) \cdot \dot{q} \tag{6.1}$$

Here, $\vec{v}$ denotes the $(r \times 1)$ vector of end-effector velocity of the manipulator and J represents its $(r \times n)$ Jacobian matrix. The Jacobian is derived from the geometric Jacobian. Vector $\dot{q}$ is the $(n \times 1)$ vector of joint velocities.

The *redundant degrees of mobility* of a redundant manipulator are determined by the number $\delta = (n - r)$. It is important to state here, that the Jacobian is a function of the instantaneous manipulator configuration. For some configurations, the Jacobian can degenerate. Then, the manipulator is in a *singular configuration*. The range-space and null-space of the Jacobian further help to understand the concept of redundancy.

The *range space* of J denotes a subspace $R(J)$ in $\Re^r$ of end-effector velocities that can be generated from joint velocities. The *null space* of J is a subspace $N(J)$ in $\Re^n$ of joint velocities that do not produce any end-effector velocity in the given posture. In a singularity, the dimension of the range space is reduced. A non-redundant manipulator then looses mobility. It can not create joint velocities that produce end-effector velocities. In a singularity, the dimension of the null-space increases, according to equation (6.2).

$$Dim(R(J)) + Dim(N(J)) = n \tag{6.2}$$

6.1.2 Advantages of redundant systems

A redundant system has great advantages that are caused by its permanent existence of a null-space *N(J)* that is non-zero. This means that there are infinite solutions of the differential kinematic problem formulated in (6.1), for non-singular configurations. This also applies to the inverse problem. A non-zero *N(J)* allows to utilize the *self-motion* of the manipulator to influence its geometric pose while keeping end-effector position and orientation constant.

This null-space motion of redundant manipulators can then be used, to improve its mobility. In particular, when inverting the forward kinematics, optimization techniques can be used to choose the joint space variables such, that additional constraints are satisfied.

This is then formulated as an optimization problem. For instance obstacles can be additionally avoided during motion. Other popular techniques are to choose a specific joint space trajectory to avoid kinematic singularities, or to reduce the joint speeds during motion to minimize energy consumption. A good coverage of inverse kinematic procedures for redundant manipulators is provided in (Sciavicco and Siciliano 1999).

In the case of a coupled human–exoskeleton system, the redundancy of an exoskeleton can be exploited to adjust the robots geometric posture to the posture of the human arm. This is an important advantage of redundant exoskeletons and will be further discussed in the following paragraphs.

6.2 Redundancies in human–exoskeleton systems

A non-redundant exoskeleton is likely to interfere with human motion in specific configurations, in particular in singular configurations. Despite the advantages in dexterity provided by redundant exoskeletons, there are also challenges stemming from it. Those depend mostly on the particular case that is the specific kinematic structure (the DH parameters, so to say) of the exoskeleton and the control architecture that has been implemented by the developers. An exhaustive coverage of redundancy resolution is therefore not within the scope of this article. The reader is referred to the references of typical exoskeletons, quoted within this paragraph.

When looking at a human wearing an exoskeleton, the total kinematics of the system can be described as a parallel kinematic loop that consists of 2 serial chains, one for the exoskeleton and one for the human limb. Both chains are attached at the base and the tip and sometimes also at intermittent places such as, e.g. on the upper-arm and the forearm. It is important that the workspace of the exoskeleton and the human-arm overlap.

Fig. 6.1 illustrates some typical kinematic structures of coupled human–exoskeleton systems. End-point based exoskeleton systems, which are body or wall grounded and only attach to the hand of the human operator are shown in (a). Exoskeletons that are body or wall-grounded, kinematically equivalent to the human limb, and attached at several locations along the limb are illustrated in (b). Exoskeletons that are not kinematically equivalent to the human limbs but are also attached on several points along the user limbs are illustrated in (c).

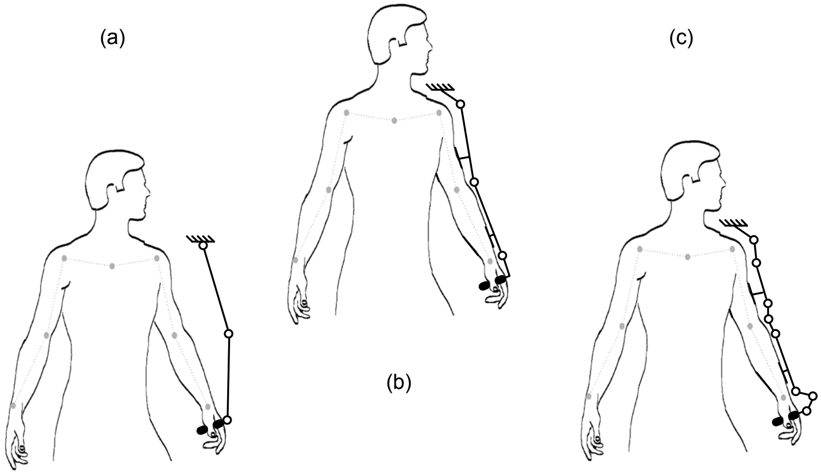

Fig. 6.1. Illustration of 3 different types of exoskeletons. (a) end-point based, (b) kinematically equivalent to human limb, (c) kinematically different with respect to human limb

In general, most exoskeletons feature at least 7 degrees of freedom, in order to be as dexterous and agile as the human arm. Note that some authors (Carignan et al. 2005) (Schiele and Helm 2006) assume a higher redundancy of the human arm. So it is natural that also exoskeleton structures exist with multiple degrees of redundancy. When discussing redundancy with respect to a human–exoskeleton system, besides the available working range there are two more main effects worth to be addressed.

6.2.1 Matching redundancy at the human–robot interfaces

First, the redundancy of the human arm and exoskeleton should be matched such, that actuation torques can be delivered to the human joints unambiguously. The goal of delivering torques to the human joints is crucial for relaistic force-feedback in virtual reality or bilateral telemanipulation scenarios. Furthermore, inducing accurate joint trajectories (e.g. $\dot{q}(t), \tau(t)$) to human joints or human joint groups is important in human–exoskeleton systems for functional motor rehabilitation. Joint torques to the exoskeleton are often derived from Cartesian Forces by the Jacobian transpose J^T, according to equation (6.3)

$$\tau = J^T(q) \cdot \gamma \tag{6.3}$$

Here, τ represents the $(n \times 1)$ vector of Joint torques and γ represents the $(r \times 1)$ vector of Cartesian forces. Mostly, the dimension of γ is chosen to be 6, to include all Cartesian forces and torques. It is important to notice, that also here the range and null-space of the transpose Jacobian exist. For a further detailed description of range and null-space of J^T, please refer to (Sciavicco and Siciliano 1999).

In order to match unambiguously the joint space variables to the human joint space variables, the redundancy of the exoskeleton must be constraint. This will be described together with the second issue below.

The second important role of redundancy to be considered applies to bilateral telemanipulation, where a second robot is remotely controlled as a slave by the master exoskeleton. There, it must be possible to match the geometric pose of the exoskeleton to the geometric pose of a remotely controlled slave robot. Only then, a remote control of the slave can be optimal. The human can then use its own arm redundancy to control the redundancy of the slave robot. This is important for applying realistic situation awareness in contact situations of the slave robot with its environment and to avoid obstacles with the slave during Cartesian motion.

Matching the geometric pose of exoskeleton and remote robot can be done by a direct joint to joint mapping only, if the slave robot and the exoskeleton are kinematically equivalent. If they are not, inverse kinematic algorithms must be used that pick a joint space solution such that the pose of both devices is matched to the human arm pose. A common solution applied, is to constrain the slave robot pose to the *elbow orbit angle* of the exoskeleton. The elbow orbit angle is used as a constraint to choose a solution out of the solution set of the redundant manipulators inverse kinematics equation. Such an algorithm has been described by (Kreuz-Delgado et al. 1992). This constrain also allows to chose a meaningful set of joint torques for display to the human.

For the exoskeletons depicted by Fig. 6.1 (a), feedback forces can be applied only to the human hand. Only operational space forces and velocities can be imposed. Such an exoskeleton has been proposed for instance in (Williams-II et al. 1998) for the upper extremity and in (Hesse and Uhlenbrock 2000) for the lower extremity. Those devices are unable to influence the human arm redundancy and are mostly not redundant themselves. This means in practice, that for all locations in operational space, the human limb has an infinite number of possible joint space configurations, while the exoskeleton does not. In functional rehabilitation, for instance, such exoskeleton systems are unable to induce exact joint trajectories to the human joints. Their loading onto the human joints could even be dangerous, if motion is created in the human joints outside their natural working range. To illustrate this case, consider an exoskeleton applying force on the hand of a fully stretched human arm. There is the danger of hyperextending the elbow due to the joint space ambiguity (in fact, the elbow could move into 2 directions). While this is a great disadvantage in terms of safety, such designs have the advantage of being independent to alignment of the exoskeleton kinematic structure to the human limb structure. As long as the operational space motion is equivalent to the human arm, the physical interaction will feel good and a large common workspace can exist. Safety is left to the understanding of the operator, however. He will need to avoid consciously the workspace-end singularities of his limbs. Such designs are not optimal for bilateral telemanipulation tasks. The human can not control the configuration of the exoskeleton, and thus, not control the configuration of a slave robot that could be remotely linked into the control loop.

The exoskeleton class illustrated schematically by Fig. 6.1 (b), contains exactly the same degrees of redundant mobility then the human arm, excluding the shoulder-girdle. Thus, 7 degrees of freedom. They are attached at the end-point, i.e. the hand, as well as on the other movable links, i.e. the upper-arm and the forearm. An exoskeleton with such a kinematic structure has been proposed for instance by (Bergamasco et al. 1994). In order to induce exact joint trajectories and to match the natural redundancy, their joints must be aligned to coincide with the human joints. This is difficult. Such exoskeletons can control a slave-robot with geometric pose correspondence and deliver accurate feedback forces to the human joints. This can be done, for instance, by means of constraining the configuration of the robot with the elbow orbiting angle, as described above. Also safety constraints can be implemented at the level of its joint space. Yet, we have to keep in mind that the robotic axes must be perfectly aligned to the human joints. Undesired reaction forces can otherwise be created in the human joints by a kinematic mismatch.

In order to improve the fit between the human limb and the robotic device, a class of exoskeletons is being developed similar in structure to the one depicted in Fig. 6.1 (c). Such exoskeletons possess multiple degrees of redundancy, to cope with interaction of not only the human arm, but also with the human shoulder and shoulder-girdle. Such hyper-redundant devices have been proposed in (Schiele and Visentin 2003a) (Kim et al. 2005). They feature a greater working-range than the exoskeletons in Fig. 6.1(b) and also allow to match the instantaneous human joint pose to a slave robot. This can be done by optimization of the inverse kinematics. Also, for bilateral telemanipulation, an explicit mapping between the exoskeleton joints and the robot joints can be performed, which is computationally more efficient.

The difference of this class of exoskeletons with respect to the class depicted in Fig. 6.1 (b) lies in the fact that no exact alignment is required between the exoskeleton and the human. Thus, their redundancy is exploited for additional comfort of the user.

Chapter 7

Towards Intuitive Control of Space Robots: A Ground Development Facility with Exoskeleton

A. Schiele, M. De Bartolomei, F.C.T. van der Helm

Adopted from *IEEE/RSJ International Conference on Intelligent Robots and Systems, Beijing, Oct. 2006, pp. 1396–1401 (Added Section 7.3.3)*

This paper describes a novel ground development facility that is currently being built at the European Space Agency. The facility can be used to develop and test new man–machine interfaces for tele-control of dexterous space manipulators. Furthermore, the facility allows comparing performance of existing input devices, such as conventional joysticks, with novel devices, such as exoskeletons. The Ground Test-bed allows conducting tele-manipulation experiments with a real robot and to measure performance metrics during remote operations. The experimental comparisons planned to be undertaken with the test-bed are outlined.

7.1 Introduction

The European Space Agency aims at developing a humanoid-like assistant robot that can be used to support crew on the International Space Station and during possible future manned exploration missions to the Moon or Mars. This robot is called Eurobot (Schoonejans et al. 2004). Eurobot, equipped with anthropomorphic 7 degree of freedom (d.o.f.) arms, will be controllable in two major modes. During autonomous mode, the robot will perform pre-planned activities with support of its on-board autonomy system. The on-board autonomy system will monitor the robot environment and will help avoiding collisions with known or unforeseen obstacles.

In remote-manipulation mode, crew or operators from ground will be able to control the arms of the robot in direct tele-manipulation. The choice of appropriate man–machine interfaces for these tasks is important and many different technologies exist and are proposed. However, in space robotics, choice of input devices is mostly rather conservative. Control of presently available space manipulators, such as SSRMS on the space station, or RMS on the space shuttle is currently restricted to using a set of two 3 d.o.f. joysticks, without force-feedback. With the emergence of a number of smaller and more dexterous manipulators developed for space applications, such as DEXTRE, the Robonaut (Bluethman et al. 2003) or Eurobot, we have to reconsider whether conservative man–machine interfaces alone are still appropriate. The question arises whether interfaces such as joysticks, are sufficiently capable to exploit all functional advantages offered to the tele-operators by modern space robots. Novel input devices, such as haptic masters or exoskeletons might be better suited for execution of certain remote-control tasks. At ESA, currently two devices are considered for manual control of Eurobot, an exoskeleton and a conventional joystick workstation. It is still under discussion whether to use force-feedback or not. While exoskeletons can allow redundancy control on the fly, facilitate commanding of three dimensional trajectories and might ultimately lead to saving precious crew-time in operation and training, they also might have disadvantages related to controllability, safety or the ability to perform precise and confined tasks.

In order to rigorously trade off advantages and disadvantages of both systems, we decided to embark on a series of performance tests with both types of man–machine interfaces. We therefore started developing a ground demonstration facility that allows integrating a Joystick man–machine interface (MMI) and an Exoskeleton MMI with a prototype of the Eurobot robot.

It is our goal to perform a variety of realistic tasks with Eurobot in remote control to analyze the advantages and disadvantages of each system by means of performance metrics. Potentially, such analysis will provide us with data that can be used for man–machine interface design in the future. If advantages of conservative approaches and novel devices, such as exoskeletons, are merged, we believe, a truly intuitive system could be developed for robot control. We decided to investigate remote-control without force-feedback first, to investigate the fundamental differences between the devices. However, the facility used as a basis for those tests can be extended to include force-feedback control at a later stage.

It is the goal of this paper to provide a detailed description of the ground development facility, which is currently being developed to carry out performance analysis experiments with joysticks and exoskeletons for human–machine interaction. Moreover, a first pilot experiment is described and discussed, that demonstrates functionality of the currently available test system.

7.2 Implementation

7.2.1 Overview

The ground test-bed developed at ESA consists of 4 major sub-systems. While some of them currently consist of commercially available items, in the near future they will be fully replaced with custom developed units.

A block diagram of the ground demonstration facility is presented in Fig. 7.1. The first major element is the Eurobot prototype with BarrettHand™ including their controllers. The second element is the robot workstation personal computer (PC), which contains the experiment software, the graphical user interface (GUI) for robot activation and monitoring and serves as central station to receive/distribute commands from/to the various man–machine interfaces. The joystick and its interface are integrated with this sub-system directly. The robot workstation communicates with the robot controller via a proprietary fiber-optic link (ArcNet™). The third major sub-system is the ESA exoskeleton (EXARM) together with its control station that communicates via Ethernet to the robot workstation. The EXARM has a direct link via analog and digital input lines to the exoskeleton workstation. A fourth element of the set-up is a graphical workstation PC used for displaying an animated 3D virtual reality model of

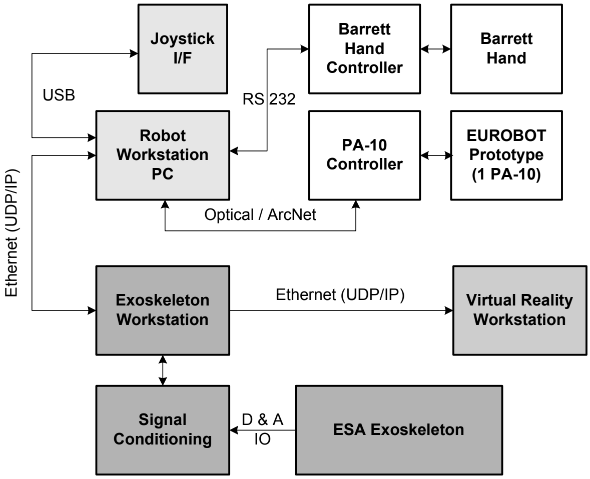
Joystick I/F
Barrett Hand Controller
Barrett Hand
USB
RS 232
Robot Workstation PC
PA-10 Controller
EUROBOT Prototype (1 PA-10)
Optical / ArcNet
Ethernet (UDP/IP)
Exoskeleton Workstation
Ethernet (UDP/IP)
Virtual Reality Workstation
Signal Conditioning
D & A IO
ESA Exoskeleton

Fig. 7.1. Block diagram of test-bed for prototyping and operation testing of man–machine interfaces for robot control

the exoskeleton in real-time. Also this PC can be linked to the exoskeleton workstation via Ethernet.

7.2.2 Eurobot prototype

Mechanical setup

The Eurobot prototype currently consists of a triangular structural base, to which 3 Mitsubishi Heavy Ind., PA-10 robot arms are attached. The 7 d.o.f robots are attached in a symmetric configuration around the Eurobot body, at 120° distance intervals. The Eurobot structure is attached to the wrist of a large industrial 6 d.o.f. COMAU SMART-3 6.125A robot, which is used for weight support of the entire Eurobot prototype. The Comau robot is equipped with a wrist 6 d.o.f. force and torque sensor that will be used in the future for on-line gravity compensation during movement of the Eurobot prototype. However, the on-line compensation is not implemented at this time. One of the arms is equipped with a BarettHand™ end-effector (Townsend 2000), to allow grasping objects of regular and irregular shapes.

This arm will be used for performing the man–machine interface comparison experiments. The other arms are equipped with TBK RH-707 Micro grippers. They can grasp robotically compatible interfaces. Pictures of the Eurobot prototype set-up are shown in Fig. 7.2 and Fig. 7.6.

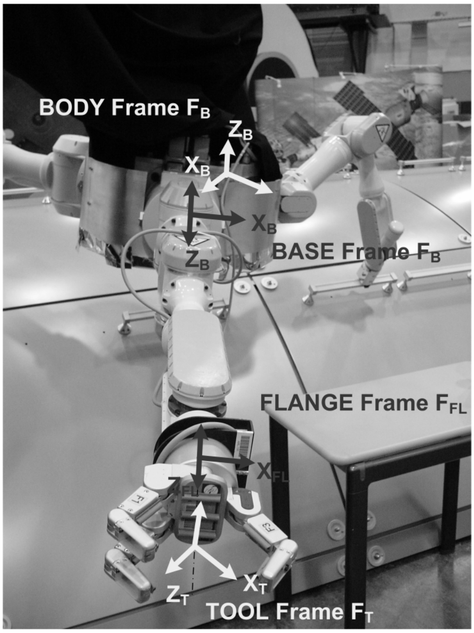

Fig. 7.2. Coordinate frame assignment of the Eurobot prototype (PA-10 standard frames shown in dark, added frames shown in light colour)

Controllers

The PA-10 arms are controlled by their proprietary controllers at this time. They provide a software application program interface (API), that we used in the development of the experimental software on the robot workstation. The API allows a very low-level access to the robot controller functionality. Commanding of joint or Cartesian set-points at interpolator level is possible. The BarrettHand™ is controlled via serial line (RS232) from the robot workstation PC. The hand motion-controller is located inside the Eurobot prototype body.

The COMAU robot controller is a derivative from a commercial version allowing low-level access as well, for flexible usage. It can be interfaced from a normal PC via a BIT3 VME/ISA bus adaptor.

7.2.3 Robot workstation

Overview of experiment software

The overall architecture of the experiment software is shown in Fig. 7.3. It has been developed under the Microsoft Visual C++ .NET environment and executes under Microsoft Windows XP on the robot workstation PC. The software is composed of a main GUI and several supporting software modules described hereafter.

The *Motion Planner Module* is in charge of controlling the PA-10 arm motion. This module exploits the PA-10 "Real Time Control Mode" in which Cartesian set-points are expected at a given frequency through the PA-10 C API I/F. The motion planner

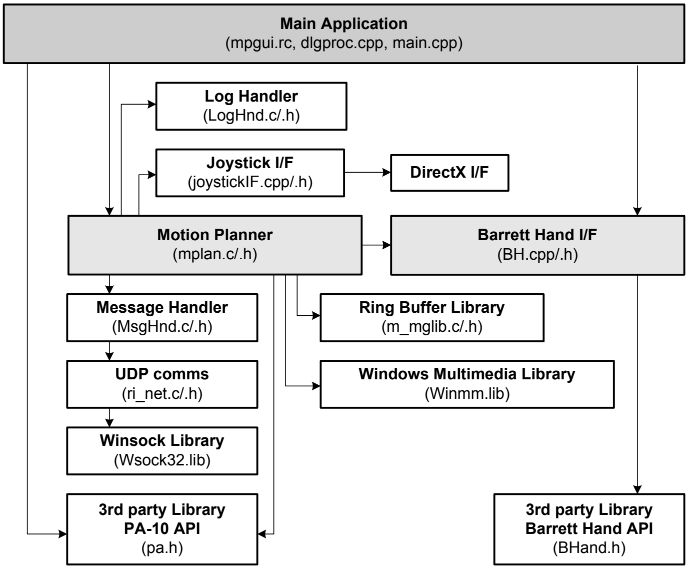
Main Application
(mpgui.rc, dlgproc.cpp, main.cpp)
Log Handler
(LogHnd.c/.h)
Joystick I/F
(joystickIF.cpp/.h)
DirectX I/F
Motion Planner
(mplan.c/.h)
Barrett Hand I/F
(BH.cpp/.h)
Message Handler
(MsgHnd.c/.h)
Ring Buffer Library
(m_mglib.c/.h)
UDP comms
(ri_net.c/.h)
Windows Multimedia Library
(Winmm.lib)
Winsock Library
(Wsock32.lib)
3rd party Library
PA-10 API
(pa.h)
3rd party Library
Barrett Hand API
(BHand.h)

Fig. 7.3. Block diagram describing architecture of the experiment software implemented on robot workstation PC. The multi-threading architecture provides real-time capability for robot control.

implements a periodic interpolator that runs every 40 ms. The interpolator is implemented as a function callback attached to a timer. The timer makes use of the Microsoft Windows multimedia library. This timer is very precise and runs the callback function at the operating system (OS) kernel priority. This ensures real time performance to the robot control. The interpolator can run in different modes that can be selected via a command or buttons on the GUI:

In HOLD mode, the same set-point is continuously sent and the arm remains still.

In SET-POINT mode, a destination frame can be specified via the GUI that must be reached by the robot TOOL frame in a given amount of time. The destination frame is reached via a linear trajectory.

In JOG mode, it is possible to jog the arm via the GUI. The movement occurs linearly. It is possible to select the axis along/around which to translate/rotate the arm. It is furthermore possible to specify velocity and the reference frame in which motion occurs.

In TRACKING mode, a dedicated software thread is started to deal with UDP / IP communications. This thread uses the *Message Handler Module* which in turn uses the *UDP Communication Module*. The tracking thread opens an UDP socket and waits for an incoming UDP datagram. When a datagram arrives, the message formatting is checked. If it complies with the message structure, the set-point inside the message is written into a FIFO ring buffer that is implemented in the *Ring Buffer Module*. This buffer is read by the motion interpolator that sends the set-point to the robot arm.

The UDP message structure illustrated in Fig. 7.4 has been implemented. The 1st byte in the command field denotes the tracking command. If this byte is set to 2, it notifies that the packet contains a set-point. The second byte contains the command for the BarrettHand™ (0 for Open, 1 for Close).

Commands 4 bytes	**Packet ID** 32 bit int	**Homogeneous Transformation Matrix** 12 x 32 bit float

Fig. 7.4. Implemented datagram of UDP/IP protocol

The Packet ID is a monotonically increasing integer, starting from 0 at start-up. Assuming that the sender (e.g. the exoskeleton workstation) delivers the packets at the same frequency than the motion interpolator (of the PA-10), then, the packet ID can be used for communication acquisition and synchronization.

In JOYSTICK-CONTROL mode, a dedicated software thread is activated to read periodically the joystick inputs via the dedicated *Joystick Interface Module*. The inputs are acquired through the standard Microsoft DirectX interface. These inputs are sent, through the ring buffer, to the motion interpolator.

In TRACKING mode, the set-points sent to the arm are directly received from the UDP interface. In all other modes, it is the task of the motion interpolator to compute the following set-point to be sent to the robot manipulator. However, in all modes a velocity scaling algorithm is applied on the set-points prior to transmitting them to the PA-10. The algorithm works as follows: Let T be the interpolator period, $P(t-T)$

the arm pose reached at previous run of the interpolator and *P(t)* the current set-point, then, the algorithm calculates translation and rotation magnitude to move from *P(t-T)* to *P(t)*. For translational magnitude, a vector *V* is defined that describes the translation from *P(t-T)* to *P(t)*. For the rotation, an angle Θ is defined that describes the rotation of *P(t)* with respect to *P(t-T)* around a vector *R*. *R* is formulated in angle-axis notation and derived from the set-point rotation matrices transmitted through the network. If speed limits are exceeded, the algorithm applies the following reductions: For translation speed, if the norm of *V* between two set-points is greater than the maximum allowed translation *VMAX* (user defined variable), a new translation component *V'* is recalculated, having same direction of *V* but magnitude equal to *VMAX*. For angular speed, if Θ is greater than the maximum allowed rotational *THETAMAX* (user defined variable) between two consecutive set-points, a new rotation component is recalculated as a rotation of *THETAMAX* around the same vector *R*. The motion planner module allows changing the maximum rotation and translation speeds at any time, even during motion, via the GUI or a joystick button input.

The BarrettHand™ is controlled via the *Barrett Hand Interface Module*. This module implements a dedicated low priority thread dealing with hand command requests (e.g. Init, Open, Close). This additional interface is necessary because the C API provided with the BarrettHand™ is composed by blocking functions, i.e. they do not return until the command is completed.

The *Log Handler Module* has been implemented for recording of the experimental data. It allocates memory for data storage in real time. It is possible to save data to files in several formats. The log handler is configurable and can record the set-points, elapsed experiment time, certain software state changes, the network performance by monitoring packet loss, BarrettHand™ status and others.

Summary of control approach

Both input devices, joystick and exoskeleton, generate Cartesian set-points that are exchanged as homogeneous transformation matrices between the sub-systems. The matrices are interpreted by the robot as translations and rotations of the robot TOOL coordinate frame with respect to the robot BODY frame. Fig. 7.2 illustrates the assignment of coordinate frames to the Eurobot arm. The two additional frames TOOL and BODY have been defined in the experimental software, in order to allow issuing more generic motion commands to the robot. The relations between BODY-BASE and FLANGE-TOOL frames are configuration parameters in our software.

Kinematic inversion is computed by the PA-10 controller. The controller is configured to exploit the kinematic redundancy of the PA-10 to keep the joints as far from their stroke ends as possible during movement.

Motion commands are issued as follows: In TRACKING and SET-POINT modes, absolute commanding is used. The target set-point is then the desired position of the TOOL frame with respect to the BODY frame. In JOG and JOYSTICK control modes, relative commanding is used. Motion occurs with respect to the selected reference frame, which can be either the BODY or the TOOL Frame.

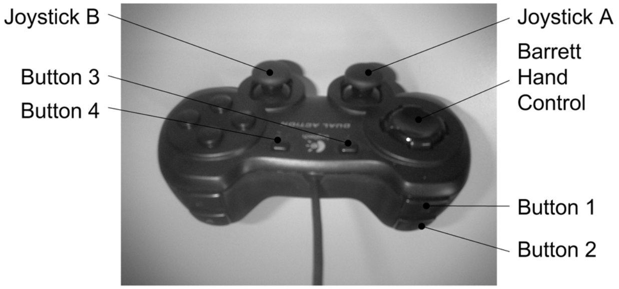

Fig. 7.5. Logitech Dual Action Joystick currently used as input device for robot control experiments. Shown are the buttons that have additional functionality

Graphical user interface

The GUI contains various fields, message boxes and buttons to activate the various control modes, to send commands and to receive and log adequate state feedback.

Joystick interface

Currently, a multi-d.o.f. Logitech Dual Action™ joystick has been integrated with the set-up. A picture of it is shown in Fig. 7.5. Motion can be commanded only if dead-man button 1 is pressed for translation or dead-man button 2 for rotation. Joystick A is used by the left thumb to control X and Y axis motion, while Joystick B is used by the right thumb to control the Z axis movement. Via Button 3 and 4, the operator can choose the reference frame with respect to which the robot will be commanded (Button 3 for BODY or button 4 for TOOL frame). Frames can only be chosen when no dead-man button is pressed. If one of the dead-man buttons is pressed, Buttons 3 and 4 will decrease or increase the maximum speed of the robot. The Barrett Hand control button allows opening or closing of the BarrettHand™.

7.2.4 Exoskeleton

Description of the mechanical system

The ESA EXARM exoskeleton (Schiele and Visentin 2003a) (Schiele and Visentin 2003b) (Schiele and Visentin 2003c) is used as intuitive man–machine interface. The exoskeleton is weight-suspended by an external cable and counter-mass system in order to simulate usage inside a low-gravity environment. A picture of the exoskeleton during operations is provided in Fig. 7.6. The counter balance system does not influence dexterity of the device but fights fatigue of the operators on ground.

The EXARM features an advanced kinematic design that allows the users full freedom of arm motion.

With EXARM, about 90% of all natural arm postures can be commanded to the remotely controlled robot (Schiele and Helm 2006). Furthermore, to wear the EXARM, no adjustments to individuals are necessary. This feature enables extremely short dress-on and dress-off times (i.e. about 20 sec. only), which is desirable if the device shall be used by astronauts inside the International Space Station.

Currently, the EXARM is a sensing device only. However, a number of single-joint actuation units have been developed in parallel, to investigate the optimal actuator configuration for force-feedback in a master–slave scenario. A Hand-held push-button device allows the operator to transmit a set of commands to the robot workstation.

Exoskeleton workstation

The EXARM has 16 angular sensors that interface to the exoskeleton control PC via analog input lines. All sensors are high-precision conductive plastic potentiometers. They are powered by independent stabilized +5 V supply lines and their output signals are conditioned by impedance changers and 5th order Butterworth anti-aliasing filters. Anti-aliasing protection proved to be important when testing the system together with the PWM motor drives of the actuation units for force-feedback.

The exoskeleton workstation operating system is the real-time XPC target™. It is a flexible and easy to program environment that integrates with MATLAB Simulink and Real-Time Workshop. After acquisition of the 16 position channels into the exoskeleton control PC, a 2nd order digital filter stage smoothes the signals for further processing. Data acquisition and all further processing are performed within 1 ms intervals. All joint position values are linearly interpolated at each time step with calibration values that are hard coded. The interpolated values are used in a forward kinematic function to derive the homogeneous transformation matrix from exoskeleton CHEST coordinate

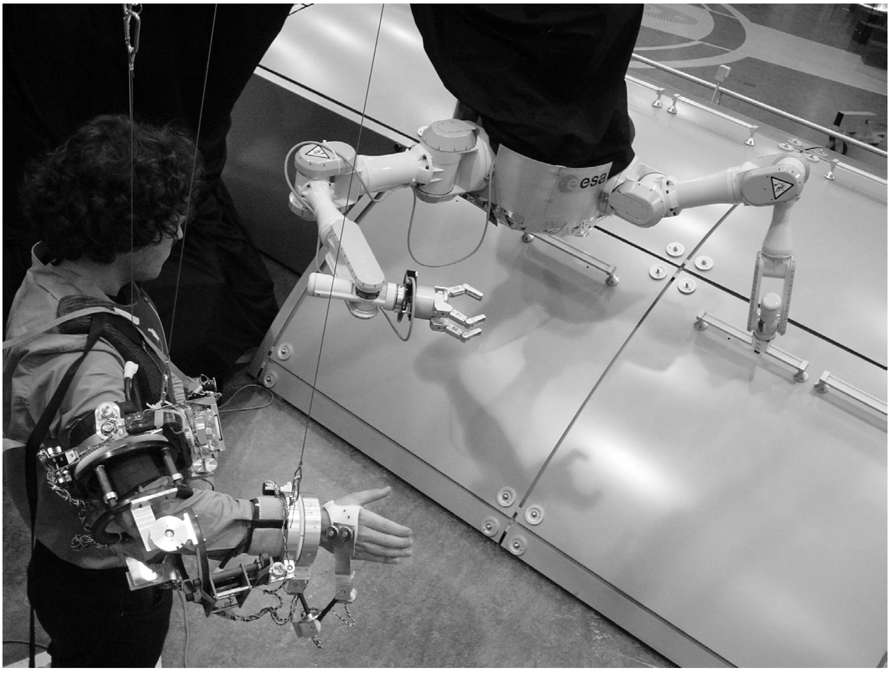

Fig. 7.6. Overview of the Exoskeleton while being used to control the Eurobot prototype. The cables, used to counterbalance the exoskeleton are visible.

frame to exoskeleton HAND frame. The matrix values are then filtered again (2nd order low pass) and send via UDP/IP to the robot controller. The UDP transmission occurs every 40 ms.

The robot controller interprets the received transformation matrix as transformation from robot BODY to robot TOOL frames (see Fig. 7.2 for reference). In order to improve the geometrical match between the robot and human arm posture, the robot TOOL frame was rotated around the y-axis of the FLANGE frame.

Furthermore, all position elements of the matrix are scaled to appropriately match the size difference between the human arm and the PA-10 robot. The network transmission speed is limited mainly by the current robot workstation capabilities (Operating system). Transmission speed from the exoskeleton workstation could be significantly increased, up to about 1 kHz. This will be important when extending the facility to include force-feedback from the robot to the MMI.

The hand-held push-button device makes use of digital input lines, to change the command bytes in the UDP datagram sent to the robot controller. This way the operator wearing the exoskeleton can start and stop transmission of set-points at any time during the experiments. At each start-up, the robot aligns itself smoothly to the current position transmitted by the exoskeleton.

7.2.5 Virtual reality workstation

The forward transformation matrices as well as the raw joint values of the exoskeleton are sent via UDP/IP to the Virtual Reality (VR) workstation PC. Transmit intervals are slower, at 500 ms, but sufficient for the graphical display.

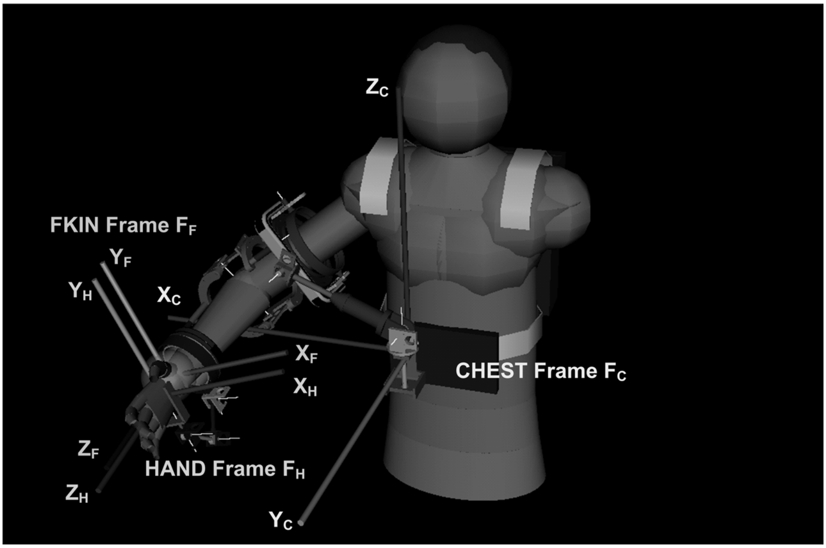

Fig. 7.7. 3D Virtual Reality Model of the ESA Exoskeleton. The model can be controlled via Ethernet and can be used for development and debugging.

The use of a 3D display workstation is mainly important during development of novel kinematic algorithms for exoskeleton-robot control. Visual feedback of device postures is crucial in the debugging phase of such developments. In Fig. 7.7, a model of the exoskeleton with the operator is shown.

The model is based on an accurate kinematic description of the exoskeleton and was used to check the results generated by the forward kinematics functions. Each joint can be actuated by the acquired raw joint sensor signals of the real exoskeleton. Furthermore a helper coordinate frame (FKIN frame) attached to an easily visible yellow sphere is included. The helper-frame position and orientation is driven by the transmitted forward homogeneous transformation matrix that is computed in the exoskeleton workstation. The visual display of the computational results allows a quick check of correctness of calibration values and proper functioning of the algorithms.

Other visualizations are available, such as a graphical model of the PA-10.

7.3 Experimental validation

7.3.1 Experimental setup

In order to demonstrate proper functioning of the test-bed, a first set of pilot experiments was conducted with joystick and exoskeleton control. A simple tracking task was given to the operator, to see whether data can be properly logged with the experiment software and to test whether the motion planner module works smoothly together with all interfaces and the robot.

The experimental task consisted of following a simple linear trajectory with the tip of a tool attached to the robots gripper. The trajectory was defined by four points along the edges of a foam parallelepiped placed inside the workspace of the robot arm. The task had to be completed in a limited and predefined time of less than 30 seconds. The position of the foam geometry with respect to the robot BODY frame was calibrated with an absolute position error of about 0.02 m. For the purpose of these first experiments the error was considered acceptable. The geometries location was identified by recording the positions of the robot when touching some of the way-points indicated on the object. Both man–machine interfaces, the joystick and the exoskeleton were used consecutively by the operator for commanding the robot. The trajectory set-points that the robot followed as well as the time required to follow the line was recorded. During usage of both man–machine interfaces, the operator was standing at the same location with respect to the Eurobot prototype and had the same view on the robot work-cell.

7.3.2 Discussion of first results

Trajectory tracking

In Fig. 7.8, two trajectories are shown, that have been recorded during the task execution of the operator. Absolute distances are shown with respect to the Eurobot BODY coordinate frame. It can be seen that the operator was able to fulfill the task and that the data logging function, the motion commanding and the interaction between

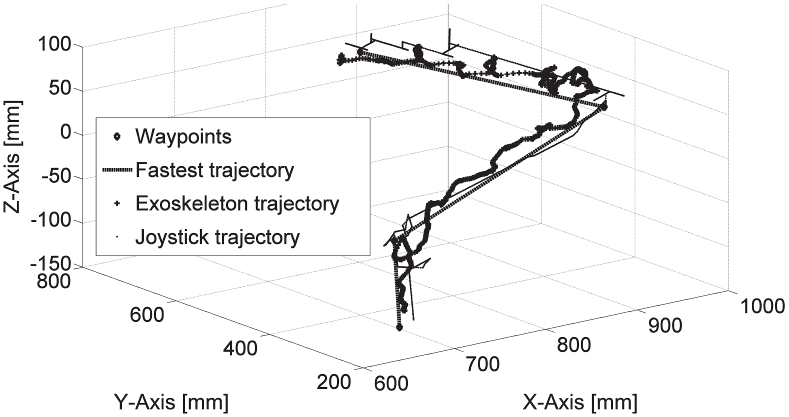

Fig. 7.8. Extract of experimental data from line-tracking experiment. Data is logged by experiment software and shows trajectories commanded with Joystick and Exoskeleton input devices.

joystick, exoskeleton and the robot functioned properly. Network related packet loss was monitored when using the Exoskeleton, but did basically not occur. Not a single Ethernet packet was lost in 10,000 transmitted packages. Considering the shape of the shown trajectories, it can be already easily noticed that significant differences exist in characteristics of the two man–machine interfaces. The Joystick can only command linear motions.

This limitation requires a precise alignment of the TOOL frame to the geometry that needs to be followed. It can be seen, that the joystick was often moved into a completely wrong direction and then corrected.

This is a result of the initial trial and error approach that operators follow when their own, visual reference coordinate system is not aligned with the TOOL coordinate frame of the robot. One reason for this strategy might be the limited time, which was available for this task. Otherwise the operator would probably check and compare the axis indicators on the Joystick and the robot, which is time consuming.

With the exoskeleton, the operator had no problem in following the right direction. However, it can clearly be seen that straight-line following is more difficult than expected. The trajectory is relatively 'bumpy' as a consequence. Both trajectories were recorded early after completion of the set-up. The operator was not trained. This could be one reason why the trajectories do not look very appealing. In any case, however, it is interesting to notice that successful execution of even such a simple task seems challenging at first, even with the intuitive exoskeleton interface.

Task execution duration

In total, the operator repeated the tracking task 5 times with the exoskeleton and 5 times with the joystick interface. The mean execution time was 110 ± 44 s for controlling the robot with the joystick and 50 ± 14 s for controlling with the exoskeleton. The large execution time required for the joystick is due to the need of aligning the robot TOOL coordinates to the task trajectory. This is needed because the joystick can only command linear straight-line motions. Orienting the TOOL coordinates is therefore necessary at each point in the tracking curve where the direction changes. In average, the initial alignment to the linear path took about 90 s.

7.3.3 Summary of first experiment results

From the preliminary results shown above, we can see clearly that differences exist between the two input devices. For the given linear trajectory task, the tracking error exerted with both devices seems similar. A large difference exists between the task execution times. Once the TOOL coordinates of the robot are well aligned to the path, the joystick can easily follow straight line trajectories. At each change of direction that is not orthogonal to the coordinate axes, however, a re-aligning of the robot is necessary when commanded by the joysticks. The task execution times would differ even more, if the operator was to follow a curved trajectory. Other joystick input devices, featuring more degrees of freedom would be better suitable for this task. This is why we will alter the setup to contain the standard SRMS and SSRMS joystick workstation. Two 3 d.o.f. joysticks will then be able to control 6 d.o.f. of the robot simultaneously. We anticipate that then, a better performance in terms of execution times can be reached.

7.4 Conclusions and future work

The detailed design of a ground development facility was shown, that can be used for conducting tele-control experiments with a robot and two types of man–machine interfaces, joysticks and exoskeletons. The robot workstation can log the experimental data. Such data can be used to analyze task performance and establish performance metrics. MMI performance analysis is required to investigate the advantages and disadvantages of conventional joystick over exoskeleton-type man–machine interfaces. A simple experiment was conducted with both MMI's. The first results show that the facility functions properly and is ready to be used in a more comprehensive study of human–machine interaction performance.

At present, ESA performs a detailed definition of tasks, performance metrics and mental load assessment techniques that will allow comparing MMI performance during robotic remote-control. A series of detailed and controlled experiments with multiple subjects is currently under preparation. Investigation of the learning behavior, in dependence on the MMI-type, can give us important clues about how to design truly intuitive devices for our astronauts in the future. Also the hardware set-up of the facility will be modified in the coming months. A number of the commercially available items will be replaced with custom developed units from ESA. For instance, the commercial PA-10 controllers will be replaced with the ESA CONTEXT controller (Bologna et al. 2004). CONTEXT will fully replace the commercial controllers and offer simultaneous control of all 3 Eurobot arms in position, compliance or any combination of those. The CONTEXT hardware will be fully integrated into the mechanical structure of the Eurobot prototype. CONTEXT will also allow modification of the inverse kinematics functions, which will allow optimizing the geometric mapping between the exoskeleton and the robot arm. In the more distant future, the PA-10 robot arms will be exchanged with manipulators currently being developed for ESA in a dedicated research project (Rusconi et al. 2004) (Hirt and Gruener 2004). Furthermore, the commercial joystick will be replaced with a custom joystick station, similar to the one that is used in the Space Shuttle and on the ISS for manipulator control.

Part IV

Actuation

Chapter 8: Bowden Cable Actuator for Force-Feedback Exoskeletons

A. Schiele, P. Letier, R.Q. van der Linde, F.C.T. van der Helm
IEEE/RSJ International Conference on Intelligent Robots and Systems, Beijing, Oct. 2006, pp. 3599–3604

Chapter 9: Performance Difference of Bowden Cable Relocated and Non-Relocated Master Actuators in Virtual Environment Applications

A. Schiele
IEEE/RSJ International Conference on Intelligent Robots and Systems, Nice, Sept. 2008, submitted

Chapter 8

Bowden Cable Actuator for Force-Feedback Exoskeletons

A. Schiele, P. Letier, R.Q. van der Linde, F.C.T. van der Helm

IEEE/RSJ International Conference on Intelligent Robots and Systems, Beijing, Oct. 2006, pp. 3599–3604

This paper introduces a novel type of actuator that is investigated by ESA for force-reflection to a wearable exoskeleton. The actuator consists of a DC motor that is relocated from the joint by means of Bowden cable transmissions. The actuator shall support the development of truly ergonomic and compact wearable man–machine interfaces.

Important Bowden cable transmission characteristics are discussed, which dictate a specific hardware design for such an actuator. A first prototype is shown, which was used to analyze these basic characteristics of the transmissions and to proof the overall actuation concept. A second, improved prototype is introduced, which is currently used to investigate the achievable performance as a master actuator in a master–slave control with force-feedback. Initial experimental results are presented, which show good actuator performance in a 4 channel control scheme with a slave joint. The actuator features low movement resistance in free motion and can reflect high torques during hard contact situations. High contact stability can be achieved. The actuator seems therefore well suited to be implemented into the ESA exoskeleton for space-robotic telemanipulation.

8.1 Introduction

Future human missions or permanent presence in space will require substantial robotic support. The European Space Agency (ESA) started developing a humanoid servicing robot for the International Space Station (ISS), called Eurobot (Schoonejans et al. 2004). Eurobot shall support astronauts during extra-vehicular activities (EVA). Two main control modes are foreseen therefore; autonomous control and manual control in a master–slave type architecture. For the manual control of the seven degrees of freedom (d.o.f.) arms of Eurobot, an exoskeleton man–machine interface is currently being developed at ESA (Schiele and Visentin 2003a) (Schiele and Visentin 2003b) (Schiele and Visentin 2003c). The exoskeleton shall provide force-feedback from Eurobot to the arms of human operators located inside the ISS. In order to provide high comfort during long-duration operations, special attention was paid to ergonomic design of the exoskeleton. The device offers a great dexterity of movement to the operators while being worn and needs no adjustments to different individuals. This is achieved by its novel ergonomic kinematic design presented in (Schiele and Helm 2006).

For creation of a good quality force-feedback with the exoskeleton under micro-gravity conditions, several actuation options exist. It could be adequate to integrate actuators, e.g. DC motors with reducers, directly into its mechanical structure. Their mass is anticipated to only modestly reduce force-feedback performance under weightlessness.

On earth, however, directly integrated actuators would need to compensate the weight of the structure and of their own, which makes it difficult to achieve good force-feedback performance. Provision of a high power output in the entire workspace at a reasonably low system mass is difficult to achieve. In order to fight their own weight, the size of motors must increase, escalating the required power from joint to joint and resulting in a significant increase of total exoskeleton mass and inertia. Eventually, a similar compact and enhanced kinematic design approach than for the 0-g version is impracticable, if gravity force cannot be compensated by external mechanisms or if the motors are not extremely lightweight and power-dense. One solution to the problem of power dense actuation for wearable interfaces can be the relocation of all actuators to the static base of the system. This way, mass and inertia of the movable part can be significantly reduced, thus, allowing an ergonomic kinematic design similar than for a reduced-G exoskeleton also on ground.

In space, actuator relocation could lead to less inertia felt by the operators during telemanipulation, as well as to a more compact design of the wearable device. This is why we decided to investigate possible solutions allowing actuator relocation.

Actuator relocation could be achieved by means of hydraulic, pneumatic or cable transmissions. Hydraulic transmissions, as well as pneumatic transmissions were discarded rather quickly, however, because their complexity is relatively high at low performance in force-feedback applications. For the ESA exoskeleton, therefore, a cable-based transmission system seemed most suitable.

Cable transmissions can be established in two different manners, either by routing cables over a set of pulleys such as implemented in (Williams-II et al. 1998) and (Frisoli et al. 2005) or by employing a Bowden cable system, in which the cable is guided inside a flexible sleeve. Because the first option leads to a rather extensive increase of mechanical complexity, the Bowden cable approach was chosen by ESA for further detailed study. The use of Bowden cables for force-reflective display design was previously reported in (Immersion-Cooporation 2004) and (Springer and Ferrier 2002). The use of such an actuator type for the ESA Exoskeleton was already postulated in (Schiele and Visentin 2003a) and (Schiele and Visentin 2003b).

However, to the current knowledge of the authors, this paper presents for the first time an investigation of the transmission behavior of Bowden cables and their influence on haptic performance in a force-feedback control.

In the first part, this paper discusses the specific transmission characteristics of Bowden cables and their influence on the required hardware architecture of the actuator. The characteristics were investigated with a first prototype at ESA and TU Delft. The design of a second, improved version of the first prototype is shown next, which was developed to investigate actuator performance in force-feedback control. It was built in cooperation with the University of Brussels.

8.2 Geometric characteristics of Bowden cable transmissions

8.2.1 Implementation

In a Bowden cable transmission, a cable is guided inside a flexible sheath. For remote actuation of a robotic joint, force is delivered to the remote joint by mechanical displacement between the cable and the outer sheath. To implement a remote-actuated rotary joint, a pull-pull configuration as illustrated in Fig. 8.1 is optimal. The cables are fixed to pulleys at both sides. The robotic joint can be actuated in both directions by respective rotation of the motor. A preloading unit, located somewhere along the transmission can be used to tension the cable-loop with respect to the sheaths.

8.2.2 Specific Bowden system characteristics

Losses and inefficiencies of Bowden transmissions are due to complex and non-linear friction phenomena. Coulomb friction, viscous friction, stiction and stick-slip, can all be present in Bowden cable transmission systems.

The primary parameters influencing efficiency of the transmission are normal forces on the cable (induced by cable tension or preload), friction coefficients resulting from material pairs and velocity of the cable inside the external sleeve.

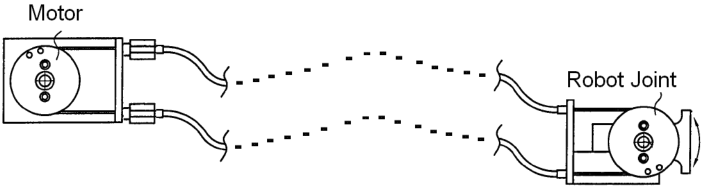

Fig. 8.1. Concept illustration of Bowden cable actuation to a robotic joint. The robotic joint represents one joint of a wearable structure such as an exoskeleton. The motors can be located e.g. on the back of the operator.

Furthermore, cable and sleeve stiffness play an important role regarding stick-slip behavior and thus, mechanical bandwidth of the transmission.

It is characteristic for Bowden transmissions that those primary parameters depend furthermore on the geometric configuration of the cable system. Basic friction effects have been described by models that are available in literature. However, understanding of the particular influence of cable geometry on the friction characteristic of a Bowden cable is not so common and is therefore treated hereafter. The main geometric parameter influencing friction between the outer housing and the inner cable is the total wrap angle of the cable system. Theoretically, the friction losses of Bowden cables are similar to those occurring when sliding a cable over a stationary cylinder at constant velocity v, as illustrated in Fig. 8.2. The force transmission efficiency F_{S1}/F_{S2} can thus be approximated as in

$$F_{S1}/F_{S2} = 1/e^{\mu\Theta} = e^{-\mu\Theta}. \tag{8.1}$$

In (8.1), μ is the coefficient of sliding friction and Θ, the wrap angle of the cable around the cylinder. In a Bowden system, Θ is the sum of all bending-angles along the transmission. In Fig. 8.3, theoretical force transmission efficiencies are shown in dependence of the wrap angle, for different friction coefficients between cable and the sheaths. Practical measurement results of different material pairs and lubrications are presented in (Ognar 1994) and (Carlson et al. 1995).

As indicated in (8.1), the bending radius should not influence the cable friction. According to cable manufacturers, the only effect of very small deflection radii is increased wear of the cable, which negatively influences the friction coefficient over time. Therefore, they recommended having minimal deflection radii r_m of

$$r_m \geq 20 \cdot D_{Cable}, \tag{8.2}$$

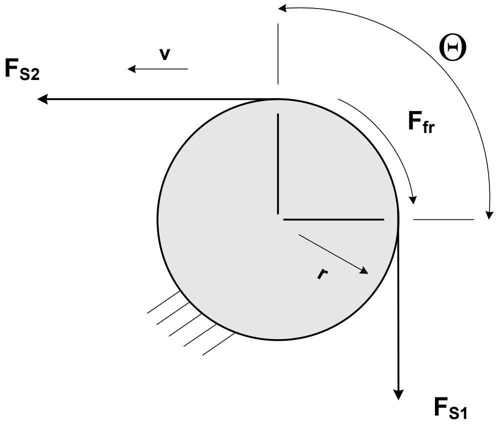

Fig. 8.2. Friction inside a Bowden cable is similar to friction of a cable routed around a stationary cylinder. Theta represents the sum of all bending angles of the transmission, from motor to joint, and is called wrap angle.

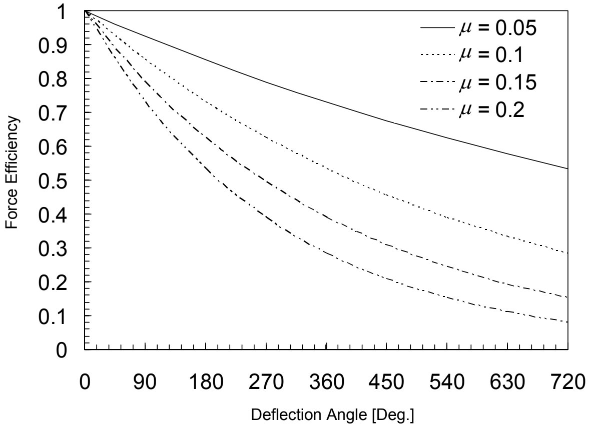

Fig. 8.3. Theoretical efficiencies of force transmission in a Bowden cable system. Curves are presented for various friction coefficients.

with D_{Cable} being the external diameter of the cable inside the sleeve. However, in a real Bowden cable system, changing wrap angle also changes cable preload and therefore has a bigger effect on force transmission efficiency as shown in theory. The preload changes during bending can be explained as follows:

The external casing often comprises of a spiraled flat steel-band or a linear arrangement of steel bands forming a tube. Those deform elastically during bending, like when bending a spiral spring. During bending, the center-line of this tube extends longer, which stretches and preloads the cable inside.

Fig. 8.4 shows the measured stretch *DeltaL* of a cable inside a Bowden cable system under load, for different wrap angles. It can be seen that if the wrap angle is increased under constant load, the preload of the Bowden cable assembly increases, resulting in increased stretch of the cable.

Cable preload influences the amount of friction loss directly, by increasing normal forces between cable and sleeve surfaces. This means that if the geometric configuration of the cable system changes under constant load, also the force transmission efficiency will change. In order to minimize this effect, cables as well as sleeves must be as stiff as possible. This is important for implementation of force control to the actuator joint. For the sleeves, linear constructions have higher stiffness than spiral-spring type constructions and are therefore preferred. Fig. 8.4 furthermore shows that stiffness of the cable is not linear over the load range.

The question arises, whether to operate a Bowden cable system better with low loading (i.e. Fig. 8.4 B) or better with high loads (i.e. Fig. 8.4 C) for force-feedback applications.

Up to now, similar configurations of Bowden cables were only used in highly loaded conditions for joint actuation (Veneman et al. 2005). Operation at exclusively high load linearizes the cable stiffness; however, has the negative effect of creating high friction. The approach works fine for position control applications, if large motors can be used

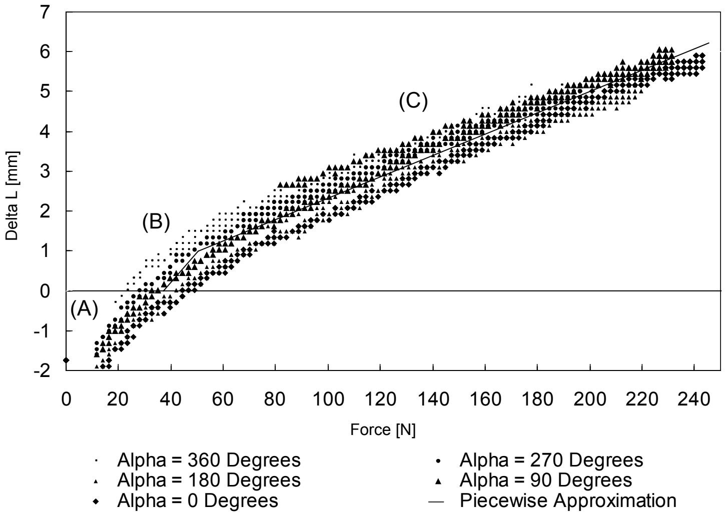

Fig. 8.4. Measured cable stretch *DeltaL* in function of actuator force. The influence of wrapping angle *Alpha* on cable stretch is shown at different actuator loads. Measurements were done with the first actuator prototype.

to overcome the frictional force. In principle, a low load is better for haptic applications, because friction in the system is lower. As a consequence, the torque dynamic range can be higher, which can lead to a better haptic rendering capability. Furthermore, smaller motors can be used, to keep the system mass within acceptable limits. However, if cable preload is too low, the cable can detach from the pulleys, which introduces slack into the system. This effect is apparent in the experimental results presented in Fig. 8.4 (A), as negative stretch *DeltaL*.

In order to avoid such slack of the cable, stiff spiral springs were inserted in series with the sleeve and the robotic joint structure in the first prototype. These springs counteract the effect of slack at low loading, if they are slightly tensioned. Furthermore, the springs reduce the influence of the wrap angle to the cable preload. It is important to dimension the spring stiffness appropriately. If they are too soft, they significantly limit the contact stiffness that the actuator can create in a force-feedback application. A cable transmission model was developed at the TU Delft, which allows performing such optimizations.

Another effect that has to be considered in the hardware configuration of a Bowden cable actuator is *stick-slip*. During movement, stick-slip causes vibration that is characterized by a saw-tooth displacement over time evolution. The motion is governed by a static friction force in the stick phase and a viscous friction force in the slip phase. As the presence of vibrations can be highly detrimental to the mechanical bandwidth and torque dynamic range of the system, stick-slip has to be minimized. Following solutions were found out to reduce stick-slip and to improve the Bowden cable transmission characteristics:

- *Use of friction couples whose coefficient of friction increases with speed.* When the coefficient of friction increases with the speed, the phenomenon will not occur, because a static equilibrium between the driving force and the friction force will be ensured. Few material pairs offer this characteristic. The most common is poly-tetra-flourethylene (PTFE) on PTFE. The actuator uses therefore PTFE coated steel cables in combination with a PTFE liner inside the sleeve.

- *Use friction couples with a very small friction coefficient* in general. PTFE on PTFE is well suited.

- *Use cables and sleeves with high stiffness.* Therefore, it is optimal to use pre-stretched 7 × 19 cable construction with a Kevlar reinforced linear shell-type external sleeve. The 7 × 19 cable construction ensures good flexibility of the cable at high stiffness.

- *Use the actuator in a low preload condition.*

The investigations presented above were performed with the first prototype shown in Fig. 8.5. The prototype consists of a DC motor with gearbox, encoder, potentiometer and differential tendon force sensor on the actuator side, and one torque sensor, potentiometer and load bar at the joint side. The load torque sensor is integrated into the pulley spokes on the robotic joint (not visible in Fig. 8.5). Different masses can be attached to the load bar, to simulate actuator loading. This set-up was used to proof the overall concept of Bowden cable actuation. However, its hardware has undergone too many changes during the development, which is why we decided to build a second, better constructed prototype for carrying out the master–slave control experiments. The second prototype includes all elements that were found necessary for a good Bowden cable actuator.

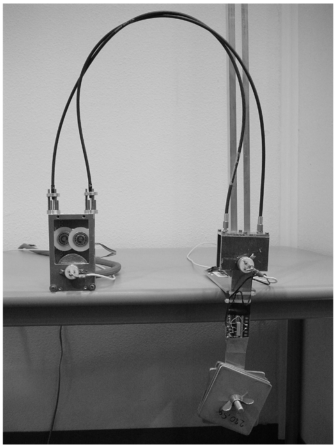

Fig. 8.5. First Bowden cable actuator developed at ESA. The prototype was used to investigate the basic cable transmission characteristics.

8.3 Bowden cable transmission in force feedback

8.3.3 Mechanical setup

Similar to the first set-up, the second prototype is built from two devices linked by the cables: the motor joint (Fig. 8.6, right) and the robot joint (Fig. 8.6, left). The motor joint consists of a brushed DC motor with a cable capstan reducer (reduction ratio of 10:1). This type of reducer allows zero backlash and extremely high efficiency (≈ 99%) at the expense of a low torque to volume ratio. In order to investigate influence of backlash to the actuator at a later stage, an adjustable backlash unit is included in the motor-side of the prototype. The robot joint consists of a bar, representing an articulation of the exoskeleton. The cables are attached to the joints in a pull-pull configuration, just like before. They consist of PTFE-coated steel cables sliding in slightly preloaded, low weight, Kevlar-reinforced cable housings. The sleeves also contain the inner Teflon-coated liner.

The pretension is obtained by a spring system, which can be locked to conduct experiments also under high preload conditions later on. Each side of the master contains 500 pulses per revolution encoders.

A torque sensor is included in each pulley. With a diameter of 42 mm they reach a maximum torque of 2.5 Nm with a resolution bellow 1 mNm. The two torque sensors will allow studying the cable friction behavior between the two joints, in various configurations, more deeply in the future. In addition, we developed a simple joint representing a joint of the slave robot. This slave joint prototype was used during the force-feedback experiments shown below. The slave joint consists of a simple brushed

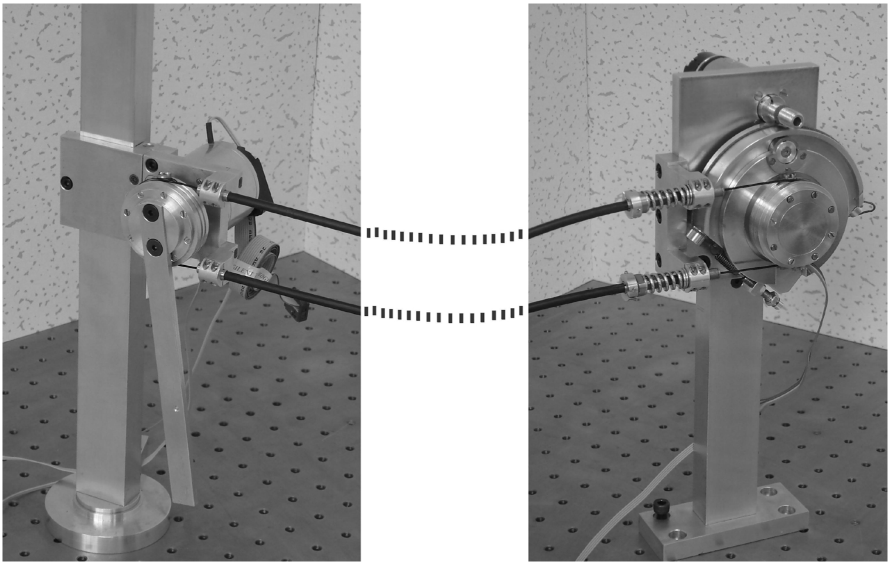

Fig. 8.6. Motor joint (right) and robot joint (left) of the second prototype developed to investigate force-feedback performance with a slave joint.

DC motor with planetary gearbox (reduction ratio of 81:1) and a 100 pulses per revolution encoder. A bar equipped with a strain gage force sensor is attached to the gearbox output-shaft. The whole slave setup can be located next to a stiff steel wall to conduct contact experiments in a one d.o.f master–slave set-up with the cable actuator as a master.

8.3.4 Controller

A dSpace DSP control board (Ds 1103) interfaces sensors and current amplifiers of both, master and slave. The control updating rate is fixed for all the experiments at 1 kHz. As mentioned already above, the primary purpose of this system is to show the feasibility to use Bowden cable transmissions for force feedback telemanipulation within the ESA exoskeleton. The chosen motor controller structure is shown in Fig. 8.7.

The controller is a 4 channel (4C) type, similar to that proposed by Lawrence (Lawrence 1993). The control principle consists of exchanging torque and position information between master and slave for command of the opposite side. The position information is compared to the local values through proportional-derivative (PD) controllers, represented by C_m and C_s. The torque commands can be used in open loop or through proportional-integral (PI) controllers, represented by C_{fm} and C_{fs}. The position and the torque commands are then added to create the actuator set-points. Torque commands on the master side are acquired from the torque sensor on the robotic joint side of the master.

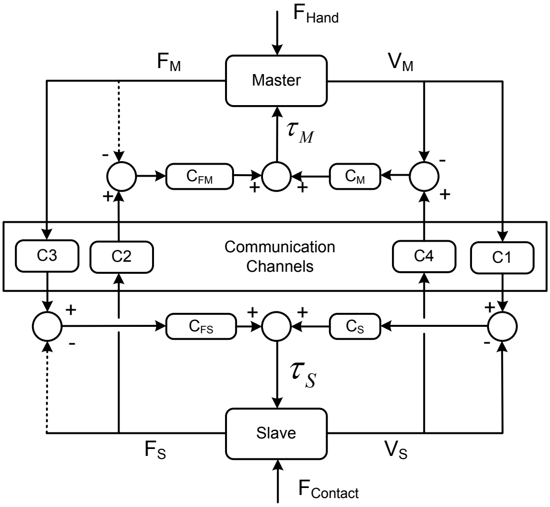

Fig. 8.7. Structure of the 4 channel controller that was used for the force-feedback experiments carried out with the Bowden cable actuated master.

8.3.5 Force-feedback performance experiments

Telemanipulation experiments are currently being carried out with the Bowden cable actuated master commanding the slave system in free motion and in hard-contact situations. The results presented below are an extract from the ongoing experiments with the system. The choice of the 4C control architecture is a consequence from poor results that we have achieved with conventional 2 channel control approaches (i.e. direct force feedback). With direct force-feedback, we were unable to exhibit stable behavior when the slave experienced a hard contact.

Fig. 8.8 to Fig. 8.10 show results attained by using the 4C controller with open loop force control during the experiments. The robot joint of the master was moved by the operator hand to command the slave remotely. Free motion took place during the first seconds of the experiment. After about 2.8 seconds, the slave was rotated far enough to contact the steel surface next to it. The solid line in all graphs corresponds to recordings of the cable actuator (i.e. the master), whereas the dashed line represents recordings of the slave. It can be seen in Fig. 8.9 that a residual torque of about 0.1 Nm remains during free motion. It is important to notice that, for these results, no local friction compensation is used on the master side. The reduction of free motion resistance is done by the 4C controller only.

In hard contact, Fig. 8.8 and Fig. 8.9 show very small position and torque tracking errors, which proofs good actuator transparency and a stable behavior. The maximum contact stiffness that can be replicated with the Bowden cable actuator is illustrated in Fig. 8.10. The stiffness is in the order of 8.6 Nm/rad. For this measurement set, the springs between the sleeves and the joint structure were clamped, to see the maximum attainable stiffness of the actuator. When the springs are used, to avoid friction variation with the wrapping angle, the actuator stiffness is limited to the spring stiffness. In Fig. 8.10, the stiffness is only limited by the flexibility of the cable system, the control architecture and the flexibility of the slave bar.

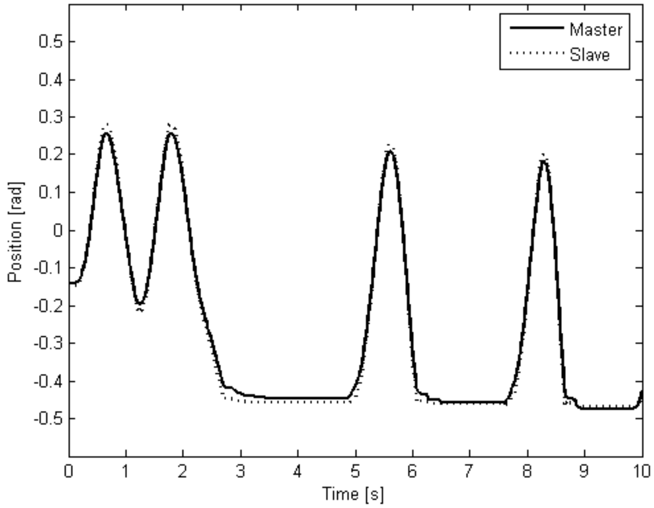

Fig. 8.8. Experimental results from master–slave control with Bowden cable actuator. Position tracking capability.

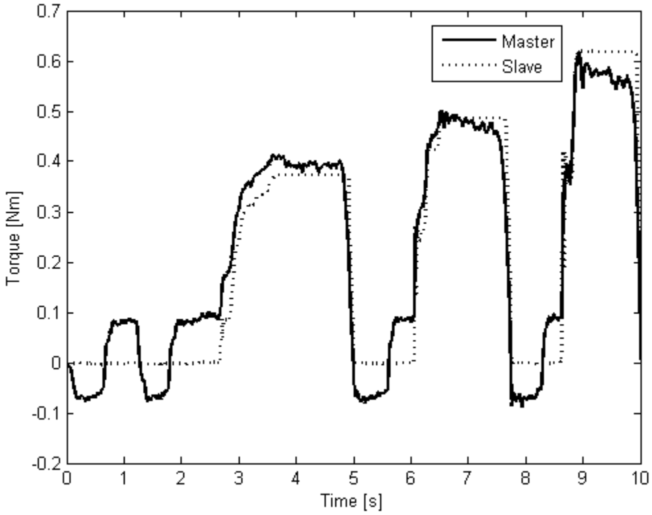

Fig. 8.9. Experimental result from master–slave control with Bowden cable actuator. Torque tracking capability in contact situation.

Similar experiments were also conducted with additional local force feedback control, aiming at reducing free motion resistance even further. Although almost similar results to the ones presented in Fig. 8.8 were achieved in free motion, contact of the slave with the surface caused more unstable behavior of the master. The position tracking error was bigger.

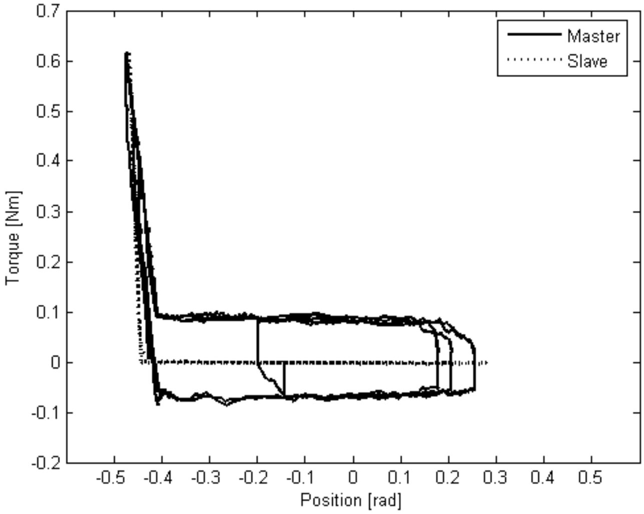

Fig. 8.10. Experiment results from master–slave control with Bowden cable actuator. Contact stiffness of master actuator and slave in hard contact situation.

In general, the feeling of the actuator in free motion and in contact situations is very good when used with a 4C controller without local force feedback. The results shown above confirm the possibility to use the actuator for the ESA exoskeleton in a space application.

8.4 Future work

The experimental results shown above have proven suitability of the actuator to work in a low load condition. This condition resembles use inside a micro gravitational environment. The next step will be to investigate how the actuator will perform in a force-feedback control under higher load conditions. In order to analyze whether the actuator will be truly usable on ground, we need to conduct force-feedback experiments with additional masses attached to the robot joint of the master actuator. Those experiments will allow investigation of actuator performance when additional weight compensation of adjoining mechanical linkages is simulated. While these tests had been carried out with the initial prototype, they have not been confirmed with the new hardware set-up yet.

Furthermore, the high load experiments will have to be repeated under varying wrapping angles of the Bowden cable system. The compensation springs of the new set-up must then be used to compensate for varying preload of the Bowden actuator.

Only when these two additional experiment sessions have been successfully conducted, we can truly be sure that the developed actuator is usable also on ground. In a positive case, the presented actuator could provide a great benefit to many terrestrial robotic applications. In principle, all robots requiring a large workspace at a low system mass could make use of such an actuator. In particular, this actuator would be suitable for the vast range of wearable and non-wearable haptic devices, which suffer from the same lack of power dense actuation.

8.5 Conclusions

Geometric specificities of Bowden cable transmissions are presented, that have been analyzed during experiments with a first Bowden cable actuator prototype.

(1) A suitable hardware configuration is shown, to implement remote actuation to a robotic joint via Bowden cable transmissions.

(2) Furthermore, the capability is demonstrated to use a Bowden cable actuator for haptic applications in a low load configuration, with good force-feedback performance and contact stability in hard contact situations with a slave.

(3) We have demonstrated that our Bowden cable actuator can, already now, be successfully used for actuation of the ESA human arm exoskeleton in space.

(4) The Bowden cable actuator can help to increase compactness of wearable human machine interfaces, by shifting design complexity from the movable part of the system, to the stationary one. By enabling compactness, the actuator opens the way to a more advanced kinematic design of the devices, which can enable better comfort and ergonomic properties during human–machine interaction.

Chapter 9

Performance Difference of Bowden Cable Relocated and Non-Relocated Master Actuators in Virtual Environment Applications

A. Schiele

IEEE/RSJ International Conference on Intelligent Robots and Systems, Nice, Sept. 2008, submitted

It is the goal of this paper to present performance differences between a Direct Drive master actuator (DD) and a Bowden Cable relocated master actuator (BCD) in a typical force-feedback tele-manipulation experiment with a virtual slave. The BCD actuator is a candidate actuator for implementation in a wearable exoskeleton, in order to reduce mass and inertia on each joint of the movable structure.

The BCD performance matches the one of the DD in terms of torque and position tracking in a 4 channel control. The maximum rendered contact stiffness is suitable for implementation in the ESA human arm exoskeleton, with a maximum of about 36 Nm/rad. When, instead of the DD, a relocated BCD actuator is implemented in an exoskeletons movable structure, the mechanical output power-density can be increased by more than 5 fold up to 31 mNm/cm^3, with comparable performance. The specific power is then increased by more than 6 fold, to 13 Nm/kg. The Bowden Cable transmission wrapping angle alters the free movement friction only marginally by about 50 mNm only. The tracking performances are hardly affected and the contact stiffness increases with increasing wrapping angle. Transmission wrapping angles of up to 270 Deg. are tested.

9.1 Introduction

Force-feedback master devices, such as wearable robots or haptic exoskeletons (Zoss and Kazerooni 2006) (Bergamasco et al. 1994) all suffer from the same limitation in power density and specific power of their actuators (Jansen et al. 2000). Therefore, it is desirable to relocate a large amount of mass of the actuator system, such as e.g. the motors and parts of the gear transmission, away from the movable structure of the robot. This is done, for instance by means of cable transmissions (Frisoli et al. 2005) (Veneman et al. 2005). Recently we have analyzed different master actuator technologies (Letier et al. 2006) suited for implementation in the ESA human arm exoskeleton (Schiele 2008b) that allow to level performance while reducing mass and inertia on the moving structure. In particular, we have proposed and validated a novel Bowden cable drive (BCD) actuator in (Schiele et al. 2006b), that allows relocating the drive motor of each joint of a moveable structure by means of Bowden cable transmissions. We have shown good performance of the actuator in (Schiele et al. 2006b), with a real slave joint in a force-feedback master–slave scenario. However, we did not quantify its performance differences with respect to conventional actuators, such as Direct Drives (DD) that are also typical actuators in wearable robot systems. Furthermore, up to now, the exact influence of the transmissions bending angle on the achievable performance was not studied. Since in Bowden cable transmissions, the tendon is guided from the motor unit to the joint inside a flexible sleeve, variations in the bending angle of the sleeve, cause the friction inside the drive-train to vary. In (Schiele et al. 2006b) we have explained causes of such variation of friction coefficient and hypothesized that in a low-load scenario, these effects can be minimized by correct pairing of materials (PTFE coated steel cables within PTFE coated sleeves) and correct choice of control strategies. This paper will address the performance differences over a range of cable wrapping angles experimentally.

A novel haptic master–slave setup was built in cooperation with an industrial consortium (SAS Brussels, Univ. Libre de Bruxelles, Micromega Dynamics S.A. Liege), which allows to directly compare the performance of a DD and a BCD master actuator, w.r.t. position and torque tracking of the slave joint, attainable contact stiffness and residual friction of the master during free-air movement of the slave. The new setup allows studying the influence of the transmission wrapping angle on the BCD system behavior. Specific wrapping angles can be set, in the range of 0–270 Degrees. The master actuator hardware can be altered easily between both, DD and BCD configuration. The haptic loop simulator was developed to prototype the larger architecture required for actuating the full ESA human arm exoskeleton. It is modular and allows extending the number of joints to be controlled up to the number required to interface the exoskeleton. The master input joint of the haptic simulator resembles a typical joint inside the exoskeleton. Instead of attaching to the human arm, however, a handle is provided that allows operator input to the teleoperator system.

It is the goal of this paper to compare the performance of a Bowden cable relocated master actuator with the performance of a Direct Drive actuator in a typical force-feedback experiment. The influence of the Bowden cable transmission deflection (wrapping angle) on tracking performance, residual movement friction and on maximum achievable contact stiffness is presented.

9.2 Overview of experimental setup

In order to allow a fair comparison between the two master joint architectures, the single d.o.f. haptic-loop simulator interfaces them with the same infrastructure w.r.t. communication channels, electronics, software and sensors.

9.2.1 Architecture of haptic loop simulator

The haptic-loop simulator consists of 4 modular, interconnected systems that are depicted schematically in Fig. 9.1. The first sub-system is the master actuator along with its sensors, conditioning electronics and connection to a CAN bus network. The haptic loop controller, which is the core of the system, is implemented on an x86 PC running the real-time QNX Neutrino™ kernel. The controller is interfaced via a TCP/IP connection to the slave physics simulator, which is the third part of the system. Visualization of the slave is performed on a 3^{rd} PC.

9.2.2 Master actuator I: direct drive motor with cable capstan reducer

A picture of the Direct Drive configuration of the master actuator is shown in Fig. 9.2. In this configuration, a DC motor (Maxon A-max 32) is linked via a 10:1 cable capstan reducer to the output handle of the system. The cable capstan reducer has a high efficiency in the order of 99%, at zero backlash. The output handle of the master joint

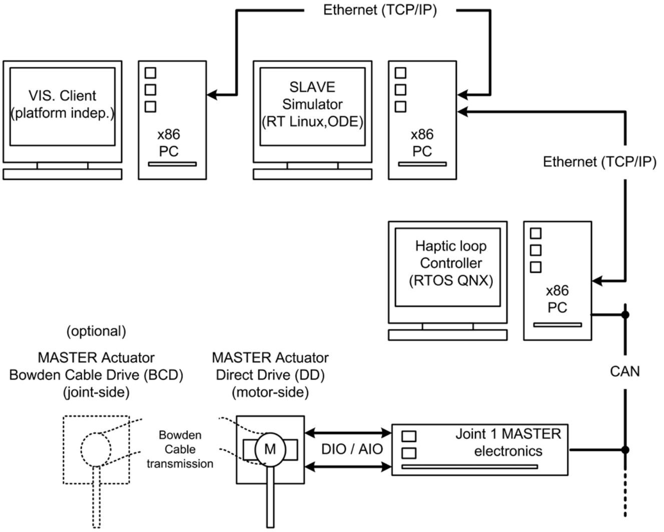
Ethernet (TCP/IP)
VIS. Client (platform indep.)
x86 PC
SLAVE Simulator (RT Linux,ODE)
x86 PC
Ethernet (TCP/IP)
Haptic loop Controller (RTOS QNX)
x86 PC
CAN
(optional)
MASTER Actuator Bowden Cable Drive (BCD) (joint-side)
MASTER Actuator Direct Drive (DD) (motor-side)
Bowden Cable transmission
M
DIO / AIO
Joint 1 MASTER electronics

Fig. 9.1. Overview of the haptic-loop one degree of freedom (d.o.f.) simulator. The framework has been implemented for testing 1 d.o.f force-feedback master joints with a slave joint in a virtual contact environment. The simulator can be extended for multiple degrees of freedom.

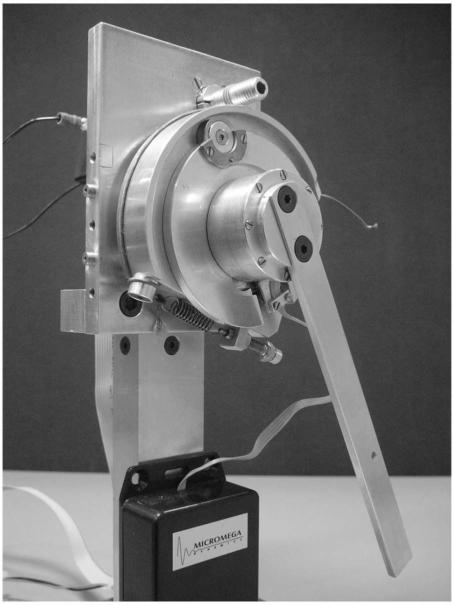

Fig. 9.2. Direct Drive (DD) master actuator implemented in the 1 d.o.f. haptic loop simulator. The DD consists of a DC motor with 10:1 cable capstan reducer and an output shaft. A torque sensor is integrated into the structure, before the output bar. The motor contains a 500 pulse/rev. optical encoder.

can be used by the operators as input to the telemanipulation system. The operator can move the virtual slave and feel the reflected forces of the slave's contact simulation. Between the cable capstan and the output handle, a torque sensor is installed, that measures the torque T_M at the master output. The torque sensor readings are acquired by strain-gage measurements on flexible spokes integrated in the cylindrical output shaft.

The sensor is designed for a maximum torque of 1.25 Nm, with a sensitivity of 3.7 V/Nm. With the conditioning electronics and AD converters, the readings feature a resolution below 0.1 mNm. A 500 pulse per revolution optical encoder is attached on the rear of the motor shaft, for master position X_M measurement and velocity (V_M) estimation. The DD joint is designed to allow a maximum joint speed of about 180°/s, which is suitable for testing typical haptics scenarios.

The mass of the motor, along with the cable capstan and excluding the mechanical support structure amounts to about 0.95 kg at a volume of about 331 cm^3. The actuator can deliver a maximum output torque of up to 2 Nm, but its current is limited to fit the torque sensor specification.

9.2.3 Master actuator II: direct drive motor with cable capstan reducer and Bowden cable transmission

When the master actuator mechanical structure is altered to the BCD, the system looks like depicted in Fig. 9.3. Instead of an output handle on the motor-side, now, a pulley

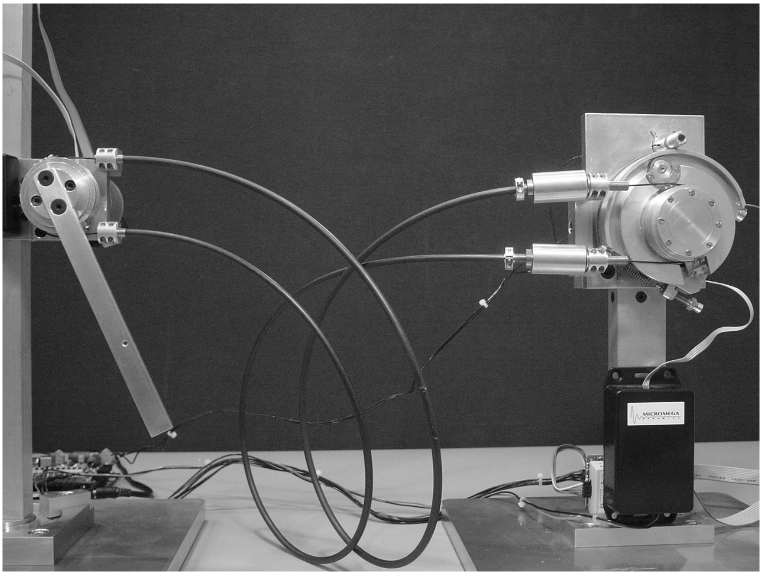

Fig. 9.3. Bowden Cable Drive (BCD) actuator version implemented in the 1 d.o.f. haptic loop simulator. The master actuator consist of a DC motor with 10:1 cable capstan reducer (right) that is connected to an output bar via a Bowden Cable transmission (left). A torque sensor is integrated directly before the output bar along with a 500 pulse/rev. optical encoder.

is fixed, that holds the cables of the beginning Bowden cable transmission. In this configuration, the output handle for the operator is on the joint-side (Fig. 9.3, left). A transmission wrapping angle of about 360° is shown on the picture. Between the cable pulley on the joint-side and the output handle, again a torque sensor is integrated by strain-gages on the spokes of the pulley. This sensor is designed for a maximum torque of 2.5 Nm, with a sensitivity of 1.8 V/Nm. Its minimum resolution after AD conversion is slightly worse, at about 0.17 mNm. The joint-side of the BCD contains a second 500 pulse per revolution encoder. The mass of the joint-side of the BCD sums to about 0.15 kg at a volume of 64 cm^3. As can be seen in Fig. 9.3, the DC motor and cable capstan reducer are the same for this configuration.

9.2.4 Haptic loop controller implementation

The haptic loop controller is responsible for the timely exchange of data between the master actuator and the slave at a fixed rate of 500 Hz. It also implements the control algorithms of the system. The implemented control-loop resembles the one schematically illustrated in Fig. 9.4. Previous experiments presented in (Schiele et al. 2006b) had already shown superior quality of the force-feedback loop with a real slave, when a 4-channel controller similar to the ones proposed in (Lawrence 1993) or (Hashtrudi-Zaad and Salcudean 2002) is used.

With respect to the controller structures proposed in (Lawrence 1993) or (Hashtrudi-Zaad and Salcudean 2002), we do not consider master or slave impedances as

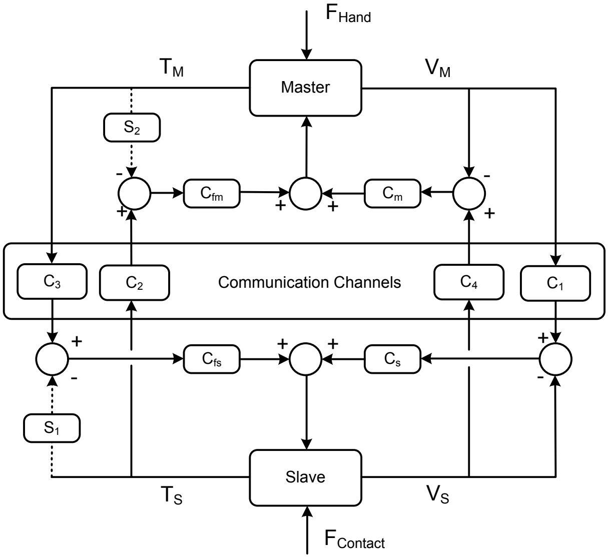

Fig. 9.4. General teleoperation controller architecture implemented in the haptic-loop simulation workstation. The 4-channels architecture was adopted from (Lawrence 1993). The impedance of the slave and master, has not been incorporated into the controllers C_{fs}, C_s (slave) or C_{fm}, C_m.

direct input to the force (C_{fm}, C_{fs}) or position (C_m, C_s) controllers. Those controllers are implemented as generic PID controllers, for maximum flexibility of use with the simulator.

The PID controllers were tuned differently for the DD and the BCD. The PI force controllers and the PD velocity controllers were tuned manually, to optimize for stability in hard contact. The transmission filters C_1 to C_4, as well as switches S_1 and S_2 can take values of 0 or 1, depending on the type of controller that shall be implemented. In our case C_1–C_4 are all equal 1.

Local force-control was enabled for both actuators by enabling switches S_1 and S_2. The torque commands from the slave to the master were scaled to reach a maximum continuous output torque on the master side of about 0.5 Nm during a strong contact.

9.2.5 Slave joint simulator and visualization client

A screen-shot of the virtual model of the slave is shown in Fig. 9.5. While the contact simulation is implemented on an x86 running a real-time version of Linux, the visualization client runs on a normal Windows PC. The contact simulation makes use of the Open Dynamics Engine (ODE) and is implemented as an embedded system, which keeps most computational resources free for the collision detection, collision response and implemented slave dynamic computations. Contact between the slave output-bar (shown in Fig. 9.5) and the wall is simulated by a spring-dashpot parallel system. All simulation parameters can be set via configuration scripts on the joint simulator.

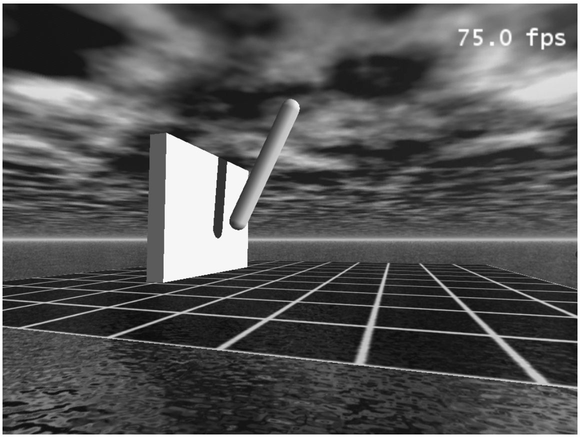

Fig. 9.5. Screen-shot of the visualization client displaying the slave joint output and the virtual wall used for contact simulation. Contact modeling is performed by the Open Dynamics Engine (ODE), while the visualization is implemented in OpenGL

9.3 Method

The haptic performance comparison between the DD and BCD master actuator was performed by manually moving the output handle of the master joint through a set of motion sequences typical for haptic applications (about 0–2 Hz). Such sequences were (1) free motion, (2) motion into contact, as well as (3) mixed free and contact movements. Thus, testing was preliminary and not performed over a large frequency band, e.g. by automated multisine frequency input. During all movements, the master position X_M, torque T_M as well as slave position X_S and torque T_S were measured at 2 ms intervals. During experiments with the DD actuator, the motor encoder and the motor-side torque sensor were used (corresponding to Fig. 9.1), while during measurements with the BCD actuator, the encoder as well as the torque sensor on the joint-side of the master actuator setup was used. Measurements of the BCD actuator were repeated for transmission wrapping angles ranging from 0–270 Deg., in steps of 30 Degrees. The cable system was not preloaded, while slack of the cable on the pulleys was avoided during installation.

The torque and position tracking capability of both actuators is analyzed by graphical plots, as well as by determining correlation with the slave data, which indicates the degree to which the master and slave measures are related. Root mean square (RMS) error is calculated for position tracking, not for the torques due to the scaling. Residual friction of the DD as well as for the BCD drive for multiple cable transmission wrapping angles is determined and compared. The maximum achievable contact stiffness of the two drives for all configurations is analyzed.

9.4 Results

9.4.1 Torque and position tracking capability

The torque and position tracking capabilities of the Direct Drive master and the Bowden Cable Drive master are depicted in Fig. 9.6. It can be seen in the left drawing of (a), that the DD actuator torque tracks the slave torque well in the three contacts, despite the forced offsets of maximum torques. The DD position tracking is shown in the right illustration of Fig. 9.6 (a).

The visible overshoot of the X_M position shows that the operator pressed stronger than the maximum torque that could be delivered by the drive.

For the BCD actuator, Fig. 9.6 (b) shows similar graphs for contact torque tracking in the left and position tracking in the right illustration, for a transmission wrapping angle of 0 Degrees. In both cases, for DD as well as for BCD, no oscillations can be seen during the contact situation, which shows good stability of both systems. On the right drawings in Fig. 9.6 (a) and (b), it can be seen that during free movement, a residual friction force T_{FM} remains for both master actuators systems.

In order to analyze the tracking behavior of both actuators better, we show scatter plots of T_S / T_M and X_S / X_M in Fig. 9.7. Pearson's correlation coefficients were determined for the data pairs, in order to get a quantitative measure of the noisiness of the respective tracking relationship between master and slave. The correlation coefficient of T_S and T_M for the DD is $r_{DDT} = 0.9951$, and $r_{DDX} = 1.0$ for the position tracking (Fig. 9.7 a).

The RMS position error is $E_{DD} = 0.02$ Rad. For the BCD, the correlation coefficients for the torque tracking are, for wrapping angles from 0–270 Degrees in steps of 90 (Fig. 9.7 b): $r_{BCDT0} = 0.9885$, $r_{BCD90} = 0.9913$, $r_{BCD180} = r_{BCD270} = 0.9829$. For the same wrapping angles, all correlation coefficients of X_S / X_M are equal to 1.0. The RMS posi-

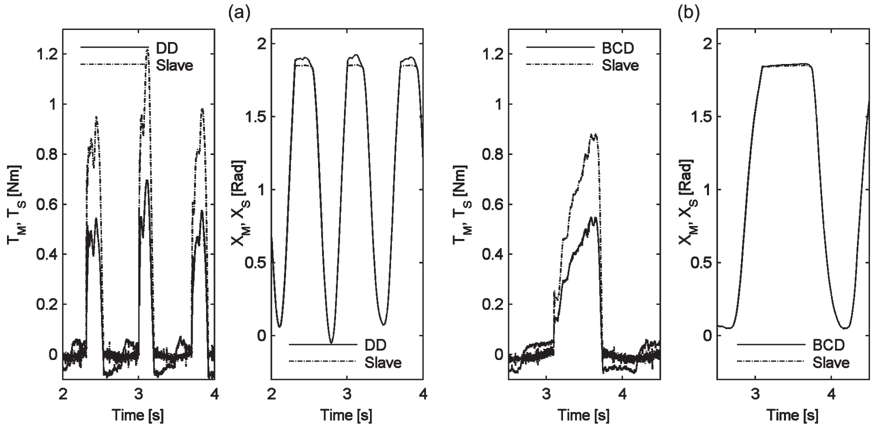

Fig. 9.6. In (a) the typical position and torque tracking capability of the Direct Drive (DD) actuator is shown. Note that the torque T_M was scaled down w.r.t T_S intentionally. In (b), the same characteristic is shown for the Bowden Cable Drive (BCD) master.

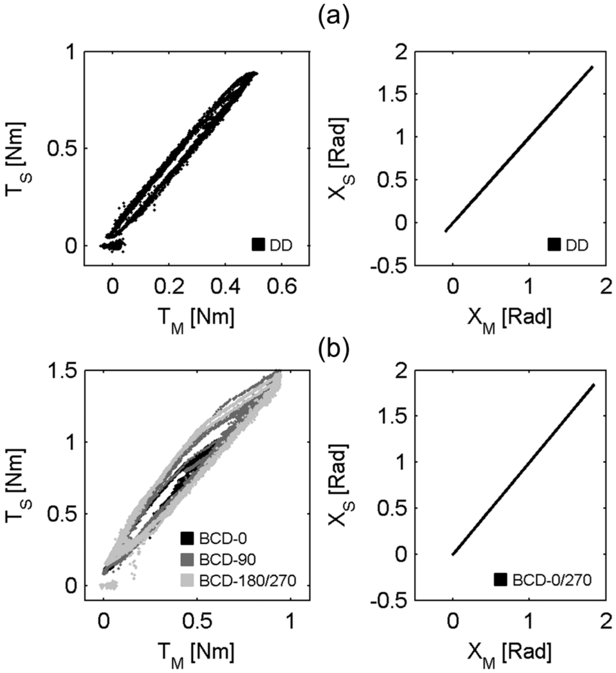

Fig. 9.7. Contact torque of slave T_S shown over contact torque of master T_M, as well as slave position X_S over master position X_M in (a) for Direct Drive actuator (DD). In (b) for the Bowden Cable Drive actuator (BCD). Scatter plots are shown for different wrapping angles 0, 90 and 180–270 Deg of the transmission lines. For all graphs, the Pearson's Correlation coefficients were determined to assess the noisiness of the tracking.

tion tracking errors for all wrapping angles from 0–270 Deg. are: $E_{BCD0\text{-}270} < 0.001$ Rad. From the slopes of the left illustrations depicted in Fig. 9.7 (a) and (b), the scaling of the master torque with respect to the slave torque can be seen.

9.4.2 Residual friction torques in cyclic free movement

The residual friction torque T_{FM} remaining in the master actuators is depicted in Fig. 9.8 for the DD, and the BCD in all transmission line configurations. Boxplots show the spread of the absolute friction torque $|T_{FM}|$ over an entire experiment per condition. The box indicates with its lower and upper horizontal lines the lower and upper quartile of the measured values. The median is indicated as bar within the box. The mean is indicated by a cross. The whiskers show the spread of the rest of the data. All values further away than 1.5 times the inter-quartile range are shown as outliers, by a plus symbol. The friction loads are not normally distributed. The BCD residual friction at 0 Deg. wrap angle is higher (0.046 ± 0.015 Nm) than the DD residual friction (0.041 ± 0.021 Nm). The mean friction for the BCD is rising from 0 to 270 Deg. of cable wrap angle, up to the maximum of 0.06 ± 0.018 Nm at 270 Degrees.

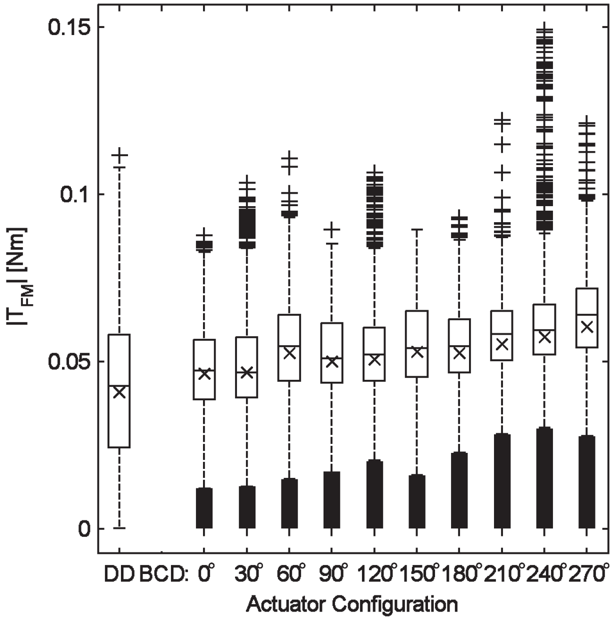

Fig. 9.8. Boxplots showing the absolute measured residual friction $|T_{FM}|$ in the Direct Drive (DD) actuator and in the Bowden Cable Drive (BCD) actuator for cable transmission wrapping angles from 0–270 Deg.

The rising friction loads over increasing cable wrap angle is not monotonically increasing, but a clear trend towards higher friction load at larger wrapping angles can be seen.

9.4.3 Contact stiffness in hard contact situations

The maximum achievable contact stiffness of the DD master actuator with respect to the simulated slave stiffness is shown in Fig. 9.9 (a).

The scatter data depicts the true measurement points, whereas the lines are linear fits through the data, which are used to determine the approximate stiffness values. The DD actuator can render a contact stiffness of about 41.3 Nm/rad. The measured contact stiffness at the slave reaches to about 73 Nm/rad. Fig. 9.9 (b) shows the measured values attained for the BCD master actuator. With 0 Deg. of transmission wrap angle, the actuator reaches a contact stiffness of about 24 Nm/rad. The contact stiffness increases with higher cable transmission wrapping angles. At 180 Deg., it is 31 Nm/rad and at 270 Deg. of transmission deflection it amounts to about 36 Nm/rad. Scattered measurement data is only shown for 0 Deg. cable wrap angle, to keep the illustration as clear as possible. The other lines in Fig. 9.9 (b) are the linear fits on the measured data. The vector norms L_P of the residual errors between fit and measured data indicate the goodness of fit (L_P: Slave: 0.73; DD: 1.18; BCD0: 3.61; BCD180: 10.99; BCD270: 12.12).

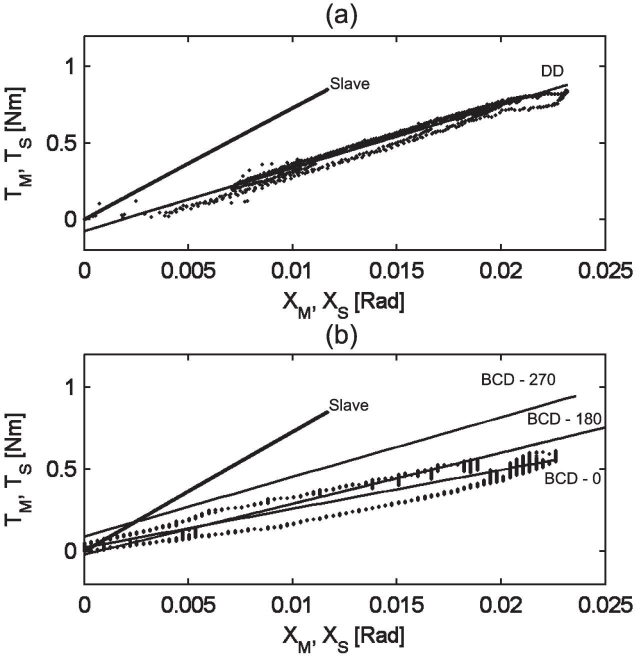

Fig. 9.9. Maximum contact stiffness reached with the Direct Drive actuator (DD) in (a) and with the Bowden Cable Drive (BCD) actuator in (b) for different wrapping angles of the cable transmission (0, 180, 270 Deg.). In (a) scatter data is shown with a linear fit for the stiffness. In (b), the original data is only shown for the BCD-0 Deg. condition, for clarity of display.

9.5 Discussion

We can see that the Bowden Cable Drive master actuator is a valid option for integration in a wearable haptic system. By changing the mechanical joint structure of a wearable robot to contain only the output mechanism of the Bowden Cable Drive actuator, the mass can be reduced from 0.95 kg to 0.15 kg. The power density of the movable device is thereby increased by 5.2 fold, from 6.0 mNm/cm^3 (DD) to 31.25 mNm/cm^3 (BCD). The specific power per joint can be raised by even 6.4 times, from 2.1 Nm/kg (DD) to 13.33 Nm/kg (BCD). It is shown that for torque and position tracking, the BCD actuator has a similarly good performance than the DD actuator. The correlation analysis confirms good linearity with only little torque and position noise and confirms that both master devices can work in a stable haptic simulation loop. Free motion friction of the BCD actuator is higher than the one of the DD. The maximum difference for the worst case scenario, however, is only 60 mNm. For a cable transmission that is wrapped by 270 Deg. This difference seems hardly relevant for choosing the better drive for implementation into an arm exoskeleton. Since the human torque sensing resolution for human arm joints is likely above this limit (Tan et al. 1994), we can consider the tracking performance of the two actuators similar. The increase in free movement friction was expected. However, the local force control loop around the BCD actuator compensates the added friction of the cable system well.

Interesting effects are shown with regard to the maximum contact stiffness that can be rendered by both actuators. The DD actuator renders a higher contact stiffness overall. The BCD has a variable contact stiffness that depends on the wrapping angle of the cable transmission. The range from 24–36 Nm/rad seems acceptable for a wearable haptic master and the difference between the two actuators could hardly be felt. Interestingly, the maximum contact stiffness of the BCD increases with increasing wrapping angle of the cable transmission. This might be due to increasing pre-load of the transmission that, in turn, increases Coulomb friction and stiffness of the cable, as explained in (Schiele et al. 2006b). Results indicated in (Diolaiti et al. 2006) can be used to exploit these effects. It is reported there, that additional Coulomb friction and viscous damping in a master device can help to stabilize a telemanipulation system. This could open a way to improve our BCD controller. By increasing pre-load of the cable system by the correct amount, we should be able to operate the device with higher force gains that could result in higher contact stiffness rendered stably. However, for this, a model of the master actuator is necessary. We will leave this to future research.

In summary we can state the following. If we consider that typically an exoskeleton contains up to 7 or more actuators, the main benefit of the BCD lies in increasing power density, specific power and reducing mass and inertia of the mechanically moving system. At the expense of maximum contact stiffness that can be rendered. Reflected inertia reduction can be achieved for BCD actuators if larger actuators are used.

9.6 Future work

In order to optimize the BCD controller setting, a full dynamic identification of the setup should be performed, to allow a more in-depth analysis of maximum position and force bandwidth, and cable transmission system behavior. Furthermore, an experiment should be conducted to investigate whether human operators are sensitive to the variation between Direct Drive and Bowden Cable Drive.

9.7 Conclusion

(1) Implementation of a Bowden Cable Drive actuator on an exoskeleton joint can increase the available power density by more than 5 fold per joint and the specific power by more than 6 fold, with respect to the tested low reduction Direct Drive actuator.
(2) The performance in terms of position and torque tracking of the slave in a haptic master–slave application is nearly identical for BCD and DD master actuators.
(3) The contact stiffness that can be rendered by the presented DD master joint is higher than the one of the BCD.
(4) The contact stiffness of the BCD increases if the wrapping angle of the cable transmission increases.

(5) Residual friction in the master actuator is worse for the BCD with at most 60 mNm difference with respect to the tested DD at 270 Deg. wrapping angle of the Bowden cable transmission. This can be considered negligible from a human sensing point of view, at least for the joints of the human arm.

Part V

Exoskeleton Prototypes

Chapter 10: The ESA Human Arm Exoskeleton for Space Robotics Telepresence

A. Schiele, G. Visentin
In Proc. of 7th International Symposium on Artificial Intelligence, Robotics and Automation in Space (i-SAIRAS), Nara, 2003

Chapter 11: The Ergonomic EXARM Exoskeleton

A. Schiele,
Chapter 8.3, Invited Contribution: *Wearable Robots: Biomechatronic Exoskeletons, J. Pons Ed., John Wiley & Sons, 2008, pp. 248–255*

Chapter 10

The ESA Human Arm Exoskeleton for Space Robotics Telepresence

A. Schiele, G. Visentin

In *Proc. of 7th International Symposium on Artificial Intelligence, Robotics and Automation in Space (i-SAIRAS), Nara, 2003*

This Paper describes the design of the ESA Human Arm Exoskeleton, which has been developed to enable force-feedback telemanipulations with redundant robotic arms. It is described, how several shortcomings of previous telemanipulation systems were eradicated, to meet the system requirements for a lightweight, easy wearable and comfortable system.

The patented novelties towards prior arm exoskeletons are enlightened, and the methodology is shown, according to which the system was designed.

The prototype, which has been developed at ESTEC is described in detail, outlining the special features of the design.

10.1 Introduction

Future Space-missions, will make use of advanced humanoid-like robots. These multi-DOF robotics are envisaged as crew assistants for Extra-Vehicular Activities (EVA) on the International Space Station or as explorers / first colonizers on planetary surfaces. The advantage of these systems lays onto their ability to operate in conventional robot programmed modes as well as in telemanipulation and telepresence modes.

Telepresence allows the execution of tasks in highly unstructured environments, where human judgment, real-time motion coordination and handling ability are needed. In a typical application scenario, a humanoid-like robot maneuvers in a non-live hostile environment, while being remotely controlled from a human operator situated in a save location. Such scenarios could be deep-sea robotics applications, offshore and de-mining operations, hazardous and nuclear materials treatment etc.

Thereby, vision, touch and forces are the senses, which, if fed back from these working environments, enable precise perception of the dynamics and geometrical constraints of operation. As a result, the human operator feels like being in place of the robot.

Feedback mechanisms are required therefore, to immerse the human operator in the robotic working environment. In many telerobotics applications, the hand is the only interface to which force and touch feedback is applied, mostly by means of hand exoskeletons or tactile joysticks. However, for applications where entire humanoid-like robots maneuver in complex, unstructured environments, it is necessary to be aware of the end-effector motion as well as of the arm configuration. Controlled nullspace motion can be essential to avoid obstacles. For that, feedback to the operator hands is insufficient, as no constraints, which affect robotic limb-motion can be perceived. Consequently, to implement whole-body haptic feedback and to command accurate limb-motion, a device, strapped around the operators limbs is needed.

The ESA human arm exoskeleton is such a device (Fig. 10.1).

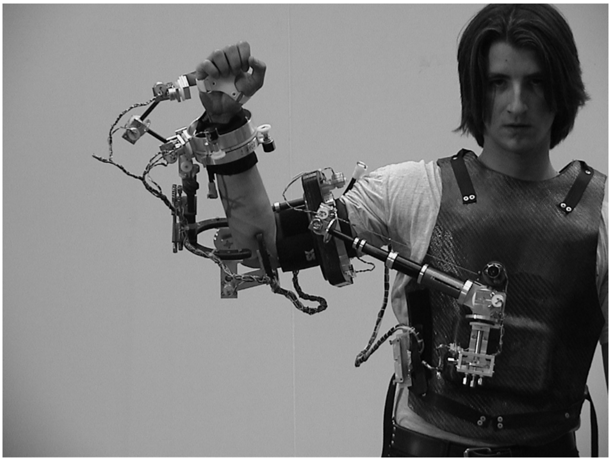

Fig. 10.1. ESA Human arm Exoskeleton as worn during operation (Feedback actuators detached)

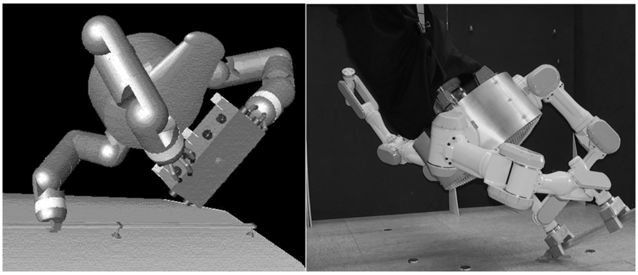

Fig. 10.2. Simulated Eurobot operating on ISS module (left). Eurobot prototype crawling along a structure in ESTEC Robotics Lab (right).

It is being developed in connection with the "Eurobot" concept, which foresees of a humanoid servicing robot, designed to work on the exterior of the International Space Station, allowing teleoperation from the pressurized inside of the Station.

Using remote tactile feedback to control external robotics, Astronauts can fulfill more complex handling operations as if being packed into their bulky space suits during EVA. Moreover, avoiding EVA greatly reduces the danger for the crew, saves preparation time, extensive crew training and finally, overall mission costs.

Especially for unexpected emergencies, the Eurobot concept enables to quickly interact with the outside environment (Fig. 10.2). Eurobot will be equipped with 3 arms, kinematically similar to human arms (seven degrees of freedom (d.o.f.) each, 21 d.o.f. in total). The astronauts will be outfitted with video goggles, force reflecting hand exoskeletons and the ESA arm exoskeleton to feel like being in place of the robot.

During telemanipulations, the robotic arms shall be slaved to the arm exoskeletons (Fig. 10.3). The human arm pose, sensed by the exoskeleton joint-sensors, is fed to a robot controller, which drives the robot arms to the corresponding pose. Furthermore, the Exoskeleton shall feature actuators connected to its joints, to allow exerting torque on the operator arm such, that:

- The operator perceives forces, which the robot arm experiences in executing the commanded motion.
- The operator perceives intrinsic or artificially introduced limitations.

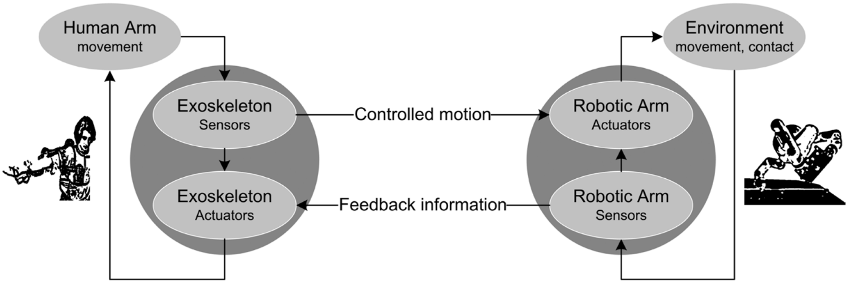

Fig. 10.3. Typical Exoskeleton Control Scenario

Medical & Health Sector, Hospitals, Medical Research Centres	**Energy Providers, Oil Industry**
• Rehabilitation (passive gymnastics) • Strength enhancement • Active orthesis	• Nuclear • Offshore • Extreme environment tasks
Entertainment, Movie, Fitness Industry	**Hazardous Material Handling, Disposal Industry**
• Entertaining fitness (e.g. with video goggles • Natural animation of virtual characters • Accessory for video-gaming	• Bomb defusing • De-mining operations • Biological decontamination

Table 10.1. Possible terrestrial applications for the ESA exoskeleton

Due to its innovative design, the ESA exoskeleton can additionally be used to enable new goods and services outside the Space Domain. Wherever telepresence technology already exists, this arm exoskeleton enables new applications (Table 10.1).

10.2 A brief review about drawbacks of prior exoskeletons

The main goal during the design of the exoskeleton was, to overcome the known shortcomings of comparable systems:

- Inability to mimic entire range of human arm movements (i.e. shoulder, elbow, wrist)
- Limited adjustability (5th – 95th percentile Male population)
- Inability of being wearable systems
- Not permitting long-time operations due to high weight

Why these points are important, is described hereafter: Prior exoskeleton systems restrict the total possible range of human arm movements, due to the bulkiness of their mechanics. Huge mechanisms, mostly situated at the top of the shoulder, limit the natural workspace of the human arm. The bulkiness of the mechanics seems to result from the need to keep the mechanism joints precisely aligned to the corresponding human arm joints. These alignments are necessary for all exoskeletons featuring 7DOF, while copying the kinematics structure of the human arm. Unfortunately, during human arm movement, the physiological joint axes do not remain stable as in a robot. Taken our multifaceted shoulder-joints as an example, we can say that keeping an attached mechanism accurately aligned to the real joints during shoulder-girdle movements seems unfeasible. Exoskeleton designers therefore constructed more complex and heavy mechanisms to cope with these problems. Unluckily, such systems cause a heavily disturbed master-arm movement during feedback operations, which creates quite uncomfortable feelings for the operator.

A further major disadvantage of those exoskeletons is the following: Aligning such mechanics requires knowing the precise positions of the related joints in the human arm. This implies determining the human joint axes of each new user, which makes adjustment to different users very difficult and time consuming.

All prior exoskeleton systems are non-wearable systems, which means that they are somewhere fixed outside the human body. Movements like bowing down, turning around and walking, which might be necessary for operational freedom, are therefore constrained. Moreover, during operations in reduced-gravity, such as inside the Space Station, a non-wearable force-feedback system creates reaction forces onto the operator body (A force-feedback joystick can already push away the astronaut from the control station). It is a fact that such impacts evoke major problems for intuitive handling operations. Currently, this is solved by strapping the astronaut's limbs and bodies somewhere to the control stations.

10.3 Design requirements

Resulting from these disadvantages, the new ESA exoskeleton was designed to meet the following primary requirements:

- Range of human arm motion shall be fully applicable.
- Mechanism shall be easily adjustable for the 5th to 95th percentile of male population.
- The Exoskeleton shall be a wearable system.
- A lightweight design shall keep the total mass below 10 kg.
- Actuators for torque-feedback shall be implemented in the wearable part.
- Actuation by the means of cable transmissions to reduce the weight of the arm-segment.

10.4 Design methodology

For the design of the exoskeleton, a three-dimensional computer model of the human arm was created first, to allow verifying any proposed mechanism.

Of course, the purpose of the model was not, to exactly mimic the physiological motion of the limbs and bones of the human arm, but to mimic it in terms of resulting movements. Realistic movements of this model were then recorded as trajectories in Cartesian Space. Afterwards, during kinematics simulations, robotic models of proposed exoskeleton mechanisms were forced to follow these trajectories while being attached to the model of the arm. A proposed mechanism was considered feasible, when no collisions between the simulated body segments occurred. Furthermore, it had to follow the trajectory without reaching into singularities, which disturb smooth motion.

10.5 Approach

Thus, the human arm was simulated in a computer as a serial link manipulator, whose kinematics was described by Denavit-Hartenberg Parameters.

To determine these parameters, we had to understand, how the joints in the real human arm are articulated, how long the involved body segments are and how these

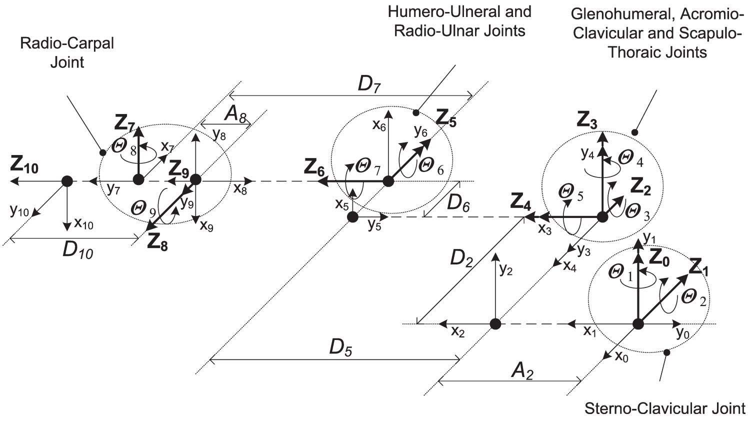
Radio-Carpal Joint
Humero-Ulneral and Radio-Ulnar Joints
Glenohumeral, Acromio-Clavicular and Scapulo-Thoracic Joints
D_7
A_8
Z_7
Θ_8
x_7
y_8
x_6
y_6
Z_5
Z_3
y_4
Θ_4
Z_{10}
Z_9
y_7
x_8
Z_6
Θ_7
Θ_6
Θ_5
Z_2
Θ_3
y_{10}
x_{10}
Θ_9
y_9
x_9
x_5
y_5
D_6
Z_4
x_3
D_{10}
Z_8
y_3
x_4
y_1
Z_0
Z_1
D_2
y_2
Θ_1
Θ_2
x_2
x_1
y_0
D_5
x_0
A_2
Sterno-Clavicular Joint

Fig. 10.4. Kinematics of human arm.

work together during motion of the arm. However, these human factors are difficult to find and most resources referred to old studies, such as (Chaffin and Andersson 1984) (Roebuck et al. 1975) and (Clauser et al. 1969).

To obtain link length data, anthropometrists dissected cadavers and estimated the static location of joint centers-of-rotation. The link length was then defined as the length along a segment's main axis from joint to joint. These resulting values were statistically regressed onto the subject's stature. Thus, link length values are given as percentiles of the population and as proportions of stature.

The standard error of this data is estimated to be approximately 1.0 cm for the bone-length estimates. The use of these statistical data, allowed us to model the proportions of a human arm and to identify the DH Parameters for the kinematics description (Fig. 10.4).

In terms of link length, our model is based on values, valid for the 5th to 95th percentile of U.S. male population. A stature of 1.80 m was chosen for the beginning. At a later stage, however, the resulting exoskeleton design was tested with a smaller sized and a bigger sized model of the human arm (representing 5th and 95th percentile respectively).

For the shoulder girdle, five degrees of freedom were needed, two representative for the attachment of the human arm on the sternum (Sterno-clavicular Joint) and three to describe the complex movements of the glenohumeral, acromioclavicular and scapulothoracic joints.

The elbow motion was simulated with two d.o.f., one for flexion and extension occurring in the humero-ulnar joint, and one for forearm pronation and supination, which takes place in the radio-ulnar joints.

For the wrist, two joints were implemented, to simulate the ellipsoidal joint, whose perpendicular axes have an offset of about 2 cm.

Additionally to creating this kinematics description, the functional anatomy of the upper limb system was studied, to be able to implement the limb-motion as realistic as possible. Joint mobility values, such as typical joint limits and ranges of movements

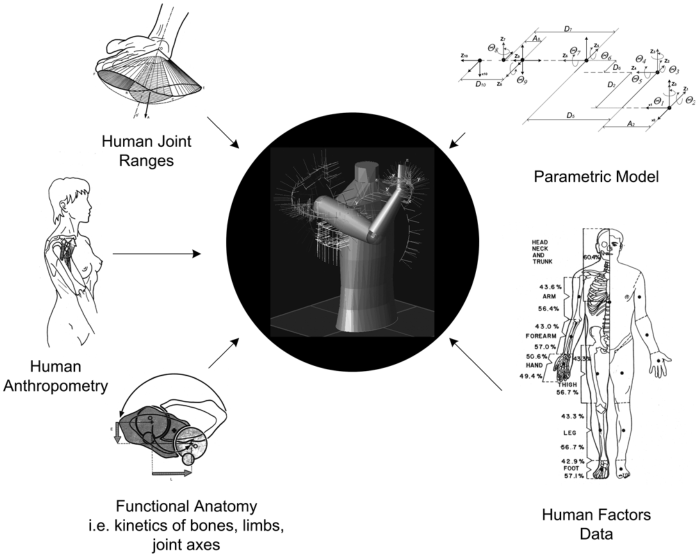
Human Joint Ranges
Parametric Model
Human Anthropometry
HEAD NECK AND TRUNK
60.4%
43.6%
ARM
56.4%
43.0%
FOREARM
57.0%
50.6%
HAND
49.4%
43.3%
THIGH
56.7%
43.3%
LEG
66.7%
42.9%
FOOT
57.1%
Functional Anatomy
i.e. kinetics of bones, limbs,
joint axes
Human Factors
Data

Fig. 10.5. Information needed to realistically simulate human arm motion.

were taken from (Kapandji 1992). Functional anatomy describes exactly the movements of the articulated limbs, during major arm movements. Trajectories of such typical movements where then simulated and recorded in Cartesian Space (Fig. 10.5).

Typical simulated movements were: (1) **Shoulder movements**: Circumduction, Abduction and Retroversion according to "Codeman" Paradoxon, Flexion and Extension, Horizontal Ab/Adduction. (2) **Elbow movements**: Flexion and Extension, Pronation and Supination. (3) **Wrist movements**: Flexion and Extension, Abduction and Adduction During the subsequent kinematics simulation, the proposed mechanism had to be reconfigured many times, to optimize its performance together with the simulated arm. Especially shoulder circumduction turned out to be a difficult task for the exoskeleton, not to reach into singularities. Fig. 10.6 describes the final configuration of the accepted mechanism.

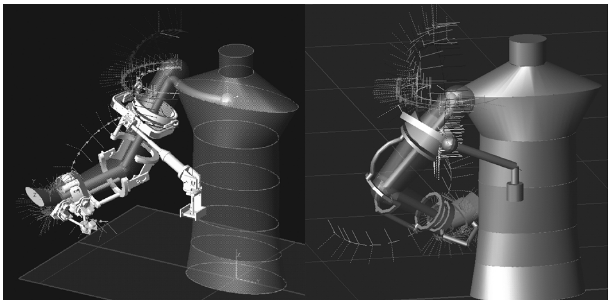

Fig. 10.6. Chosen structure for Exoskeleton. Detailed designed Exoskeleton on opaque torso (left). Preliminary test-model (right)

10.6 Results from mechanism design

The outcome of the simulations was the following:

- The exoskeleton performs best, if its kinematics structure is entirely different from that of the arm.
- The optimal position to fix the base of the exoskeleton is at the chest of the operator.
- A prismatic joint enables use of the entire human arm workspace.
- A spherical joint on the attachment of the mechanism on the upper-arm prevents driving into dead-lock positions during long movements.
- Three parallel kinematics for the shoulder, elbow and the wrist, are the optimum solution for combined man-machine motion.
- If the three parallel kinematics are not adjusted to the human joints, the mechanism still works fine.

10.7 Description of the prototype

The ESA arm exoskeleton is fixed on a carbon-fiber chest plate, which resembles half an armor top. The plate is secured to the human chest by straps (Fig. 10.1). The carbon-fiber plate serves as structural base for the chain of joints that articulate the sleeve. It provides a stiff reference for the exoskeleton's base. Most of the mechanical parts are machined aluminum parts, whereas the large structural parts to enclose the operator's arm were built of carbon-fiber reinforced plastics. This reduced weight while keeping stiffness of the overall structure. To reduce friction, we equipped every exoskeleton joint with ball bearings. Consequently, the mechanism pursues every human arm motion unobtrusively. A back plate, which holds the feedback motors, is currently in the design phase. The joints can be actuated from that motors by a series of flexible tendons. Altogether the exoskeleton master-arm comprises 16 degrees of freedom. Every axis is equipped with an angular sensor to gain information about the joint-angles. The joints are grouped in three major sub-assemblies: (1) The shoulder-assembly (6 d.o.f.); (2) The elbow-assembly (4 d.o.f.); (3) The wrist-assembly (6 d.o.f.).

Whereas these three assemblies build up one single mechanism (Fig. 10.7), they will be separately explained in more detail.

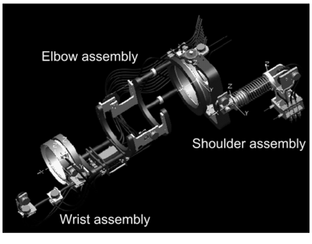

Fig. 10.7. The three exoskeleton assemblies

10.7.1 The shoulder assembly

The shoulder assembly includes six axes, five revolute and one prismatic. Thanks to the arrangement of the joints, the movement of the exoskeleton does not limit natural shoulder-girdle movement, neither in extent nor in dexterity. Fig. 10.8 shows the shoulder assembly as it is attached to an operator body.

Whereas the proximal end is attached to the chest-plate, the distal end of that mechanism is located at the base of the upper-arm, where it is secured by an inflatable air cushion (Fig. 10.9). This cushion, made of silicone rubber can be inflated through the attached squeeze pumps. When inflated, the ring creates a non-slipping fixation between the human arm and the outer aluminium rings, which constitute the fixations for the exoskeleton mechanical structure.

For applying a feedback torque to the user arm, joints 1 and 2 can be actuated by motors. Activation is planned to takes place remotely, by pulling tendons, which are fixed with pulleys on the joint-axis. The motors will be relocated to a plate, which is attached to the back of the operator. The prismatic joint consists of a telescopic beam, which is extended by a preload spring. A tendon, attached to the inside tip of the telescopic beam and running through it, forces the telescope to collapse by counteracting the extension spring. Joints 4 and 5 are purely passive joints. Joint 6 can be actuated and is used to enforce the roll rotation of the upper-arm. Joints 4, 5 and 6 have their axis intersecting in a point, which allows them to act as a single spherical joint articulation at the distal end of the first assembly (Fig. 10.10).

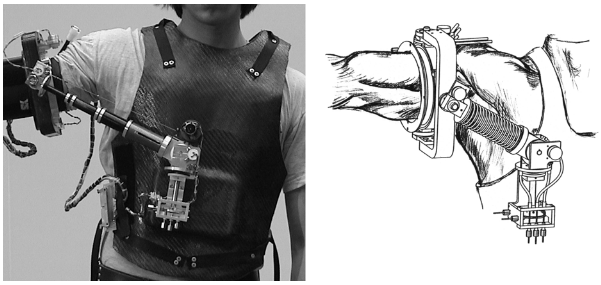

Fig. 10.8. Shoulder assembly attached to human operator (left: Exoskeleton Prototype, right: Artist impression)

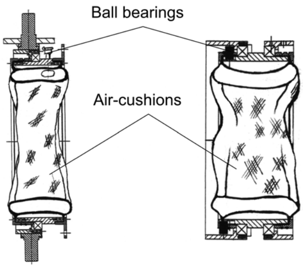

Fig. 10.9. Section-cut of Exoskeleton fixations on arm. (left: upper arm fixation, right: forearm fixation)

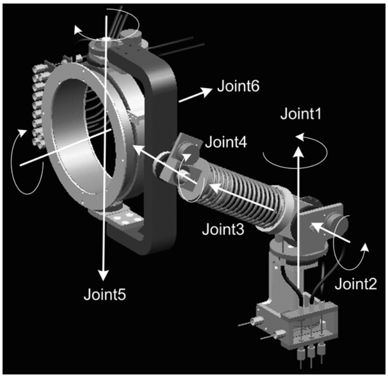

Fig. 10.10. Front view on the shoulder-assembly (3D Catia model)

10.7.2 The elbow assembly

The elbow-assembly comprises 4 axes and is attached to the distal end of the shoulder assembly (Fig. 10.11). Starting from the left, two twin adjustable-length telescope beams provide the means to adapt the length of the exoskeleton to the human upper arm. The length can be regulated by adjusting two screws, one at each beam. For the entire exoskeleton, no other adjustment is necessary. The first joint is a tendon-actuated revolute joint, which will be able to feed back torques to enforce flexion or extension in the human elbow joint. The second joint (prismatic), and the third joint (revolute) are passive joints and compensate alignment errors. These passive joints guarantee accurate sensing and undisturbed force-reflection to the elbow. The distal end of the elbow assembly contains another inflatable air cushion to attach the exoskeleton on the forearm and comprises another revolute joint (Fig. 10.9 left). The actuation of the 4th joint can enforce forearm pronation and supination.

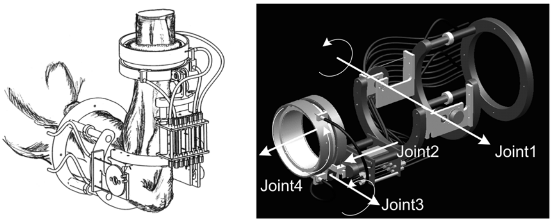

Fig. 10.11. Elbow assembly. (left: Artist impression of attached assembly, right: 3D Catia model showing the joint axes)

10.7.3 The wrist assembly

The third part of the exoskeleton features 6 axes. The proximal end of the assembly is also attached to the forearm-air-cushion and the distal end is fixed on a hard-plastic glove. Once more, some passive joints have been integrated. In the top-view, three revolute joints 3, 4 and 5 can be seen (Fig. 10.12 right). Whereas joints 3 and 5 are purely passive, two tendons can actuate joint 4. This enforces wrist abduction and adduction,

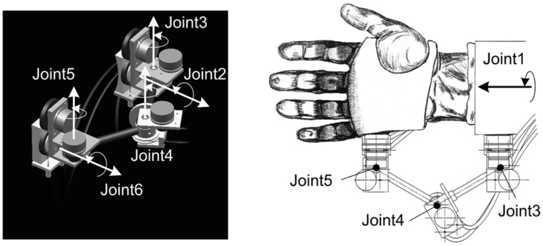

Fig. 10.12. Wrist assembly. (left: 3D Catia model showing the joint axes, right: artist impression of attached assembly

causing passive movements in joints 3 and 5. If the tendons actuate joint 4 clockwise, abduction is enforced. As soon as the tendons drive joint 4 counter-clockwise, adduction is enforced. To understand how torque is exerted to wrist flexion and extension, the isometric-view will be helpful (Fig. 10.12 right). Imagine joints 2 and 6 both tendon actuated. If, both joints turn clockwise, the attached exoskeleton links will drive the human wrist upwards, (conversely counter-clockwise rotation drive downwards) or, if both joints are blocked, no wrist flexion can occur. As the human wrist is not spherical but an ellipsoid joint (two main axes not striking trough one common point), joint 1 needed to be introduced, to compensate the eccentricity of any combined adduction and flexion movements.

10.7.4 Tendon actuation

Actuation torque shall be remotely transmitted using cable tendons, routed along the exoskeleton structure from the motors, sitting on the back chest-plate, to each active joint. For the tendons 7x19 multi stranded 1 mm diameter wire cable was selected to minimize bending friction and bear loads up to 50 Nm. To effectively transmit torques with a cable tendon transmission, the cables must be preloaded to half of their working load, due to elasticity. The detailed implementation is still under investigation. All rotational joints foreseen for actuation have two tendons each, allowing clockwise and counter-clockwise motions (Fig. 10.13). The tendons will be routed on the exoskeleton through flat-wire spiral sleeves. The guidance-length of these flat wire spirals can be changed with respect to the tendon length, which can preload the tendons running through.

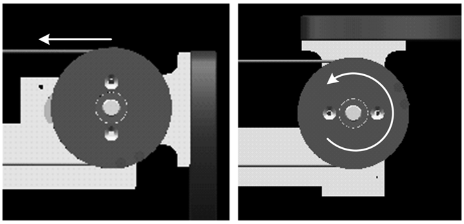

Fig. 10.13. Joint actuation principle

10.8 Novelties

A major innovation of the ESA exoskeleton stands in the approach to kinematics. There is no attempt to imitate the human shoulder, elbow or wrist kinematics. In contrary, an alternative kinematics chain offering the same freedom of motion is bridged over the human joints. This chain and the human joints form a closed kinematics loop that:

(1) For the shoulder begins at the sternum, bridges over the claviscapular and glenohumeral joints and ends in the middle of the humerus bone.

(2) For the elbow begins at the middle of the humerus bone and ends at the middle of the forearm.

(3) For the wrist starts at the middle of the forearm and ends in the middle of the palm.

Even though the kinematics of the exoskeleton and the human arm are different, any posture of the human joints (i.e. shoulder-girdle, elbow, ellipsoid wrist joint) can be univocally determined by the corresponding posture of the exoskeleton. Advantages of this approach are:

- The weight of the system is not carried by the arm but by the thorax (hence the spine).
- The complete range of human shoulder, elbow and wrist motion will be possible, when the exoskeleton is worn.
- The exoskeleton joints are simpler and smaller.
- No major alignment between the human joints and any of the exoskeleton joints is needed.
- The Exoskeleton is a wearable system.

The second innovation will be the use of cable tendon transmissions, guided trough flat-wire spiral sleeves. This special use of tendon transmission allows relocating the drive units on the back plate of the exoskeleton where their weight is carried by the thorax. The result is an extremely light arm that can be driven by smaller drives.

The third improvement results from the combination of kinematics as well as the use of adjustable limbs and inflatable arm collars. This shall make it possible to adapt the exoskeleton to any human subject (5th – 95th percentile male population) by adjusting the length of only one Exoskeleton limb. Else, no alignments are required.

The first prototype of the exoskeleton, however, does not allow such diversity of users. The reason is the fixation on the upper-arm, which requires inserting the human arm in a large-diameter thin-section ball bearing. For very muscular or fat people, the diameter of 127 mm is too little to insert their arm. Thus, for the moment, not everybody can use the exoskeleton. The interaction will be studied in more detail.

10.9 Future work

At the moment we work on the control between Eurobot and the Exoskeleton. At this stage we try to telemanipulate one arm of Eurobot with the ESA Exoskeleton. Furthermore, currently the design of the back-plate carrying the force-feedback actuator is in its first stage. In the near future, the fixation on the upper arm will be re-worked, to allow the exoskeleton being worn by people with larger upper arm diameters. Also the telescopic mechanism will be re-designed, to provide higher torsion stiffness. A hand-exoskeleton will be integrated into the system, to allow telepresence operations of the entire arm and the hand.

Chapter 11

The Ergonomic EXARM Exoskeleton

A. Schiele

Chapter 8.3, Invited Contribution: *Wearable Robots: Biomechatronic Exoskeletons, J. Pons Ed., John Wiley & Sons, 2008, pp.248–255*

This Paper summarizes the design features of the ergonomic EXARM exoskeleton. It introduces the targeted application as man–machine interface for control of a space robot manipulator. Challenges for designing a device compatible with varying astronaut crew and for long duration task executions in space are outlined. The implementation status of the EXARM exoskeleton is presented. It's mechanical structure, as well as actuation and control approach are outlined.

11.1 Introduction

The ESA human arm exoskeleton, EXARM (Schiele and Visentin 2003a) (Schiele and Helm 2006) is being developed as a human machine interface for master–slave robotic tele-operation with force-feedback. The EXARM shall allow astronauts inside the International Space Station (ISS) to remote-control EUROBOT (Didot et al. 2006), a space humanoid robot, on the outside.

EUROBOT shall assist crew during maintenance on ISS, as well as support future manned or unmanned exploration missions to other celestial bodies in our solar system (e.g. Moon or Mars). In a first instance, however, EUROBOT will be dedicated to supporting extra-vehicular activities (EVA) on ISS. Depending on the application, the robot can be equipped with two or three redundant, 7 degree of freedom (d.o.f.) robotic arms. With respect to other space manipulators, such as the SRMS or SSRMS, each arm of EUROBOT is equal in function and size to a human arm. For ISS applications the third arm is used as a leg for fixing the robot to the exterior structure of the station. For planetary use, EUROBOT will have two arms only and will be supported by a movable, centaur-like, base. In both cases, a versatile set of end-effectors will be provided, that the robot can exchange for different tasks (e.g. assembly, inspection, transportation, etc.). Two different modes of operation are foreseen for the control of EUROBOT.

During autonomous mode, arm movement can be pre-planned and offline programmed. This mode is used to operate in well-defined, structured environments. Typically, EUROBOT will then handle orbital replacable units (ORU's), e.g. on ISS, that are equipped with robotically compatible interfaces. In that case, on-board hazard detection and obstacle avoidance will still be used.

During manual control mode, a more reactive force-feedback control based on master–slave teleoperation is envisaged. Force-feedback with a human operator in the loop allows operations in unstructured environments that are difficult to model a priori from ground. An example of an unstructured environment would be a regolithic or sandy planetary surface that is scattered with rocks. On ISS, for instance, unstructured environments are those that contain soft structures, such as Multi-layer insulation (MLI) panels, fluid lines, or similar. Those environments exist mostly on an active work-site, on which astronauts carry out maintenance, installation or repair tasks. But also during close cooperation of the remote controlled robot with an astronaut during an EVA, a sort of reactivity is required that can best be provided by a human that joins as a master into the control loop of the slave-robot. In manual control mode, the human operator can quicker adapt to the situation and react with faster recovery actions than any autonomous path-planning and re-planning algorithm today could provide. This mode is therefore foreseen for crew-assistance or for fast intervention in the case of contingency. In order to make the master–slave control mode as intuitive as possible for the astronauts, the EXARM exoskeleton was developed.

The exoskeleton senses the motion of the astronaut's arms and translates it to the robot arm. At the same time, the device feeds forces and torques back to the operator's arms. Such forces can for instance be measured from contacts of the robot with the real environment, or more likely, result from collisions of the robot with imposed virtual constraints. By those constraints, the robot end-effector and limbs can be kept in a safe work envelope at all times. This is important to restrict robot motion in the near vicinity of life-critical and sensitive hardware infrastructure. An exoskeleton provides significant advantages over other input devices, such as e.g. force-feedback joysticks. A key advantage is the possibility to control the robot end-effector in Cartesian Space, while also controlling its joint-space motion, or geometrical pose of the robot. This is an important asset for freely navigating in complex environments. Control of the pose of dexterous seven degree of freedom robots is otherwise difficult to achieve. In a pure Cartesian control, such robots exhibit a self-motion that is induced by its inverse kinematics algorithms. Seven degree of freedom robots have an infinite number of solutions for joint-space trajectories to reach a specific Cartesian location. In order to choose an appropriate solution, their iterative inverse kinematic algorithms optimize for a specific constraint, that is chosen by the developer. One constraint typically used is to avoid singular positions of the manipulator. Thus, during movement of the arm, the pose of the arm is altered in order to avoid the manipulators singularities. This pose adjustments induces the so called self-motion. The self-motion can drive the robot limbs into unwanted collisions with the environment. With an exoskeleton that controls the pose of the robot, forces and torques created on each robot segment can be translated as torque-feedback to the corresponding joints of the human arm. This gives the robot operators an intuitive understanding and feel of the robot configuration at all times.

The challenges for designing the EXARM exoskeleton resulted from its application scenario.

The device must be able to support long-duration commanding of the slave robot. An EVA supported operation on ISS lasting in the order of 6 hours is not unusual. Furthermore, EXARM needs to be used by a large range of users, with different statue and mass. Therefore, the exoskeleton has to be as “ergonomic” and “comfortable” as possible. Quick adaptability to varying user statues without requiring mechanical adjustments and software calibration was another desired feature for the exoskeleton. The design of EXARM followed a novel approach for ergonomic exoskeletons presented in (Schiele and Helm 2006). A new actuation principle was developed as well (Schiele et al. 2006b), in order to make the implementation of the ergonomic structure feasible from a practical point of view. The ergonomic properties of the exoskeleton will be detailed in the following paragraphs.

11.2 Challenges and innovation for an ergonomic exoskeleton

In general, any force or torque fed back from an exoskeleton to the user must be counteracted by the user body. When force or torque-feedback devices are used inside a reduced gravity (μ-G) environment, only body-grounded feedback should be used. Then, force or torque applied to the operator via the device will create an appropriate reaction force in the operator muscles. Such forces will always apply between body segments only. In non body grounded, fixed-base force-feedback devices, the forces or torques stemming from the slave can only be counteracted by the inertia of the entire operator body. As a consequence, when force feedback is applied, e.g. to the operator arm, his entire body will be set into motion. Such a force or torque-feedback would be highly counter intuitive. It would push away an operator, rather than helping him to interpret the correct contact situation of the remotely located robot with its environment. In contrast to most currently existing exoskeletons, the EXARM has been implemented as wearable, body-grounded device. The EXARM is designed as compact and portable system as well, because this gives more flexibility during operational use. After a typical operation with the exoskeleton inside ISS for instance, the device can be easily stowed away or transported to another station segment. A portable device will also not disturb the floating sensation that Astronauts are used to, during their stay in μ-G. However, the EXARM needed to be also compatible for 1-G use. This is crucial for development and testing on ground. Therefore, EXARM had to be as lightweight as possible. Lightweight structural materials, such as carbon fibre reinforced plastics (CRP) were employed. As mentioned above, another key challenge was to develop an exoskeleton that can fit a large range of user statues without requiring complex adjustment and calibration procedures. Astronaut crew statues lie within the 5th percentile Japanese female and the 95th percentile U.S. male population (1.49–1.90 m). Some previous exoskeleton developments contain mechanically adjustable limbs whose length can be changed for aligning the exoskeleton principle axes to the human joint axes. Alignment, however, of an exoskeleton to the human arm joints is difficult, as explained in detail in (Schiele and Helm 2006). Alignment is difficult because the positions of the human joint axes are not exactly known and because they change during movement of the joint. Furthermore, the axis positions vary between subjects. Should an exoskeleton be misaligned, interaction forces are created between the device and the human operator. Those interaction forces can be relatively large in magnitude (up to over 200 N), and contribute significantly to discomfort of the device. Moreover, those interaction forces can restrict the natural range of motion, the workspace, of the human arm. In order to avoid the disadvantages stemming from requiring alignment, the EXARM design was tailored to be independent of individual statues and biomechanics, within the range typical for astronaut crew. A large benefit from this design feature is the capability of the EXARM to be dressed on quickly to different operators. Dressing on and dressing off the exoskeleton takes not longer then about 30 seconds for an untrained person. This allows for the required fast intervention capability in contingent situations.

11.3 The EXARM implementation

11.3.1 Mechanical

The EXARM exoskeleton is a serial manipulator. It consists of 16 degrees of freedom in total, out of which only 8 degrees of freedom are to be actuated. The remaining 8 degrees of freedom are passive. The passive joints are for alignment compensation and are permanently free to move with the serial chain. Despite those non-controlled joints, the EXARM can be actuated fully, when worn by an operator. Then it resembles a closed parallel loop robot, together with the human arm. This tolerates existence of passive joints in the structure of the exoskeleton. EXARM can thus be controlled and transmit

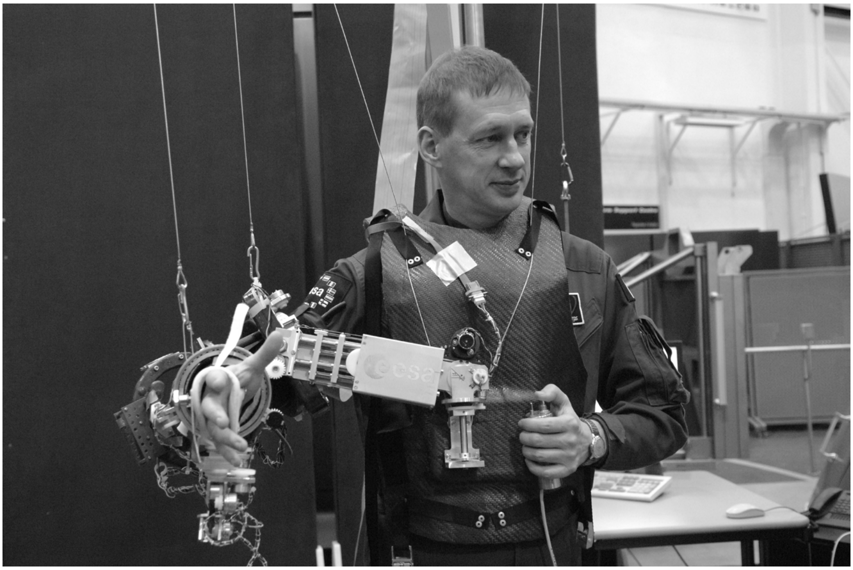

Fig. 11.1. The ESA ergonomic exoskeleton worn by ESA Astronaut Frank De Winne during an evaluation session

torque to all human joints on the right arm, from the shoulder to the wrist. The base of the exoskeleton is attached to a chest-vest. The structure is fixed on metal-inserts implemented the CRP sheet of the vest (Fig. 11.1). Next, the exoskeleton is attached on the upper-arm and on the forearm of the operators, by means of inflatable air-cushions. At the most distal tip, the device can be secured on the palm with an orthopedic glove. The operator's fingers are free to move. This allows for implementation of a simplified grasping interface later on.

The upper- and forearm attachments allow rotation of the limbs. The EXARM incorporates 6 degrees of freedom for interacting with the operators shoulder movement. The surfaces depicted in (Fig. 11.2) show the optically measured and averaged shoulder workspace of five different test persons. Data was measured with optical markers attached to bony landmarks on the human arm. Four Optotrack 3020 camera systems were used. The dark grey surface shown is the workspace boundary that the MPII bony landmark (base of the index finger) can draw, when the EXARM is worn. The more transparent, light grey surface depicts the boundary of the naturally available shoulder workspace, when the exoskeleton is not worn. For visual clarity, a virtual skeleton model is projected onto the data.

The model has a statue of 1.80 m. It can be seen that almost the entire workspace of the human shoulder is available while wearing the EXARM. Also for the elbow and the wrist, the full workspace of the natural limb is available when wearing the exoskeleton, without restrictions.

All joints of the EXARM are equipped with high-precision conductive plastic potentiometers, to sense the human arm motion. Four joints of the shoulder articulation

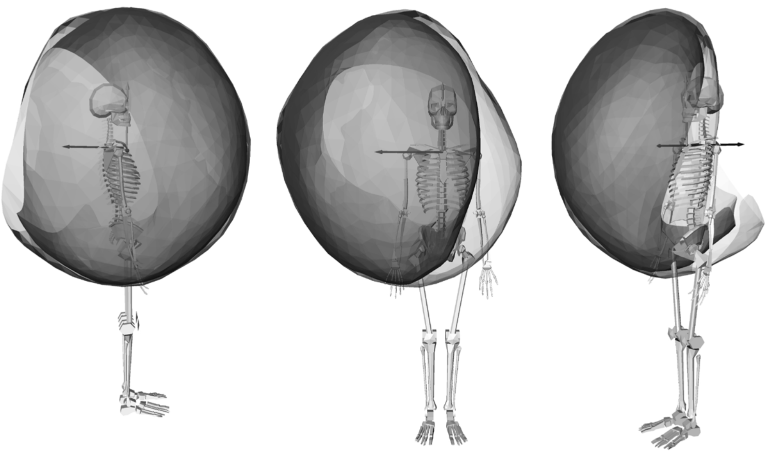

Fig. 11.2. The measured shoulder workspace of the right arm. The naturally available workspace is shown in light grey, whereas the workspace available while wearing the EXARM exoskeleton is shown in grey. Data was measured with optical markers attached to the human arm, averaged over 5 tested persons and wrapped with a surface.

have additional provisions for actuation. Those joints, as well as all other actuated joints on EXARM, are equipped with cable-pulleys. The pulleys convert the linear motion of externally guided cable tendons into joint motion. All pulleys are equipped with integrated torque sensors for motor control. Between the upper arm and the forearm, the exoskeleton incorporates 3 d.o.f., for enabling natural elbow flexion and forearm pro-supination. Only two of those joints, are equipped with pulleys for actuation. For enabling a natural motion of the operator wrist, 6 joints are implemented into the EXARM structure. Only 2 of those joints are actuated for torque-feedback to wrist ab/adduction and wrist flexion/extension. In summary, the kinematic structure of the EXARM can be described as “bridging over the human joints”. Bridging means that the exoskeleton provides a different type of kinematic structure than the human arm, while offering the same type of motions. The structure does explicitly not imitate the limb kinematics and contains motorized links that are not tightly coupled to each other. Adjustment of the limb sizes of the current EXARM prototype to individuals is therefore not necessary for persons within 1.75 ± 0.09 m statue and 68.7 ± 12.8 kg mass. The EXARM does not create constraint forces on the human joints during movement, even when misalignments to the principal human joints exist. This is why wearing the exoskeleton feels natural and very comfortable for the operators. More detail on the ergonomic design and rationale thereof can be found in (Schiele and Helm 2006).

In total, the EXARM weights about 5 kg only, out of which the mass of the movable system along the human arm is less than 2.5 kg. For testing and operating in our laboratory environment, the device is suspended on a counter-balancing system. Most structural components of the exoskeleton are laminated CRP parts. Functional components carrying motors, joint sensors, or bearings are implemented in aluminum.

11.3.2 Motorization

While the serial exoskeleton structure is fixed onto the operator's chest, the motor units are fixed to an external plate. In the future, this will be a wearable back-plate. Bowden Cable transmissions transfer the actuator motion from the motor units to the EXARM joints. This joint actuation of EXARM allows keeping the mass of the device to a minimum. The only provisions for actuation required in the moving exoskeleton system, are the pulleys which hold the cable tendons. Before deciding on which actuation technology to use, an extensive survey and prototyping campaign was carried out to compare various different actuator technologies. Actuators, such as DC motors in various configurations (e.g. direct drive, low reduction, highly reduced), ultrasonic motors, as well as passive devices such as magneto-rheologic fluid-brakes were prototyped. The main scope of the prototyping was to determine performance differences between the technologies in a haptic master–slave control loop. Secondly, the campaign aimed at searching the best suitable candidates allowing for a lightweight and portable exoskeleton implementation. The selection criteria were, among others, actuator torque to mass ratio, dynamic range, maximum peak torque, torque rise time, power consumption and so forth. Controllability was analyzed experimentally by quantifying metrics such as transparency in free-air motion and stability in contact of the slave with the environment. For the experimental analysis a variety of controller implementations were tested as well, from simple position-error controllers up to complex multi-channel controllers. A summary of the motor prototyping is provided in (Letier et al. 2006). While the best haptic performance was still reached by lowly reduced DC motors, their torque to volume ratio, as well as their torque to mass ratio was poor. This is why we decided to relocate the motors from the structure by Bowden Cable transmissions, as mentioned above.

The cable actuation train was successfully tested in a one degree of freedom haptic loop with the exoskeleton. The performance was determined within a typical master–slave control scheme (Schiele et al. 2006b). The Bowden Cable actuator can transmit a torque of approximately 1.5 Nm to the EXARM joints, which is sufficient in magnitude for creating a haptic feedback. The free movement friction is only about 0.1 Nm, which can hardly be felt at the level of the operator arm. By relocating the motors from the exoskeleton joint, we could increase the power-density on the exoskeleton joints by more then six-fold, from 2.5 to 16.0 $\mathrm{mNm/cm^3}$. The mass on each exoskeleton joint spent for actuation was thereby reduced from about 1 kg per joint to only about 150 g. The final one-degree of freedom actuator prototype is shown in (Fig. 11.3) on the test bench, before integration into EXARM.

On the left, an output bar emulates a joint of the EXARM exoskeleton. On the right-side, the relocated DC motor unit with Cable Capstan Reducer can be seen. A reduction ratio of 10:1 was implemented in the drive train. This was a good compromise trading off the maximum output torque the motor can deliver at acceptable mass and size, against the increase of the apparent inertia.

With a low reduction ratio, the contribution of the motor inertia to the felt end-effector inertia is smaller.

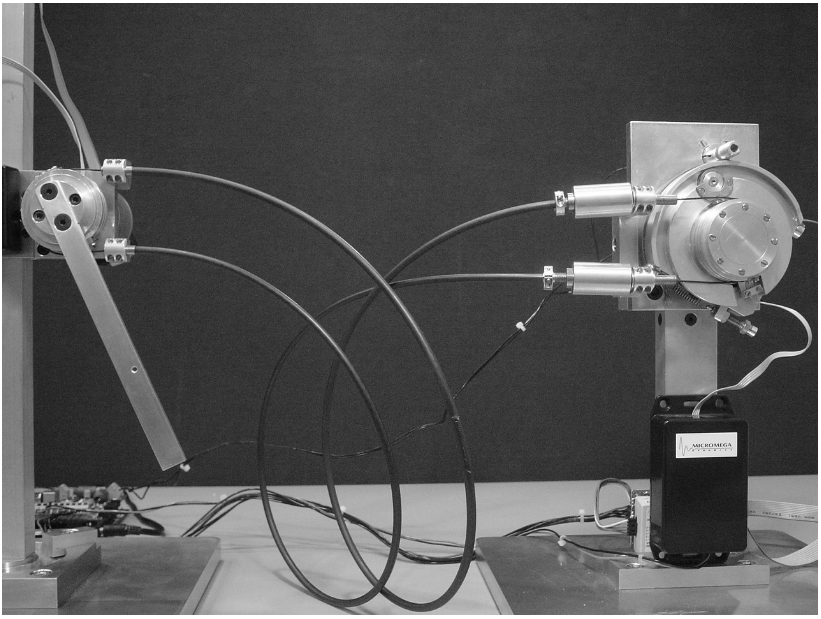

Fig. 11.3. The Bowden Cable Actuator of the EXARM on the test bench. The relocation of the motor unit from the exoskeleton joint allowed to increase the joint power density by more then six fold.

Together with the relocation of the motors, this helps to significantly increase the transparency of the exoskeleton. In both sides of the transmission, strain-gage based torque sensors are integrated into spokes (not visible) of the cable pulleys. On the motor-side of the joint, a 500 pulses per revolution incremental encoder is used for speed estimation. The control scheme found to be well performing for haptic interaction with the real slave robot joint is based on a 4-channel controller as proposed in (Lawrence 1993). Because the EXARM is kinematically not equivalent to the slave robot it shall control (16 d.o.f. versus 7 d.o.f), the multi degree of freedom bilateral control is challenging.

11.3.3 Interface to Eurobot

While for EUROBOT, a robot arm shall be used that is custom developed by ESA (Rusconi et al. 2004), currently an industrial Mitsubishi PA-10 is used for controller development and testing (Schiele et al. 2006a). For the forward link between the exoskeleton and the slave-robot, several strategies are used, ranging from end-point control with inverse kinematics optimization to joint-cluster to joint mapping. In the first method, an additional constraint is imposed on the solution of the slave-robot inverse kinematics that controls the geometric pose of the slave. The constraint is the angle of the elbow-plane with respect to the horizontal plane. In the second method, joint clusters of the EXARM are mapped onto single joints of the slave robot. This is a modified, explicit, joint to joint mapping. The joint clusters are selected such, that the robot joint motion imitates the motion of the human joints. For the force-feedback telemanipulation, an inverse mapping is performed for the joint torques. The real-time control of the exoskeleton runs under a QNX Neutrino operating system, on the exoskeleton controller computer. This computer communicates with the slave robot controller, or alternatively with a computer running a virtual model of the slave in a contact environment. The environment makes use of the open dynamics engine (ODE). All computers communicate via an Ethernet point to point link using TCP/IP. For the current 1 d.o.f implementation, set-points are exchanged between the master and the slave at 500 Hz sampling frequency. Control set-points of the 4-channel controller are among others, the joint velocities and joint torques. Data from the motor units of the exoskeleton are transferred to the exoskeleton controller via a CAN bus network. Because this is limiting the data rate for the full force-feedback implementation of EXARM, in the future, this shall be replaced by a real-time SpaceWire link that is currently under development at ESA.

11.4 Summary and conclusion

Up to now, various upper arm exoskeletons have been proposed for force-feedback tele-operation and haptic interaction with virtual environments, as well as for rehabilitation and physical training (Bergamasco et al. 1994) (Frisoli et al. 2005) (Williams-II et al. 1998) (Tsagarakis and Caldwell 2003) (Sanchez et al. 2006). Most such exoskeletons are designed like classical serial manipulator robots. Compatibility with the natural kinematics of the operators and comfort were not given much attention. Nevertheless, especially for rehabilitation exoskeletons, a poor user compatibility was reported and indicated a need for better physical human–robot interaction (Hidler and Wall 2005), (Colombo et al. 2000). More recent developments of exoskeletons try to approach those problems with innovative solutions. The Georgetown Univ. Exoskeleton (Carignan et al. 2005) for instance, aims at solving the alignment problem for the shoulder with an additional joint for scapula rotation.

The ESA EXARM exoskeleton has some distinct and innovative features for user ergonomics and improved physical human–robot interaction, that are:

- The EXARM has an ergonomic kinematic structure that is inherently prone to misalignment between the operator physiological joints and the robotic exoskeleton joints. Therefore, the EXARM does not create interaction forces that disturb or even harm the operator. Also, the EXARM does not restrict the natural motion of the human limbs.
- The EXARM actuation is entirely relocated from the device. This way, the EXARM can be lightweight, compact, wearable and portable.
- Those main features allow the EXARM to (1) operate smoothly with a large range of user statues without requiring adjustments, to (2) be highly comfortable during long duration tasks, to (3) be easily and fast dressed on and off (less then 30 seconds) and to (4) interact with the complete range of shoulder, elbow and wrist motion naturally.

Chapter 12

Discussion

12.1 Recapitulation of the goal

The goal statement for this thesis was:

It is the goal of this thesis to research how a wearable exoskeleton-type robot can be designed to be ergonomic and *truly compatible* with human operators.

This overall goal was divided into following sub-goals:
- Research how a kinematic exoskeleton structure can be made robust to variation of physical parameters between users.
- Investigate the human acceptance to such ergonomic exoskeletons with regard to the optimum of extended physiological proprioception.
- Research how an ergonomic exoskeleton can be used to control non human-like robots.
- Research how an actuation system needs to be designed to enable implementing a lightweight, compact and portable exoskeleton that can create body-grounded force-feedback.

While solving the research goal posed above, it is pursued to:
- Understand and establish the underlying geometrical and physical principles of smooth physical human–robot interaction (pHRI) with exoskeletons.
- Keep the resulting architecture of the exoskeleton *truly human compatible*, such that it offers interaction with the complete functional workspace of the human arm without generation of kinematic constraints.

12.2 Fundamentals of ergonomic exoskeletons

In this thesis, the fundamental theory of physical interaction between exoskeletons and humans has been established. For the first time, the human exoskeleton interaction has been modelled and thoroughly analyzed. The two geometrical models used for this purpose are verified and used experimentally to optimize an exoskeleton design. The goal of finding the fundamentals of ergonomic exoskeleton robot design has been achieved.

It is shown in this thesis that drawbacks of prior exoskeletons with respect to physical human–robot interaction (pHRI) lie in their underlying assumptions about the structure of the human limb.

In Chapter 2 it is explained that macro-misalignments and micro-misalignments will always exist between the axes of rotation of the human and the exoskeleton, if the exoskeleton is designed such that it copies the structure of the human limb. All prior exoskeletons presented in Chapter 1 were designed on this principle. Macro-misalignments are caused by a wrong assignment of degrees of freedom. For instance, the human shoulder is often assumed to be an ideal 3 d.o.f. spherical joint. If now an exoskeleton aims at aligning with an identical set of joints to the physiological ones, this works well for small motions in the shoulder, but causes large shifts of the respective centres of rotation if angles larger than 90 degrees are commanded (see Fig. 2.1). Such misalignments request a limitation of the device workspace a-priori, in order to prevent injury or significant discomfort to the operator. The same principle applies, if an exoskeleton joint is seemingly well aligned to a physiological joint. It is shown in Chapter 5 that perfect alignment of even a single degree of freedom exoskeleton joint to a human hinge joint is not possible. Micro-misalignments in the order of easily ± 0.1 m can exist already after short periods of movement. The pHRI model presented in Chapter 4 was instrumental to derive the true offsets at stake during the experiments. This was done by numerical model parameter estimation. It is also shown in Chapter 5 that these misalignments are the cause of large interface forces between the human and the robot during movement, even in the absence of actuation forces. Interface loads at the human–robot interface for conventionally designed exoskeletons are shown to be in the order of 18 N along the direction of the moving limb, including constraint torques between an exoskeleton attachment cuff and the limb in the order of 0.1 Nm. While these mean loads seem not significantly large, we have also shown that peak forces of up to 230 N and peak interface torques of up to 1.5 Nm can be created. Such magnitudes of loads are within the range of actuator torques for typical haptic devices, such as explained in Chapter 5.

From Part II of this thesis, it becomes clear that such interface loads are responsible for discomfort experienced by the tested subjects. The data presented in Chapter 4 and 5 of this thesis, thus supports the fact that kinematic mismatch between an exoskeleton designed to align to the human limb is the main cause of discomfort for the operators. Through the pHRI model parameter estimation, we have proven that even a seemingly well aligned conventional exoskeleton is a basis for disturbed pHRI. It is expected that the interface forces do not only prohibit comfort but also decrease the performance of haptic perception. This will still need to be investigated, as well as the effect of such forces to operators in other applications such as with rehabilitation exoskeletons or power enhancing devices.

During the time of this research, also other, independent researchers concentrated on the effects of kinematic mismatch between humans and exoskeletons. In (Hidler and Wall 2005), the authors show that natural patterns of movement are altered if a wearable rehabilitation robot is kinematically not as capable as a human limb. In (Neckel et al. 2007), it is shown that also joint moments naturally occurring in the human limb are affected by this. This has very negative impact on the outcome of robotic rehabilitation with exoskeletons.

With the results and theory presented in this thesis, for the first time such effects have been related to the geometry of the combined human robot system, which enables finding solutions.

In Chapter 3 we have elaborated a novel kinematic design paradigm for wearable exoskeletons that enables wearability independent from the physiological parameters of the operator limbs and thus independent from alignment and variability between operators.

The presented paradigm includes the key essence to building an exoskeleton kinematical structure that can smoothly interact with the human limbs, enabling the exoskeleton to:

- Interact with the complete functional workspace of the human limb for a large range of users
- Induce exact torque, position and velocities to the human joints at all times
- Not cause discomfort or safety hazards for the users during long-duration use

This human compatible behaviour is reached by an exoskeleton that is designed to:

- be wearable,
- never have more than 6 d.o.f. between two consecutive attachment points on the human limb
- explicitly not copy the kinematic structure of the adjoining human limb, thus be *non-anthropomorphic*.

The second prototype, the EXARM exoskeleton, presented in Chapter 11 incorporates such a design with a total of sixteen degrees of freedom. In order to enable a compact and lightweight implementation of such a device, some joints must be passive, non-actuated.

These fundamental rules for ergonomic exoskeleton kinematic structures are shown to successfully function by the results presented in Chapter 3 and Chapter 5. In Chapter 3 we show that nearly the entire natural functional workspace of the human limb is still available when the exoskeleton is dressed on. This is shown with four different subjects ranging from 1.74–1.90 m in stature (See Fig. 3.22).

In Chapter 5 it is shown that interface forces created by the ergonomic exoskeleton are significantly smaller. Measured interface forces are about 70% smaller than in conventional exoskeletons and measured torques were at least 60% smaller than in previous exoskeletons. This is shown for fourteen subjects ranging from 1.63–1.93 m in stature.

The presented exoskeleton kinematic structure features no singularities when dressed on. It is shown by evidence from kinematic movement simulations, that during combined human–exoskeleton motions in multiple trajectories of the shoulder workspace, the device always smoothly follows the input motion of the human. No self-motion of the mechanical structure is present (Chapter 3).

The design rule of wearability of the exoskeleton aims at reducing risk of injury to the operator due to the kinematic redundancies in the human arm, as explained in Chapter 6. If an end-point or encounter type device transfers loads to the human hand, no exact torques can be introduced in the human joints. Since the human arm in itself is a highly redundant system. For the Gait trainer (Hesse and Uhlenbrock 2000) it was reported that such transfer of loads on the limbs distal tip can cause harm to the joints by risk of hyperextension.

The second design rule presented above, equally relates to the existence of redundancies. If an exoskeleton is wearable but features more than 6 d.o.f. between two attachment points, no exact torque can again be transferred to the biological joints, in that case, due to the kinematic redundancy of the exoskeleton.

The third rule that states to explicitly not copy the kinematic structure of the human limb results from the fact that copying the kinematic structure requires alignment. As explained above, and in more detail in Chapters 2 and 3, sufficiently good alignment to the biological joints is never possible.

Altogether, those three fundamental rules for exoskeleton design ensure that the exoskeleton can be worn by users of varying stature and mass, without requiring alteration of the exoskeletons kinematic structure. This enables a comfortable feel, fast dress-on and dress-off of the device, and allows to use the device for extended durations. This was a part of the goal of this work.

Still, the mechanical implementation of the exoskeleton with such kinematics needed to be lightweight, compact and portable. The prototypes explained in Part V have successfully demonstrated that their implementation as extremely lightweight devices is possible, despite the many degrees of freedom. Chapter 12.3 will discuss the mechanical implementation of the ergonomic exoskeleton in more detail. The acceptance of humans to this design is discussed in Chapter 12.4. The feasibility of controlling a slave-robot in a tele-manipulation scenario with a multi degrees of freedom anthropomorphic robot was proven for the forward mapping in Part III. It is shown that a robot with dissimilar kinematic structure can be intuitively controlled. More detailed discussions are contained in Chapter 12.5. The actuation system of the device is a crucial element for mass reduction. The solution of the actuation problem is shown by the feasibility of relocating the actuators away from the movable structure. The relocation by means of a Bowden Cable transmission, as shown in Part IV of this thesis is new and enables the exoskeleton to be lightweight and compact while featuring similarly good performance in a haptic control scenario than devices with actuators directly integrated into their structure. Motorization will be discussed in Chapter 12.6.

12.3 On mechanical design

The mechanical feasibility of developing an ergonomic exoskeleton is a key research focus in this thesis and was shown to be viable.

The mechanical design needs to support the ergonomic kinematic design paradigm formulated in Chapter 3 and needs to enable the building of a low mass, compact and portable device. It is shown in this thesis that implementation of an ergonomic exoskeleton with a total mass of about 5 kg is possible.

The first prototype, the ARMEX exoskeleton, proposed in Chapter 3 and Chapter 10, contains 16 d.o.f., in order to satisfy the ergonomic design theory presented above. In order to keep the device as lightweight and compact as possible, some of the degrees of freedom of the device are not actuated. For the ARMEX exoskeleton, the under-actuation had been proposed as follows. Eight out of the sixteen joint axes are to be actuated, while the other eight are to be passive. Considering the fact that the exoskeleton, together with the human arm builds a parallel robot, this approach is feasible, as shown in Chapter 3 and 10. Or, otherwise formulated, the inclusion of passive, non-actuated compensatory joints into an arm exoskeleton, can make construction of an ergonomic exoskeleton feasible.

The mechanical structures of the ARMEX (Chapter 10, used in Chapter 3) and the EXARM (Chapter 11, used for Chapter 4 and 5) prototypes are slightly different. Their total mass, without actuators is 4.5 kg and 5 kg respectively. For both prototypes, the mass carried by the human arm is only about 2.4 kg, without the actuators, but already containing the means for integrating the Bowden Cable drive systems introduced in Part IV. As stated in Chapter 7, the additional mass impact on the movable exoskeleton structure in a fully actuated device will be minute, with about 150 g on each actuated joint. This mass is already contained inside the existing prototypes, since all joints incorporate already mass and volume dummies for the pulleys.

When not worn, both exoskeleton prototypes can be stowed in a very small volume of about 0.4 m (l) × 0.4 m (w) × 0.3 m (h). See Fig. 3.20 in Chapter 3 for a picture of the ARMEX when dressed off.

Both prototypes feature 6 axes for interacting with the shoulder, which proved to be feasible to allow interaction with the entire shoulder-workspace of the human arm (see Chapter 3 and Chapter 10). Kinematic simulation has revealed that the mechanical arrangement of these six joints is optimal for the task of interacting with the shoulder, as shown by the results in Chapter 3. The presence of the linear joint in this structure (see Chapter 3, Fig. 3.10) is important, to keep the device compact and independent from alignment. This way, the translation motion bridging from the operators torso to the upper arm fixation of the exoskeleton is taken over by the first three joints, while the rotary components are covered by the truly orthogonal set of joints four to six. This arrangement of joints can not reach into singularities if the arm is inserted in the upper-arm attachment ring, and thus enables seamless interaction with natural movement. Kinematic modelling with the approach described in Chapter 3 was necessary to arrive at this solution. Without a model capable of performing realistic functional movement of the human arm, the successful kinematic design would not have been possible.

In the meantime, also other researchers have approached the problem of a singularity free shoulder interfaces. In (Carignan et al. 2005) a good solution is provided. The axes of a roll-pitch-roll joint for the shoulder are twisted to move the singular positions of the joints in a less important part of the workspace, however, their solution limits the workspace and is still based on kinematic alignment to the sternoclavicular joint. In (Mihelj et al. 2007) the problem of shoulder actuation and singularity is solved for the ARMin orthosis by very complex and bulky mechanisms.

The prismatic shoulder joint of the exoskeleton has been redesigned for the EXARM. Compare Figures Fig.11.1 (Chapter 11) and Fig. 10.1 (Chapter 10). An innovative engineering solution allows actuation of this linear joint by a rotary Bowden Cable actuator, very similar to the other joints. This is enabled by a dedicated cable routing inside a multiple stage linear telescope which allows extending as well as contracting the joint by pulling action on two different cables exiting the joint. Those two cables are then fixed on a pulley, like on the other axes as well. For the final implementation of this new rotary-to-linear actuator in the new X-Arm-II prototype, please refer to Fig. 13.2 and 13.3 in the future directions section (Chapter 13).

The other joint groups, the elbow and the wrist, are implemented in a similar way, as described in detail in Chapter 3.

It is shown in Chapter 5, that the kinematic system of the first two prototypes had some drawbacks. The compensation joints on the elbow articulation, for instance, had a wrong dimensioning. This was revealed through interface force measures and identification of the measured forces with the pHRI model presented in Chapter 4. Detailed performance analysis with the pHRI model has enabled optimization of the kinematic parameters for the next prototype. In Chapter 13, the third prototype (X-Arm-II) that is currently being finalized is shown. All shortcommings identified from this work are removed by its new set of kinematic parameters.

For mechanical and dynamic modelling of human–robot interaction, the model identification of the pHRI model described in Chapter 5 has shown that the attachment stiffness of the exoskeleton on the human arm ranges typically within 200–400 N/m. Knowing a range of real values for this stiffness enables to better model the human operator within a teleoperator system analysis. This opens the way to a better controller implementation in the future.

12.4 On human acceptance

To quantify how the human compatible design of the exoskeleton is actually perceived by humans was another cornerstone in this thesis. It is shown that tested persons prefer an ergonomic exoskeleton design over a conventional one.

This question, however, has different aspects which will be discussed here. In principle, three forms of human acceptance exist with regard to pHRI: The subjective experience, which is split in conscious experience by a subject as well as the sub-conscious experience of the subject and the objectively experienced physical human–robot interaction.

In Chapter 5, results from an experiment are shown that aimed to reveal conscious subjective and objective aspects of the experienced pHRI of 14 different test subjects with the exoskeleton. The experiment concentrated on interaction with a single joint of the exoskeleton that was altered between ergonomic and conventional settings. It is clearly shown there that the pHRI is smoother when the exoskeleton is in ergonomic setting, featuring less interaction loads and a greater available working range. To proof variation in subjectively experienced comfort, however, is an extremely difficult task in such an experiment.

Many different factors have an influence to the experiment, such as the time of the day when it is performed, distractions during the experiment, as well as sincerity of correct voting over long experiment durations. Since two variables were randomized in this experiment, namely the pressure of the attachment and the kinematic setting of the exoskeleton, only the most dominant effects showed excursion on the subjective rating scales of the test subjects. The pressure variation showed influence on the rated mental demand, physical demand and effort ratings of the subjects. While a high attachment pressure caused mental demand during the signal tracking task to decrease, it significantly increased the required effort and physical demand. The subject group chose an optimum attachment pressure of 20 mmHg. This pressure showed also optimum performance in the objective experiment ratings. The kinematic condition rating showed only an effect on the mental demand subjective rating. Less mental demand is necessary to perform the tracking task if the kinematic setting of the exoskeleton joint is ergonomic. Surprisingly, however, the kinematic variation did not show a strong effect on the subjective comfort ratings but showed strong effects on most objective ratings. This might be due to the fact that the task, as well as the overall design of the experiment contained other factors that influenced the comfort of the subjects stronger than the kinematic variation.

However, it is also shown in Chapter 5, that the ergonomic design did not work optimal for all tested subjects, which very likely is the true reason that it didn't show good response in the subjective ratings averaged over the group. By means of the pHRI model presented in Chapter 4, it was shown why the kinematic setting variation did not show an advantage for some subjects. The theoretical model proved to be crucial! The pHRI model analysis with measured data revealed a non-optimal dimensioning of the passive compensation joint parameters of the EXARM. The linear compensation joint of the elbow articulation must be updated, in order to make the kinematic structure truly feasible for the user range that was tested (stature: 1.63–1.93 m, mass: 55–95 kg). Also, the spread of statures tested does not exactly coincide with the spread required by the NASA standard for astronaut crew, which is 1.49–1.90 m (NASA-STD-3000/T). However, the experiment allowed valuable insights in the geometric dependence of task performance and exoskeleton design and helped to identify shortcomings in our kinematic structure. Such rigorous analysis of wearable robots has not been presented before.

Nevertheless, the combination of subjective with objective task performance ratings confirmed that the best setting of the exoskeleton was in ergonomic configuration at the optimum attachment interface pressure chosen by this group.

Subconscious effects of the ergonomic design on the operators are best discussed when speaking about robot control and force-feedback application.

Apart from the two experiments presented, the two prototypes were used extensively by test persons during multiple demonstrations to student groups, professionals and robotics experts visiting our lab at ESA. This revealed other facets to subjectively perceived operator experiences with the exoskeleton. Most users wearing the device were amazed by the simplicity of dressing on and off, which after all took never more than about 10–30 seconds. Furthermore, reactions of the users to the availability of workspace were extremely good. Unfortunately, only very few visitors had previous experiences with other exoskeletons, which makes a comparative analysis difficult. Nevertheless, it can be stated that the device caused enthusiasm in most visitors that have tried it.

12.5 On robot control

A cornerstone to be investigated in this thesis was to proof that an exoskeleton with an ergonomic, *non-anthropomorphic* kinematic structure can still be used as an intuitive master device in a telemanipulation scenario with a slave robot. It works.

It is shown in Part III of this thesis that the EXARM prototype was successfully used to control a redundant anthropomorphic robot in an unilateral telemanipulation task. The force-reflection in a bilateral telemanipulation scenario is proven in Part IV, for a single degree of freedom interaction.

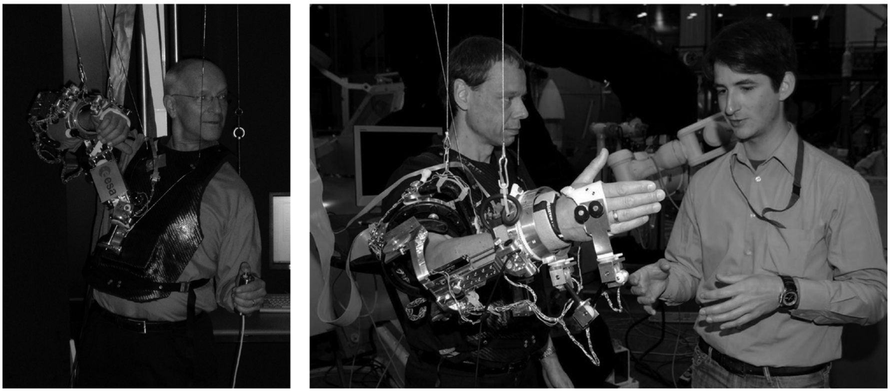

Fig. 12.1. EXARM exoskeleton during evaluation by to Astronauts. They were tasked to perform a pick and place task with a telemanipulated Mitsubishi PA-10 robot. Their input provided valuable information for improving the design. ESA Astronaut Claude Nicollier (CH) (left). ESA Astronaut Christer Fuglesang (DEN) (middle) with the author.

The ability of the exoskeleton to function successfully in a telemanipulation scenario has several aspects that will be covered in this paragraph. The kinematic mapping between master and slave, as well as the ability to function as intuitive interface for task execution has been covered in this thesis.

First, the feasibility of matching the kinematics between master device and slave device is important. It is explained in Chapter 6 that redundant slave robot manipulators in bilateral telemanipulation require some form of redundancy resolution. Several strategies were shown. In Chapter 7 results from the successful implementation of a Cartesian mapping between the exoskeleton and the slave robot are reported. The robots redundancy resolution, in these experiments, was carried out locally, by optimizing its joint space solution to stay away from its joint limits. This was a first approach, but already successfully confirmed that the exoskeleton indeed can be used as an intuitive input device.

Comparisons between the exoskeleton as input device and a multi d.o.f. joystick have shown, that the exoskeleton allows more intuitive and thus faster interaction with the slave robot. Task execution times from a simple line following experiment were about 50% quicker with the exoskeleton. The reason for the slow interaction with the joystick was the requirement to re-align the robots tool-frame coordinates at each point where the direction of the target path was changed. Curved motions were not possible with the joystick interface. In fact, when six dimensional motions, sometimes called "flying" motions, of the end-effector are to be commanded, the exoskeleton allows this very quickly and intuitively.

More qualitative testing was performed in the meantime. Most visitors to the ESA automation and robotics laboratory since 2006 were asked to perform another task with the setup described in Chapter 7. Test persons were asked to pick up an item from a pole and place it back with the slave robot, both, with the exoskeleton and with the joystick interface. During the initial experiments described in Chapter 7, a large difference in the required task execution times was already apparent. In this slightly more complex experiment an even larger difference in the execution times was quantitatively observed.

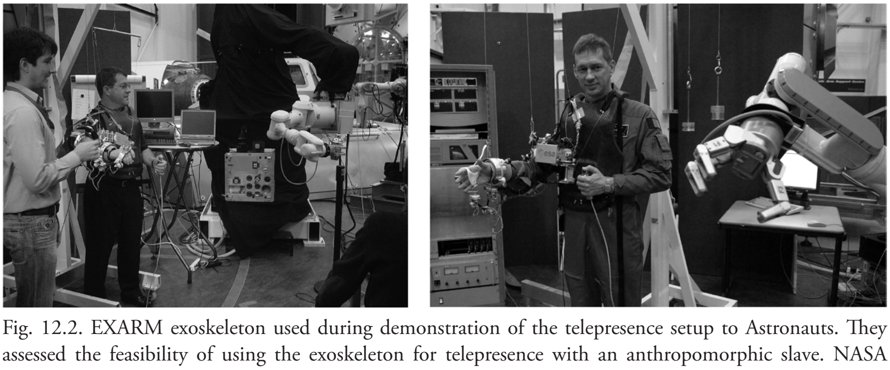

Fig. 12.2. EXARM exoskeleton used during demonstration of the telepresence setup to Astronauts. They assessed the feasibility of using the exoskeleton for telepresence with an anthropomorphic slave. NASA Astronaut Nicholas Patrick (left). ESA Astronaut Frank De Winne (B) (right).

The master–slave setup described in Chapter 7 was evaluated also during preliminary experiments with astronauts to analyze their acceptance to such technologies. Four astronauts that all had completed their robotics training at NASA Johnson-Space Centre JSC have tried the pick-and-place on a pole task with the exoskeleton.

The astronaut evaluations were performed in the frame of introducing Eurobot as an EVA support robot for ISS. ESA astronaut Frank De Winne (Fig. 5 right) was very enthusiastic about the exoskeleton and found the exoskeleton intuitive and well suitable to manipulate objects quickly and efficiently. The only NASA astronaut that tested the exoskeleton was Nicholas Patrick (Fig 5 left), who himself was one of the developers of the first EXOS Inc. exoskeleton (Burdea 1996), before his career as an astronaut. Comments from ESA astronaut Claude Nicollier (Fig. 4 left), who has significant experience with space robotic operation in space, have revealed that a redundancy resolution of the slave robot at the level of the master interface would be preferable over the Cartesian mapping in our setup. According to him, this could be an additional advantage of the exoskeleton over the existing joystick interfaces.

Since in the frame of this thesis, no other means of coupling the exoskeleton to a robot could be tested an approach of how this could be implemented is briefly outlined in Chapter 13. Should the slave robot not be anthropomorphic, then it is better to use Cartesian coordinates as done in this thesis, in Chapter 7.

An exoskeleton can thus be used to control a slave robot remotely despite its kinematic dissimilarity to both, the human arm and the slave robot. It is important to note here that if two redundant robots need to be controlled, an exoskeleton for each arm of the operator is the only solution. Four joystick workstations would otherwise be required and force-feedback to the operator body would not be possible at all.

12.6 On actuation

The investigation of actuating exoskeletons in a way such that they can be kept lightweight is a central topic of this research. A viable solution has been found.

12.6.1 Single degree of freedom actuation

In order to enable implementation of an ergonomic kinematic structure in an exoskeleton, it is necessary to relocate at least some of the actuators away from the movable structure. The Bowden Cable actuator presented in Part IV was successfully tested in haptic control loops with real slave joints (Chapter 8) and with virtual, simulated slave joints in simulated contact environments (Chapter 9) and thus showed the feasibility of relocating motors from the movable structure of the exoskeleton.

The performance of the Bowden Cable Drive (BCD) nearly matches the one of direct drive DC motors integrated with 10:1 cable capstan reducers. The huge advantage towards direct drives in the exoskeleton joints is the significantly lower mass BCD's allow for the actuation system in the mechanical moving exoskeleton structure, as described in Chapter 9. The Bowden Cable Actuator allows increasing specific power on each joint by more than six fold from 2.1 Nm/kg to 13.3 Nm/kg, and increases the joint power-density thereby more than five fold from 6.0 mNm/cm^3 to 31.3 mNm/cm^3.

Comparisons were done for DC motors of equal size. If now, a larger DC motor can be employed by relocation through the cable transmissions, also the reflected inertia to the operator can be increased. Because otherwise, a smaller motor with a higher gear reduction would be required inside the movable structure.

Before convening to the Bowden Cable transmissions, an extensive prototyping campaign was carried out to identify suitable actuator candidates for portable exoskeletons. Different actuator technologies were traded off in terms of their

- Maximum power density and specific power
- Maximum output torque
- Backlash
- Dynamic range
- Maximum contact stiffness reachable
- General quality of perceived haptic feedback in a master–slave scenario

Among the prototyped actuators were a piezoelectric actuator, a custom built magnetorheological fluid brake, a brushed and a brushless DC motor with and without backlash-free cable capstan reducers, as well as the DC motor relocated by the Bowden Cable transmissions. Relocation of the DC motor from the mechanical structure by means of hydraulic transmissions was studied as well, but proofed infeasible due to the large mass required for pistons with sufficient stroke and diameter to produce the torques required.

During this thesis it was relatively quickly pursued to investigate the reachable performance of Bowden Cable actuators, since relocation is the only way to keep apparent inertia, mass and complexity of the movable exoskeleton structure to a minimum. To reduce the mechanical complexity of the movable arm exoskeleton structure is important for a lightweight implementation. Since the ergonomic kinematic design approach results in a structure featuring sixteen degrees of freedom in total, reduction of the complexity with regard to actuator implementation is a strict requirement.

Independently, the group of Prof. Bergamasco in Pisa has developed another arm exoskeleton as well (Frisoli et al. 2007). Their actuators are also relocated by cable transmission, but routed, similar to the FreFlex device (Repperger et al. 1996) along the mechanical structure. Their approach to implementing the gear reduction after the transmission is very smart, since the cable stiffness as seen by the joint output is basically increased by multiplication with the gear ratio. However, the cable routing inside the exoskeleton again, does not allow a sufficiently compact design that could additionally tolerate the existence of passive joints for making the exoskeleton more ergonomic. Another novel exoskeleton has been developed by the Univ. of Washington (Perry et al. 2007) that also uses cable transmissions routed over multiple pulleys. It has the same disadvantage of being excessively complex and heavy.

This is why much research was invested in this thesis to create a Bowden cable based remote actuation that rather simplifies the mechanical system of the exoskeleton. For each actuated joint, only a pulley with two bearings is required and some mechanical structure to hold the external cable sleeves. No coupling between joints is created, which is not the case for other types of cable transmissions. No other group so far had investigated the use of such actuators, let alone in a haptic control loop. It must have been the complicated tribological behaviour of such systems that turned other researchers off. As described in detail in Chapter 8, the hardware architecture for such an actuator is crucial. It is instrumental to reduce stick-slip in this otherwise very susceptible transmission to friction. But it was demonstrated that if used in a haptic scenario with low pre-load, good performance can be achieved. The comparison with direct drives in Chapter 9 confirmed that the Bowden Cable transmission is an ideal option for integration in an arm exoskeleton.

12.6.2 Full actuation

It is shown that the transmission wrapping angle has some influence on the achievable contact stiffness and free movement friction. With increasing wrapping angle of the transmission the maximum contact stiffness increases along with the free movement friction. This is an important finding. In ARMEX, as well as in the EXARM prototype, no actuator has been integrated so far. However, the new X-ARM-II prototype that contains 8 actuators has already been designed, manufactured and is currently being electrically integrated.

Based on the findings in Chapter 9, I decided to apply a combination of actuator technologies to this new device. Those exoskeleton axes that require the largest actuation torques will be actuated by a Bowden Cable actuator. The largest torques are required for the first three joints on the exoskeleton, they provide force-feedback to the shoulder. For those joints, the variation of the transmission's wrapping angle will be small since they are fixed on the vest of the exoskeleton, and thus static. The variable contact stiffness, which could be seen as a disadvantage of the Bowden Cable Drive will play no role. The benefit is that a large mass otherwise required in the exoskeleton structure will be eliminated. The elbow flexion/extension joint will also be actuated with a BCD for the same reason. Other joints, that only transfer smaller torques, will be actuated by a direct drive motor coupled via a backlash-free cable capstan reducer and direct drive motors with small reduction planetary gears. This way, optimum power efficiency for the overall system can be reached with an optimum of haptic performance. Since integration of the X-Arm-II is currently ongoing, the detailed implementation is outlined in Chapter 13.

The choice of varying technologies for varying locations within the exoskeleton is supported by following facts about human perception. Human operators feature a worse torque sensing resolution in their proximal parts of the upper extremity and a better torque sensing resolution in the distal parts of the upper extremity (Tan et al. 1994). It is thus ideal from a haptic device design viewpoint to use the Bowden Cable actuators, which possess larger friction variation during free-air movement for interacting with the proximal human joints. The human operator will not even sense this variation at the level of the elbow or the shoulder. Direct drives will be used for the distal joints on the arm, where humans feature a better torque sensing resolution. This way an optimal mass reduction can be performed and a portable exoskeleton device can be implemented.

Why should a device be designed to perform better than a human can sense?

The results presented in this thesis were enabled by the combination of theoretical analysis and practical implementation in prototypes. They confirm that it is feasible to build exoskeletons that are lightweight, compact, portable and able to interact with the complete workspace of the human limb. A mechanical and kinematic structure can be conceived that is independent from alignment to individual users. It is shown that human operators perform tasks better with an ergonomic exoskeleton and that their mental demand during task execution decreases. The feasibility of implementing a lightweight actuator with good force-feedback performance is possible.

In summary, it can be concluded that the design approach postulated in this thesis is suitable to synthesize biological and technological requirements optimally for the design of truly human compatible exoskeleton robots.

Chapter 13

Future Directions

13.1 The new X-Arm-II exoskeleton

With the ending of this thesis, my research on ergonomic human arm exoskeletons will not end. In contrary – a new prototype containing full actuation is nearly finished, the first fully actuated, portable and ergonomic human arm exoskeleton X-Arm-II. It's total mass including eight actuators is 6.2 kg. This mass includes the relocated motor units. The prototype before electrical integration is shown in Fig. 13.1.

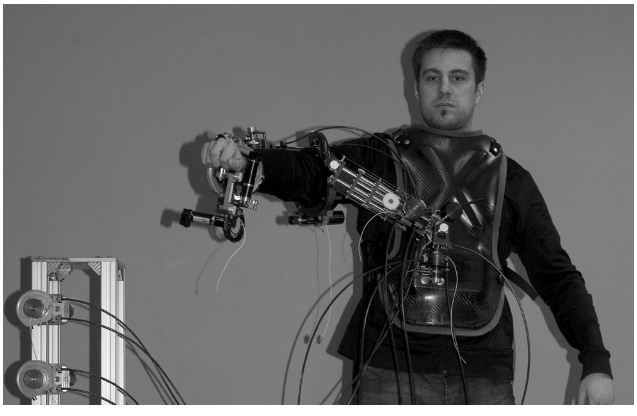

Fig. 13.1. New prototype: X-Arm-II exoskeleton integrated with all eight actuators for full force-feedback to the human arm. The Bowden Cable transmissions are shown. Two of the four relocated motor units are shown on an external stand. They can be integrated with a back-pack in the next instance. The other four actuators are directly integrated into the device.

13.1.1 Mechanical improvements

In contrast to the previous EXARM prototype, the link parameters of the joints were up-dated to allow better interaction with users in the range of 1.5–1.9 m stature. Furthermore, the mechanical structure was optimized to feature an even larger portion of the workspace. The updated link parameters were retrieved from the analysis performed in Chapter 5. The mechanical improvements to enlarge the workspace were derived from the experiments described in Chapter 3. The main changes with respect to the earlier prototypes, apart from the implementation of actuators are:

(1) The upper-arm link length between the upper arm attachment and the elbow joint can now be varied from 0.145 to 0.215 m. Before, the range was from 0.18 to 0.22 m. This tailors the mechanical design of the new X-Arm-II better to the range of individuals required by the NASA standard for space station crew (NASA-STD-3000/T 1999). This up-dated link parameter enables to reduce the relative link length of the forearm exoskeleton with respect to the human arm. In Chapter 5, it became apparent that for some subjects the forearm articulation was too large.

(2) The forearm link length was up-dated indirectly through changing the stroke range of the linear elbow compensation joint. The range of the linear compensation joint was updated to be 0.147–0.217 m. Previously, this range was 0.167–0.217 m and was too short, such that the reaction forces could not be compensated for all subjects tested in Chapter 5.

(3) The diameter of the upper-arm enclosure was enlarged from 0.127 m to 0.134 m, to allow operators with larger upper-arm diameters to wear the device and to fix the exoskeleton upper-arm attachment more proximal to the shoulder for more users.

(4) The link connecting the linear shoulder joint with the upper-arm attachment cuff was implemented as a mono-wing with two sets of pre-loaded dual angular contact bearings. This removed a bulk of mechanics that was located between the human arm and the torso when the exoskeleton was attached and the human arm was hanging down. With this change, the device is more comfortable in the rest position.

(5) The entire elbow articulation was also implemented as a mono-wing, in order to enlarge the workspace available with the exoskeleton on the left hemisphere of the body. See Fig. 3.22 (a) in Chapter 3 to see the light-grey area that was not covered by the available workspace with the exoskeleton. Now, X-Arm-II should interact with 100% of the shoulder workspace.

(6) All joints were re-designed to incorporate a set of pre-loaded angular contact bearings in each axis, to remove mechanical backlash of the system.

(7) Structural optimization techniques were used to make the mechanical parts as lightweight as possible. Optimization methods based on FEM analysis (tree-growth principle) was used. All parts were produced on CNC multi-axes milling machines.

(8) Enclosing structural parts were again implemented by means of carbon fibre composites.

(9) The mechanical axles of all joints were implemented in titanium, in order to gain further mass reduction.

(10) A new motor-stand was developed, which holds the motor-sides of the Bowden Cable drives linked to the first three axes of the shoulder and to the elbow drive.

13.1.2 Actuator implementation

As discussed in Chapter 12.6, it was deemed optimal to implement a mix of different actuator technologies into the novel prototype.

(1) Axes one, two and three (shoulder flexion & abduction) are actuated with Bowden Cable drives similar to the ones presented in Chapter 8 and 9. Axes four and five are passive. Axis six (upper-arm rotation) is actuated by a direct drive motor similar to the direct drive used for benchmarking in Chapter 9. Axis seven (elbow flexion) is actuated by a Bowden Cable drive. Axis eight and nine are passive. Axis ten (forearm rotation) is actuated by a direct drive motor, just like for the upper arm. Axis eleven can be blocked. Axis twelfe (wrist flexion) is actuated by a DC motor with low gear reduction (14:1) and a timing belt. Timing belts proved to be suitable to implement a compact, backlash-free and back driveable system. By the small reduction (1.8:1) of the timing-belt stage, the backlash of the planetary gear is reduced to a minimum. Axis twelve (wrist ab/adduction) is actuated similarly to axis eleven. All further distal axes are passive. This implementation is slightly different to the one proposed in Chapter 3 and Chapter 10. Mainly, the actuators for the wrist were placed on the more proximal joints that were passive before. This shifts the center of mass closer to the shoulder.

(2) In order to eliminate the influence of normal loads of the cable transmission on the strain gages integrated within the drive pulleys, all torque sensors are encapsulated with casings and sliding bearings that take-up normal loads. This way, the linearity of the sensors is better. Fig. 13.2 (right) shows a close-up photograph on the mechanical structure of the first three axes, before electric integration and before insertion of the cable transmissions. In Fig. 13.3 (right) the internals of the torque sensors are shown for the four axes containing the Bowden Cable drives.

(3) Fig. 13.2 (left) and Fig. 13.3 (middle) show the linear joint that is actuated by Bowden Cable transmissions as well. Rotation of the main pulley can extend or contract the multi staged linear joint. Torque, is also here sensed directly in the output of the joint.

(4) The output torque of the actuators for upper-arm and forearm rotation can not be measured like in the other joints (by spokes and strain gages inside pulleys), since they have a hollow-shaft through which the arm is fed. A trick is used. Instead of measuring the torque on the output of the motor-shaft, the reactive torque on the

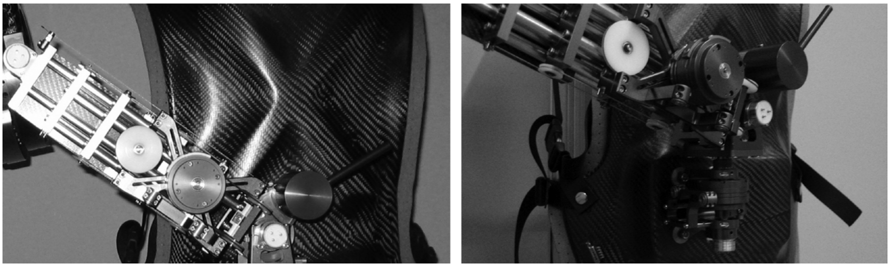

Fig. 13.2. Details of the implementation of drives in the X-ARM-II exoskeleton. The first three joints incorporate the Bowden Cable actuators. Pulleys for the receiving end of the cable transmission can be seen. All pulleys contain torque sensors integrated into their internals.

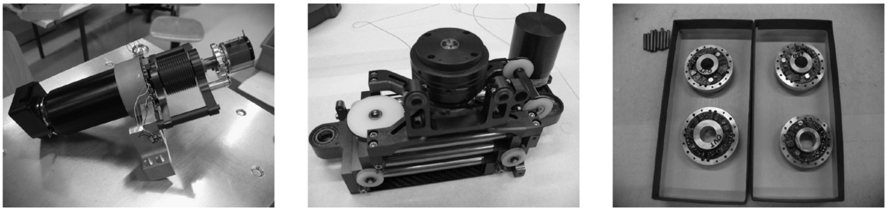

Fig. 13.3. Drive components of the X-Arm-II. The drive of joint 6 (upper arm rotation) before integration (left). The telescopic drive that converts purely rotary actuation into translational movement (middle). Four of the pulleys with integrated strain-gages and signal conditioning electronics before integration into the pulley casings.

motor casing is measured. Fig. 13.3 (left) shows the implemented architecture of this drive.

13.2 Exoskeleton motor control and actuator system

One of the most important topics to be addressed in the future is the electronic actuator control hardware. In order to reduce complexity of the required electrical harness of the exoskeleton, low power and extremely compact motor control units should be incorporated in a modular way on the exoskeleton.

One critical issue is the distribution of all measured data at a fast servo rate above 500 Hz (Chapter 7). Data distribution includes readings of the joint potentiometers, joint encoders, as well as for the torque sensors. While the position readings do not necessarily need to be acquired with more than 12 bit, the torque sensors have to be acquired with a high resolution of 16 bit to enable further use of at least 12 stable bits. Altogether a bus structure for the exoskeleton needs to be developed that can handle data rates of eight joints as high as possible. Preferably, data rates of above 1 kHz would be desirable, to aid the controller design for haptic telemanipulation. With the current implementation of a CAN-bus network (Chapter 7), the bandwidth of the data bus is already on its limit.

Therefore, ESA is currently investigating the possibility to develop a miniaturized motor control chip containing a space-wire interface optimized for deterministic real-time communications. This will open-up the way for communications with hundreds of Megabits.

In order to increase the output power of each joint on the exoskeleton, brushless motors should be used in a next instance. Their main advantage, besides creating a cleaner electrical environment, is their external motor winding. It could be cooled from outside, in order to drive higher currents into the drive to create higher torques. This would be a succession on the water cooled DC brushed drives used in the Exos Arm Master.

13.3 Bowden cable actuator identification

In order to optimize the motor controllers of the Bowden Cable actuator developed within this thesis, a full dynamic identification should be performed. This will allow model-based control and possibly open the way to a further improved system performance in terms of free movement friction, reachable contact stability in a telemanipulation scenario or overall transparency of the drives. If the couloumb friction can be estimated online, the gains could be altered to optimize the reachable contact stiffness. This would exploit the fact that additional damping and coulomb friction tolerates higher gains in a telemanipulation system (Diolaiti et al. 2006).

13.4 Multi-axis robot control with force feedback

The next step in this research is the coupling of the fully actuated X-Arm-II exoskeleton with a slave robot in bilateral telemanipulation with force-feedback. This work-step has already commenced. A lightweight robotic manipulator with suitable torque sensors will be used as a slave device in the envisaged telemanipulation experiments.

The research will concentrate on how to map the force and velocity information between the ergonomic exoskeleton and the anthropomorphic robot optimally. A first analysis will be performed with a dynamic simulator of the robot.

In order to use the exoskeleton for redundancy resolution of the slave, an explicit mapping can be implemented if the slave robot is anthropomorphic in structure. That is, if the slave robot features a roll-pitch-roll shoulder, a pitch elbow and a roll-pitch-roll wrist, then, simply the motion of the human joints must be mapped in a 1:1 relationship to the motion of the robot. The slave robot will automatically feature the same posture than the human arm. The actual motion of the end-effector will be affected by the difference in the link lengths between human and robot but it was observed that through visual feedback this can be compensated. However, the detailed effects are unknown. Because the ergonomic kinematic structure of EXARM is neither identical to the one of the slave robot nor identical to the human arm, a trick has to be applied. Since the exoskeleton can move smoothly together with the human arm, it is evident that an explicit correspondence must exist between the motion of the exoskeleton joints and the motion of the human joints. Thus, the exoskeleton to human joint mapping needs to be derived first, and then transferred to the robot by replacing the human joints with the one of the robot. This relationship will still need to be derived and implemented on the slave robot for a proof.

13.5 Man–machine interface comparisons

In this thesis, preliminary experiments have been performed to analyze the advantages of an exoskeleton type system with respect to conventional joystick input devices. In follow-up research, it will need to be investigated more rigorously what the advantages and disadvantages of such systems are.

Ideally, an experimental study will be performed with expert users, such as ESA and NASA astronauts and the original crew workstation present in the shuttle and on the station. This will then allow researching quantitatively the advantages of both systems. Then, they can be incorporated into one to serve as a truly intuitive telemanipulation workstation tailored for the use in space robotics.

13.6 Materials for flight model exoskeleton

Another important aspect for the use of an exoskeleton from within a space station such as ISS is the use of materials. It will need to be investigated whether the Bowden Cable actuator system is compatible with the requirements on space station internal infrastructure. Requirements formulated in the applicable standards are stringent and demand for materials with low off-gassing, low particle generation, electric compatibility and so forth. The development of a flight prototype of this exoskeleton is therefore still a major step.

Chapter 14

Conclusions

Following conclusions can be drawn from this thesis. They provide the first fundamentals of ergonomic exoskeleton design.

(1) It is feasible to build truly ergonomic wearable exoskeletons with technology existing today that are independent of alignment to individuals within a range of statures of at least 1.63–1.93 m and are safe and comfortable to use.
(2) Wrong interpretation of the kinematic structure of the human limbs has caused wrong assumptions about the requirements on the kinematic structures of earlier wearable exoskeletons, which has caused their unsmooth interaction with humans.
(3) Offsets between the axes of rotation of a human and an exoskeleton are in the order of tens of centimetres in various directions, even if at the start of movement both systems are well aligned.
(4) Such offsets create peak interaction forces and torques between the human and the exoskeleton attachments reaching up to above 200 N along the axis of the human limb and above 1.4 Nm around the attachment point, if no ergonomic kinematic structure is used.
(5) In exoskeletons that imitate the human limb's kinematic structure, these interaction loads limit the voluntary range of motion near the motion stroke ends of each joint and cause a limitation of available workspace.
(6) The nine degree of freedom kinematic model of the human arm and simulation approach presented in this thesis, allows analyzing the interaction capability with a proposed exoskeleton design a-priori, before building costly prototypes.
(7) The proposed single degree of freedom physical human–robot interaction (pHRI) model enables the prediction of interaction forces during combined movements

of human and exoskeleton and enables the identification of the respective centres of rotation and the attachment stiffness from measured force data.

(8) To be truly ergonomic, an exoskeleton must be explicitly *non-anthropomorphic* in its kinematic structure and wearable. It needs to offer the same range of motion than the human limb, must explicitly not copy their structure to be robust to misalignment and not possess more than six degrees of freedom between two consecutive attachments.
(9) To be ergonomic, an exoskeleton must not feature singularities within the possible workspace of the human arm, when worn by an operator.
(10) To be ergonomic, an exoskeleton must contain compensatory joints to not require alignment to the axes of motion of the human limb. Those joints can be passive.
(11) The passive joints of an ergonomic exoskeleton must feature sufficient stroke in both directions at all times during movement.
(12) An ergonomic exoskeleton allows interaction with a significantly larger workspace than offered by previous exoskeletons.
(13) An ergonomic exoskeleton creates significantly less interaction forces during movement.
(14) The EXARM exoskeleton prototype is the first truly ergonomic exoskeleton.
(15) The EXARM exoskeleton lowers the interaction forces during movement by 70%, the torques by 60% and allows an about 20% larger range of elbow motion than exoskeletons that are non-ergonomic. It also enables a significantly larger overall workspace with the human arm.
(16) Human operators perceive significantly less mental load when performing a tracking task with ergonomic exoskeletons than with non-ergonomic exoskeletons.
(17) The most comfortable interface pressure between exoskeleton and the human arm, as chosen by 14 test persons, is 20 mmHg ± 10 mmHg. This is a compromise between experiencing low mental demand and low effort and physical demand.
(18) The attachment stiffness between an exoskeleton and the human arm typically ranges from about 200 to about 400 N/m.
(19) The best overall performance for a tracking task can be reached by an ergonomic exoskeleton that is attached at the optimum attachment pressure of 20 mmHg.
(20) The EXARM ergonomic exoskeleton can be donned and doffed extremely fast because no alignment or calibration is required for different users. It takes about 30 sec. for untrained operators.

(21) An ergonomic exoskeleton of non-anthropomorphic structure can be used in unilateral telemanipulation with a slave robot of any kinematic structure. It can reduce task execution times significantly with respect to joystick type interfaces.
(22) If an ergonomic exoskeleton can be used in bilateral telemanipulation, it will be a device enabling full extended physiological proprioception.

(23) To enable a portable, lightweight and compact ergonomic exoskeleton design for force-feedback telemanipulation, at least some of the exoskeleton's actuators

must be relocated from the moving mechanical structure that encloses the human limb.

(24) To enable low apparent inertia, and good performance in force-feedback applications, relocation of low (10:1) reduction DC brushed motors can be performed by means of Bowden Cable transmissions if the torque after the transmission is measured by a sensor and actively compensated.

(25) The use of Bowden cable transmissions to relocate actuators from a movable exoskeleton structure allows increasing the power density on an exoskeleton joint by more than five fold (from 6 to 31 mNm/cm^3) and increasing the specific power by more then six fold (from 2 to 13 Nm/kg), when compared to low-reduction DC motors that are integrated directly into the structure of the exoskeleton.

(26) The contact stiffness achievable by a Bowden Cable actuator in a hard contact with a virtual slave is in the range of 24–36 Nm/rad with regard to the contact stiffness of about 41 Nm/rad reachable by a Direct Drive under the same conditions.

(27) An optimum synthesis between compactness of design and performance in a haptic control can be achieved by using Bowden Cable actuators for the proximal joints in an exoskeleton and direct drive actuators with low gear reduction in the distal joints of an exoskeleton.

(28) If force-feedback master–slave control of bi-manual anthropomorphic slave robots is to be performed from within a micro-gravity environment, the only option is to use two portable body-grounded exoskeletons.

(29) A portable ergonomic exoskeleton for bilateral control with a robot can be implemented with a total mass of about 6 kg.

(30) The previous approach to designing anthropomorphic exoskeletons for the control of anthropomorphic robots is wrong and can not enable extended physiological proprioception.

References

Acosta, A. M., Benes, J. L., Haut, B. H., Gudukas, T. L., Laughlin, J. J., Saltzman, S. M., and Dewald, J. P. A. (2003). "Upper extremity multi-degree of freedom torque generating abilities in able-bodied individuals." *25th Annual International Conference of the IEEE EMBS*, Cancun, Mexico, pp. 1429–1432.

Adelstein, B. D., and Rosen, J. M. (1992). "Design and Implementation of a Force Reflecting Manipulandum for Manual Control Research." in *Advances in Robotics*, H. Kazerooni, Ed., American Society of Mechanical Engineers New York, pp. 1–12.

Alami, R., Albu-Schaeffer, A., Bicchi, A., Bischoff, R., Chatila, R., Luca, A. D., Santis, A. D., Giralt, G., Guiochet, J., Hirzinger, G., Ingrand, F., Lippiello, V., Mattone, R., Powell, D., Sen, S., Siciliano, B., Tonietti, G., and Villani, L. (2006). "Safe and Dependable Physical Human–Robot Interaction in Anthropic Domains: State of the Art and Challenges." presented at: *IEEE International Conference on Intelligent Robots and Systems*, IEEE, Beijing, China.

Ambrose, R. O., Aldridge, H., Askew, R. S., Burridge, R. R., Bluethmann, W., Diftler, M., Lovchik, C., Magruder, D., and Rehnmark, F. (2000). "Robonaut: NASA's space humanoid." *IEEE Intelligent Systems and Their Applications*, 15(4), pp. 57–63.

Anderson, R. J., and Spong, M. W. (1989). "Bilateral Control of Teleoperators with Time Delay." *IEEE Transactions on Automatic Control*, 34(5), pp. 494–501.

Asanuma, H., and Keller, A. (1991). "A Neurological basis of motor learning and memory." *Concepts of Neuroscience*, 2, pp. 1–30.

Barbeau, H., McCrea, D. A., O'Donovan, M. J., Rossignol, S., Grill, W. M., and Lemay, M. A. (1999). "Tapping into spinal circuits to restore motor function." *Brain Research, Brain Research Reviews*, 30(1), pp. 27–51.

Bejczy, A. K., and Salisbury, J. K. (1980). "Kinesthetic Coupling between operator and remote manipulator." *Proceedings International Computer Technology Conference*, San Francisco, pp. 197–211.

Bergamasco, M., Allotta, B., Bosio, L., Ferretti, L., Parrini, G., Prisco, G. M., Salsedo, F., and Sartini, G. (1994). "An Arm Exoskeleton System for Teleoperation and Virtual Environments Applications." *IEEE International Conference on Robotics and Automation (ICRA)*, San Diego, pp. 1449–1454.

Bluethman, W., Ambrose, R., Diftler, M., Askew, S., Huber, E., Goza, M., Rehnmark, F., Lovchik, C., and Magruder, D. (2003). "Robonaut – A robot designed to work with humans in space." *Autonomous Robots*, 14, pp. 179–197.

Bologna, P., Mondellini, C., Crudo, E., Didot, F., and Foresti, L. (2004). "CONTEXT – Space A&R Controller Capabilities Extension." *8th ESA Workshop on Advanced Space Technologies for Robotics and Automation*, Noordwijk, Netherlands.

Brown, M., Tsagarakis, N., and Caldwell, D. G. (2003). "Exoskeletons for human force augmentation." *Industrial Robot*, 30(6), pp. 592–602.

Burdea, G. C. (1996). *Force and Touch Feedback for Virtual Reality*, John Wiley & Sons, New York.

Burgar, C. G., Lum, P. S., Shor, P. C., and Loos, H. F. M. V. d. (2000). "Development of robots for rehabilitation therapy: The Palo Alto VA/Stanford experience." *Journal of Rehabilitation Research and Development*, 37(6), pp. 663–673.

Butefish, C., Hummelstein, H., Denzler, P., and Mauriz, K. H. (1995). "Repetitive training of isolated movements improves the outcome of motor rehabilitation of the centrally paretic hand." *Journal of the Neurological Sciences*, 130(1), pp. 59–68.

Butterfass, J., Grebenstein, M., Liu, H., and Hirzinger, G. (2001). "DLR-Hand II: Next Generation of a Dextrous Robot Hand." *IEEE International Conference on Robotics and Automation*, Seoul, Korea, pp. 109–114.

Caldwell, D. G., Favede, C., and Tsagarakis, N. (1998). "Dextrous Exploration of a Virtual World for Improved Prototyping." *IEEE International Conference on Robotics and Automation*, Leuven, Belgium, pp. 298–303.

Caldwell, D. G., Kocak, O., and Andersen, U. (1995). "Multi-armed dexterous manipulator operation using glove/exoskeleton control and sensory feedback." *IEEE/RSJ International Conference on Intelligent Robots and Systems*, Pittsburgh, PA, pp. 567–572.

Carignan, C., Tang, J., Roderick, S., and Naylor, M. (2007) "A Configuration-Space Approach to Controlling a Rehabilitation Arm Exoskeleton." *10th IEEE International Conference on Rehabilitation Robotics*, Noordwijk, Netherlands, pp. 179–187.

Carignan, C., Liszka, M., and Roderick, S. (2005). "Design of an arm exoskeleton with scapula motion for shoulder rehabilitation." *IEEE 12th International Conference on Advanced Robotics*, Seattle, WA, pp. 524–531.

Carlson, L. B., Veatch, B. D., and Frey, D. D. (1995). "Efficiency of prosthetic cable and housing." *Journal of Prosthetics and Orthotics*, 7(3), pp. 96–99.

Chaffin, D. B., and Andersson, G. A. (1984). *Occupational Biomechanics*, Wiley-Interscience, New York.

Clauser, C. E., McConville, J. T., and Young, J. W. (1969). "Weight, volume, and center of mass of segments of the human body." *AMRL-TR-69-70*, Aerospace Medical Research Laboratories, Wright-Patterson AFB, Yellow Springs, Ohio.

Colombo, G., Joerg, M., and Dietz, V. (2000a)"Driven gait orthosis to do locomotor training of paraplegic patients." *International Conference of the 22nd Annual EMBS*, Chicago, IL, USA, pp. 3159–3163.

Colombo, G., Joerg, M., Schreier, R., and Dietz, V. (2000b). "Treadmill training of paraplegic patients using a robotic orthosis." *Journal of Rehabilitation Research and Development*, 37(6), pp. 693–700.

Denavit, J., Hartenberg, R. S., Evanston, and Ill. (1955). "A kinematic notation for lower pair mechanisms based on matrices." *ASME Journal of Applied Mechanics*, pp. 215–221.

Dewald, J. P. A., Pope, P. S., Given, J. D., Buchanan, T. S., and Rymer, W. Z. (1995). "Abnormal muscle coactivation patterns during isometric torque generation at the elbow and shoulder in hemiparetic subjects." *Brain*, 118, pp. 495–510.

Didot, F., Schoonejans, P., Stott, R., Battistoni, G., Ferraris, S., Estable, S., and Ahrns, I. (2006). "Eurobot Underwater Model: Testing the Co-operation between Humans & Robots." *9th ESA Workshop on Advanced Space Technologies for Robotics and Automation*, ESA, Noordwijk, Netherlands.

Dietz, V., Colombo, G., and Jensen, L. (1996). "Locomotor training in paraplegic patients." *18th International Conference of the IEEE Engineering in Medicine and Biology Society*, Amsterdam, pp. 595–596.

Dietz, V., and Harkema, S. J. (2004). "Locomotor activity in spinal cord-injured persons." *Journal of Applied Physiology*, 96(5), pp. 1954–1960.

Diolaiti, N., Niemeyer, G., Barbagli, F., and Jr., J. K. S. (2006). "Stability of Haptic Rendering: Discretization, Quantization, Time Delay, and Coulomb Effects." *IEEE Transactions on Robotics*, 22(2), pp. 256–268.

Frisoli, A., Borelli, L., Montagner, A., Marcheschi, S., Procopio, C., Salsedo, F., Bergamasco, M., Caboncini, M. C., Tolaini, M., and Rossi, B. (2007). "Arm rehabilitation with a robotic exoskeleton in Virtual Reality." *10th IEEE International Conference on Rehabilitation Robotics*, Noordwijk, Netherlands, pp. 631–642.

Frisoli, A., Rocchi, F., Marcheschi, S., Dettori, A., Salsedo, F., and Bergamasco, M. (2005). "A New Force-Feedback Arm Exoskeleton for Haptic Interaction in Virtual Environments." *Eurohaptics Conference and Symposium on Haptic Interfaces for Virtual Environment and Teleoperator Systems. First joint World Haptics Conference*, Pisa, pp. 195–201.

Goertz, R. C. (1964). "Manipulator Systems Development at ANL." *12th Conference on Remote Systems Technology*, ANS, pp. 117–136.

Goldspink, G., and Williams, P. E. (1990). "Muscle fibre and connective tissue changes associated with use and disuse." *Foundations for practice, Key issues in neurological physiotherapy*, L. Ada and C. Canning, eds., Heinemann, London, pp. 197–218.

Golombek, M. P., Anderson, R. C., Barnes, J. R., Bell, J. F., Bridges, N. T., Britt, D. T., Brueckner, J., Cook, R. A., Crisp, D., and Crisp, J. A. (1999). "Overview of the Mars Pathfinder Mission: Launch through landing, surface operators, data sets, and science results." *Journal of Geophysical Research*, 104(4), pp. 8523–8553.

Grange, S., Conti, F., Rouiller, P., Helmer, P., and Baur, C. (2001). "Overview of the Delta Haptic Device." *EuroHaptics*.

Hannaford, B. (1989a). "A design framework for teleoperators with kinesthetic feedback." *IEEE Transactions on Robotics and Automation*, 5(4), pp. 426–434.

Hannaford, B. (1989b). "Stability and performance tradeoffs in bi-lateral telemanipulation." *IEEE International Conference on Robotics and Automation*, Scottsdale, Arizona, USA, pp. 1764–1767.

Hart, S. G., and Staveland, L. E. (1988). "Development of the NASA-TLX (Task Load Index): Results of Empirical and Theoretical Research." *Human Mental Workload*, P. A. Hankock and M. Meshkati, eds., Elsevier Science, North-Holland, pp. 139–182.

Hashtrudi-Zaad, K., and Salcudean, S. E. (2002). "Transparency in Time-Delayed Systems and the Effect of Local Force Feedback for Transparent Teleoperation." *IEEE Transactions on Robotics and Automation*, 18(1), pp. 108–114.

Hayward, V., and Astley, O. R. (1996). "Performance Measures for Haptic Interfaces." *Robotics Research, 7th International Symposium*, pp. 195–207.

He, J., Koeneman, E. J., Schultz, R. S., Huang, H., Wanberg, J., Herring, D. E., Sugar, T., Herman, R., and Koeneman, J. B. (2005). "Design of a Robotic Upper Extremity Repetitive Therapy Device." *IEEE International Conference on Rehabilitation Robotics*, Chicago, IL, USA, pp. 95–98.

Hesse, S., and Uhlenbrock, D. (2000). "A mechanized gait trainer for restoration of gait." *Journal of Rehabilitation Research and Development*, 37(6), pp. 701–708.

Hidler, J. M., and Wall, A. (2005). "Alterations in Muscle Activation Patterns during Robotic-assisted walking." *Clinical Biomechanics*, 20(2), pp. 184–193.

Hirt, M., and Gruener, G. (2004). "Dextrous Robot Arm." *8th ESA Workshop on Advanced Space Technologies for Robotics and Automation*, ESA, Noordwijk, Netherlands.

Hirzinger, G., Sporer, N., Albu-Schaeffer, A., Haehnle, M., Krenn, R., Pascucci, A., and Schedl, M. (2002). "DLR's torque-controlled light weight robot III – are we reaching the technological limits now?" *IEEE International Conference on Robotics and Automation*, pp. 1710–1716.

Hirzinger, G., Albu-Schaeffer, A., Haehnle, M., Schaefer, I., and Sporer, N. (2001). "A new generation of torque controlled light-weight robots." *IEEE International Conference on Robotics and Automation*, Seoul, Korea, pp. 3356–3363.

Hirzinger, G., Brunner, B., Dietrich, J., and Heindl, J. (1993). "Sensor-based space robotics-ROTEX and its telerobotic features." *IEEE Transactions on Robotics and Automation*, 9(5), pp. 649–663.

Hogan, N., Krebs, H. I., Charnnarong, J., Srikrishna, P., and Sharon, A. (1992). "MIT – MANUS: A Workstation for Manual Therapy and Training I." *IEEE International Workshop on Robot and Human Communication*, Tokyo, pp. 161–165.

Hogan, N. (1985). "Impedance control: An Approach to Manipulation, Part I, II, III." *ASME Journal of Dynamic Systems, Measurement, and Control*, 107(1), pp. 1–24.

Hollerbach, J. M., and Jacobsen, S. C. (1996). "Anthropomorphic Robots and Human Interactions." *1st International Symposium on Humanoid Robots*, Waseda University, pp. 83–91.

Hunter, I. W., and Lafontaine, S. (1992). "A comparison of muscle with artificial actuators." *5th IEEE Solid-State Sensor and Actuator Workshop*, Hilton Head Island, SC, pp. 178–185.

Immersion-Cooporation. (2004). "The cybergrasp.", www.immersion.com/3d/product/cyber_force.php.

Jacobsen, S. C., Smith, F. M., Backman, D. K., and Iversen, E. K. (1991). "High performance, high dexterity, force reflective teleoperator II." *ANS Topical Meeting on Robotics and Remote Systems*, Albuquerque, NM.

Jacobsen, S., Iversen, E., Knutti, D., Johnson, R., and Biggers, K. (1986). "Design of the Utah/M.I.T. Dextrous Hand." *IEEE International Conference on Robotics and Automation*, pp. 1520–1532.

Jansen, J., Richardson, B., Pin, F., Lind, R., and Birdwell, J. (2000). "Exoskeleton for Soldier Enhancement Systems Feasibility Study." *ORNL/TM-2000/256*, Oak Ridge National Laboratory, Tennessee.

Johnson, E. G., and Corliss, W. A. (1967). "Teleoperators and Human Augmentation." *AEC-NASA Technology Survey*, Office of Technology Utilization.

Kapandji, I. A. (1992). *Funktionelle Anatomie der Gelenke – obere Extremitaet*, Ferdinand Enke Verlag, Stuttgart.

Kazerooni, H., and Steger, R. (2006). "The Berkely Lower Extremity Exoskeleton." *ASME Journal of Dynamic Systems, Measurement, and Control*, 128(1), pp. 14–25.

Kiguchi, K., Iwami, K., Yasuda, M., Watanabe, K., and Fukuda, T. (2003). "An exoskeletal robot for human shoulder joint motion assist." *IEEE/ASME Transactions on Mechatronics*, 8(1), pp. 125–135.

Kim, Y. S., Lee, J., Lee, S., and Kim, M. (2005). "A Force Reflected Exoskeleton-Type Masterarm for Human–Robot Interaction." *IEEE Transactions on Systems, Man, and Cybernetics*, 35(2), pp. 198–212.

Krebs, H. I., Volpe, B. T., Aisen, M. L., and Hogan, N. (2000). "Increasing productivity and quality of care: Robot-aided neuro-rehabilitation." *Journal of Rehabilitation Research and Development*, 37(6), pp. 639–652.

Kreuz-Delgado, K., Long, M., and Seraji, H. (1992). "Kinematic analysis of 7 DOF manipulators." *International Journal of Robotics Research*, 11(5), pp. 469–481.

Lawrence, D. (1993). "Stability and Transparency in Bilateral Teleoperation." *IEEE Transactions on Robotics and Automation*, 9(5), pp. 624–637.

Lemay, M., Hogan, N., and Dorsten, J. W. v. (1998). "Issues in Impedance Selection and Input Devices for Multipoint Powered Orthotics." *IEEE Transactions on Rehabilitation Engineering*, 6(1), pp. 102–105.

Letier, P., Avraam, M., Horodinca, M., Schiele, A., and Preumont, A. (2006). "Survey of Actuation Technologies for Body-Grounded Exoskeletons." *EuroHaptics*, Paris.

Linde, R. Q. V. D., Lammertse, P., Frederiksen, E., and Ruiter, B. (2002) "The HapticMaster, a new high-performance haptic interface." *EuroHaptics*, Edinburgh, UK, pp. 1–5.

Lum, P. S., Burgar, C. G., and Shor, P. C. (2004). "Evidence for Improved Muscle Activation Patterns After Retraining of Reaching Movements with the MIME Robotic System in Subjects with Post-Stroke Hemiparesis." *IEEE Transactions on Neural Systems and Rehabilitation Engineering*, 12(2), pp. 186–194.

Lum, P. S., Burgar, C. G., and Shor, P. C. (2003). "Use of the MIME robotic system to retrain multi-joint reaching in post-stroke hemiparesis: why some movement patterns work better than others." *25th Annual International Conference of the IEEE EMBS*, Cancun, Mexico, pp. 1475–1478.

Massie, T. H., and Salisbury, J. K. (1994). "The PHANToM Haptic Interface: A Device for Probing Virtual Objects." *International Mechanical Engineering Exposition and Congress*, Chicago, pp. 295–302.

Mihelj, M., Nef, T., and Riener, R. (2007). "ARMin II – 7 DoF rehabilitation robot: mechanics and kinematics." *IEEE International Conference on Robotics and Automation*, Rome, Italy, pp. 4120–4125.

Military-Handbook. (1991). "Anthropometry of US Military Personal."

Mitsubishi-Heavy-Industries-Ltd. "General Purpose Robot PA10 Series, Instruction Manual."

Mosher, R. S. (1967). "From handyman to hardiman." *SAE Automotive Engineering Congress*, Detroit, MI, USA, Paper No. 670088.

NASA-STD-3000/T. (1999). "International Space Station Flight Crew Integration Standard." NASA.

Neckel, N. D., Nichols, D., and Hidler, J. M. (2007). "Joint Moments Exhibited by Chronik Stroke Subjects While Walking with a Prescribed Physiological Gait Pattern." *IEEE 10th International Conference on Rehabilitation Robotics*, Noordwijk, Netherlands, pp. 771–775.

Nef, T., Mihelj, M., and Riener, R. (2007). "ARMin: a robot for patient-cooperative arm therapy." *Journal of Medical and Biological Engineering and Computing*, 45(9), pp. 887–900.

Oda, M., Inaba, N., Takano, Y., Nishida, S., Hayashi, M., and Sugano, T. (1999) "Onboard Local Compensation on ETS-VII Space Robot Teleoperation." *IEEE/ASME International Conference on Advanced Intelligent Mechatronics*, Atlanta, USA, pp. 701–706.

Ognar, G. (1994). "Entwicklung eines bowdenzug pruefstands fuer tribologische untersuchungen and bowdenzuegen," Ph.D. Thesis, Technical University of Vienna, Vienna.

Parker, L. E., and Draper, J. V. (1998). "Robotics Applications in Maintenance and Repair." Handbook of Industrial Robotics, 2nd Edition, S. Nof, Ed.

Perry, J. C., Rosen, J., and Burns, S. (2007). "Upper-Limb Powered Exoskeleton Design." *IEEE/ASME Transactions on Mechatronics*, 12(4), pp. 408–416.

Pratt, G., and Williamson, M. (1995). "Series Elastic Actuators." *IEEE/RSJ International Conference on Intelligent Robots and Systems*, Pittsburgh, pp. 388–406.

Rahman, T., Sample, W., Seliktar, R., Alexander, M., and Scavina, M. (2000). "A body-powered functional upper-limb orthosis." *Journal of Rehabilitation Research and Development*, 37, pp. 675–680.

Raibert, M. H., and Craig, J. J. (1981). "Hybrid position/force control of manipulators." *ASME Journal of Dynamic Systems, Measurement, and Control*, 102(1), pp. 275–282.

Ramanathan, R., Eberhardt, S. P., Rahman, T., Sample, W., Seliktar, R., and Alexander, M. (2000). "Analysis of Arm Trajectories of Everyday Tasks for the Development of an Upper-Limb Orthosis." *IEEE Transactions on Rehabilitation Engineering*, 8(1), pp. 60–70.

Reinkensmeyer, D., Lum, P., and Winters, J. (2002). "Emerging Technologies for improving access to movement therapy following Neurologic Injury." *Emerging and Accessible Telecommunications, Information and Healthcare Technologies*, J. M. Winters, C. Robinson, R. Simpson, and G. Vanderheiden, Eds., RESNA Press.

Reinkensmeyer, D. J., Kahn, L. E., Averbuch, M., McKenna-Cole, A., Schmitt, B. D., and Rymer, W. Z. (2000). "Understanding and treating arm movement impairment after chronic brain injury: Progress with the ARM Guide." *Journal of Rehabilitation Research and Development*, 37(6), pp. 653–662.

Reinkensmeyer, D. J., Dewald, J. P. A., and Rymer, W. Z. (1999). "Guidance-based quantification of arm impairment following brain injury: a pilot study." *IEEE Transactions on Rehabilitation Engineering*, 7(1), pp. 1–11.

Remis, S. J. (1990). "Design of an Exoskeleton with Kinesthetic Feedback: Lessons Learned." *IEEE International Conference on Systems Engineering*, Pittsburgh, PA, USA, pp. 109–112.

Repperger, D. W., Hill, B. O., Hasser, C., Roark, M., and Phillips, C. A. (1996). "Human tracking studies involving an actively powered, augmented exoskeleton." *15th Southern Biomedical Engineering Conference*, Dayton, OH, USA, pp. 28–31.

Repperger, D. W., Remis, S. J., and Merrill, G. (1990). "Performance measures of teleoperation using an exoskeleton device." *IEEE International Conference on Robotics and Automation*, Cincinnati, OH, USA, pp. 552–557.

Riener, R., Luenenburger, L., Jezernik, S., Anderschitz, M., Colombo, G., and Dietz, V. (2005a). "Patient-Cooperative Strategies for Robot-Aided Treadmill Training: First Experimental Results." *IEEE Transactions on Neural Systems and Rehabilitation Engineering*, 13(3), pp. 380–394.

Riener, R., Nef, T., and Colombo, G. (2005b). "Robot-aided neurorehabilitation of the upper extremities." *Medical and Biolocial Engineering and Computing*, 43(1), pp. 2–10.

Roebuck, J. A., Kroemer, K. H. E., and Thomson, W. G. (1975). *Engineering Anthropometry Methods*, Wiley, New York.

Romilly, D. P., Anglin, C., Gosine, R. G., Hershler, C., and Raschke, S. U. (1994). "A functional task analysis and motion simulation for the development of a powered upper-limb orthosis." *IEEE Transactions on Neural Systems and Rehabilitation Engineering*, 2(3), pp. 119–129.

Rosen, J., Hannaford, B., and Burns, S. (2003). "Neural control of an upper limb powered exoskeleton system – grant report." *First NSF Robotics and Computer Vision (RCV) Workshop*, Las Vegas.

Ruoff, C. F. (1994). "Overview of space telerobotics." *Teleoperation and Robotics in Space*, S. B. Skaar and C. F. Ruoff, Eds., American Institute of Aeronautics and Astronautics, Washington DC.

Rusconi, A., Magnani, P., Grasso, T., Rossi, G., Lodoso, J. F. G., and Magnani, G. (2004). "DEXARM – A Dextrous Robot Arm for Space Applications." *8th ESA Workshop on Advanced Space Technologies for Robotics and Automation*, ESA, Noordwijk.

Salcudean, S. E., Wong, N. M., and Hollis, R. L. (1995). "Design and Control of a Force-Reflecting Teleoperation System with Magnetically Levitated Master and Wrist." *IEEE Transactions on Robotics and Automation*, 11(6), pp. 844–858.

Sanchez, R. J., Liu, J., Rao, S., Shah, P., Smith, R., Rahman, T., Cramer, S. C., Bobrow, J. E., and Reinkensmeyer, D. J. (2006). "Automating Arm Movement Training Following Severe Stroke: Functional Exercises With Quantitative Feedback in a Gravity-Reduced Environment." *IEEE Transactions on Neural Systems and Rehabilitation Engineering*, 14(3), pp. 378–389.

Sanchez, R., Reinkensmeyer, D., Shah, P., Liu, J., Rao, S., Smith, R., Cramer, S., Rahman, T., and Bobrow, J. (2004). "Monitoring Functional Arm Movement for Home-Based Therapy after Stroke." *26th Annual International Conference of the IEEE EMBS*, San Francisco, CA, USA, pp. 4787–4790.

Schiele, A., Romstedt, J., Lee, C., Henkel, H., Klinkner, S., Bertrand, R., Rieder, R., Gellert, R., Klingelhoefer, G., Bernhardt, B., and Michaelis, H. (2008). "Nanokhod Exploration Rover, A Rugged Rover Suited for Small, Low-Cost, Planetary Lander Missions" *IEEE Robotics and Automation Magazine*, to appear, June 2008

Schiele, A. (2008a). "Case Study: quantification of constraint displacements and interaction forces in nonergonomic pHR interfaces." *Wearable Robots: Biomechatronic Exoskeletons*, J. L. Pons, Ed., John Wiley & Sons, pp. 149–154.

Schiele, A. (2008b). "Case study: The ergonomic EXARM exoskeleton." *Wearable robots: Biomechatronic exoskeletons*, J. L. Pons, Ed., John Wiley & Sons, 248–255.

Schiele, A. (2008c). "An Explicit Model to predict and Interpret Constraint Force Creation in pHRI with Exoskeletons." *IEEE International Conference on Robotics and Automation*, Pasadena, in press.

Schiele, A., Bartolomei, M. D., and Helm, F. v. d. (2006a). "Towards Intuitive Control of Space Robots: A Ground Development Facility with Exoskeleton." *IEEE/RSJ International Conference on Intelligent Robots and Systems*, Beijing, pp. 1396–1401.

Schiele, A., and Helm, F. v. d. (2006). "Kinematic Design to Improve Ergonomics in Human Machine Interaction." *IEEE Transactions on Neural Systems and Rehabilitation Engineering*, 14(2), pp. 456–469.

Schiele, A., Letier, P., Linde, R. v. d., and Helm, F. v. d. (2006b) "Bowden Cable Actuator for Force-Feedback Exoskeletons." *IEEE/RSJ International Conference on Intelligent Robots and Systems*, Beijing, pp. 3599–3604.

Schiele, A., and Visentin, G. (2003a). "The ESA Human Arm Exoskeleton for Space Robotics Telepresence." *7th International Symposium on Artificial Intelligence, Robotics and Automation in Space*, NASA, ESA, JAXA, Nara, Japan.

Schiele, A., and Visentin, G. (2003b). "Exoskeleton for a human arm, especially for spatial applications." *EP1364755*, European-Patent-Office, Ed., AT, BE, BG, CH, CY, CZ, DE, DK, EE, ES, FI, FR, GB, GR, HU, IE, IT, LI, LU, MC, NL, PT, RO, SE, SI, SK, TR.

Schiele, A., and Visentin, G. (2003c). "Exoskeleton for the human arm, in particular for space applications." *US2003223844*, U. S. Patent-Office, Ed.

Schoonejans, P., Stott, R., Didot, F., Allegra, A., Pensavalle, E., and Heemskerk, C. (2004). "Eurobot: EVA-Assistant Robot for ISS, Moon and Mars." *8th ESA Workshop on Advanced Space Technologies for Robotics and Automation*, ESA, Noordwijk.

Sciavicco, L., and Siciliano, B. (1999). *Modelling and Control of Robot Manipulators*, Springer.

Shimamoto, M. S. (1993). "TeleOperator/telePresence System (TOPS) Concept Verification Model (CVM) Development." *Recent Advances in Marine Science and Technology*, Honolulu, pp. 97–104.

Simpson, D. C. (1974). "The Choice of Control System for the Multi Movement Prosthesis: Extended Physiological Proprioception (EPP)." *The Control of Upper Extremity Prostheses and Orthoses*, P. Herberts and C. C. Thomas, Eds., Springfield, IL, pp. 146–150.

Smith, M. E., Garraway, W. M., Smith, D. L., and Akhtar, A. J. (1982). "Therapy impact on functional outcome in a controlled trial of stroke rehabilitation." *Archives of physical medicine and rehabilitation*, 63(1), pp. 21–24.

Springer, S. L., and Ferrier, N. J. (2002). "Design and control of a force reflecting haptic interface for teleoperational grasping." *ASME Journal of Mechanical Design*, 124(2), pp. 277–283.

Squyres, S. W., Arvidson, R. E., Baumgartner, E. T., Bell, J. F., Christensen, P. R., Gorevan, S., Herkenhoff, K. E., Klingelhoefer, G., Madsen, B. M., Morris, R., Rieder, R., and Romero, R. A. (2003). "Athena Mars Rover Science Investigation." *Journal of Geophysical Research*, 108(12), pp. 8062 ff.

Sunderland, A., Tinson, D. J., Bradley, E. L., Fletcher, D., Langton-Hewer, R., and Wade, D. T. (1992). "Enhanced physical therapy improves recovery of arm function after stroke. A randomized controlled trial." *Journal of Neurology, Neurosurgery, and Psychiatry*, 55, pp. 530–535.

Tan, H. Z., Srinivasan, M. A., Ebermann, B., and Cheng, B. (1994). "Human Factors for the Design of Force-Reflecting Haptic Interfaces." *3rd International Symposium on Haptic Interfaces for Virtual Environments and Teleoperator Systems*, Chicago, IL, pp. 353–359.

Thilmann, A. F., Burke, D. J., and Rymer, W. Z. (1993). *Spasticity: Mechanisms and Management*, Springer-Verlag, Berlin.

Townsend, W. T. (2000). "The BarrettHand grasper – programmably flexible part handling and assembly." *Industrial Robot: An International Journal*, 27(3), pp. 181–188.

Tsagarakis, N. G., and Caldwell, D. G. (2003). "Development and Control of a "Soft-Actuated" Exoskeleton for Use in Physiotherapy and Training." *Autonomous Robots*, 15(1), pp. 21–33.

Tsagarakis, N., Caldwell, D. G., and Medrano-Cerda, G. A. (1999). "A 7 dof pneumatic Muscle Actuator (pMA) powered Exoskeleton." *IEEE International Workshop on Robot and Human Interaction*, Pisa, Italy, pp. 327–333.

Venema, S. C., and Hannaford, B. (2001). "A probabilistic representation of human workspace for use in the design of human interface mechanisms." *IEEE/ASME Transactions on Mechatronics*, 6(3), pp. 286–294.

Veneman, J. F., Ekkelenkamp, R., Kruidhof, R., Helm, F. C. T. v. d., and Koij, H. v. d. (2005). "Design of a Series Elastic- and Bowdencable-based actuation system for use as torque actuator in exoskeleton-type training." *9th IEEE International Conference on Rehabilitation Robotics*, Chicago, IL, USA, pp. 496–499.

Vukobratovic, M., Hristic, D., and Stojiljkovic, Z. (1974). "Development of active anthropomorphic exoskeletons." *Medical and Biolocial Engineering and Computing*, 12(1), pp. 66–80.

Williams-II, R. L., North, D., Murphy, M., Berlin, J., and Krier, M. "Kinesthetic Force/Moment Feedback via Active Exoskeleton." *The Image Society Conference*, Scottsdale AZ.

Williams-II., R. L., North, D., Murphy, M., Berlin, J., and Krier, M. (1998). "Kinesthetic Force/Moment Feedback via Active Exoskeleton." *The Image Society Conference*, Scottsdale AZ.

Wu, G., Helm, F. C. T. v. d., Veeger, H. E. J., Makhsous, M., Roy, P. v., Anglin, C., Nagels, J., Karduna, A. R., McQuade, K., Wang, X., Werner, F. C., and Buchholz, B. (2005). "ISB recommendation on definitions of joint coordinate systems of various joints for the reporting of human joint motion – Part II: shoulder, elbow, wrist and hand." *Journal of Biomechanics*, 38, pp. 981–992.

Zinn, M., Khatib, O., Roth, B., and Salisbury, J. K. (2004). "New Actuation Approach for Human-Friendly Robot Design." *International Journal of Robotics Research*, 23(4), pp. 379–398.

Zoss, A., and Kazerooni, H. (2006). "Design of Electrically Actuated Lower Extremity Exoskeleton." *Advanced Robotics*, 20(9), pp. 967–988.

Acknowledgment

This work has allowed me to learn about science, research and people. In the past years I had the exceptional luck to be allowed to conduct this research while being employed at the same time. I was given the opportunity to extend my knowledge deeply and to benefit from working on such an inspiring and satisfying project. I benefited from meeting many researchers in the community and could build a strong network of partnerships and friendship.

This part of my thesis is dedicated to the people that have contributed to the outcomes of this work in so many different ways.

Without the constant support of my promotor Frans van der Helm and my Department Head at ESA, Constantinos Stavrinidis, this research would have certainly not reached the level it did. Frans, you have supported me from the start of this project through the end. Your trust in my ideas allowed me to succeed and by offering to be my “doctor father”, as we call it in Germany, you taught me how to properly conduct scientific research. Integrating with your department at Delft proofed to be an ideal match for man–machine interaction research. I am very grateful to your sharp, constructive and goal-oriented guidance on this project and to the many discussions we had on exoskeletons, biomechanics, and about writing scientific articles, often during night and otherwise unusual times. Mr. Stavrinidis enabled the implementation of this research from ESA side. Fully committed to support me from all ends, he always lent a sympathetic ear, shuffled time free for me and provided the resources necessary to build the prototypes. More importantly, however, your very enthusiastic support inspired me in difficult times and pushed me to proceed to a conclusion. I am looking forward to continuing this interesting collaboration between Delft and ESA and bringing it to a next level.

Richard van der Linde, you are a key character around this work. I remember calling you the first time to ask whether I could join your lab in Delft with the exoskeleton research. *Hell yea’* was your answer, and this is where my research took off. Your help in the definition of this work proofed invaluable and our many discussions on robotics, actuator systems and modelling approaches were always inspiring and charged with good ideas. Sometimes unusual ones, but who knows, some day we might realize them. Some of our trips to Munich or Pisa were great fun and I will never forget the many lessons about life as an engineer that I learned from you, such as how to correctly smoke a Cigar. Many discussions with other members of the Lab. in Delft will stay in my memory. I am thankful for enlightening talks about robot design and control that I had with Erik Fritz, Goeran Christiansson, Ruben Lee, Martijn Wisse, Daan Hobbelen and Jan van Frankenhuyzen. Hopefully, since my research is now completed, I can be present for more than just the sporadic drop-in and talks.

Within our Lab. at ESA, I especially owe thanks to Maurizio De Bartolomei and Gianfranco Visentin. Maurizio, it was your support and your knowledge in the field of robotics, control and software architectures for robotics that enabled us to show this very cool demonstration of the exoskeleton-robot teleoperation to Discovery Channel. Day and night we worked in the Lab to keep the deadline, do you remember? Gianfranco, I thank you for generously giving me the freedom to fulfil my ideas within the Automation and Robotics Lab. at ESA. You were always open for discussion and giving advice, what I appreciate. Discussions about the do's and don'ts with Hans Ranebo and the advice of our new colleague Johan Kohler to some of the contents of this work were very valuable and in certain ways enabled me to think out of the box. I owe my gratitude to my colleagues of the robotics group, Francesco Grassini, Michel van Winnendael, Luc Joudrier and Pantelis Poulakis for their understanding during my busy times and for their support.

I would also like to thank my trainees, master students and young graduates at ESA for their support and for giving me the opportunity to learn guiding them in their research projects. My thanks go to Daniel Baer, for his enthusiasm when supporting the building of the first Bowden Cable prototype, to Armin Wedler and Florian Oszwald for many interesting questions they have asked on mechanical and actuator system design (that allowed me to explain and understand it myself), to Karlijne van Liebergen and to Gaspar Gil Gomez. Also, I benefited from many fruitful discussions on problem solving in robotics that I had with Renato Salles. I still hope that we will build this mono-propellant actuator one day!

The support of my line hierarchy at ESA, in particular, of Gianfranco Visentin, Hanspeter Lutz, Constantinos Stavrinidis and Paolo Donzelli allowed me to realize this research while holding an employment at ESA.

Through my work as a robotic system engineer, I had the pleasure to exchange ideas with multiple researchers in space robotics. I am happy that the exoskeleton was well received by our project people in the human spaceflight directorate. It was the support of Frederic Didot, Philippe Schoonejans and Reiner Steinmeyer that has created the necessary momentum to actually use the exoskeleton for future robotics developments at ESA. Through the support of Mr. Dieter Isakeit, I was able to finance and build the next prototype, the X-Arm-II.

My thanks go to engineers and robotics researchers, outside ESA as well, that have supported this work in many different ways. In particular, I would like to thank Pierre Letier, More Avraam, Tanguy Fautre, Jean-phillipe Verschuuren, Jean-Marc Wislez and Michel Ilkoviz for their support, enthusiasm and openness in developing a fourth exoskeleton for ESA in a separate project. I owe gratitude to the team of University of applied sciences in Zweibruecken for their great support in designing and manufacturing the new X-Arm-II prototype. In particular, I would like to thank Prof. Patrick Klaer for is enthusiasm and motivation of the team, to Mr. Hans-Peter Seiberth for his great support in the design of the new prototype and wonderful collaboration, and to Mr. Christian Neu and Erik Engelmann, for their *golden hands*.

I would like to thank Constantinos Kapellos for the many discussions and insights he as provided me with the implementation of robotic teleoperation, and to my colleagues at DLR in Germany for providing and sharing their knowledge in advanced manipulator design and telemanipulation interface design for space robotics. In particular, my thanks go to Prof. Gerd Hirzinger for his openness to collaborate and for hosting me in his Labs during multiple visits that proved fruitful and inspiring. Since the beginning of this research I could be assured of his support. I would like to thank Klaus Landzettel and Carsten Preusche for discussing implementation of space robotic telemanipulation at many occasions and for allowing me to visit ongoing operations with the Rokviss experiment.

The last months have created momentum. The exoskeleton is about to be used inside an ESA project and plans are being made to extend the research on exoskeleton robot systems with other national and international partners. I am excited to what is about to come and feel ready to make a new step in my life. Let's try to fly this exoskeleton!

Here, I especially would like to thank my family. I am very thankful that you supported and encouraged me and always believed in my goals. Also, I would like to thank my friends. I am sorry to have disappeared from the scene for a while during the last months of this research… My beloved Juliane, you have helped me in so many ways. I am deeply grateful for your understanding and your ever lasting and loving support. I have chosen the ribbon bookmark in red extra for you.

Curriculum Vitae

Personal Data

April 28, 1978	**Born in Bad Bergzabern, Germany**

Education / Professional Experience

2003–2008	**Ph.D. study at TU Delft** Faculty of Mechanical Engineering, Biomechanical Engineering Department, Topic: “Fundamentals of Ergonomic Exoskeleton Robots”
2002-present	**Senior Robotic System Engineer, ESA, Automation & Robotics Section** Initialization and conducting research and development and support to ESA space robotics projects.
2001–2002	**Independent Freelancer** Mechanical design and simulations to support ongoing space projects.
11.2001	**Dipl. Ing. (FH) MEMS Engineering (Micro-Electro-Mechanical Systems), University of Applied Sciences, Kaiserslautern, Germany,** *Cum Laude,* Best graduate student of Faculty (Ranking: No. 1/58), Thesis: “Development of a Human Arm Exoskeleton for Space Robotics Telepresence: From Biomechanics to Mechanism Design” ‘Robert Bosch Award’ for outstanding achievements during Master Thesis research, from Robert Bosch Society & GmbH, 2002
1997	**Abitur at Otfried von Weissenburg Gymnasium, Dahn, Germany**